Norwegian University
of Life Sciences

Master's Thesis 2022 60 ECTS
Faculty of Chemistry, Biotechnology and Food Science

The Impact of a Structurally Conserved Second Sphere Residue in Lytic Polysaccharide Monooxygenase Catalysis

Rannei Skaali
Master of Chemistry

ACKNOWLEDGEMENTS

The research presented in this master's thesis was performed in the Natural Product Chemistry and Organic Chemistry group and the Protein Engineering and Proteomics (PEP) group at the Faculty of Chemistry, Biotechnology and Food Science at the Norwegian University of Life Sciences (NMBU).

I want to express my gratitude to Professor Morten Sørlie for the opportunity to work in his research group. I am so thankful for all your valuable advice, encouragement, and profound belief in my work and abilities. Moreover, I would like to extend my gratitude to my co-supervisor, Dr. Kelsi Hall, for her unwavering support and guidance. Your patience and kindness cannot be overstated.

The stopped-flow experiments performed during this thesis work would not have been possible without the support and nurturing of Dr. Ivan Ayuso-Fernandez. Thank you for helping me with everything stopped-flow related and sharing your vulnerable time with me. I would also like to thank Dr. Lukas Rieder for his *Af*AA11B research, making this thesis work exciting and promising, and for always answering my questions. Furthermore, I am grateful to all the brilliant people I have shared a laboratory with. Special thanks to Ole Golten for all your helpful advice and good conversations. I am also thankful for the friendship I have established with my fellow master's students Maja Mollatt, Ingrid Rokke Elvebakken, Mildrid Angard Hoff, Oda Larsen Hamarheim, and Marianne Sundet Frøseth.

Finally, I would like to thank my family for supporting me for the last five years, finishing my degree at Ås. A special thanks to my fiancé Martin Hansen for listening to my monologues about LPMOs, even though I know you do not understand what I have been talking about. I could not have done this without your endless support and love.

Rannei Skaali

Ås, May 2022

SUMMARY

Lytic polysaccharide monooxygenases (LPMOs) are redox enzymes that enhance the degradation of recalcitrant polysaccharides available in biomass. Understanding the catalytic mechanism of LPMOs is of supreme importance in achieving the full potential of LPMOs in biomass conversion into valuable products. However, limited research covers the roles of individual amino acids involved in LPMO catalysis. This master's thesis work provides insight of the impact of the gatekeeper residue on LPMO catalysis, as the gatekeeper residue is structurally conserved in all LPMOs families. The gatekeeper residue in *Af*AA11B (E160) and *Nc*AA9C (Q180) was mutated to Glu, Gln, Asp, or Asn to observe the catalytic effect of changing the length and charge of the gatekeeper residue functional group. A gatekeeper residue of carboxylic acid nature introduced a negative charge near the copper center, whereas an amide gatekeeper residue was neutrally charged. The impact of the distance between the copper center and the gatekeeper functional group was assessed when the gatekeeper residue was either Glu or Asp, or Gln or Asn.

Altering the length and charge of the gatekeeper side-chain were demonstrated to have a clear impact on several essential features for LPMO catalytic activity. *Af*AA11B and *Nc*AA9C with a gatekeeper residue with relatively long side-chain of negative charge were identified with low redox potential of the copper site with low peroxidase activity and high oxidase activity. This high oxidase activity was associated with high catalytic activity of substrate oxidation in the presence of O_2 and an external reductant during turnover. Substrate turnover with H_2O_2 supply was most efficient for the *Af*AA11B with a gatekeeper residue containing a long carboxylic acid functional group in the side chain. Furthermore, altering the electronic properties of the *Nc*AA9C copper center also affected the transportation of radicals generated in the active site from the reaction between *Nc*AA9C-Cu(I) and H_2O_2 in the absence of a substrate. As such, our results suggest two different routes through the LPMO to transport the oxidative holes.

This study demonstrates the importance of the gatekeeper residue in two different LPMO families (AA9 and AA11) with different substrate specificity (cellulose and chitin). The gatekeeper residue appears essential in critical LPMO features such as electronic properties of the copper center, oxidase activity, peroxidase activity, and substrate turnover. Conclusively, this study provides a basis for future studies on the LPMO catalytic mechanisms of recalcitrant polysaccharide degradation.

SAMMENDRAG

Lytisk polysakkarid monooksygenaser (LPMOer) er redoksenzymer som bidrar til nedbrytning av vanskelig nedbrytbare karbohydrater tilgjengelig i biomasse. Forståelse av den katalytiske mekanismen til LPMOer er essensiell for å oppnå LPMOers fulle potensial i nedbrytningen av biomasse til verdifulle produkter. Likevel er det begrenset forskning som dekker rollene til individuelle aminosyrer involvert i LPMO katalyse. Denne masteroppgaven gir innsikt i «gatekeeper» residuens påvirkning av LPMO katalyse, fordi «gatekeeperen» er konservert i alle LPMO familier. «Gatekeeperen» i *Af*AA11B (E160) og *Nc*AA9C (Q180) ble mutert til Glu, Gln, Asp eller Asn for å observere den katalytiske effekten av å endre lengden og ladningen til den funksjonelle gruppen i «gatekeeperen». En «gatekeeper» med en karboksylsyre som funksjonell gruppe i sidekjeden introduserte en negativ ladning nær koppersenteret, imens et amid «gatekeeper» residue var nøytralt ladet. Effekten av avstanden mellom koppersenteret og «gatekeeperens» funksjonelle gruppe ble analysert ved å mutere «gatekeeperen» til enten Glu eller Asp, eller Gln eller Asn.

Variasjon av lengde og ladning på «gatekeeperens» sidekjede ble vist å påvirke flere essensielle egenskaper avgjørende for LPMO katalytisk aktivitet. *Af*AA11B og *Nc*AA9C med en «gatekeeper» med en relativt lang, negativt ladet sidekjede ble identifisert med lave redokspotensialer for koppersetet med påfølgende lav peroksidaseaktivitet og høy oksidaseaktivitet. Denne høye oksidaseaktiviteten ble assosiert med høy katalytisk aktivitet ved substratoksidasjon hvor O_2 og en ekstern reduktant var til stede. Substratomsetning med tilførsel av H_2O_2 var mest effektiv for LPMOen med en «gatekeeper» med en lang, karboksylsyre funksjonell gruppe i sidekjeden. Videre påvirket også variasjonen i koppersenterets elektroniske egenskaper for *Nc*AA9C transporten av radikaler generert ved reaksjonen mellom LPMO-Cu(I) og H_2O_2 i fravær av substrat. Våre resultater antyder at det finnes to ulike transportruter for de frie radikalene gjennom LPMOer.

Denne studien demonstrerer viktigheten til «gatekeeperen» i to ulike LPMO familier (AA9 og AA11) med ulik substratspesifisitet (cellulose og kitin). «Gatekeeperen» virker essensiell for viktige egenskaper til LPMOen, slik som elektroniske egenskaper til koppersenteret, oksidaseaktivitet, peroksidaseaktivitet, og substratomsetning. Denne studien gir et grunnlag for videre forskning av LPMOers katalytiske mekanisme for nedbrytning av vanskelige nedbrytbare karbohydrater.

TABLE OF CONTENTS

ABBREVIATIONS

Å	Ångström (0.1 nanometers)
A_{280}, A_{610}	Absorbance of ultraviolet light at 280/610 nanometers
AA	Auxiliary activity
AEC	Anion exchange chromatography
Af	*Aspergillus fumigatus*
ANOVA	Analysis of variance
Ao	*Aspergillus oryzae*
AU	Absorbance units
AX (1-4)	GlcNAc (A1, N-acetyl-D-glucosamine), $(GlcNAc)_2$ (A2), $(GlcNAc)_3$ (A3), $(GlcNAc)_4$ (A4)
AX_{OX} (1-3)	Oxidized (GlcNAc) ($A1_{OX}$), oxidized $(GlcNAc)_2$ ($A2_{OX}$), oxidized $(GlcNAc)_3$ ($A3_{OX}$)
BEH	Ethylene bridged hybrid
BMD1	Buffered minimal media
bp	Base pair
BSA	Bovine serum albumin
CAZy	Carbohydrate active enzyme database
CAZyme	Carbohydrate active enzyme
CBM	Carbohydrate-binding module
CBP	Chitin-binding protein
CDH	Cellobiose dehydrogenase
CE	Carbohydrate esterase
ChitO	Chitooligosaccharide oxidase
CV	Column volumes
D	Intersheet spacing (between two adjacent polymer sheets)
DAD	Diode array detector
DMP	Dimethoxyphenol
DMSO	Dimethyl sulfoxide
DNA	Deoxyribonucleic acid
DP	Degree of polymerization
E. coli	*Escherichia coli*
E^0_{cell}	Cell potential
E^0_{red}	Standard reduction potential
EDTA	Ethylenediaminetetraacetic acid
F	Faraday's constant
g	Relative centrifugal force
GH	Glycoside hydrolase
GlcNAc	N-acetyl-D-glucosamine
GT	Glycosyltransferase
HIC	Hydrophobic interaction chromatography
HILIC	Hydrophilic interaction chromatography

HP	High-performance
HRP	Horseradish peroxidase
ICS	Ion chromatographic system
IEC	Ion-exclusion chromatography
K	The equilibrium constant
kDa	kilodalton
L2	Loop 2
L3	Loop 3
LB	Lysogeny broth
LC	Liquid chromatography
LC	C-terminal loop
LDS	Lithium dodecyl sulfate
LPMO	Lytic polysaccharide monooxygenase
MBP	Maltose binding protein
Nc	*Neurospora crassa*
nm	Nanometers
OD	Optical density
P. pastoris	*Pichia pastoris*
PAD	Pulsed amperometric detection
PASC	Phosphoric-acid swollen cellulose
PCR	Polymerase chain reaction
Pipes	Piperazine-N, N'-bis (2-ethanesulfonic acid)
PL	Polysaccharide lysase
Q1	Quartile 1 (first quartile)
Q3	Quartile 3 (third quartile)
R	The gas constant
ROS	Reactive oxygen species
rpm	Revolutions per minute
S.O.C.	Super optimal broth
Sc	*Streptomyces coelicolor*
SDS-PAGE	Sodium dodecyl sulphate polyacrylamide gel electrophoresis
SEC	Size exclusion chromatography
Sm	*Serratia marcescens*
TAE	Tris-Acetate-EDTA
TE	Tris-EDTA
TMP	N, N, N', N'-tetramethyl-1,4-phenylenediamine
UV	Ultraviolet
v	Electrons transferred in a reaction
v/v	Volume per volume
w/v	Weight per volume
WT	Wild type
YNB	Yeast nitrogen base
YPD	Yeast extract peptone dextrose
ΔG^0	Gibbs free energy

1 INTRODUCTION

Modern society has gained economic growth and reduced unemployment and energy poverty throughout the golden petroleum age. Fossil fuels covered approximately 84% of the world's energy demand in 2019 (Rapier, 2020). This energy resource is classified as a non-renewable energy source, as the fossil fuels reservoir comprises hydrocarbons generated from the decomposition of organic material over millions of years. Hence, the petroleum age is naturally coming to an end, as the fossil fuels reservoir will be depleted. Besides, fossil fuel combustion generates greenhouse gas emissions, which shows a cause-and-effect relationship with global climate change. Fossil fuel combustion is also related to local air pollution. Local air pollution is causing one of the world's most significant health and environmental problems (Ritchie and Roser, 2017). A reduction of fossil fuels combustion is required to achieve a sustainable energy system, economy, and world population health. In this regard, biomass has come into interest, as biomass represents a renewable carbon source. Biomass cannot replace fossil fuels as an energy resource alone, though it might reduce fossil-based material's combustion and generate a carbon-negative cycle, hence, addressing the sustainability goals set forth by the United Nations. To commercialize biomass-based energy, materials, and chemicals, we need to reduce the processing costs and improve the involved biotechnology tools (Wyman et al., 2005). Cost reduction and improvement of biotechnology tools require an increased understanding of the different environmental technologies involved in biomass conversion. Following, the understanding of the primary source of biomass, *i.e.,* carbohydrates, is essential.

1.1 CARBOHYDRATES

Carbohydrates are classified as monosaccharides, oligosaccharides, and polysaccharides, depending on the sugar's number of polyhydroxy aldehyde or ketone units. Each polyhydroxy aldehyde or ketone unit is assembled by oxygen, hydrogen, and five or six carbon atoms. Carbohydrates with one polyhydroxy aldehyde or ketone unit are monosaccharides, such as D-glucose. Combining two or more monosaccharide units generates an oligosaccharide, whereas a combination of more than 20 monosaccharide units is a polysaccharide. Cellulose and chitin are the most abundant polysaccharides in nature (Beckham et al., 2011, Beckham and Crowley, 2011).

1.1.1 CELLULOSE

1.1.1.1 STRUCTURE

In cellulose, D-glucopyranose units are connected by β-1,4-glycosidic bonds in homopolymer chains (O'Sullivan, 1997). In these unbranched chains, every other D-glucopyranose unit is rotated 180°, generating the repeating unit cellobiose (Figure 1.1A). Such cellulose chains may have a degree of polymerization (DP) as long as 10 000 D-glucopyranose units (O'Sullivan, 1997).

One cellulose chain may interact by hydrogen-bonding networking with another cellulose chain if the affinity for the other cellulose chain is greater than the affinity to the solvent (Figure 1.1B). The internal hydrogen-bonding network generates planar sheets, which together with van der Waals forces and hydrophobic hydration on the cellulose surface forms tightly packed microfibrils (O'Sullivan, 1997). This conformation is what makes cellulose crystalline.

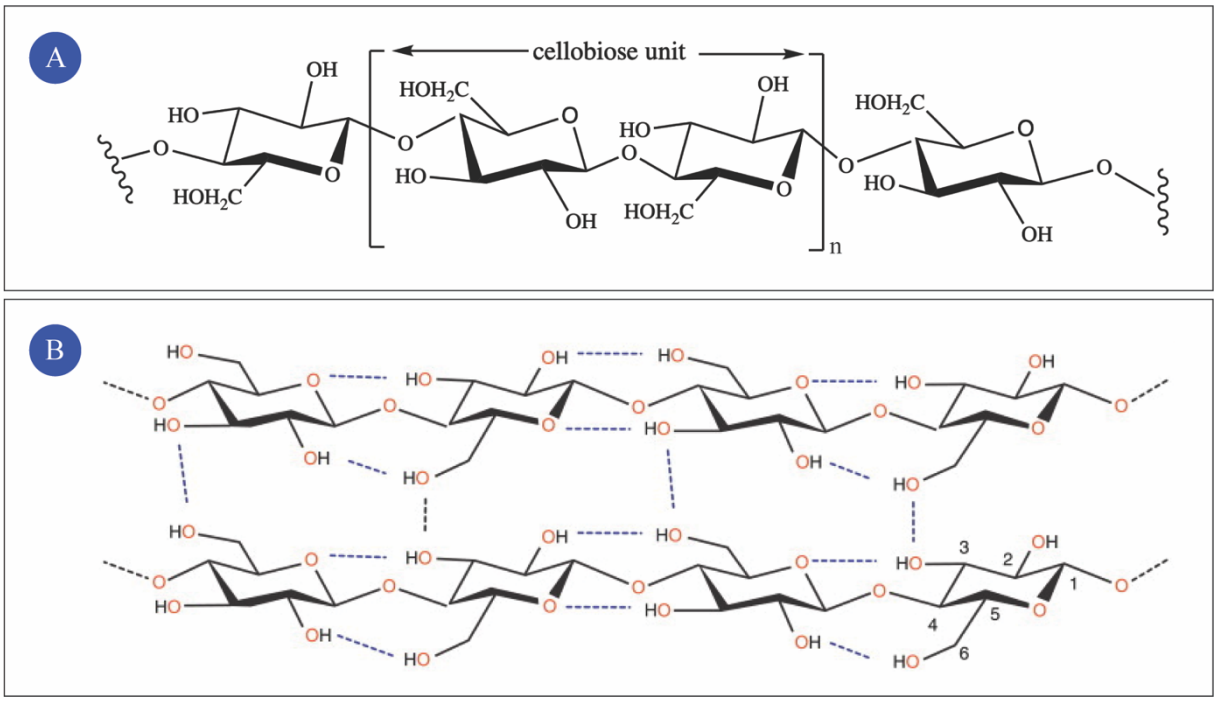

Figure 1.1: The cellulose chain of D-glucopyranose units. *(A) Every other D-glucopyranose unit is rotated 180⁰, generating the disaccharide cellobiose as the repeating unit, which is connected by β-1,4-glycosidic bonds. The figure is adapted from Mollatt and Skaali (2021) (unpublished work). (B) Hydrogen bonds, van der Waals forces, and hydrophobic interaction on the cellulose surface generates a crystalline structure of cellulose. Carbon numbering is included on the lower right D-glucopyranose unit. The illustration is derived from Hemsworth et al. (2013).*

1.1.1.2 POLYMORPHISM

Crystalline cellulose may exist in several forms, as the organization of the homopolymer cellulose chains is the establishment of cellulose polymorphs. Cellulose I is referred to as native cellulose because this is the naturally occurring cellulose polymorph (Vanderhart and Atalla, 1984). Because the hydrogen bonding pattern varies in cellulose I, generating two different unit cells, this polymorph may be subcategorized as cellulose Iα and Iβ. Following is a marginally different intersheet spacing (D) of the cellulose sheets. Cellulose Iβ (D = 3.89 Å) is for this reason more thermodynamically stable than Iα (D = 3.91 Å) because cellulose Iβ exhibits the densest packing of the cellulose sheets (Poma et al., 2016). By treating cellulose I with either 1) regeneration, *i.e.,* dissolving and reprecipitation of native cellulose, or 2) mercerization, *i.e.,* swelling of native cellulose in sodium hydroxide, cellulose II is generated (O'Sullivan, 1997). The resulting difference between cellulose I and II is the chains' orientation. In this regard, the chains are oriented in parallel or antiparallel sheets in cellulose I and II, respectively (Gardner and Blackwell, 1974). Cellulose I and II are the fundamentals for cellulose III, as treatment with amines of cellulose I and II generates cellulose III_I and III_{II}, respectively (Wada et al., 2004). The treatment of cellulose III_I and III_{II} with glycerol under 206 °C generates cellulose IV_I and IV_{II} (O'Sullivan, 1997).

The specific treatment generating the different cellulose polymorphs affects the cellulose crystallinity, as cellulose crystallinity is defined by the density of the cellulose crystal. For this reason, native cellulose is more crystalline than the other cellulose polymorphs (Igarashi et al., 2007). Furthermore, the inner core of a cellulose crystal is more crystalline compared with the crystal surface due to the reduced amount of intramolecular hydrogen bonds on the cellulose surface. As the cellulose surface has a lower structural order, the cellulose surface is sub-crystalline or amorphous (Ding and Himmel, 2006).

1.1.1.3 APPLICATION

Cellulose is an essential structural polysaccharide, as the plant cell wall consists of 35-50% cellulose. Decomposed cellulose may be used in food technology, pharmaceuticals, and chemicals due to its biodegradable and biocompatible properties of cellulose (Gupta et al., 2019). Cellulose is also an essential resource for biofuel.

1.1.2 CHITIN

1.1.2.1 STRUCTURE

Chitin is in many ways as cellulose, differing from cellulose with an acetylated amino group at C2. Hence, N-acetyl-D-glucosamine (GlcNAc) is the monomer of chitin, which is connected by β-1,4-glycosidic bonds generating an unbranched chain (Figure 1.2A). The GlcNAc units are rotated 180° relative to each other, which generates the disaccharide and repetitive unit chitobiose (Beckham and Crowley, 2011). A three-dimensional hydrogen-bonding network is also observed between and within chitin chains (Figure 1.2B), generating a crystalline structure of microfibrils (Prashanth and Tharanathan, 2007).

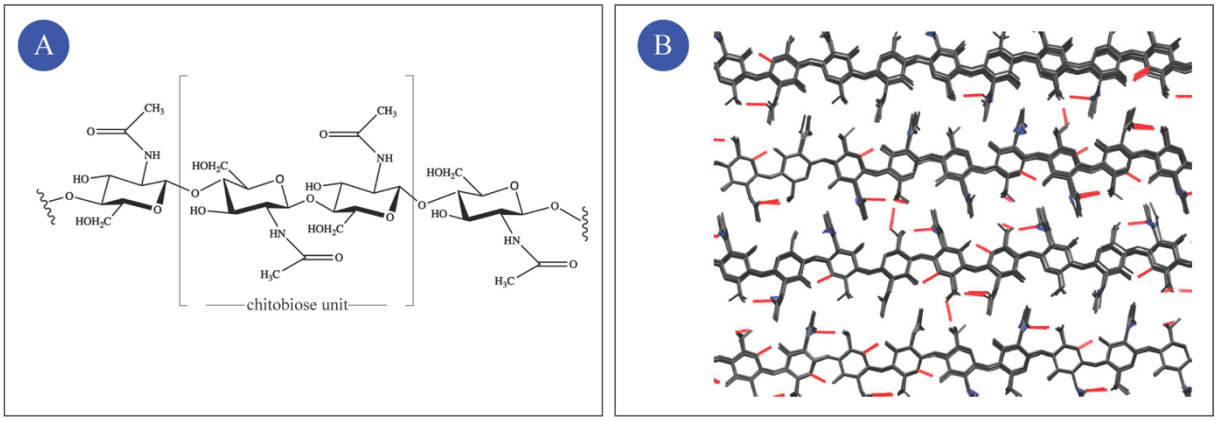

Figure 1.2: The chitin chain of N-acetyl-D-glucosamine units. *(A) β-1,4-glycosidic bonds connect GlcNAc units, which generate unbranched homopolymer chains. Chitobiose is the repetitive unit generated from 180⁰ rotation of every other GlcNAc unit. The figure is derived from Mollatt and Skaali (2021) (unpublished work). (B) The internal hydrogen-bonding network for chitin represented by α-chitin. Red and blue lines represent hydrogen bonds from oxygen and nitrogen atoms, respectively. The illustration is adapted from Beckham and Crowley (2011).*

1.1.2.2 POLYMORPHISM

The crystalline structure of chitin may be organized in different ways, generating chitin polymorphs, *i.e.,* α-, β-, and γ chitin. α chitin is the chitin polymorph most abundant in nature and consists of antiparallel chitin chains with the reducing ends of GlcNAc oriented in opposite directions of each other (Minke and Blackwell, 1978). The antiparallel structure makes the α polymorph the most crystalline of the chitin polymorphs because a higher number of hydrogen bonds are obtained between the sheets, which generates higher stability and density of the crystalline structure compared with β and γ chitin. β chitin comprises parallel chitin chains, where the reducing ends are oriented in the same direction (Gardner and Blackwell, 1975). In some chitin crystals, the chitin chains are oriented with two parallel chains followed by one antiparallel chain. This crystalline structure is called γ chitin (Kaya et al., 2017).

1.1.2.3 APPLICATION

As for cellulose, chitin is also an abundant polysaccharide in nature. Chitin is an essential component in the shell of shrimps and crabs, and in the cell wall of fungi and algae (Beckham and Crowley, 2011). Decomposition of chitin generates chitosan, chitooligosaccharides, and other derivatives. Due to the shorter chains and higher water solubility than pure chitin, chitosan and chitooligosaccharides are easier applicated. Applications such as biofuels, bioplastics, agriculture technologies, and medicines have been emphasized (Kurita et al., 1993, Rinaudo, 2006).

1.2 DEGRADATION OF CARBOHYDRATES

The natural fermentation process of crystalline carbohydrates is slow due to the crystalline structure of the carbohydrates in biomass (Wolfenden et al., 1998). Hence, the crystalline structure must be disrupted by microbial or thermochemical conversion to generate biomass-based energy, materials, and chemicals competitive with fossil-based alternatives (Figure 1.3) (Cheah et al., 2020). Biomass can be thermochemical converted to syngas and following transformed to ethanol. However, the thermochemical conversion of biomass is shown to be less environmentally friendly than the microbial conversion (Mu et al., 2010). Microbial conversion of biomass includes the hydrolysis of glycosidic bonds connecting the monomer units of the carbohydrates (saccharification) and fermentation of the sugar units (Cheah et al., 2020). Pretreatment technologies optimize the efficiency of the microbial conversion of biomass (Sharma et al., 2019).

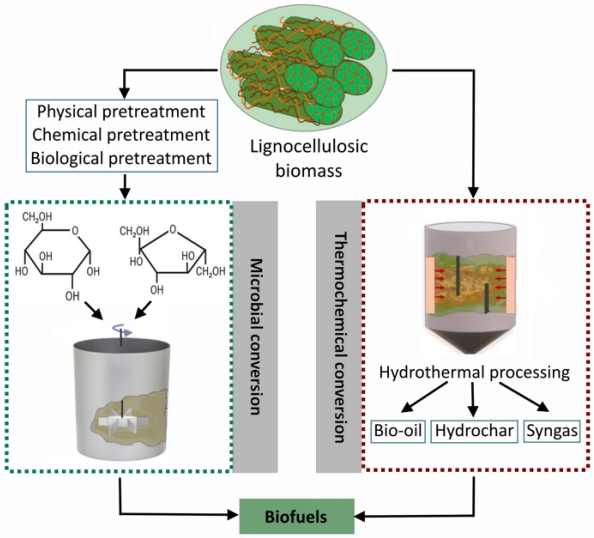

Figure 1.3: Disruption of the crystalline carbohydrate structure of biomass. *Biomass may be disrupted by microbial or thermochemical conversion to generate biomass-based energy, materials, and chemicals, where pretreatment technologies may be used prior to the microbial conversion. The illustration was derived from Cheah et al. (2020).*

The pretreatment technologies of choice are physical, chemical, physicochemical, and biological pretreatment. However, which pretreatment technique used to disrupt the crystalline carbohydrate structure depend on the biomass type, economic capital, and environmental impact (Limayem and Ricke, 2012, Menon and Rao, 2012). Today's ongoing problems in pretreatment technology are biomass energy content and environmental effects related to the economy, as the pretreatment technology is considered an expensive step in carbohydrate decomposition from a biomass stock (Naresh Kumar et al., 2019). Ideally, pretreatment technology should lead to a more straightforward decomposition of biomass without the economic and energy consumption drawbacks present today (Kumar and Sharma, 2017, Prasad et al., 2016).

Chemical pretreatment is one of the pretreatment technologies introduced above, which involves pretreating the biomass with a chemical. The chemical may be an alkaline, ionic, or acidic solution (Cheah et al., 2020). Unfortunately, an additional washing step must be added prior to saccharification due to inhibitors generated by acidic solutions. Another drawback is the corrosive effect of acids, making acidic chemical pretreatment technology environmentally toxic (Kumar and Sharma, 2017). The ionic pretreatment is more environmentally friendly, though this chemical pretreatment technology is expensive (Cheah et al., 2020).

Instead of adding a chemical to the biomass, the biomass may be pretreated physically or mechanically by a physical pretreatment. Microwave irradiation and freezing are physical pretreatment technologies that are more environmentally friendly than chemical pretreatment (Cheah et al., 2020). Freezing breaks down the cell walls due to the increased water volume going from liquid to solid-state, which is also a cheap pretreatment technology (Rooni et al., 2017). Microwave irradiation reduces the crystallinity of the carbohydrates due to the high energy radiation, though the pretreatment technology is expensive (Jędrzejczyk et al., 2019). Physical pretreatments that are of low cost and environmentally friendly are milling and extrusion (Cheah et al., 2020). The biomass particle size is reduced dramatically by milling (Cheah et al., 2020). Extrusion changes the biomass particles structurally, generating char and gaseous products (Maurya et al., 2015). However, a drawback of physical pretreatment is that the pretreatment method generally consumes more energy than the biomass energy content (Menon and Rao, 2012).

A combination of physical and chemical pretreatments generates the pretreatment technology physicochemical pretreatment. Such a combination may cause a more effective disruption of

the crystalline carbohydrates structure of the biomass than a single pretreatment (Cheah et al., 2020). An example is a combination of the chemical alkali pretreatment with the physical milling pretreatment (Kumar and Sharma, 2017). Moreover, the steam explosion is another example of physicochemical pretreatment, which involves decompression of the biomass by steam and pressure variation (Kumar and Sharma, 2017).

The crystalline structure of carbohydrates may also be disrupted by biological pretreatment, which occurs naturally in an organism by certain microorganisms (*i.e.,* fungi and bacteria) and organisms (*i.e.,* insects, worms, and gastropods) (Cheah et al., 2020). Some fungi and bacteria secrete enzymes that pretreat the biomass. Insects, worms, and gastropods may also pretreat biomass due to their mechanical, enzymatic, and physiological properties (Devi et al., 2020, Trincone, 2018, Varelas and Langton, 2017). Because this pretreatment occurs naturally there are mild environmental conditions and there is no need for energy input. Compared with the other pretreatment technologies, biological pretreatment is not favored because the method is time-consuming, and some of the biomass may be consumed (Cheah et al., 2020).

Regardless of pretreatment technology, the overall goal is to prepare the biomass for microbial conversion by making the glycosidic bonds available for hydrolysis. Carbohydrate active enzymes (CAZymes) are responsible the hydrolysis of glycosidic bonds in recalcitrant carbohydrates (Cantarel et al., 2009).

1.3 CARBOHYDRATE ACTIVE ENZYMES

CAZymes catalyze generation and degradation of complex carbohydrates and glycoconjugates (Cantarel et al., 2009). According to the carbohydrate active enzyme database (CAZy), approximately 3000 CAZyme families are divided into five classes, *i.e.,* glycoside hydrolases (GHs), glycosyltransferases (GTs), polysaccharide lyases (PLs), carbohydrate esterases (CEs), and carbohydrate-binding modules (CBMs). GHs are the CAZyme class which is best characterized by the five CAZy classes due to their extensive biotechnological and biomedical applications and will, for this reason, be the focus in the emphasis of carbohydrate active enzymes (Cantarel et al., 2009).

1.3.1 GLYCOSIDE HYDROLASES

GHs accounts for the hydrolysis of glycosidic bonds in complex polysaccharides (Teeri, 1997). Cellulases, chitinases, and amylases are GHs that catalyze the hydrolysis of glycosidic bonds in cellulose, chitin, and starch, respectively (Hamre et al., 2019, Igarashi et al., 2011, Reilly, 2007). Hydrolysis may occur at random internal sites or the reducing or non-reducing end of the polysaccharide, on the condition that the CAZyme is an endo- or exoacting GH (Hamre et al., 2019).

GHs catalyzation of glycosidic bond hydrolysis may occur independently or in synergy with other CAZymes (Hamre et al., 2019, Igarashi et al., 2011). Cel7A and Cel6A are exoacting cellulases that operate in synergy to catalyze the hydrolysis of glycosidic bonds from the reducing and non-reducing end of cellulose, respectively (Igarashi et al., 2011). Examples of two endoacting GHs, *e.g.,* CelZ and CelY, operating in synergy have also been observed (Zhou and Ingram, 2000).

1.3.2 AUXILIARY ACTIVITY FAMILIES

Initially, it was believed that GHs were the main enzymes catalyzing the degradation of recalcitrant carbohydrates (Merino and Cherry, 2007). It was later discovered that GHs and other carbohydrate active enzymes can act in synergy with auxiliary activity (AA) families. Ten AA families are known thus far, classified in the CAZy database according to biochemical characterizations and sequence similarities (Levasseur et al., 2013). Seven of these AA families, *i.e.,* AA9, AA10, AA11, AA13, AA14, AA15, and AA16, are classified as lytic polysaccharide monooxygenases (LPMOs) (Levasseur et al., 2013). LPMOs include enzymes that potentially catalyze the degradation of plant cell walls by making the recalcitrant carbohydrates comprising the plant cell wall accessible for the GHs (Levasseur et al., 2013). The AA family classification was established when the families GH61 and CBM33 were discovered to differentiate from other GHs and CBMs families, by increasing their catalytic activity in the presence of divalent metal ions (Harris et al., 2010). Following, the members of family GH61 and CBM33 were reclassified as AA9s and AA10s, respectively, as the enzymes were shown to be oxidative by catalyzing the glycosidic bonds cleavage using a reductant and molecular oxygen (Horn et al., 2012, Vaaje-Kolstad et al., 2010).

1.4 LYTIC POLYSACCHARIDE MONOOXYGENASES

LPMOs are redox enzymes that catalyze the oxidation of one of the carbons in a scissile glycosidic bond of recalcitrant polysaccharides, resulting in the hydrolysis of the glycosidic bond. This LPMO function was first demonstrated by Vaaje-Kolstad et al. (2010). However, the oxidative cleavage of glycosidic bonds catalyzed by LPMOs was noted earlier (Vaaje-Kolstad et al., 2005a). Because most research covers the LPMO families AA9, AA10, and AA11, these families will be the focus when describing these redox enzymes.

1.4.1 LPMO STRUCTURE

1.4.1.1 THREE-DIMENSIONAL STRUCTURE

LPMOs show structure similarities throughout the different families by exhibiting an immunoglobulin or fibronectin-like core of the catalytic domain (Vaaje-Kolstad et al., 2017). The core structure of the catalytic domain comprises a β sandwich with two β sheets, where each β sheet composes of seven or eight β strands connected by helices and loops (Vaaje-Kolstad et al., 2017). The typical LPMO fold is presented in Figure 1.4 for families AA9, AA10, and AA11. The three-dimensional structure of the catalytic domain of family AA9 is illustrated by *Neurospora crassa* AA9C (Isaksen et al., 2014). Family AA10 is represented by the well-studied *Serratia marcescens* AA10A (Vaaje-Kolstad et al., 2005a). *Sm*AA10A is also referred to as CBP21 (*mw* 21 kDa) because the AA10s were known as chitin-binding proteins (CBPs) before they were identified as LPMOs (Vaaje-Kolstad et al., 2005a). *Aspergillus fumigatus* AA11B illustrates the three-dimensional structures of family AA11, which is a recently characterized LPMO (Rieder et al., 2021b). The crystal structure of *Af*AA11B is not yet characterized, though a model of the catalytic domain has been estimated based on the 72.6% sequence identity with *Aspergillus oryzae* AA11 (Rieder et al., 2021b).

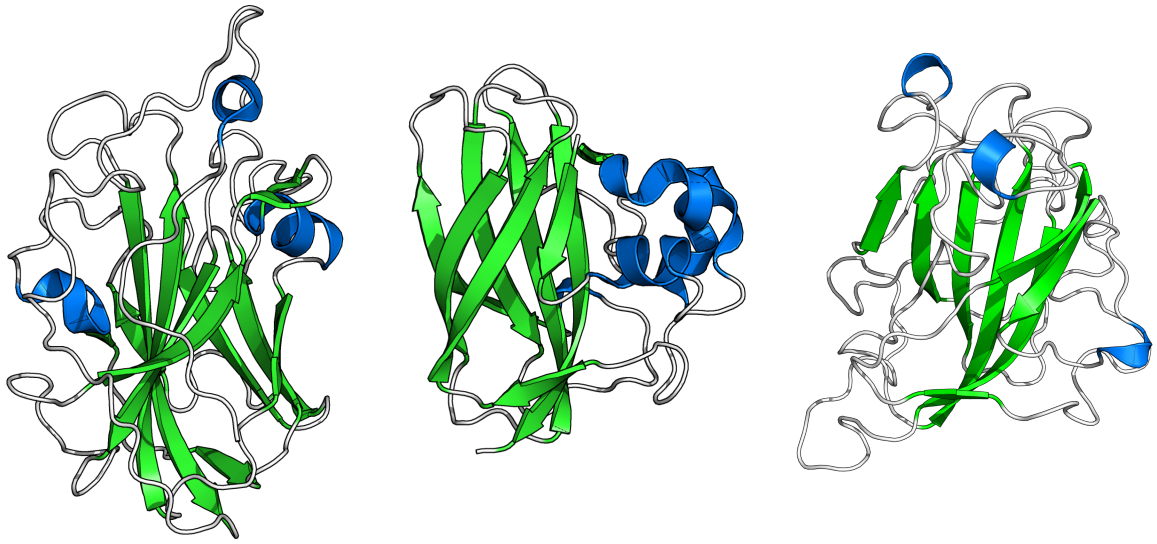

Figure 1.4: Three-dimensional structure of enzymes in family AA9, AA10, and AA11. *β strands, helices, and loops are colored in green, blue, and white, respectively. Family AA9, AA10, and AA11 are represented by the catalytic domain of NcAA9C (PDB ID: 4D7U), SmAA10A (PDB ID: 2BEM), and AfAA11B, respectively. The crystal structure of AfAA11B is not yet characterized, and the illustration is based on using the SWISS-MODEL server and AoAA11 as a template (72.6% sequence identity) (PDB ID: 4MAH).*

The catalytic domain of LPMOs is, in some cases, linked to a CBM. CBMs were briefly introduced in Chapter 1.3 and are classified in the CAZy database according to their amino acid similarity (Levasseur et al., 2013). These modules are hypothesized to increase catalytic efficiency by increasing substrate-binding affinity (Hashimoto et al., 2000). The catalytic domain of *Nc*AA9C is linked to CBM1 by a 50 amino acids long linker with a high serine and threonine content (Borisova et al., 2015). Moreover, *Af*AA11B is also observed with a module connected to its catalytic domain, *i.e.,* the X278 module. Even though the X278 module is not assigned to any family in the CAZy database yet, the module is believed to function as a CBM (L. Rieder, pers. com., 2021). The *Af*AA11B catalytic domain and the X278 are connected by 102 amino acids long linker (Rieder et al., 2021b). In contrast, *Sm*AA10A is a single domain LPMO, also classified as a CBM of family 33 in the CAZy database (Levasseur et al., 2013).

1.4.1.2 SUBSTRATE-BINDING SURFACE

Helices and loops connect the β strands in the core structure of the LPMO and generate the unique substrate-binding surface of each LPMO (Vaaje-Kolstad et al., 2017). The substrate-binding surface is flat and believed to interact with crystalline substrates containing a flat surface (Aachmann et al., 2012, Vaaje-Kolstad et al., 2010). However, studies have shown that

LPMOs also interact with soluble substrates (Isaksen et al., 2014, Rieder et al., 2021b). One region of the substrate-binding surface is loop 2 (L2). L2 is observed between the β1-2 strands and β1-3 strands for fungal and bacterial LPMOs, respectively (Hemsworth et al., 2014, Li et al., 2012, Wu et al., 2013). Furthermore, some AA9s include a region of helices and loops that interact with the L2 region, referred to as loop 3 (L3). L3 is located between the β3-4 strands in AA9s (Borisova et al., 2015). The substrate-binding surface of AA9s also exhibits loop short (LS) and long C-terminal loop (LC) regions close to the L2 region (Wu et al., 2013). It is speculated whether the amino acid composition, *i.e.,* the aromatic residues, of the substrate-binding surface loops L2, L3, LS, and LC give rise to substrate recognition, specificity, and binding (Li et al., 2012, Vaaje-Kolstad et al., 2005b, Wu et al., 2013). The substrate-binding surface loops illustrated by *Nc*AA9C, CBP21, and *Ao*AA11 are highlighted in Figure 1.5 as representative LPMOs for the families AA9, AA10, and AA11, respectively.

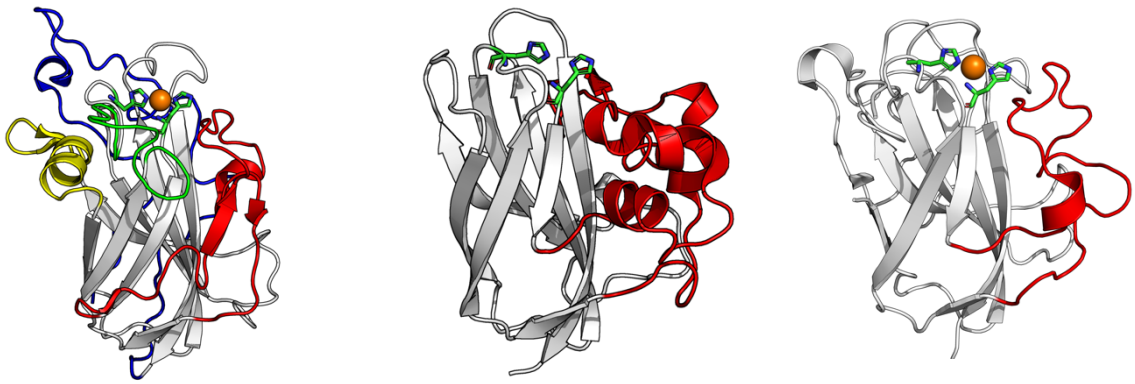

Figure 1.5: Catalytic domains of family AA9, AA10, and AA11 with the substrate-binding surface loops. *Loop regions L2, L3, LS, and LC, are colored in red, green, yellow, and blue, respectively. NcAA9C, CBP21, and AoAA11 represent family AA9, AA10, and AA11, respectively. The relative position of the substrate-binding surface loops to the catalytic center of each LPMO family is also illustrated by highlighting the Cu as a sphere and Cu coordinating histidine residues as sticks. Because the crystal structure of CBP21 was not solved with a Cu in the active site, Cu is missing from the AA10 representation.*

The catalytic center is in the substrate-binding surface and is fully conserved in all LPMO families. This catalytic center comprises two histidine residues coordinating one copper atom and is referred to as the histidine brace. Quinlan et al. (2011) showed that the Cu^{2+} ion was bound strongly to the LPMO compared with other divalent metal ions, such as Zn^{2+}, Ni^{2+}, and Mg^{2+}. Hence, LPMOs are defined as copper-dependent enzymes. The copper is coordinated with four to six ligands in its oxidized form, where three of these ligands are nitrogen atoms from the histidine brace, and one ligand is an aromatic residue (Kjaergaard et al., 2014). This

aromatic residue is typically a tyrosine in the proximal-axial position of copper, which generates an octahedral geometry, or a phenylalanine, which generates an unusual compressed trigonal-bipyramidal geometry due to steric hindrance. One or two water molecules fulfill the copper coordination sphere (Kjaergaard et al., 2014). However, the copper-coordination changes when Cu(II) is reduced to Cu(I), where the number of ligands is reduced from a maximum of six ligands to four cooper-coordinated ligands (Beeson et al., 2015). Cu(I)-coordination includes three nitrogen ligands from the histidine brace and one cosubstrate ligand. Following, the aforementioned plane geometry of the substrate binding surface is formed (Vaaje-Kolstad et al., 2010). Notably, this change in ligand-binding occurs without rearranging the residues in close proximity to the copper center (Kjaergaard et al., 2014). Figure 1.6 presents the typical catalytic center for family AA9, AA10, and AA11. *Nc*AA9C, CBP21, and *Af*AA11B illustrate the copper center of family AA9, AA10, and AA11, respectively.

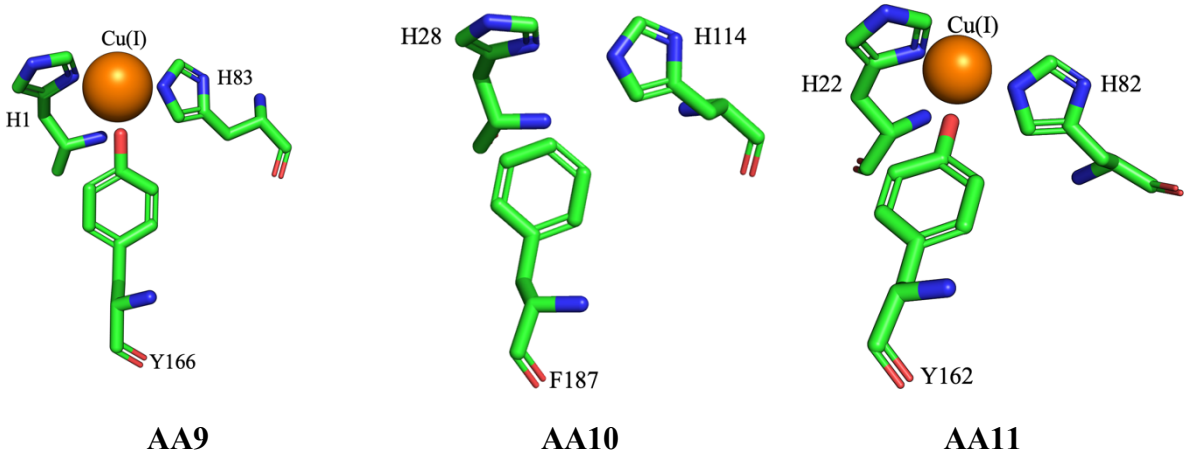

Figure 1.6: Catalytic center for family AA9, AA10, and AA11. *Amino acid residues associated with the copper center (sphere) are represented as green, blue, and red sticks to highlight the carbon, nitrogen, and oxygen atoms in the residues, respectively. Family AA9, AA10, and AA11 are represented individually by NcAA9C, SmAA10A, and AfAA11B.*

1.4.1.3 THE CATALYTIC TRIAD

The aromatic residue associated with the copper center is a tyrosine in AA9s and AA11s and phenylalanine (or tyrosine) in AA10s. It is believed that this aromatic residue is part of a catalytic triad (Figure 1.7). Preliminary LPMO experiments revealed four catalytic triads, *i.e.,* Tyr-Gln-His, Tyr-Glu-Asn, Phe-Glu-Arg, and Phe-Glu-Asn (unpublished work). Cellulose-active LPMOs comprise the catalytic triads Tyr-Gln-His (AA9s and AA10s) and Phe-Glu-Arg (AA10s), whereas chitin-active LPMOs comprise the catalytic triads Phe-Glu-Asn (AA10s) and Tyr-Glu-Asn (AA11s). The catalytic triad for an LPMO is believed to be essential regarding

the enzymatic activity and are part of what we call the second sphere residues, *i.e.,* the residues beyond the copper-coordinating residues. It is hypothesized that the specific combination of amino acid residues in the catalytic triad and their interaction is relevant (K. Hall, pers. com., 2021).

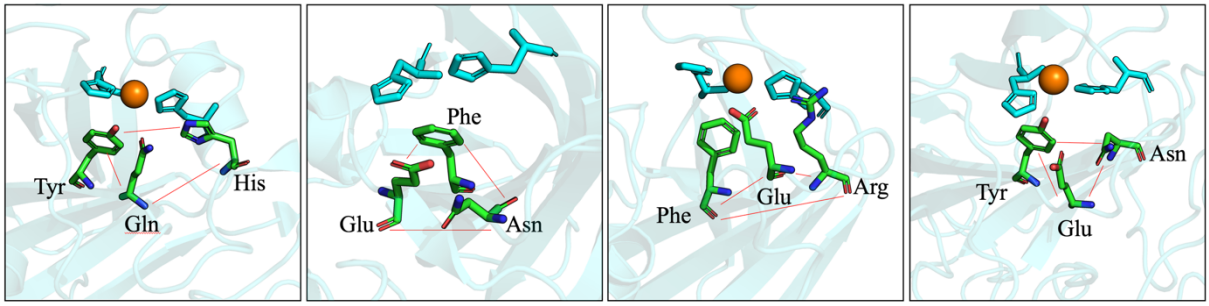

Tyr-Gln-His	**Phe-Glu-Asn**	**Phe-Glu-Arg**	**Tyr-Glu-Asn**
AA9 AA10	AA10	AA10	AA11

Figure 1.7: Catalytic triads observed in LPMOs. *The catalytic triads are presented in sticks relative to the histidine brace (cyan sticks). An orange sphere represents the Cu atom. Carbon, nitrogen, and oxygen atoms of the catalytic triad residues are presented in green, blue, and red, respectively. The catalytic triad Tyr-Gln-His is represented by NcAA9C. CBP21 is used as example to represent the catalytic triad Phe-Glu-Asn. Phe-Glu-Arg is presented by Streptomyces coelicolor AA10C (PDB ID: 4OY7). AfAA11B presents the catalytic triad Tyr-Glu-Asn.*

1.4.1.4 THE GATEKEEPER RESIDUE

The glutamine or glutamate in the catalytic triad is structurally conserved in all LPMOs (Vaaje-Kolstad et al., 2017). This residue is modulated to gate a tunnel that connects the LPMO's catalytic center and the glycosidic substrate (Bissaro et al., 2018). Hence, this residue is commonly referred to as the gatekeeper residue. The gatekeeper residue was first defined by Bissaro et al. (2018) in CBP21, then as conserved glutamate at position 60. They described how Glu60 possesses three conformational rotamers, *i.e.,* R1-R3 (Figure 1.8). The rotamers are possibly controlling the access to the catalytic center by changing the width of the tunnel.

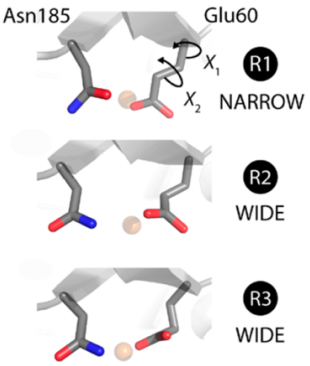

Figure 1.8: Conformational rotamers of Glu60. *The different conformations are of three stages (R1, R2, and R3), where the proposed gated tunnel is most spaced (~1.6 Å) in the R3 conformation of Glu60. The figure is adapted from Bissaro et al. (2018).*

Rotamer R1 generates a narrow gate tunnel, whereas the gate tunnel is wider in the R2 and R3 conformation due to the orientation of the side-chains of Glu60 (Bissaro et al., 2018). A wider tunnel results in easier access to the catalytic center. The maximum radius of the tunnel is estimated to be approximately 1.6 Å (Bissaro et al., 2018). Large molecules like ascorbic acid (AscA) cannot pass the gate tunnel due to size exclusion (Bissaro et al., 2018). Hence, the reduction of the copper center is favored prior to glycosidic substrate binding. In contrast, small molecules will access to the catalytic site through the gate tunnel. In this regard, it is believed that the supply of O_2, $O_2^{\cdot-}$, H_2O_2, and H_2O to the catalytic site may be regulated by this gatekeeper residue based on the conformational change of the tunnel (Bissaro et al., 2018). However, control of catalytic center access is yet not defined (Bissaro et al., 2018).

The importance of Glu60 in CBP21 related to chitin binding was discovered in 2005 (Vaaje-Kolstad et al., 2005b). Then, the mutation of Glu60 in CBP21 resulted in reduced activity toward chitin (Vaaje-Kolstad et al., 2005b). Later, the term “gatekeeper” may seem excluding as the gatekeeper residue has been hypothesized to do more than gate the catalytic site of an LPMO (Figure 1.9). Bissaro et al. (2020b) postulated a hydrogen-bonding network generated during the oxidative catalysis of β-chitin and H_2O_2 activation, where the network was occurring between the side-chains of Glu60 in CBP21, CBP21-Cu(I), and the β-chitin substrate. This hydrogen bonding aligned H_2O_2 with the Cu(I) ion at 2.98 Å and positioned the LPMO relative to the substrate (1.88 Å). Wang et al. (2018) also reported this caging of H_2O_2 with a hydrogen-bonding network between H_2O_2, the gatekeeper Gln162 in the *Lentinus similis* expressed *Ls*AA9A (PDB ID: 7NIM), and the histidines of the *Ls*AA9A catalytic center (H78 and H147). Hence, the gatekeeper residue is essential regarding LPMO activity and operational stability. Moreover, Bissaro et al. (2020b) also hypothesized that Glu60 controlled the relative positioning of reactive oxygen species (ROS) derived from H_2O_2 through hydrogen bonding. Hence, the gatekeeper residue appears essential in controlling hydroxyl radical reactivity and activation of H_2O_2 (Wang et al., 2018, Bissaro et al., 2020b).

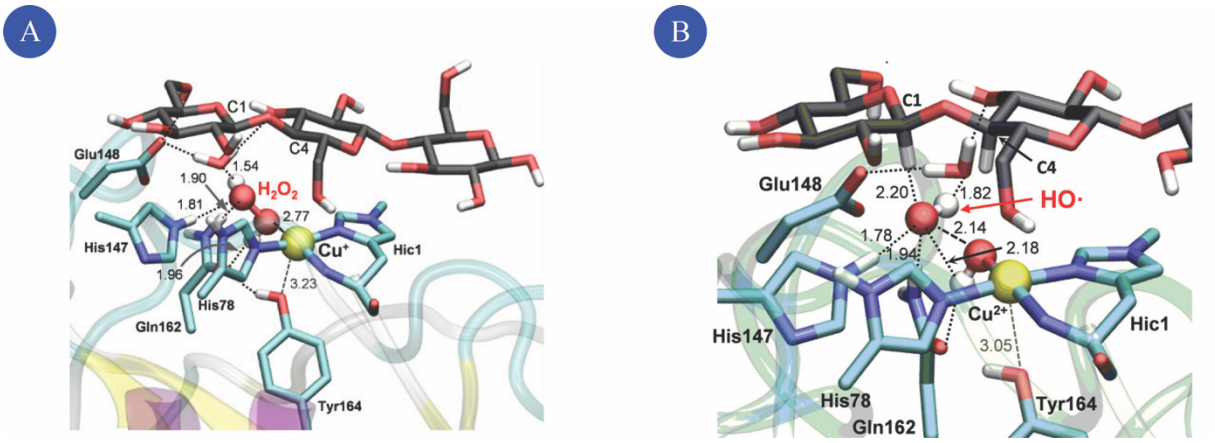

Figure 1.9: Roles of the gatekeeper residue. *The gatekeeper residue is postulated to be involved in "caging" of (A) H_2O_2 and the following (B) reactive oxygen species generated from H_2O_2. This caging effect might prevent oxidative damage and possibly change the positioning of the reactive LPMO intermediate for productive catalysis during turnover. The illustration is derived from Wang et al. (2018).*

1.4.2 SUBSTRATE INTERACTION WITH THE LPMO

The relative positioning of the LPMO to the substrate is affected by the flexibility of substrate binding surface loops (Aachmann et al., 2012, Beeson et al., 2015). A closed environment follows, which may reduce the transition state energy in favor of substrate binding (M. Sørlie, pers. com., 2021).

1.4.2.1 SUBSTRATE SPECIFICITY

LPMOs of various AA families exhibit different substrate specificity. AA9 LPMOs, such as *Nc*AA9C, are cellulose and β-glucan (xyloglucan) active enzymes (Agger et al., 2014, Borisova et al., 2015). In contrast, LPMOs of family AA11 exhibit chitin activity. However, *Af*AA11B activity is observed for the soluble chitooligosaccharides (Rieder et al., 2021b). LPMOs of family AA10 express activity on both cellulose and chitin. Attempts have been made to illustrate structural determinants of substrate specificity, though without success (Vaaje-Kolstad et al., 2017).

1.4.2.2 OXIDATIVE REGIOSELECTIVITY

Hydrolysis of glycosidic bonds occurs because of LPMO catalyzed oxidation of different carbon atoms in a glycosidic substrate, and this is referred to as oxidative regioselectivity (Chylenski et al., 2019). LPMOs are classified according to the oxidized carbon. Type 1, Type 2, and Type 3 LPMOs catalyze oxidation of the C1, C4, and C1 or C4 position in the glycosidic

substrate, respectively (Phillips et al., 2011). A schematic representation of LPMO catalyzed oxidation of the C1 and C4 position in cellulose is presented in Figure 1.10. The products from oxidation of the C1 or C4 position in a glycosidic substrate are aldonic acid and 4-gemidol-aldose, respectively (Phillips et al., 2011). Aldonic acid and 4-gemidol-aldose are the hydrated forms of lactone and 4-ketoaldose.

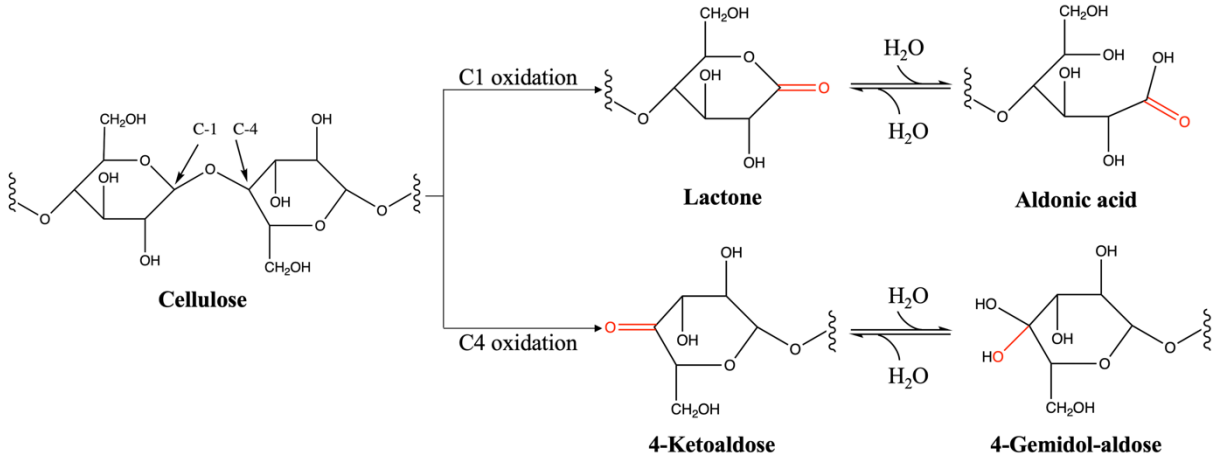

Figure 1.10: Illustrated oxidative regioselectivity. *LPMOs catalyze the oxidative cleavage of glycosidic bonds, and the oxidation may occur at different carbon atom positions. Oxidation of the C1 and C4 position in cellulose generates lactone and 4-ketoaldose, respectively. The lactone and 4-ketoaldose are in equilibrium with their hydrated forms, i.e., aldonic acid and 4-gemidol-aldose.*

LPMOs of family AA9 have shown to catalyze the oxidation of both the C1 and C4 position of cellulose. As such, the AA9 LPMO *Heterobasidion irregulare* AA9B (PDB ID: 5NNS) is a Type 1 LPMO, oxidizing the C1 position in phosphoric-acid swollen cellulose (PASC) (Liu et al., 2018). In contrast, *Nc*AA9C is a Type 2 LPMO which catalyze the oxidation of the C4 position in cellulose, cellulose oligomers, and β glucans (xyloglucan) (Agger et al., 2014, Borisova et al., 2015). *Ls*AA9A is a Type 3 LPMO, which catalyze the oxidation of both the C1 and C4 position in PASC (Frandsen et al., 2016). However, AA10s and AA11s catalyze the oxidation of the C1 position, *e.g.,* both *Sm*AA10A and *Af*AA11B are Type 1 LPMOs, catalyzing the oxidation of the C1 position in chitin and soluble chitooligosaccharides, respectively (Rieder et al., 2021b, Vaaje-Kolstad et al., 2005a). Nonetheless, cases of C1/C4 oxidation have been observed among AA10s, such as *Micromonospora aurantiaca* AA10B (PDB ID: 5OPF) acting as a Type 3 LPMO active on PASC (Forsberg et al., 2018).

The structural basis of oxidative regioselectivity is yet unknown. However, Borisova et al. (2015) specified that the solvent-facing axial position of the copper center is unrestricted in C4 oxidizing LPMOs of family AA9, whereas the same position in C1 oxidizing AA9s appears

restricted by the catalytic triad tyrosine. An intermediate arrangement is observed in C1/C4 oxidizing AA9 (Borisova et al., 2015). Similar observations have been made for LPMOs of family AA10 (Forsberg et al., 2014).

1.4.3 THE CATALYTIC MECHANISM OF LPMOS

1.4.3.1 REDUCTION OF COPPER

Substrate binding is shown to be more sufficient by LPMO-Cu(I) than LPMO-Cu(II) (Kracher et al., 2018). Moreover, due to the proposed mechanism of gatekeeper tunneling, reduction of the copper atom is favored to occur prior to substrate binding (Bissaro et al., 2018). "Priming" reduction of the copper atom follows when a reducing agent, such as ascorbic acid, cysteine, or gallic acid, donates one electron to the LPMO-Cu(II) (Vaaje-Kolstad et al., 2010). The reductants AscA, gallic acid, and cysteine are presented in Figure 1.11 in their neutral form. A redox enzyme such as cellobiose dehydrogenase (CDH) may also reduce copper by donating one electron (Phillips et al., 2011).

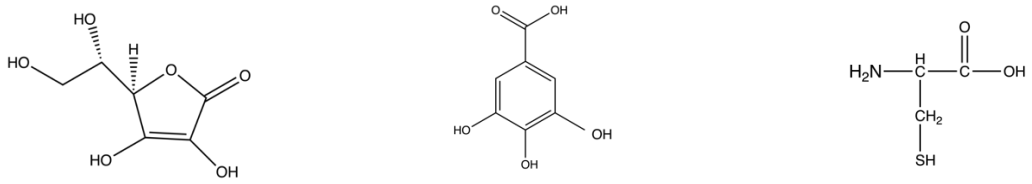

AscA **Gallic acid** **Cysteine**

Figure 1.11: Electron donors. *AscA, gallic acid, and cysteine are commonly used reductants in LPMO catalysis. The illustration presents the reductants in their neutral forms.*

One electron is needed for every catalytic cycle for the LPMO to catalyze the oxidation of a C1 or C4 position in a glycosidic substrate, leading to the hydrolysis of a glycosidic bond (Kuusk et al., 2018). "Priming" reduction of LPMO is presented in Equation 1. Stepnov et al. (2021) implied that "priming" reduction of LPMO is not rate-limiting under normal reaction conditions. However, Frommhagen et al. (2016), Kuusk et al. (2019), and Kracher et al. (2016a) presented various effectivity for different reductants in CBP21 catalysis.

(1) $\text{LPMO-Cu(II)} + e^- \rightarrow \text{LPMO-Cu(I)}$

Equation 1: "Priming" reduction of LPMO. One electron is donated from a reducing agent to the copper in the catalytic center, reducing the Cu(II) to Cu(I).

Experimental setups using ascorbic acid as a reductant is common (Stepnov et al., 2021). AscA was also used as a reductant during discovering of the LPMO's oxidative properties (Vaaje-Kolstad et al., 2010). Nevertheless, Stepnov et al. (2021) showed that using AscA as an electron donor in LPMO catalysis is suboptimal due to its sensitivity to unbound copper. Copper sensitivity is also observed using cysteine as the reductant in LPMO catalysis Stepnov et al. (2021). This sensitivity is associated with autooxidation of the electron donor, which causes artificial *in-situ* H_2O_2 production (Loose et al., 2018). In contrast with AscA and cysteine, gallic acid does not appear to be as sensitive to free copper, possibly due to complex formation between the free copper and gallic acid (Stepnov et al., 2021).

1.4.3.2 THE COSUBSTRATE

LPMO-Cu(I) needs a cosubstrate to catalyze the oxidative cleavage of glycosidic bonds in recalcitrant polysaccharides. The LPMO catalytic scenarios, *i.e.,* the LPMO reactions under oxygen and H_2O_2 conditions, are presented in Equation 2.

(2) (A) $R\text{-}H + O_2 + 2e^- + 2H^+ \rightarrow R\text{-}OH + H_2O$

(B) $R\text{-}H + H_2O_2 \rightarrow R\text{-}OH + H_2O$

Equation 2: LPMO catalytic scenarios oxidizing the substrate R-H. (A) The LPMO reaction under oxygen conditions demands two electrons after the "priming" reduction. (B) The peroxygenase reaction does not demand electrons after the LPMO "priming" reduction.

As the LPMO naming implies, the true cosubstrate was first thought to be molecular oxygen. One proposed reaction mechanism by Bertini et al. (2018) using O_2 as cosubstrate is presented in Figure 1.12, which shows how O_2 is proposed to interact with "primed" LPMO. This interaction, involving one electron transferred from LPMO-Cu(I) to O_2, generates the intermediate LPMO-Cu(II)-OO•. Bertini et al. (2018) suggested that the two next reaction steps involve proton-coupled electron transfers, first generating the intermediate LPMO-Cu(II)-OOH followed by LPMO-Cu(II)-O•. The LPMO-Cu(I) is restored by an oxygen-rebound mechanism which results in the hydrolyzation of a glycosidic bond in the polysaccharide substrate. Beeson et al. (2015), Walton and Davies (2016), and Meier et al. (2018) proposed alternative mechanisms for the monooxygenase reaction.

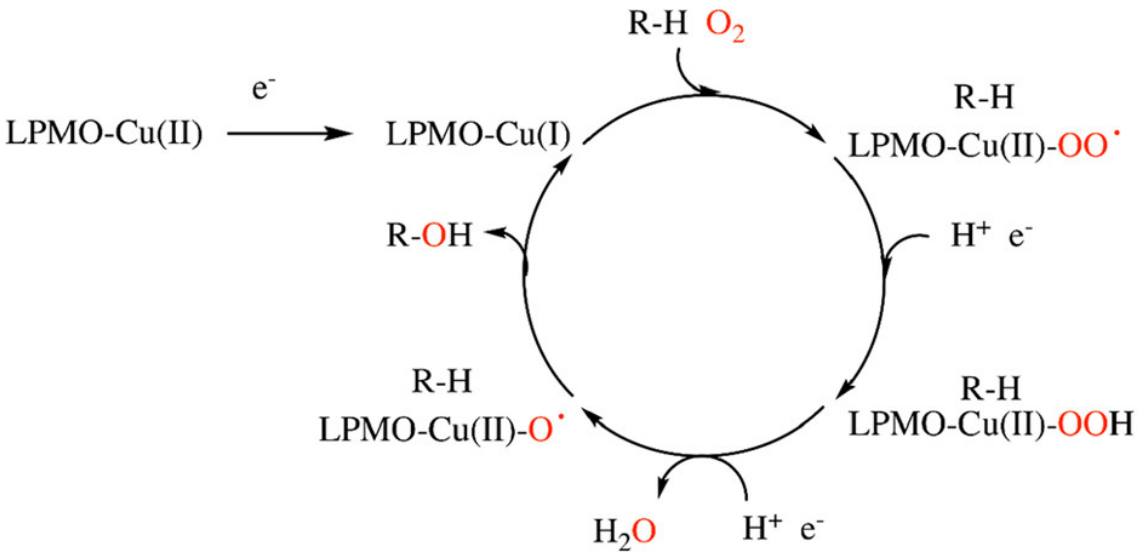

Figure 1.12: The reaction mechanism of LPMO catalyzed reaction in oxygen conditions proposed by Bertini et al. (2018). *LPMO-Cu(II)-OO• is generated from the interaction between O_2 and "primed" LPMO. After proton-coupled electron transfers, the two following intermediates, i.e., LPMO-Cu(II)-OOH and LPMO-Cu(II)-O•, are generated. Finally, LPMO-Cu(I) is restored by an oxygen-rebound mechanism. Oxidation of a glycosidic bond in the substrate follows. The illustration is derived from Chylenski et al. (2019).*

The hydrolysis of one glycosidic bond demands two electrons if O_2 is the true cosubstrate, as illustrated in Equation 2A (Bertini et al., 2018). This is one of the reasons why O_2 is considered not to be the true cosubstrate. Potentially, the first electron is delivered to the catalytic center after the "priming" reduction of copper. However, the second electron must be delivered later in the catalytic cycle, at a point where the copper site is shielded from the solvent (Bissaro et al., 2017). This is not the case in a scenario where H_2O_2 is the cosubstrate, as H_2O_2 does not demand electrons after the "priming" reduction of the LPMO (Equation 2B). Furthermore, the peroxygenase reaction is orders of magnitude faster compared with the LPMO reaction under oxygen conditions. Bissaro et al. (2017) compared the catalytic rate (~ 0.3 min^{-1}) for a monooxygenase reaction in a commercial cellulolytic enzyme cocktail with the peroxygenase catalytic rate (4.2 min^{-1}). Even higher differences were observed by Kuusk et al. (2018). Product formation was also monitored by Bissaro et al. (2017) using 25 µM isotope-labeled H_2O_2 and 200 µM non-labeled O_2. Generated aldonic acid exhibited isotope-labeled oxygen atoms, supporting H_2O_2 being the true cosubstrate.

H_2O_2 as the preferred LPMO cosubstrate is now accepted (Bissaro et al., 2017). Wang et al. (2018) proposed the peroxygenase reaction mechanism (Figure 1.13). "Primed" LPMO donates one electron to H_2O_2, which results in O-O bond break generating two unbound hydroxyl

radicals (•OH) (Wang et al., 2018). The postulated hydrogen-bonding pattern generated between the gatekeeper residue, the copper center, and the substrate directs one of the unbound •OH to interact with the LPMO intermediate (Bissaro et al., 2020b, Wang et al., 2018). As a result, LPMO-Cu(II)-OH is generated. The second unbound •OH abstracts one proton from the intermediate LPMO-Cu(II)-OH and produces LPMO-Cu(II)-O• (Wang et al., 2018). This second unbound •OH is also directed by the proposed hydrogen-bonding pattern (Bissaro et al., 2020b, Wang et al., 2018). Following, the hydrogen atom is abstracted from the LPMO complex rather than the substrate. The intermediate LPMO-Cu(II)-O• hydrolyzes the glycosidic bond prior to restoring the LPMO-Cu(I) complex (Wang et al., 2018).

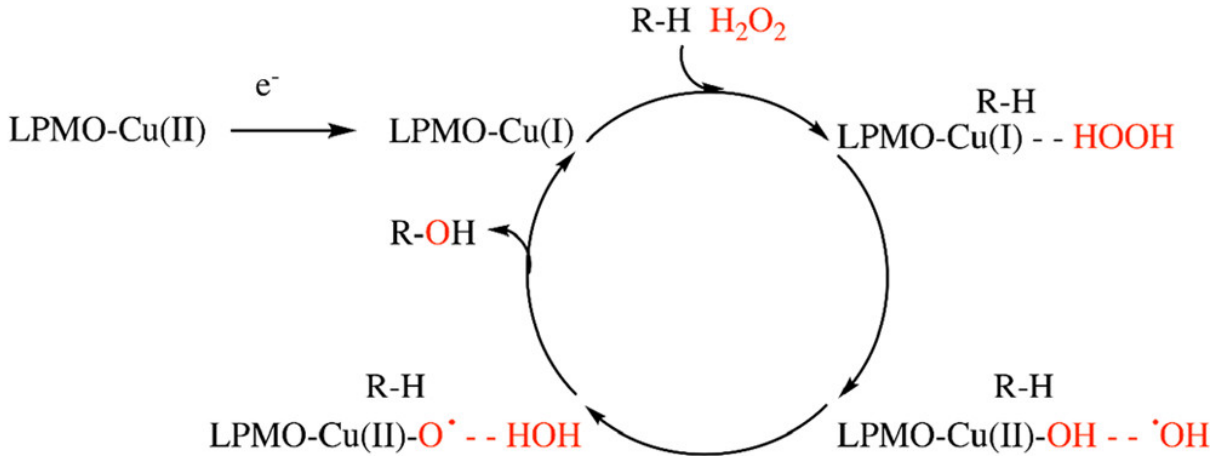

Figure 1.13: The peroxygenase reaction mechanism of an LPMO proposed by Wang et al. (2018). *One electron transfer from LPMO-Cu(I) results in two free •OH. One of the two free radicals interacts with the LPMO and creates the intermediate LPMO-Cu(II)-OH. The second free hydroxy radical interacts with this intermediate and generates LPMO-Cu(II)-O•. LPMO-Cu(II)-O• hydrolyzes a glycosidic bond resulting in bond cleavage, and the LPMO-Cu(I) is restored. The illustration originates from Chylenski et al. (2019).*

LPMOs can catalyze the oxidative cleavage of glycosidic bonds in the presence of molecular oxygen only, even though H_2O_2 is supposedly the preferred cosubstrate. LPMO-Cu(I) can act as a reducing agent on molecular oxygen, generating H_2O_2. This reduction is presented in Equation 3 and may also be referred to as the *in-situ* H_2O_2 production of an LPMO (Hangasky et al., 2018). Discussions are made if LPMO catalyzed oxidative cleavage of glycosidic bonds using O_2 as cosubstrate occur at all (Bissaro et al., 2020b, Courtade et al., 2020, Hangasky et al., 2018, Wang et al., 2020). Hence, the increased catalytic rate for the peroxygenase reaction compared with the monooxygenase reaction is reasonable.

(3) $O_2 + 2e^- + 2H^+ \rightarrow H_2O_2$ $E^0 = 0.695$ V

Equation 3: Reduction of molecular oxygen generates H_2O_2. The reduction potential of molecular oxygen reduction is 0.695 V (Milazzo et al., 1978).

It is speculated that LPMO catalyzed oxidative cleavage of glycosidic bonds occurring under oxygen conditions are dependent on the LPMOs *in-situ* hydrogen peroxide production (Stepnov et al., 2021). This *in-situ* H_2O_2 production is related to the LPMO/O_2 cell potential (E^0_{cell}), *i.e.,* the LPMO's ability to donate electrons to molecular oxygen and generate H_2O_2 (Equation 3). The standard reduction potential (E^0_{red}) of reducing O_2 to H_2O_2 is 0.695 V (Milazzo et al., 1978). E^0_{red} of reducing LPMO-Cu(II) to the Cu(I) state is dependent on the LPMO. This *in-situ* H_2O_2 production of an LPMO may be of biological significance and has been indicated for LPMOs of family AA9, AA10, and AA11 (Hangasky et al., 2018, Rieder et al., 2021b, Stepnov et al., 2021).

1.4.4 LPMO STABILITY

Suboptimal reaction conditions during LPMO oxidative catalysis may affect the stability of the LPMO, such as H_2O_2 accumulation in solution or substrate depletion (Bissaro et al., 2017). "Primed" LPMO can react with O_2 or H_2O_2 in the absence of a glycosidic substrate or if the substrate-binding is weak or inaccurate (Forsberg et al., 2018, Loose et al., 2018). The exposed Cu(I) site can then be re-oxidized, which generate reactive oxygen species and free Cu(II) ions (Bissaro et al., 2017). Free Cu(II) ions are reduced to Cu(I) ions by an external reductant, and the free Cu(I) ions may catalyze unproductive side reactions besides the oxidative catalysis, such as autooxidation of the reductant generating excess H_2O_2 (Bissaro et al., 2017). Excess H_2O_2 may increase the amount of generated ROS in the active site of the LPMO. ROS released from the catalytic center may cause oxidative damage to the cooper-coordinating histidines and second sphere residues (Kracher et al., 2018). LPMO-Cu(I) reacting unproductive beside the oxidative catalysis is presented in Figure 1.14.

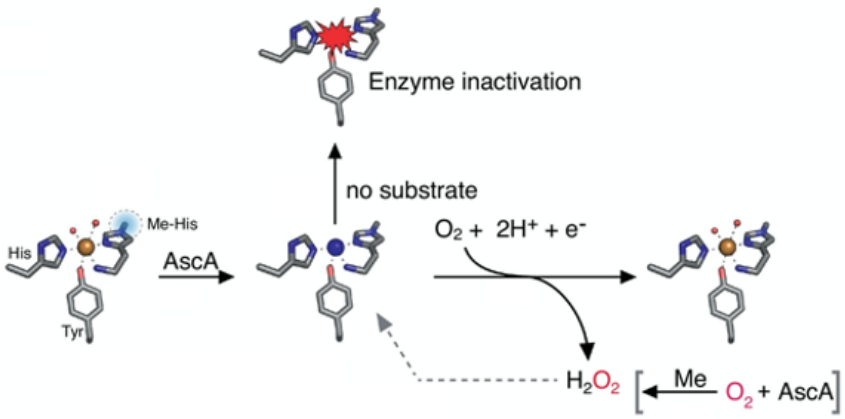

Figure 1.14: Reactive oxygen species generated in the absence of glycosidic substrate. *"Primed" LPMO may be re-oxidized by hydrogen peroxide or oxygen in the absence of a glycosidic substrate or by low substrate-binding. These mechanisms are not fully elucidated, but it is believed that these scenarios will lead to enzyme inactivation. The figure is adapted from Forsberg et al. (2019).*

1.4.4.1 AVOIDANCE OF OXIDATIVE DAMAGE

The avoidance of oxidative damage is crucial for an LPMOs catalytic efficiency. Removing oxidative damaging electrons from the catalytic center to the protein surface of an LPMO has been discussed in terms of "hole-hopping" (Gray and Winkler, 2015). "Hole-hopping" is described as electron tunneling reactions (Gray and Winkler, 2015). Hence, these hypothetical tunneling reactions protect the catalytic center from auto-oxidative damage. Side-chains of specific amino acids, *e.g.,* Trp and Tyr, are hypothesized to guide the oxidative holes to the protein surface by generating amino acid radicals. Chains of Trp and Tyr are observed in approximately one-third of all proteins (Gray and Winkler, 2015). Research has previously shown several enzymes with these electron transfer chains (Brettel and Byrdin, 2010, Jiang et al., 2013, Minnihan et al., 2013, Yu et al., 2012). Jones et al. (2020) showed that introducing •OH to LPMO-Cu(I) in the absence of substrate resulted in oxidation of the aromatic tyrosine and tryptophan residues close to the LPMO's copper center. The work of Jones et al. (2020) proposed an electronically coupled pathway between the aromatic residues of the catalytic triad and the copper coordinating histidine residues.

1.4.4.2 STOPPED-FLOW SPECTROSCOPY

The generation of amino acid radicals described above may be hypothesized and estimated with stopped-flow spectroscopy (Hedison et al., 2021, Jones et al., 2020). Stopped-flow spectroscopy enables monitoring of biochemical reactions with reaction time between 50 and 100 ms, generating high resolution and sensitivity of enzymatic kinetic data. A schematic representation of a stopped-flow mixing system is presented in Figure 1.15.

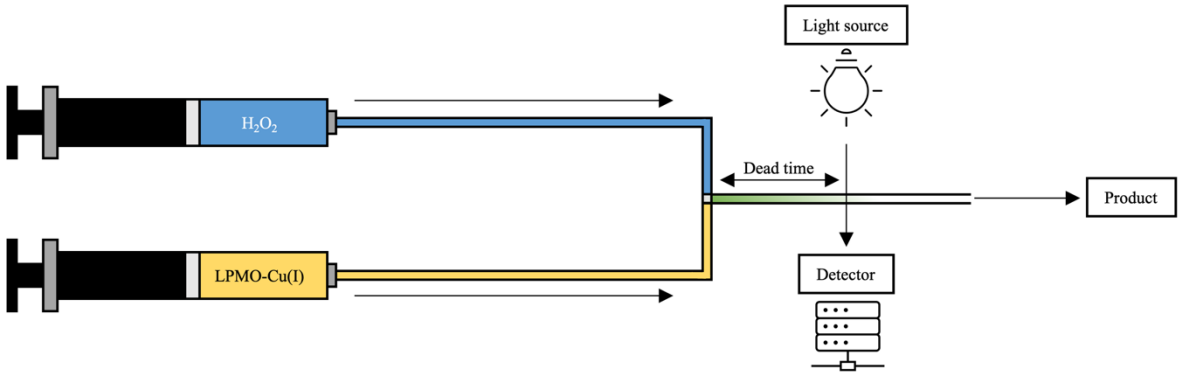

Figure 1.15: Schematic presentation of a stopped-flow mixing system. *The illustration indicates how two reagents are mixed rapidly in a stopped-flow instrument. A light source, i.e., UV/VIS or fluorescence, is emitted into the mixture, and a detector registers a change in absorbance. The dead time is highlighted as the time from the mixing point until the light is emitted through the reaction mixture.*

Activation of the drive mechanism pushes two reagents, *e.g.,* LPMO and reductant, to the mixer, where the LPMO and reductant are mixed rapidly (< 1 ms). An aging loop is used to constrain the mixture for an established incubation time (AppliedPhotophysics, 2018). Post incubation, the drive mechanism pushes the "primed" LPMO and reductant towards the observation cell, where the reagents are introduced to a third reagent, *e.g.,* hydrogen peroxide (AppliedPhotophysics, 2018). The observation cell is now filled with recently mixed LPMO-Cu(I), reductant, and hydrogen peroxide, resulting in a total mixture volume of 40-150 µL (AppliedPhotophysics, 2018, Bagshaw, 2013). A UV/VIS or fluorescence light source emits light that interacts with the mixture in the observation cell. Detection is dependent on the reagents' chemical properties. Data acquisition is performed with a standard dead-time as low as 200 µs for stopped-flow instruments such as the SFM-4000 stopped-flow mixing system from BioLogic Sciences Instruments.

Component's change in absorption of light at a range of wavelengths is reported as curves. If the curves have low noise, one may estimate the rate constant for pseudo-first-order reactions with high accuracy (Bagshaw, 2013). Parameters such as rate, association, effectivity, and equilibrium constants may be estimated based on retrieved kinetic curves (Ayuso-Fernandez et al., 2019, Bissaro et al., 2020b, Sorlie et al., 2000). However, it should be noted that the origin of the potential radicals monitored through stopped-flow spectroscopy is unknown. Nevertheless, stopped-flow spectroscopy is a helpful tool in terms of LPMO research.

1.5 RESEARCH AIM

LPMOs are attractive in current and future biorefining technologies, as the redox enzymes catalyze the decomposition of recalcitrant polysaccharides available from biomass. Insight about biomass conversion to products of value is crucial for development of new environmental technologies, and following, address the sustainability goals set forth by the United Nations. The LPMOs catalytic mechanism is a key point for developing LPMO research and achieving the full LPMO potential in biomass conversion. Nonetheless, limited research covers individual amino acids involved in catalysis. This master's thesis work was a part of a larger research project, where the ultimate research goal was to gain an understanding of this LPMO catalytic mechanism for degradation of recalcitrant polysaccharides. For this reason, the gatekeeper residue of two fungal LPMOs – *Nc*AA9C and *Af*AA11B – from different families (AA9 and AA11) active on different substrate (cellulose and chitin) was studied during this master's thesis work. The gatekeeper residue of *Nc*AA9C (Q180) and *Af*AA11B (E160) was mutated, altering the length of the side-chain and the relative charge near the copper center (Figure 1.16). In *Nc*AA9C, this position was mutated to either glutamate (Q180E), asparagine (Q180N), or aspartate (Q180D). The equivalent position in *Af*AA11B was mutated to either glutamine (E160Q), asparagine (E160N), or aspartate (E160D).

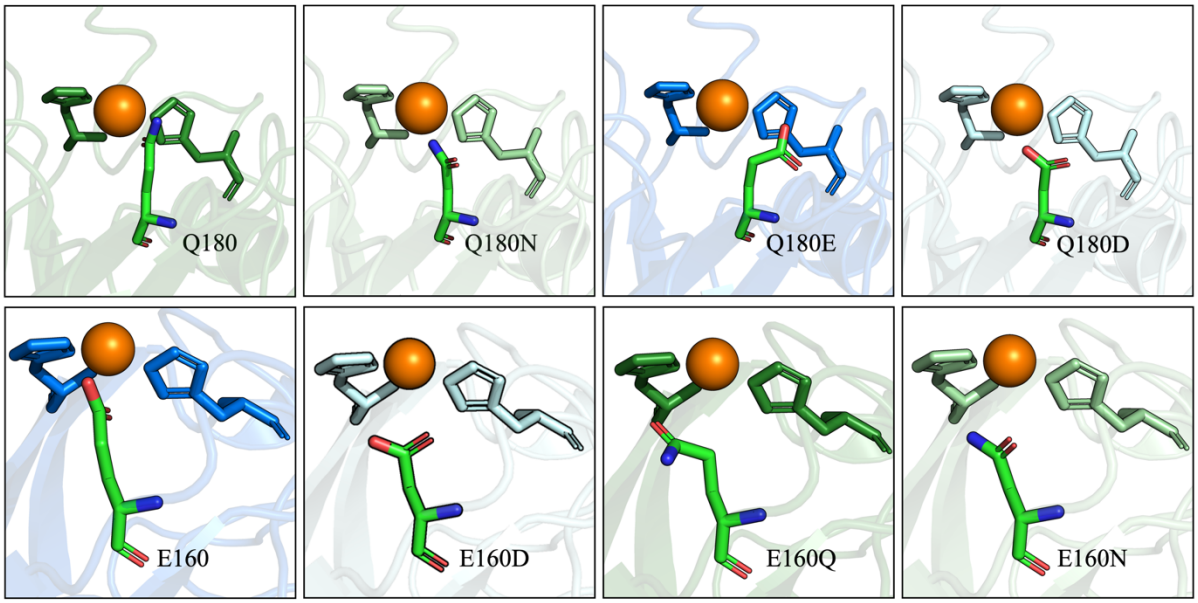

Figure 1.16: Gatekeeper mutations of NcAA9C and AfAA11B. *The gatekeeper residue of NcAA9C (Q180) was mutated to asparagine, glutamate, and aspartate. Mutations of NcAA9C are presented in the upper panels. The gatekeeper residue was also mutated in AfAA11B (E160) to aspartate, glutamine, and asparagine (lower panel). Green and blue color codes were used to indicate the gatekeeper residue's amide and carboxylic acid nature, respectively. This color-coding is maintained throughout the thesis.*

This work presents the first detailed investigation of a fungal AA family 11 LPMO with a Tyr-Glu-Asn catalytic triad with mutations of the conserved gatekeeper residue. Moreover, this was the first stopped-flow spectrophotometric investigation for a fungal AA family 9 LPMO with a Tyr-Gln-His catalytic triad with mutations of gatekeeper position, detailing the kinetics of radical transformation from the active site after LPMO-Cu(I) reacting with hydrogen peroxide. This study provides a basis for future studies on the mechanism of LPMO catalysis of recalcitrant polysaccharide degradation.

2 MATERIALS

2.1 LABORATORY EQUIPMENT

Table 2.1. Instruments. The table presents the instruments used during this master's thesis with the instruments' application and supplier.

INSTRUMENT	APPLICATION	SUPPLIER
Agilent 1290 Infinity II	HP-HILIC	Agilent Technologies
ÄKTA Pure	HIC	GE Healthcare
ÄKTA Purifier	SEC	GE Healthcare
Cary 8454 UV/Vis	Absorbance measurements	Agilent Technologies
Dionex ICS500	HP-AEC	ThermoFisher Scientific
Dionex UltiMate 3000	HP-IEC	ThermoFisher Scientific
NanoDrop™ One	Absorbance measurements	ThermoFisher Scientific
NanoPhotometer® C40	Absorbance measurements	Implen
NGC Chromatographic system	AEC	BioRad
SFM-4000	Stopped-flow	BioLogic Sciences Instruments
Varioskan LUX Multimode Microplate Reader	Amplex Red assay Breslmayr assay Bradford protein assay OD_{600}	ThermoFisher Scientific

Table 2.2. Laboratory equipment. Equipment specifications and supplier used during this experimental work are included in this table.

EQUIPMENT	SPECIFICATION	SUPPLIER
Anaerobic workstation	Whitley A95 TG	Don Whitley Scientific
Assorted glassware	• Baffle shake flasks • Beakers • Blue-cap bottles • Volumetric flasks • Graduated cylinders	Schott-Duran/VWR
Autoclave tape	12 mm	Merck
Automatic pipettes	Finnpipette F2 Pipettes Single channel pipettes Multichannel pipettes	Thermo Scientific
Balancers	-	VWR
Biosafety cabinet	Av-100	TelStar
Block heater	-	ThermoFisher Scientific
Centrifugal bottles and tubes	• Cellstar® 15 mL, 50 mL	• Greiner Bio-One • Merck

Centrifugal filters	• Amicon® Ultra-15, 15 mL • Macrosep® Advance, 15 mL	• Merck • Pall
Centrifuge rotors	• F-35-6-30 rotor • FA-45-30-11 • Fiberlite™ F9-6 × 1000 LEX Fixed Angle Rotor • Fiberlite™ F21-8 × 50y Fixed Angle Rotor • Swing-Bucket rotor	• Eppendorf • Eppendorf • ThermoFisher Scientific • ThermoFisher Scientific • Eppendorf
Centrifuges	• Concentrator Plus • MiniSpin tabletop • Sorvall Lynx 6000 • 5430/5430R	(1) Eppendorf (2) Eppendorf (3) ThermoFisher Scientific (4) Eppendorf
Concentration system	VivaFlow 200 tangential crossflow concentrator	Merck
Cryo tubes	2 mL	Sarstedt
Cuvettes	• Semi-Micro cuvettes 12.5 × 12.5 × 45 mm • Hellma™ Suprasil™ Quartz 104B Semi-Micro Cell cuvettes	• Merck • ThermoFisher Scientific
Disposable pipettes	1 mL, 3 mL	VWR
Electroporation cuvette	Gene Pulser/MicroPulser	Bio-Rad
Electrophoresis cell	Mini-PROTEAN Tetra System	Bio-Rad
Electrophoresis gel	Mini-PROTEAN TGX Stain-FreePrecast Gel	Bio-Rad
Filter plate	96-well	Corning
Freezer	• -20 °C • -80 °C	• Bosch • SANYO
Fridge	4 °C	Bosch
Gene pulser II	-	Bio-Rad
HPLC vials with caps	200 µL	Thermo Scientific
Ice maker	KF 145	PORKKA
Imaging System	GelDoc Go	Bio-Rad
Incubators	• Multitron Standards • Static incubator • Thermomixer C • T100 Thermal Cycler	• Infors • Termaks • Eppendorf • Bio-Rad
Inoculation loops	1 µL	Merck
Magnet	-	IKA

Magnetic stirrer	Fisherbrand™	ThermoFisher Scientific
Microtiter Microplate	96-Well, 280 µL	ThermoFisher Scientific
Milli-Q® Direct water purification system	Direct 1	Merck
Mini-Sub GT cell	9.2 × 25.5 × 5.6 cm	Bio-Rad
Parafilm	5 cm	VWR
PCR tubes	200 µL	Axygen
Petri dishes	9 cm	Heger
PowerPac™	-	Bio-Rad
PowerPac™ Basic power supply	-	Bio-Rad
Pulscontroller plus	-	Bio-Rad
pH meter	pH110M	VWR
Pipette tips	Next Generation Tip Refill	VWR
Polypropylene DeepWell Plate	96-Well, 2 mL	ThermoFisher Scientific
Polystat 36 Chiller	-	Fisher Scientific
Pumps	• Masterflex™ pump drive • Vacuum pump	• Merk • Millipore
Reaction tubes	1.5 mL	Eppendorf
Scales	-	VWR
Schlenk line	-	Made in-house
Sonicator system	Vibra-Cell™	Sonics
Spatula	-	-
Steritop filter	45 mm neck size, 0.45 µm	Merck
Syringes	Becton Dickinson hypodermic syringes, polypropylene 2 mL, 20 mL	Merck
Trays for reading SDS-PAGE	• Blue tray • UV/Stain Free Tray	Bio-Rad
Ultrasonic water bath	XUBA	Grant
Vortex	MS 3 basic	IKA
Water bath	22-65 °C	Julabo
Weighing boats	-	VWR

Table 2.3. Analytical and guard columns. The columns used during the experimental work of this master's thesis is presented in this table. Column specifications and the respective supplier are also presented.

COLUMN	SPECIFICATION	SUPPLIER
Acquity UPLC BEH Amide	1.7 µm	Waters
DEAE Sepharose FF	5 mL	Cytiva
Dionex™ CarboPac™ PA1	Analytical column: 2 × 250 mm Guard column: 2 × 50 mm	ThermoFisher Scientific
HiLoad 16/160 Superdex 75 pg	120 mL	Merck
HiTrap Phenyl HP	5 mL	Cytiva
PD-10 desalting columns	8.3 mL	Merck
ROA-Organic Acid	Analytical and guard column: 300 mm	Phenomenex

Table 2.4. Kits. The table presents an overview of the kits utilized during this experimental work.

KIT	SUPPLIER
DNA Clean and concentrator TM-5 Kit	Zymo Reasearch
E.Z.N.A® Plasmid DNA Mini Kit I	Omega BIOTEK

2.2 SOFTWARE FOR ANALYSIS

Table 2.5. Software for analysis. Applied software are presented in this table with corresponding application and supplier.

SOFTWARE	APPLICATION	SUPPLIER
Adobe Illustrator	Illustration preparation	Adobe
Bio-Kine 32 V4.74.2	Stopped-flow	BioLogic Sciences Instruments
Chromeleon 7	HP-AEC HP-HILIC HP-IEC	ThermoFisher Scientific
ChromLab	AEC	Bio-Rad
Microsoft Office Excel	Data analysis	Microsoft
PyMOL	Molecular visualization program for protein crystals	Warren Lyford DeLano
R studio	Data analysis	R studio
Simple reads	Concentration estimations	Cary WinUV
SkanIt 6.0.1	Amplex Red assay Breslmayr assay Bradford protein assay OD_{600}	ThermoFisher Scientific
Unicorn 6.4	HIC	Cytiva
Unicorn 5.2	SEC	Cytiva

2.3 REAGENTS AND CONSUMABLES

Table 2.6. Chemical reagents. The table presents the chemicals using during this experimental work, including specifications and the chemical supplier.

CHEMICAL	SPECIFICATION	SUPPLIER
2,6-Dimethoxyphenol (DMP)	$C_{18}H_{10}O_3$	Merck
Acetonitrile (ACN)	C_2H_3N	Honeywell
Agar powder	$(C_{12}H_{18}O_9)_n$	Merck
Ammonium sulphate	$(NH_4)_2SO_4$	Merck
Ampicillin disodium salt	$C_{16}H_{18}N_3NaO_4S$	Invitrogen by ThermoFisher Scientific
Amplex Red	$C_{14}H_{11}NO_4$	Invitrogen by ThermoFisher Scientific
Biotin	$C_{10}H_{16}N_2O_3S$	Merck
Bis-Tris	$C_8H_{19}NO_5$	Merck
Chloroform	$CHCl_3$	VWR
Copper sulfate	$CuSO_4$	Merck
Dextrose	$C_6H_{12}O_6$	Merck
Di-N-acetylglucosamine $(GlcNAc)_2$	$C_{16}H_{28}N_2O_{11}$	Megazyme
Dimethyl sulfoxide (DMSO)	C_2H_6OS	Merck
Dipotassium hydrogen phosphate	K_2PHO_4	Merck
Dye Reagent Concentrate (Bradford reagent)	Colorimetric acid dye	Bio-Rad
Electrocompetent *P. pastoris* BSYBG11	Yeast strain	Bisy GmbH
Ethanol	C_2H_5OH	VWR
Ethylenediaminetetraacetic acid (EDTA)	$C_{10}H_{16}N_2O_8$	Merck
Glycerol	$C_3H_8O_3$	VWR
Hydrogen chloride	HCl	Merck
Hydrogen peroxide	H_2O_2	VWR
Kanamycin sulfate	$C_{18}H_{36}N_4O_{11}$	Invitrogen by ThermoFisher Scientific
L-(+)-arabinose	$C_5H_{10}O_5$	Merck
L-ascorbic acid	$C_6H_6O_6$	Merck
L-cysteine	$C_3H_7NO_2S$	Merck
L-gallic acid	$C_7H_6O_5$	Merck
Methanol	CH_3OH	Honeywell
N-acetylglucosamine GlcNAc	$C_8H_{15}NO_6$	Megazyme

N,N,N',N'-tetramethyl-1,4-phenylenediamine (TMP_{red})	C_6H_4-1,4-$[N(CH_3)_2]_2$	Merck
NuPAGE® LDS Sample Buffer	[4×]	Invitrogen by ThermoFisher Scientific
NuPAGE® Sample Reducing Agent	[10×]	Invitrogen by ThermoFisher Scientific
One Shot™ TOP10 chemically competent *E. coli* cells	Bacterial strain	Life Technologies
Peptone	$C_{13}H_{24}O_4$	Merk, VWR
Phire Tissue Direct PCR Master Mix	[2×]	ThermoFisher Scientific
Piperazine-N,N'-bis(2-ethanesulfonic acid) (Pipes)	$C_8H_{18}N_2O_6S_2$	Merck
Potassium dihydrogen phosphate	KH_2PO_4	Merck
Sodium acetate	$C_2H_3NaO_2$	VWR
Sodium chloride	NaCl	VWR
Sodium hydroxide	NaOH	VWR
Sulfuric acid	H_2SO_4	Merck
SYBR Safe DNA gel stain	[10 000 ×] in DMSO	ThermoFisher Scientific
Tetra-N-acetylglucosamine $(GlcNAc)_4$	$C_{32}H_{54}N_4O_{21}$	Megazyme
Tetracycline hydrochloride	$C_{22}H_{24}N_2O_8$	Invitrogen by ThermoFisher Scientific
Tri-N-acetylglucosamine $(GlcNAc)_3$	$C_{24}H_{41}N_3O_{16}$	Megazyme
Tris	$C_4H_{11}NO_3$	Merck
Tryptone	C_3H_5NO	VWR
UltraPure™ Agarose	$(C_{12}H_{18}O_9)_n$	Invitrogen by ThermoFisher Scientific
Yeast extract	$C_{19}H_{14}O_2$	Invitrogen by ThermoFisher Scientific
Yeast nitrogen base (YNB)	Without amino acids, with ammonium sulphate	ThermoFisher Scientific

Table 2.7. Growth media. Prepared growth media are presented with ingredient components. All components were dissolved in Milli-Q water.

GROWTH MEDIA	COMPONENTS
Buffered minimal media (BMD1)	• 1.34% yeast nitrogen base (YNB) with ammonium sulfate and without amino acids (w/v) • 0.00004% biotin (w/v) • 1% dextrose (w/v) • 1M KP_i buffer pH 6.5
Yeast extract-peptone-dextrose (YPD)	• 1% yeast extract (w/v) • 2% peptone (w/v) • 2% dextrose (w/v) • 15 g/L agar added to generate solid YPD
Lysogeny broth (LB)	• 1% tryptone (w/v) • 1% sodium chloride (w/v) • 0.5% yeast extract (w/v) • 15 g/L added to generate solid LB

Table 2.8. Buffers and solutions. The buffers and solutions used during this experimental work are presented with ingredient components and final concentration in brackets. The application for the buffer is also presented. If the buffer was not self-made, the supplier is presented in brackets. Dilutions were made with Milli-Q water.

BUFFERS & SOLUTIONS	APPLICATION	COMPONENTS
Bis-Tris/HCl pH 6.5 [500 mM]	Stock solution: Elution buffer HIC SEC buffer Storage buffer	• 41.84 g Bis-Tris • HCl for pH adjustment • Final volume: 400 mL
Lithium dodecyl sulfate (LDS) loading dye [2×]	SDS-PAGE	• 750 µL LDS dye [4×] • 150 µL reducing agent [10×] • Final volume: 1500 µL
Pipes buffer (pH 6.0) [200 mM]	Stock solution: Redox measurements	• 480 mg Pipes • NaOH for pH adjustment • Final volume: 80 mL
Potassium phosphate pH 6.5 [200 mM]	Stock solution: Lysis buffer Binding buffer AEC Elution buffer AEC	• 1.47 g K_2PHO_4 • 2.26 g KH_2PO_4 • Final volume: 500 mL
Super optimal broth (S.O.C.) Medium (Invitrogen, ThermoFisher Scientific)	Transformation of *E. coli*	• 1% tryptone • 0.5% yeast extract • 10 mM NaCl • 2.5 mM KCl • 10 mM $MgCl_2$

		• 20 mM glucose
Sodium acetate [1 M], sodium hydroxide [0.1 M]	Mobile phase A HP-AEC	• 82.03 g sodium acetate • 5.2 mL abs. NaOH • Final volume: 1L
Sodium hydroxide [100 mM]	Mobile phase B HP-AEC	• 10.4 mL abs. NaOH • Final volume: 2 L
Sulfuric acid [5 mM]	Mobile phase HP-IEC	• 556 µL abs. H_2SO_4 • Final volume: 2 L
Tris, acetate, EDTA (TAE) buffer [1×]	PCR screen	• 40 mM Tris • 20 mM acetic acid • 1 mM EDTA
Tris, glycine, SDS buffer [1×] (Bio-Rad)	SDS-PAGE	• 0.025 M Tris • 0.192 M glycine • 0.1% SDS (v/v)
Trizma base hydrochloric acid (Tris-HCl) (pH 8.0) [1M]	Stock solution: Buffer A HILIC SEC buffer Storing buffer	• 121.14 g Tris • Final Volume: 1 L
3.1 NE Buffer [1×] (Invitrogen, ThermoFisher Scientific)	Plasmid linearization	• 100 mM NaCl • 50 mM Tris-HCl • 10 mM $MgCl_2$ • 100 µg/mL BSA

Table 2.9. Proteins and enzymes. The proteins and enzymes used during this thesis work presented with relevant specifications and the supplier.

NAME	SPECIFICATION	SUPPLIER
*Af*AA11B	Mutations: WT, E160Q, E160N, and E160D	Self-produced
BenchMark™ protein ladder	Protein standard	Life Technologies
BioLabs Protein Ladder	Protein standard	New England BioLabs Inc.
Bovine serum albumin (BSA)	For standard curves in the Bradford protein assay	Invitrogen by ThermoFisher Scientific
Catalase	From bovine liver	Invitrogen by ThermoFisher Scientific
Chitooligosaccharide oxidase (ChitO)	For production of oxidized standards	Self-produced
GeneRuler	DNA standard	Invitrogen by ThermoFisher Scientific
Horse radish peroxidase (HRP)	For Amplex Red assay	Merck
*Nc*AA9C	Mutations: WT, Q180N, Q180D, and Q180E	Self-produced

SwaI restriction enzyme	For transformation of *E. coli*	New England BioLabs Inc.

Table 2.10. Primers. The primers used during this experimental work is presented with the sequence from the 5' end to the 3' end.

PRIMER	**SEQUENCE 5' TO 3'**
*Af*AA11B_fwd	ATGATGTTTAGTAAATCTGGTTTGGTCGCT
*Af*AA11B_rev	TTATGCGTGACGGTGTCCACCGTGT

3 METHODS

3.1 CLONING OF FUNGAL LPMO GENES

The fungal full-length enzymes used in this experimental work were *Nc*AA9C and *Af*AA11B, where the gatekeeper residue of *Nc*AA9C (Q180) and *Af*AA11B (E160) were mutated. In *Nc*AA9C, this position was mutated to either Glu (Q180E), Asn (Q180N), or Asp (Q180D). The equivalent position in *Af*AA11B was mutated to either Gln (E160Q), Asn (E160N), or Asp (E160D). The respective genes were previously cloned into the pBSYP$_{GCW14}$Z expression plasmid and transformed into *Pichia pastoris (P. pastoris)* BSYBG11 by Dr. Lukas Rieder.

3.1.1 PCR SCREEN OF *Af*AA11B STRAINS

All variants of *Af*AA11B lost expression during this experimental work, and an explanation for this expression loss was investigated. A polymerase chain reaction (PCR) screen was performed to inspect the *P. pastoris* BSYBG11 strains for the presence of the *Af*AA11B gene. Dr. Kelsi Hall kindly designed primers to amplify the *Af*AA11B gene specifically.

The PCR results were analyzed with agarose gel electrophoresis. In agarose gel electrophoresis, an applied voltage moves negatively charged deoxyribonucleic acid (DNA) molecules through pores of an agarose matrix. DNA fragments are separated based on length because the DNA charge per mass ratio is stable regardless of the fragment. The gel is stained with a DNA-binding dye and the separated DNA fragments are visualized by ultraviolet (UV) radiation.

Materials:

Reagents and consumables

- *Af*AA11B_fdw
- *Af*AA11B_rev
- *P. pastoris* BSYBG11 strains harboring pBSYP$_{GCW14}$Z_*Af*AA11B
- Phire Tissue Direct PCR master mix
- SYBR Safe DNA gel stain
- TAE buffer
- UltraPure™ Agarose
- YPD media
- YPD-zeocin agar plates

Laboratory equipment

- Biosafety cabinet
- Blue tray
- GelDoc Go Imaging System
- GeneRuler 1 kb DNA Ladder
- Inoculation loop
- Tabletop centrifuge
- Mini-Sub GT cell
- Multitron Standard shaking incubator
- Termaks static incubator
- T100 Thermal Cycler

Method:

P. pastoris BSYBG11 strains harboring pBSYP$_{GCW14}$Z_*Af*AA11B variants were streaked out on YPD-zeocin plates (100 µg/mL zeocin) and incubated for two days at 30 ℃ in a Termaks static incubator. After incubation, 5 mL YPD media in 50 mL falcon tubes was inoculated with *P. pastoris* biomass from the YPD-zeocin plates. The cell cultures were incubated at 28 ℃, 180 rpm for 60 hours in a Multitron standard incubation shaker.

The PCR screen was performed on two templates: *P. pastoris* cells grown in liquid YPD media and on solid YPD-zeocin agar plates. Each PCR reaction contained 5 µL of 2 × Phire Tissue Direct PCR master mix, 10 µM primer (forward and reverse), and Milli-Q water with a final reaction volume of 10 µL. A small volume (> 0.5 µL) of liquid culture or cell biomass templates was added to each reaction. The PCR screen also included a positive control with the sequence-verified *Af*AA11B plasmids provided by Dr. Lukas Rieder. A negative control was also included without a template to check that there was no contamination in the master mix or primers. The reactions were incubated in a T100 thermal cycler following the PCR conditions stated in Table 3.1.

Table 3.1. PCR conditions for insert amplification. The cycle steps are stated with corresponding temperature (℃), duration (s), and the number of cycles.

CYCLE STEP	TEMPERATURE (℃)	DURATION (s)	CYCLES (× TIMES)
Initial denaturation	98	300	1
Denaturation	98	5	40
Annealing	61	5	
Extension	72	25	
Final Extension	72	60	1

The PCR products were analyzed by performing agarose gel electrophoresis. 300 mg agarose was dissolved in 30 mL TAE buffer (1× concentration) by microwaving the components. After cooling, the melted agarose gel, 3 µL SYBR Safe DNA gel stain (10 000 × concentration) was added to the agarose gel. The agarose gel was poured into a gel cast with a comb and left to set. After 20 minutes, the newly solid agarose gel was transferred to a Mini-Sub GT cell. The Mini-Sub GT cell was filled with 1× TAE buffer. A sample of GeneRuler 1 kb DNA ladder and the samples were loaded to the agarose gel and 120 V was applied for 20 minutes. The gel was analyzed with a GelDoc Go imaging system to look for PCR products, indicating the presence or absence of the *Af*AA11B gene.

3.1.2 TRANSFORMATION OF CHEMICALLY COMPETENT *E. COLI* CELLS

P. pastoris BSYBG11 was the strain used to express the *Af*AA11B variants. *P. pastoris* is a yeast expression system with excellent efficiency as a fungal LPMO expression host (Rieder et al., 2021a). Because of the integrative properties of the expression plasmids, *P. pastoris* incorporates the plasmid DNA into its genetic material (Cregg et al., 1985). This means the pBSYP$_{GCW14}$Z plasmids containing the *Af*AA11B variants were unable to be recovered from the BSYGB11 strains. Therefore, the pBSYP$_{GCW14}$Z expression plasmids of *Af*AA11B were transformed into *Escherichia coli* (*E. coli)*, as the plasmids exist episomally in the cytoplasm of *E. coli.* Hence, *E. coli* glycerol stocks may be generated from which the plasmids could be recovered and isolated. The pBSYP$_{GCW14}$Z expression plasmid is an *E. coli/P. pastoris* shuttle vector that can propagate in both expression hosts (Rieder et al., 2021a). One Shot™ TOP10 *E. coli* cells were used for transformation due to their high cloning efficiency and ability to propagate plasmids (Thermo Fisher Scientific, 2015).

Materials:

Reagents and consumables

- Ampicillin
- Glycerol
- LB media
- LB-ampicillin agar plates
- One Shot™ TOP10 chemically competent *E. coli* cells
- pBSYP$_{GCW14}$Z_*Af*AA11B WT and gatekeeper mutant plasmids
- S.O.C medium

Laboratory equipment

- Biosafety cabinet
- Multitron Standard incubation shaker
- Termaks static incubator
- Thermomixer C shaking incubator
- Water bath

Method:

The transformation protocol was adapted from Thermo Fisher Scientific (2015). 25 ng of pBSYP$_{GCW14}$Z_*Af*AA11B plasmids were transferred to 25 µL of thawed One Shot™ TOP10 chemically competent *E. coli* cells. The plasmids and competent cells were mixed gently and incubated on ice for 30 minutes. After ice incubation, the plasmid-cell suspension was incubated in a water bath holding 42 °C for 60 seconds and then incubated on ice again for another 60 seconds. 125 µL of pre-heated S.O.C. medium (42 °C) was added to each suspension and then incubated at 37 °C, 225 rpm for 60 minutes to recover the cells.

Following incubation, the recovery culture was plated on LB-ampicillin agar plates (100 µg/mL ampicillin). Two dilutions, *i.e.,* 5 and 100 µL, were used to ensure the selection of single colonies. The plates were incubated in a Termaks static incubator at 37 °C overnight.

A single One Shot™ TOP10-pBSYP$_{GCW14}$Z_*Af*AA11B colony was selected from each incubated LB-ampicillin agar plate. Each colony was used to inoculate 5 mL LB media (25 µg/mL ampicillin) and the cultures were incubated in a Multitron standard shaking incubator at 37 °C, 200 rpm for 16 hours. Glycerol stocks were created by mixing 500 µL of the grown cell culture with sterile glycerol to a final concentration of 40%. The glycerol stocks were stored at -80 °C.

3.1.3 TRANSFORMATION OF ELECTROCOMPETENT *P. PASTORIS* CELLS

New *P. pastoris* strains harboring the *Af*AA11B plasmids were prepared for upcoming large-scale cultivation. *Af*AA11B wild type (WT) and gatekeeper mutant plasmids isolated from *E. coli* were linearized before transformation into the expression host *P. pastoris* to increase the integration efficiency to *P. pastoris*.

Materials:

Reagents and consumables

- *E. coli* harboring pBSYP$_{GCW14}$Z_*Af*AA11B plasmids (Chapter 3.1.2)
- Electrocompetent *P. pastoris* BSYBG11
- LB media
- Sorbitol
- SwaI restriction enzyme
- YPD media
- YPD-zeocin agar plates
- 3.1 NE Buffer

Laboratory equipment

- Biosafety cabinet
- DNA Clean and concentrator TM-5 kit
- Electroporation cuvette
- Eppendorf Centrifuge 5430/5430R
- Eppendorf F-35-6-30 rotor
- E.Z.N.A® Plasmid DNA Mini Kit I
- Gene Pulser II
- Multitron Standard incubation shaker
- NanoDrop One
- Tabletop centrifuge
- Termaks static incubator
- Thermomixer C shaking incubator
- T100 Thermal Cycler

Method:

10 mL LB media (25 µg/mL zeocin) was added to 50 mL falcon tubes. A small amount of the frozen *E. coli* glycerol stock harboring pBSYP$_{GCW14}$Z_*Af*AA11B plasmids was added to each

falcon tube. The LB cultures were incubated overnight at 37 °C, 200 rpm in a Multitron Standard incubation shaker. *E. coli* cells were separated from the supernatant by centrifuging the cultures for five minutes at 5000 × g using an Eppendorf Centrifuge 5430/5430R centrifuge with an Eppendorf F-35-6-30 rotor. An E.Z.N.A® Plasmid DNA Mini Kit I was used to isolate the plasmids from the cells (OmegaBio-Tek, 2019). The plasmid isolation protocol was performed as described in the kit, except for eluting the plasmids with preheated Milli-Q water (70 °C). Plasmid concentrations were estimated by NanoDrop One and Beer-Lamberts law.

To linearize the plasmids, 2 µL SwaI restriction enzyme, 3000 ng *Af*AA11B plasmid, 10 µL 3.1 NE Buffer and Milli-Q water were mixed in a final volume of 100 µL. Following, the samples were incubated in a T100 thermal cycler at 25 °C for 120 minutes. The SwaI restriction enzyme was heat-inactivated by incubating at 65 °C for 20 minutes. A clean-up was performed post heat-inactivating to isolate the linearized plasmids, using a DNA Clean and concentrator TM-5 kit (ZymoResearch, 2021). The concentration of the linearized *Af*AA11B plasmids were estimated with NanoDrop One, as DNA absorbance at $\lambda = 260$ nm is proportional to the DNA concentration.

A mixture of 1000 ng linearized *Af*AA11B plasmids and 50 µL *P. pastoris* electrocompetent cells (purchased from Bisy) were added to a 2 mm electroporation cuvette and electroporated in a Gene Pulser II at 1.5 kV, 200 Ω, and 25 µF. After electroporation, 500 µL each of YPD media and 0.5 M sorbitol were added to the electroporated cells. The electroporated cells were incubated in a Thermomixer C shaking incubator at 30 °C, 600 rpm for three hours to allow the cells to recover. After incubation, three dilutions of the cultures were plated on YPD-zeocin agar plates (100 µg/mL zeocin). The plates were then incubated in a Termaks static incubator at 30 °C for two days.

3.1.4 SCREENING OF *P. PASTORIS* COLONIES: PROTEIN EXPRESSION TEST

P. pastoris secrete expressed protein from the intracellular space to the extracellular supernatant (Rieder et al., 2021a). To assess protein expression levels, transformed *P. pastoris* colonies can be screened by performing a protein expression test of the supernatant to identify the colonies with the highest exogenous plasmid expression. Different *P. pastoris* colonies will have varying expression levels depending on how many plasmid copies are integrated into the genome and where the plasmids are integrated (Cregg et al., 1985).

Expressed protein can be isolated from the supernatant using methanol-chloroform precipitation to separate the protein from salts present in the growth media. Protein expression can then be estimated using sodium dodecyl sulfate polyacrylamide gel electrophoresis (SDS-PAGE). Protein samples are denatured by treating the sample with heat and chemicals to generate a constant relationship between component charge and molecular weight (Reynolds and Tanford, 1970). The stable relationship enables protein separation based on size by applying a current to the sodium dodecyl sulfate polyacrylamide gel.

Materials:

Reagents and consumables

- Chloroform
- LDS loading dye
- Methanol
- *P. pastoris* harboring pBSYP$_{GCW14}$Z_*Af*AA11B plasmids (Chapter 3.1.3)
- Protein ladder
- Tris/Glycine/SDS Buffer
- YPD media

Laboratory equipment

- Biosafety cabinet
- Eppendorf Centrifuge 5430/5430R
- Eppendorf F-35-6-30 rotor
- Eppendorf FA-45-30-11 rotor
- GelDoc Go Imaging System
- Mini-PROTEAN Tetra Stain-Free Precast Gel
- Mini-PROTEAN Tetra System
- Multitron standard incubation shaker
- T100 Thermal Cycler
- UV/Stain-free tray

Method:

P. pastoris colonies (7 colonies total) were chosen from each incubated YPD-zeocin agar plate (Chapter 3.1.3) for upcoming colony screening. Each *P. pastoris* colony was used to inoculate 5 mL YPD media in 50 mL falcon tubes and incubated at 28 °C, 180 rpm for 60 hours in a Multitron standard incubation shaker to accomplish cell growth.

Cells were separated from the supernatant by centrifuging the cultivated *P. pastoris* strains in an Eppendorf Centrifuge 5430/5430R centrifuge with an Eppendorf F-35-6-30 rotor for 5 minutes at 5000 × g. The supernatants were treated with chloroform-methanol precipitation by first adding 400 µL methanol, 100 µL chloroform, and 300 µL Milli-Q water to 100 µL of each supernatant, vortexing in between each inclusion. The solutions were centrifuged for two minutes in the Eppendorf Centrifuge 5430/5430R using an Eppendorf FA-45-30-11 rotor at 14 000 × g. Centrifuging generated two separate layers, with the protein precipitated between the two layers. The protein was isolated by pipetting the uppermost layer before centrifuging

the solutions for three more minutes at 14 000 × g, generating a protein-containing pellet. Without disturbing the pellet, the methanol was carefully removed. The residual methanol evaporated in a fume hood. 10 µL Milli-Q water and 10 µL of 2 × LDS loading dye resuspended the dried pellet. Then, the samples were boiled at 95 °C for five minutes in a T100 Thermal cycler and loaded on a Mini-PROTEAN tetra stain-free precast gels in a mini-PROTEAN tetra system. A BioLabs protein ladder was included as a reference. The system was filled with 1 × Tris/Glycine/SDS buffer, and 180 V was applied to the gel. After 37 minutes, the protein migration was analyzed on a UV/Stain-free tray with a GelDoc Go imaging system. The gel images showed which *P. pastoris* colonies had the highest *Af*AA11B protein expression. Hence, the respective cell cultures were mixed with glycerol to a final concentration of 20% and used to express recombinant *Af*AA11B protein.

3.1.5 COLONY SCREENING OPTIMIZATION

Attempts were made to optimize the colony screening protocol described in Chapter 3.1.4. Protein expression can vary depending on the number of gene copies and where the genes are integrated into the *P. pastoris* genome (Cregg et al., 1985). Hence, an increased number of screened *P. pastoris* cell colonies was desired to identify colonies expressing high protein levels.

Increasing the number of screened *P. pastoris* colonies involved estimating the concentration of secreted protein by a *P. pastoris* cell using the colorimetric Bradford protein assay (Bradford, 1976). The Bradford protein assay is based on binding between Coomassie Brilliant Blue G-250 and protein, resulting in a blue color that may be monitored spectrophotometrically at 595 nm. Bovine serum albumin (BSA) is used to generate a calibration curve applied to estimate protein concentration (Bradford, 1976).

However, high protein concentrations detected in the Bradford protein assay may not necessarily indicate high protein expression. Cells that grow more will generally produce more protein. Hence, normalization for cell growth was also included when optimizing colony screening by measuring the optical density at 600 nm (OD_{600}). Measuring the OD_{600} is a well-known microbiological technique that quantifies the number of grown cells in a growth culture based on light scattering of a cell-containing sample. This protocol narrowed down the number of colonies to include in a protein expression test.

Materials:

Reagents and consumables

- Dye Reagent Concentrate (Bradford reagent)
- *P. pastoris* colonies w/ integrated *Af*AA11B plasmids
- YPD media

Laboratory equipment

- Eppendorf Concentrator Plus
- Eppendorf Swing-Bucket rotor
- Varioskan LUX plate reader
- Software: SkanIt 6.0.1
- 96-Well Microtiter Microplate
- 96-Well Polypropylene DeepWell Plate

Method:

Linearization and transformation were performed the same as per Chapter 3.1.3. The experimental design was changed by increasing the number of colonies tested. *P. pastoris* colonies were incubated in 96-Well Polypropylene DeepWell plates (2.0 mL) rather than 50 mL falcon tubes. Each well of the 96-Well Polypropylene DeepWell plates was filled with 1.25 mL YPD media. The inner wells were inoculated with a single *P. pastoris* colony (60 colonies total), whereas the outer wells contained YPD media only. In contrast, the outer wells were used as control samples and to ensure comparable growth conditions for the *P. pastoris* cultures. Breathable films were used to seal the plates to ensure proper airflow to the *P. pastoris* cultures. The colonies were incubated at 30 °C, 800 rpm for 60 hours in a Thermomixer C shaking incubator.

A Bradford protein assay was performed to determine which colonies expressed the most protein. The OD_{600} of the cultures was measured first to normalize cell growth using a Varioskan LUX plate reader with the SkanIt 6.0.1 software. 20 µL of *P. pastoris* cultures were diluted with 160 µL of Milli-Q water to ensure the measurements were within the instrument's linear range. Next, the supernatant was separated from the cells by centrifuging the 96-Well Polypropylene DeepWell plates 4 °C, 400 rpm for 10 minutes in an Eppendorf Concentrator plus with a swing-bucket rotor. 180 µL of supernatant was transferred to 20 µL of Bradford reagent in 96-Well Microtiter Microplates. Each well's absorbance was measured spectrometrically at 573 nm using the Varioskan LUX plate reader (SkanIt 6.0.1 software). No calibration curve was created as the absorbance of each *P. pastoris* colony was compared relative to each other.

The ratio between Bradford and OD_{600} measurements was calculated by dividing the Bradford protein supernatant absorbance at 573 nm by the cell absorbance at 600 nm. This ratio was used

to identify colonies expressing the most protein relative to cell growth. The 14 colonies with the highest ratio were chosen for each enzyme to screen in chloroform-methanol precipitation. A protein expression test using SDS-PAGE was performed on the 14 colonies as described in Chapter 3.1.4.

3.1.6 OPTIMIZING EXPRESSION OF *Af*AA11B

Materials:

Reagents and consumables

- BMD1 media
- Milli-Q water from different water tanks
- YPD media prepared with different peptone brands
- YPD-zeocin agar plates
- *P. pastoris* BSYBG11 strains harboring pBSYP$_{GCW14}$Z_*Af*AA11B
- *P. pastoris* BSYBG11 strains harboring pBSYP$_{DC}$Z_*Af*AA11B

Method:

P. pastoris BSYBG11 strains harboring pBSYP$_{GCW14}$Z_*Af*AA11B were grown on YPD-zeocin agar plates as described in Chapter 3.1.1. After incubation, a small-scale comparison was made between the different peptone brands used during this experimental work by preparing YPD media with the different peptone brands. Milli-Q water from different Milli-Q water sources was also included in the tests. Buffered minimal dextrose media (BMD1) was also tested as an alternative cultivation media. 5 mL cultivation media in 50 mL falcon tubes was inoculated with *P. pastoris* colonies expressing *Af*AA11B and incubated described per Chapter 3.1.1. Following incubation, a chloroform-methanol precipitation and expression test was performed on the recombinant proteins as described in Chapter 3.1.4.

To assess whether this was strain specific, an alternative *P. pastoris* strain expressing *Af*AA11B was tested. The formerly tested strains contained plasmids with the constitutive promoter P$_{GCW14}$ (Rieder et al., 2021a). Dr. Lukas Rieder also cloned the *Af*AA11B genes into the pBSYP$_{DC}$Z expression plasmid, containing the derepressed promoter P$_{DC}$ (Rieder et al., 2021a). The steps described previously were repeated to compare the strains.

3.2 PRODUCTION AND ISOLATION OF FUNGAL ENZYMES

The protocol for production and purification of *Nc*AA9C and *Af*AA11B was adapted from Rieder et al. (2021b).

3.2.1 LARGE SCALE CULTIVATION OF *Af*AA11B AND *Nc*AA9C STRAINS

Materials:

Reagents and consumables

- *P. pastoris* BSYBG11 strains harboring pBSYP$_{GC14}$Z_*Af*AA11B
- *P. pastoris* BSYBG11 strains harboring pBSYP$_{GC14}$Z_*Nc*AA9C
- YPD media
- YPD-zeocin agar plates

Laboratory equipment

- Baffles shake flasks
- Biosafety cabinet
- Multitron Standard shaking incubator
- Termaks static incubator

Method:

P. pastoris BSYBG11 strains harboring the expression plasmids pBSYP$_{GCW14}$Z_*Nc*AA9C and pBSYP$_{GCW14}$Z_*Af*AA11B were streaked out on YPD-zeocin (100 µg/mL) agar plates and incubated at 30 ºC for two days in a Termaks static incubator.

500 mL YPD media in 2000 mL baffled flasks were inoculated with *P. pastoris* colonies from the YPD-zeocin agar plates. The flasks were covered with breathable filter paper and incubated in a Multitron Standard incubation shaker at 28 ºC, 180 rpm for approximately 60 hours. A low culture volume in each flask and filter paper covering the flasks ensured proper airflow and growth conditions for the *P. pastoris* cells.

3.2.2 HARVESTING & CONCENTRATING *P. PASTORIS* SUPERNATANT

Materials:

Reagents and consumables

- Cell cultures from Chapter 3.2.1

Laboratory equipment

- Fiberlite™ F9-6 × 1000 LEX Fixed Angle Rotor
- Masterflex™ pump drive
- Sorvall Lynx 6000 centrifuge
- Steritop filter 0.45 µm
- VivaFlow 200 tangential crossflow concentrator

Method:

The supernatant for all protein replicates was separated from cells by centrifuging using a Sorvall Lynx 6000 centrifuge with a FiberliteTM F9-6 × 1000 LEX fixed angle rotor 4 ºC, 8000 × g for 15 minutes and filter sterilized with a Steritop 0.45 µm filter. A VivaFlow 200 tangential crossflow concentrator was used to concentrate the protein-containing supernatants ten-fold. Concentration was performed to shorten the loading process for the first purification step of the proteins.

3.2.3 PURIFICATION STEP 1: HYDROPHOBIC INTERACTION CHROMATOGRAPHY

Hydrophobic interaction chromatography (HIC) is a liquid chromatographic method used to separate components of different polarities. HIC is an ideal method to separate proteins due to the method's mild conditions, which keep the proteins from being degraded (Miller, 2005). Proteins in a sample will elute with different retention times depending on their affinity to the solid stationary phase, also called resin (Miller, 2005). Proteins' affinity to the resin is increased by dehydration, achieved by applying a high salt concentration to the protein sample or the aqueous mobile phase (Miller, 2005). Proteins elute by applying a buffer gradient with reduced salt concentration. The most hydrophobic components will elute with the longest retention time.

Materials:

Reagents and consumables

- HIC binding buffer:
  50 mM Bis-Tris/HCl pH 6.5
- HIC elution buffer:
  50 mM Bis-Tris/HCl pH 6.5, 50% ammonium sulfate
- Protein containing supernatants (Chapter 3.2.2)

Laboratory equipment

- HIC column: HiTrap Phenyl HP columns, 2 × 5 mL
- HIC instrument: ÄKTA Pure
- HIC software: Unicorn 6.4

Method:

HIC was the first step used to isolate *Nc*AA9C, *Af*AA11B, and gatekeeper mutants. HIC was performed with an ÄKTAPure instrument using the Unicorn 6.4 software and two HiTrap phenyl FF (HS) columns (2 x 5 mL) prepacked with the aromatic HIC resin Phenyl Sepharose (Cytiva, 2020a). Initially, the columns were flushed with Milli-Q water and equilibrated with 3 column volumes (CVs) of HIC binding buffer. The concentrated protein supernatants were dehydrated with the addition of 50% ammonium sulfate, which was added slowly to the samples. After dehydration, the protein samples were loaded onto the equilibrated columns at a 2.0 mL/min flow rate. The columns were then washed at a flow rate of 3 mL/min with approximately 6 CV of the HIC binding buffer to remove unbound proteins and until a stable baseline absorbance was obtained. Protein elution was performed by applying a buffer gradient of the HIC elution buffer, decreasing the salt concentration from 100% to zero over 22 minutes at a flow rate of 2 mL/min. Eluted protein was monitored with an ultraviolet (UV) detector at a fixed wavelength (280 nm) and collected as fractions.

SDS-PAGE was performed as described in Chapter 3.1.4 with minor modifications to decide which of the collected fractions contained *Nc*AA9C, *Af*AA11B, and the gatekeeper mutants. A sample from each fraction was diluted two-fold with Milli-Q water and 2 × LDS loading dye.

The protein concentration post-HIC was estimated for *Nc*AA9C, *Af*AA11B, and gatekeeper mutants by measuring protein absorbance for four technical replicates at $\lambda = 280$ nm using the NanoDrop One, the extinction coefficients (Table 3.2), and the Beer-Lambert law. Following, the initial protein yield was estimated using the molecular weights presented in Table 3.2.

Table 3.2. Descriptive values for *Af*AA11B, *Nc*AA9C, and the gatekeeper mutants. The extinction coefficient (ε) for *Af*AA11B and *Nc*AA9C is presented in $M^{-1}cm^{-1}$. The molecular weight for each variant is presented in g/mol.

LPMO	GATEKEEPER MUTATION	EXTINCTION COEFFICIENT (ε) ($M^{-1}cm^{-1}$)	MOLECULAR WEIGHT (g/mol)
*Af*AA11B	WT	40450	42802.5
	E160Q		42801.6
	E160N		42787.5
	E160D		42788.5
*Nc*AA9C	WT	46910	35754.93
	Q180N		35740.91
	Q180E		35755.92
	Q180D		35741.89

3.2.4 PURIFICATION STEP 2: SIZE EXCLUSION CHROMATOGRAPHY

Size exclusion chromatography (SEC) separates an analyte based on size. The size-based separation is caused by the physical properties of the stationary phase, which consists of pores (Miller, 2005). Larger molecules will not fit into the tiny pores and will elute with the shortest retention time. In contrast, smaller molecules diffuse to the stationary phase's material and achieve a longer retention time (Miller, 2005).

Materials:

Reagents and consumables

- HIC isolated *Af*AA11B WT or *Nc*AA9C WT and gatekeeper mutants
- SEC buffer: 50 mM Bis-Tris/HCl pH 6.5, 150 mM NaCl

Laboratory equipment

- Amicon® Ultra centrifugal tubes
- SEC column: HiLoad 16/160 Superdex 75 pg 120 mL
- SEC instrument: ÄKTA Purifier
- SEC software: Unicorn 5.2

Method:

HIC isolated proteins were concentrated before SEC to achieve a low loading volume for the SEC column resulting in high-resolution chromatograms. Concentration was performed with Amicon® ultra 15 mL centrifugal tubes (10 kDa cutoff), which initially were washed with Milli-Q water to remove any trace glycerine (Millipore, 2018). The proteins were concentrated at 4 °C, 5000 × g for 45 minutes using an Eppendorf 5430/5340R centrifuge with an Eppendorf F-35-6-30 rotor.

An ÄKTA Purifier with the Unicorn 5.2 software was used to perform SEC on the concentrated proteins. A HiLoad 16/160 Superdex column (120 mL), consisting of a high-resolution resin with cross-linked agarose and dextran, was equilibrated with 1 CV of the SEC buffer at a flow rate of 1 mL/min (Cytiva, 2020b). The protein samples were loaded onto the SEC column and eluted isocratically. Proteins were detected using a UV detector at a fixed wavelength ($\lambda = 280$ nm). Fractions were collected and analyzed on SDS-PAGE as described in Chapter 3.2.3. The resulting electrophoresis images were used as guidance to pool the *Nc*AA9C- and *Af*AA11B-containing fractions. The concentration of the pooled proteins was estimated with the A_{280} method as described in Chapter 3.2.3.

3.2.5 COPPER SATURATION

LPMOs are copper saturated with excess copper prior to analysis to ensure enzymatic activity and functionality of the LPMOs (Eijsink et al., 2019). Free and unbound copper may create artificial LPMO activity and therefore needs to be removed by sufficient washing (Eijsink et al., 2019).

Materials:

Reagents and consumables

- *Af*AA11B WT or *Nc*AA9C WT and gatekeeper mutants
- BSA
- Dye Reagent Concentrate (Bradford reagent)
- Storage buffer for *Af*AA11B and *Nc*AA9C: 50 mM Bis-Tris/HCl pH 6.5

Laboratory equipment

- Amicon® Ultra centrifugal tubes
- Eppendorf Centrifuge 5430/5430R
- Eppendorf F-35-6-30 rotor
- PD-10 desalting columns 8.3 mL
- Varioskan LUX plate reader
- 96-Well Microtiter Microplate

Method:

An overestimation of protein concentrations was believed to have occurred due to colored pigments from the YPD growth media interfering with the measurements at $\lambda = 280$ nm. Therefore, only a two-fold molar excess of copper was added to *Nc*AA9C, *Af*AA11B, and gatekeeper mutants instead of the standard three-fold molar excess. The copper-protein solution was incubated on ice for 30 minutes to ensure copper binding to the LPMO before protein washing.

PD-10 desalting columns with a bed volume of 8.3 mL were used to remove unbound copper from the proteins (GEHealthcare, 2007). The columns were equilibrated with 5 CVs of the

*Af*AA11B/*Nc*AA9C storage buffer. A maximum of 2.5 mL of each protein was applicated to the equilibrated column, followed by 2 × 2.3 mL 50 mM Bis-Tris/HCl pH 6.5. The last 2.3 mL of eluate was collected. Remaining free copper in the collected eluate was removed by washing the proteins three times with the *Af*AA11B/*Nc*AA9C storing buffer in Amicon® ultra 15 mL centrifugal tubes (10 kDa cutoff) using an Eppendorf 5430/5430R centrifuge with an Eppendorf F-35-6-30 rotor. Removing excess copper from LPMOs with PD-10 desalting columns and Amicon® ultra centrifugal tubes has been described previously by Stepnov et al. (2021).

The final protein concentration was estimated for the copper-saturated proteins using the Bradford protein assay and the molecular weights presented in Table 3.2. The Bradford protein assay was used to estimate the final protein concentration rather than the A_{280} method due to the speculated overestimation of protein concentration using the A_{280} method. 5 µL of sample and 200 µL of Bradford reagent were added to each well in a 96-Well Microtiter Microplate. Samples were either protein dilutions, the *Af*AA11B/*Nc*AA9C storage buffer (blank sample), or BSA. BSA was used to make the calibration curve, ranging linearly from 0.3 to 0.9 mg/mL BSA.

SDS-PAGE was performed as described previously (Chapter 3.2.3) to observe the purity of the final isolated *Nc*AA9C, *Af*AA11B, and the gatekeeper mutants. 0.2 µg and 2.0 µg of each protein were loaded.

3.3 REDOX MEASUREMENTS OF *Af*AA11B AND *Nc*AA9C

Electron transfer (ET) from an electron donor, *i.e.,* an oxidant, to an electron acceptor, *i.e.,* a reductant, is a redox reaction (Lu and Marshall, 2013). The species with the highest electron affinity has the highest reduction potential (Zanello, 2003). Equation 4 presents an example of a first-order redox reaction involving reduced N, N, N', N'-tetramethyl-1,4-phenylenediamine (TMP_{red}) and LPMO-Cu(II).

$$TMP_{red} + \text{LPMO-Cu(II)} \leftrightharpoons TMP_{ox} + \text{LPMO-Cu(I)} \quad (4)$$

Equation 4: First-order redox reaction. The equation shows a first-order redox reaction between TMP_{red} and LPMO-Cu(II), where the products TMP_{ox} and LPMO-Cu(I) are produced from the reactants (Aachmann et al., 2012).

ET is directed by the concentration of the reactants and the redox reaction's equilibrium constant (*K*). The first-order redox reaction presented in Equation 4 may be rearranged to determine the redox reaction's equilibrium constant, which is presented in Equation 5.

$$(5) \qquad K = \frac{[\mathrm{TMP_{ox}}]_{\mathrm{eq}}[\mathrm{LPMO-Cu(I)}]_{\mathrm{eq}}}{[\mathrm{TMP_{red}}]_{\mathrm{eq}}[\mathrm{LPMO-Cu(II)}]_{\mathrm{eq}}}$$

Equation 5: The equilibrium constant. *K* is defined by the quantitative relationship between product and reactant concentration at equilibrium (Aachmann et al., 2012). Here, the redox reaction between TMP_{red} and LPMO-Cu(II) is used as an example to define *K*.

Besides directing ET, *K* is involved in determining the Gibbs free energy (ΔG^0) of a redox reaction. ΔG^0 may be referred to as the driving force of ET. Therefore, a higher ΔG^0 induces a higher ET rate. Furthermore, the driving force of a redox reaction is affected by the difference in cell potential, E^0_{cell}, between the oxidant and reductant. The interaction between *K*, ΔG^0, and E^0_{cell} is presented by the Nernst Equation in Equation 6.

$$(6) \qquad \Delta G^0 = -RT\ln K = -vFE^0_{\mathrm{cell}}$$

Equation 6: The Nernst Equation. ΔG^0 is defined by the equilibrium constant K and the difference in electric potential between the oxidant and reductant (E^0_{cell}) in volts. The equation also involves the gas constant (R = 8.314466261815324 J × K^{-1}× mol^{-1}), temperature (T) in kelvin, number of electrons transferred (v), and the Faraday's constant (F = 96 485 J × V^{-1} × mol^{-1}).

Materials:

Reagents and consumables

- *Af*AA11B WT or *Nc*AA9C WT and gatekeeper mutants
- N_2 (g)
- N,N,N',N'-tetramethyl-1,4-phenylenediamine (TMP_{red})
- Pipes buffer
- TraceSELECT® water

Laboratory equipment

- Disposable cuvettes 1.5 mL semimicro 12.5 × 12.5 × 45 mm
- NanoPhotometer® C40
- Schlenk line
- Whitley A95 TG anaerobic workstation

Method:

Redox measurements for *Af*AA11B, *Nc*AA9C, and gatekeeper mutants were estimated based on the protocol described by Aachmann et al. (2012). Dr. Kelsi Hall performed the experiments involving *Nc*AA9C.

200 mM Pipes buffer and TraceSELECT® water were deoxygenated using a Schlenk line under three N_2 (g) flux and vacuum cycles for 15 minutes and 5 minutes, respectively. The Pipes buffer, TraceSELECT® water, and plastic laboratory equipment were placed in a Whitley A95 TG anaerobic workstation one day before performing the experiments to equilibrate the reagents with the anaerobic environment. TMP_{red} powder and *Af*AA11B were prepared separately in gas chromatography vials on the day the experiments were performed. These reagents were deoxygenated for 3 × 5 minutes cycles by N_2 (g) flux using a Schlenk line. A vacuum was applied for two minutes between each interval. Deoxygenation was continued with 30 minutes of incubation in the anaerobic workstation. Following incubation, 20 mM Pipes buffer was prepared with TraceSELECT® water to reduce side reactions involving free copper (Stepnov et al., 2021). LPMO and TMP_{red} were then diluted in the 20 mM Pipes buffer to the concentration of 60 and 300 µM, respectively. The dilutions were mixed 1:1 with a final volume of 60 µL, measured in triplicate. A NanoPhotometer® C40 monitored the generated TMP_{ox} under anaerobic conditions at λ = 610 nm, and the TMP_{ox} concentration was estimated based on the A_{610} and extinction coefficient (ε = 14 $mM^{-1}cm^{-1}$) (Sorlie et al., 2000). The concentration of produced TMP_{ox} was an approximation for LPMO-Cu(I) concentration due to the stoichiometry presented in Equation 4. The equilibrium constant, *K*, of the redox reaction was estimated by Equation 5. *K* was used to estimate the cell potential, $E^0_{cell,}$ for the redox couple LPMO-Cu(II)/LPMO-Cu(I) by the Nernst Equation in Equation 6. E^0_{cell} for the redox couple TMP_{red}/TMP_{ox} at 273 mV compared to the normal hydrogen electrode was used to estimate the redox potential for *Af*AA11B and *Nc*AA9C WT and gatekeeper mutants (Liu et al., 1997). The difference in *Af*AA11B and *Nc*AA9C redox potentials was analyzed by an analysis of variance (ANOVA) in R studio. Contrast analyses were performed to investigate whether the nature of the gatekeeper residue caused the difference in redox potential based on gatekeeper residue side-chain length and introduced charge close to the copper center.

3.4 OXIDASE ACTIVITY OF *Af*AA11B AND *Nc*AA9C

The oxidase activity of an enzyme is described as the ability of an enzyme to catalyze redox reactions by acting as a reducing agent. Therefore, the *in-situ* production of H_2O_2 by the LPMO in a redox reaction with molecular oxygen describes the oxidase activity of an LPMO. This oxidase activity may be estimated by performing the Kittl assay or the Amplex Red assay (Kittl et al., 2012). A schematic representation of the Amplex Red assay is presented in Figure 3.1. H_2O_2 oxidizes the compound Amplex Red to resorufin, and horseradish peroxidase (HRP)

catalyzes this reaction (Kittl et al., 2012). A suitable reductant reduces Cu(II) to Cu(I) in the active site of the LPMO. The "primed" LPMO can then produce H_2O_2 by O_2 reduction. The reductant regenerates the Cu(I) state of the LPMO.

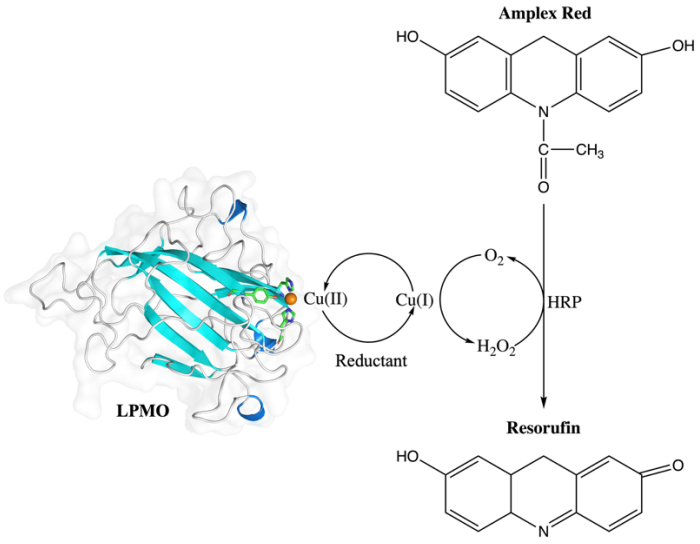

Figure 3.1: Schematic representation of the Amplex Red assay. *The compound Amplex Red is oxidized to resorufin in an HRP-coupled reaction using hydrogen peroxide, which the LPMO supplies. The illustration was derived from Kittl et al. (2012).*

The generation of resorufin may be monitored spectrophotometrically with a maximum absorbance at λ = 569 nm (Kittl et al., 2012). The absorbance of resorufin is considered proportional to the amount of H_2O_2 generated by the LPMO, which allows quantification of LPMO oxidase activity.

Materials:

Reagents and consumables

- *Af*AA11B or *Nc*AA9C WT and gatekeeper mutants
- Amplex Red
- Ascorbic acid
- Bis-Tris/HCl pH 6.5
- $CuSO_4$
- HRP
- H_2O_2
- TraceSELECT® water

Laboratory equipment

- Varioskan LUX
- Software: SkanIt 6.0.1
- 96-Well Microtiter Microplate

Method:

The Amplex Red assay was performed for *Af*AA11B, *Nc*AA9C WT and the gatekeeper mutants, following the protocol described by Kittl et al. (2012). Each sample (100 µL) was prepared in three replicates in a 96-Well Microtiter Microplate and consisted of 1 µM LPMO or $CuSO_4$, 100 µM Amplex Red, and 5 U/mL HRP dissolved in 50 mM Bis-Tris/HCl pH 6.5 and TraceSELECT® water. Control samples included three replicates without LPMO or $CuSO_4$ and one replicate without reductant for each LPMO. As the Amplex Red assay is very copper-sensitive, three replicates of flow-through obtained during the final washing step post-copper saturation for each LPMO (Chapter 3.2.5) were included to ensure no unbound copper was present in the final LPMO samples. The sample reactions were incubated at 30 °C for 5 minutes in a Varioskan LUX plate reader and initiated with 1 mM AscA. The Varioskan LUX plate reader monitored the resorufin absorbance at $\lambda = 563$ nm every ten seconds for 3000 seconds using SkanIt 6.0.1 software.

The concentration of the generated H_2O_2 by *Af*AA11B or *Nc*AA9C WT and gatekeeper mutants was estimated based on the resorufin absorption, which was considered proportional to the H_2O_2 concentration, using H_2O_2 calibration curves ranging from 0-40 µM. H_2O_2 calibration curves included 1 mM AscA to account for background activity from AscA. The monitored absorbance at 0 µM H_2O_2 was subtracted from the results to account for background absorbance. A simple linear regression of product concentration concerning time was performed in Microsoft Excel to estimate the rate of the oxidase activity of *Af*AA11B or *Nc*AA9C WT and the three gatekeeper mutants. The linear regression was based on three technical replicates monitored on three different days for *Af*AA11B WT, the gatekeeper mutants, and *Nc*AA9C Q180D, averaging to three independent replicates. For two separate days, three technical replicates were monitored for *Nc*AA9C WT and the gatekeeper mutants Q180N and Q180E, averaging to two independent replicates. Initial rates of the oxidase activity were estimated based on the first 120 seconds of the reaction for *Af*AA11B and *Nc*AA9C WT and gatekeeper mutants. Differences in *in-situ* H_2O_2 production rate were analyzed by ANOVA and contrast analyses in R studio.

3.5 PEROXIDASE ACTIVITY OF *Af*AA11B AND *Nc*AA9C

The Breslmayr assay estimates the peroxidase activity, *i.e.,* H_2O_2 consumption, of an LPMO (Breslmayr et al., 2018). Breslmayr et al. (2018) proposed the peroxidase reaction, which is very complicated and poorly understood regarding LPMOs (Figure 3.2). The hypothesis is that

2,6-dimethoxyphenol (2,6-DMP) serves as substrate and reductant in the Breslmayr assay. 2,6-DMP acts as a reductant by reducing LPMO-Cu(II) to the Cu(I) state. LPMO-Cu(I) catalyzes the oxidation of the substrate 2,6-DMP using H_2O_2, which initiates the radicalization of two 2,6-DMP substrate molecules. The two 2,6-DMP radicals undergo radical coupling, which generates the compound hydrocoerulignone. Reduction of LPMO-Cu(II) to LPMO-Cu(I) by the reductant 2,6-DMP is repeated, resulting in LPMO catalyzed oxidation of hydrocoerulignone to the product coerulignone assisted by H_2O_2. By measuring the absorbance of produced coerulignone at $\lambda = 469$ nm, the peroxidase activity of an LPMO can be estimated.

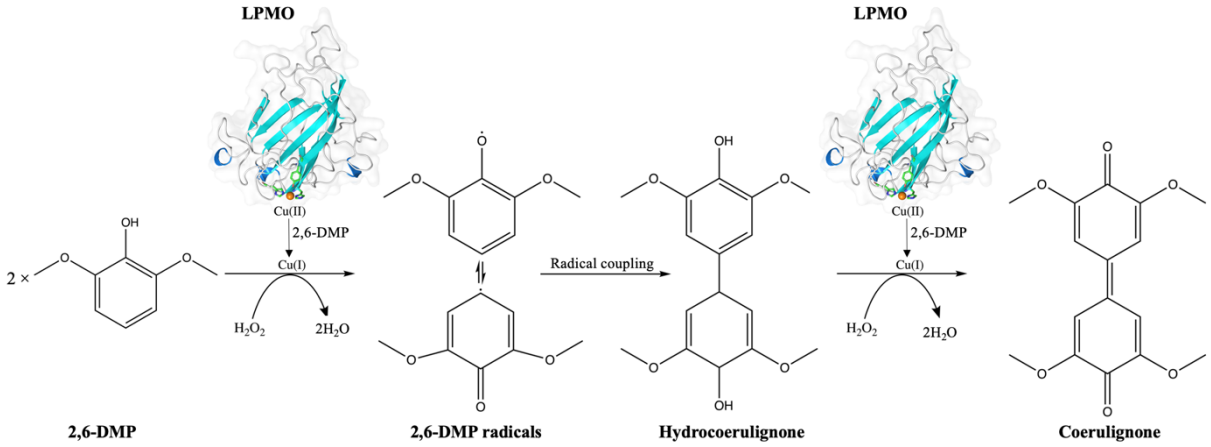

Figure 3.2: Schematic representation of the Breslmayr assay. *2,6-DMP reduces LPMO-Cu(II) to the Cu(I) state. The LPMO-Cu(I) catalyzes the oxidation of two 2,6-DMP molecules, which generates two 2,6-DMP radicals. Dimerization of two 2,6-DMP radicals generates the compound hydrocoerlignone. The LPMO catalyzes the oxidation of hydrocoerlignone to the product coerulignone. The figure was adapted from Breslmayr et al. (2018).*

Materials:

Reagents and consumables

- *Af*AA11B or *Nc*AA9C WT and gatekeeper mutants
- Bis-Tris pH 6.5
- $CuSO_4$
- H_2O_2
- 2,6-DMP

Laboratory equipment

- Varioskan LUX
- Software: SkanIt 6.0.1
- 96-Well Microtiter Microplate

Method:

The Breslmayr assay was performed for *Af*AA11B, *Nc*AA9C, and the gatekeeper mutants as Breslmayr et al. described the assay in 2018. Dr. Kelsi Hall performed the *Nc*AA9C related experiments. Triplicates of 100 µL reactions were prepared in a 96-Well Microtiter Microplate and consisted of 50 mM Bis-Tris/HCl pH 6.5, 100 µM H_2O_2, 1 mM 2,6-DMP, and Milli-Q

water. The reactions and controls were incubated at 30 ºC for 5 minutes in a Varioskan LUX plate reader and initiated with the addition of 1 µM LPMO or $CuSO_4$. Control samples included reactions without LPMO/$CuSO_4$ or H_2O_2. The Varioskan LUX plate reader measured coerulignone absorbance at λ = 473 nm every ten seconds for ten minutes using SkanIt 6.0.1 software.

A simple linear regression of the monitored coerulignone absorbance considering time was performed in Microsoft Excel to estimate the peroxidase activity of all gatekeeper variants of *Af*AA11B and *Nc*AA9C. Technical replicates monitored on three and two different occasions were included in the regression analysis, generating three and two independent replicates for *Af*AA11B and *Nc*AA9C, respectively. The differences in *Af*AA11B and *Nc*AA9C WT and gatekeeper mutants' peroxidase activity were analyzed by ANOVA and contrast analyses in R studio.

3.6 PREPARATION OF OXIDIZED STANDARDS

*Af*AA11B has shown specific activity towards soluble chitooligosaccharides, *e.g.,* $(GlcNAc)_4$ (Rieder et al., 2021b). *Af*AA11B catalyzes the oxidation of $(GlcNAc)_4$ (A4), primarily generating oxidized $(GlcNAc)_3$ ($A3_{OX}$) and $(GlcNAc)_2$ ($A2_{OX}$) with the corresponding native monomer (A1) and dimer (A2), respectively (Rieder et al., 2021b). Chitooligosaccharide oxidase (ChitO) catalyzes oxidization of N-acetylated oligosaccharides, preferably chitooligosaccharides, producing lactones that hydrolyze to aldonic acids (Ferrari et al., 2014, Heuts et al., 2007, Heuts et al., 2008). ChitO was produced and isolated to generate oxidized standards of the desired polymerization to quantify oxidized products from *Af*AA11B catalyzed oxidation of the C1 position in $(GlcNAc)_4$, leading to hydrolysis of the glycosidic bonds.

3.6.1 PRODUCTION AND PURIFICATION OF CHITO

3.6.1.1 EXPRESSION OF CHITO

Materials:

Reagents and consumables

- Ampicillin
- Arabinose
- *E. coli* BL21 strains harboring pBAD-MBP-ChitO
- Glycerol
- Kanamycin
- LB media
- Lysis buffer: 50 mM Potassium phosphate pH 6.5, 10% glycerol (v/v)
- Tetracycline

Laboratory equipment

- Baffled shake flask
- Biosafety cabinet
- Fiberlite™ F9-6 ×1000 LEX Fixed Angle Rotor
- Fiberlite™ F21-8 × 50y Fixed Angle Rotor
- Multitron Standard incubation shaker
- Sonicator
- Sorvall Lynx 6000 centrifuge
- Steritop 0.45 µm

Method:

ChitO was purified and isolated as described by Loose et al. (2014). *E. coli* BL21 strains harboring the expression plasmids p_{BAD}-MBP-ChitO were used to inoculate 12 mL LB media (50 µg/mL ampicillin, 15 µg/mL kanamycin, and 12.5 µg/mL tetracycline) directly from the -80 °C glycerol stock. The cell culture was incubated in a Multitron Standard incubation shaker at 37 °C, 200 rpm overnight. 5 mL of the overnight culture was added to 2 × 500 mL of LB media (50 µg/mL ampicillin, 15 µg/mL kanamycin, and 12.5 µg/mL tetracycline, 0.4% arabinose). The large-scale cultures were incubated in a Multitron Standard incubation shaker at 17 °C, 200 rpm for 70 hours.

After 70 hours, the cell cultures were centrifuged using a Sorvall Lynx 6000 centrifuge with a Fiberlite™ F9-6 × 1000 LEX fixed angle rotor at 4 °C, 7741 × g for 25 minutes. The centrifugation separated the supernatant from the *E. coli* cell pellet, and the cell pellet was resuspended in 35 mL lysis buffer. Sonication was used to disrupt the *E. coli* cells using 5 seconds on/off intervals for 4 minutes with 30% amplitude. The resulting lysate was centrifuged in a Sorvall Lynx 6000 centrifuge with Fiberlite™ F21-8 × 50y fixed angle rotor at 4 °C, 20 000 × g for 30 minutes. After centrifugation, the lysate was filtered through a Steritop 0.45 µm filter.

3.6.1.2 PURIFICATION OF CHITO

Purification of ChitO was performed in a two-step isolation process: 1) Anion exchange chromatography (AEC) and 2) SEC. AEC is another separation technique for protein samples which separates proteins based on charged amino acids on the protein surface. Exchangeable anions in the stationary phase resin may be exchanged with anions in the analyte, which result in sample separation (Miller, 2005). SEC was described in Chapter 3.2.4.

Materials:

Reagents and consumables

- AEC binding buffer: 50 mM potassium phosphate pH 6.5, 10% glycerol (v/v)
- AEC elution buffer: 50 mM potassium phosphate pH 6.5
  10% glycerol (v/v), 1 M NaCl
- ChitO lysate from Chapter 3.6.1.1
- SEC buffer: 20 mM Tris/HCl pH 8

Laboratory equipment

- AEC column: DEAE Sepharose FF anion exchange column
- AEC instrument: BioRad NGC Chromatography system
- AEC software: ChromLab
- SEC column: HiLoad 16/160 Superdex 75 pg 120 mL
- SEC instrument: ÄKTA Purifier
- SEC software: Unicorn 5.2

Method:

AEC was performed using a BioRad NGC Chromatography instrument with the ChromLab software and one DEAE Sepharose FF anion exchange column (5 mL). The column was equilibrated with the AEC binding buffer for 5 CVs. The protein was then loaded on the column with a 0.8 mL/min flow rate. The column was then washed at a flow rate of 3 mL/min with approximately 36 CVs of AEC binding buffer to remove unbound proteins and obtain a stable baseline absorbance. Protein elution was performed by applying a gradient of the AEC elution buffer, increasing the concentration of sodium chloride from 0 to 1 M over 120 minutes at a flow rate of 0.8 mL/min. The protein elution was detected with a UV detector (fixed λ = 280 nm), collected as one fraction, and analyzed with SDS-PAGE as described in Chapter 3.2.3. Preliminary protein yield was also estimated based on the extinction coefficient (ε = 142 670 $M^{-1}cm^{-1}$) and the molecular weight (*mw* = 94 857 g/mol) as described in Chapter 3.2.3.

Eluted ChitO was concentrated with a MacroseqAdvance Centrifugal device (30 kDa cut off) using an Eppendorf Centrifuge 5430/5430R with an Eppendorf F-35-6-30 rotor at 4 °C, 5000 × g, for 60 minutes before SEC isolation. SEC isolation was performed as described per Chapter 3.2.4, but the mobile phase was changed to 20 mM Tris/HCl pH 8.

The final concentration of ChitO was estimated as described in Chapter 3.2.3. 10% glycerol (v/v) was added to the final ChitO stock, and the protein was stored at -20 °C.

3.6.2 PREPARATION OF OXIDIZED STANDARDS

Materials:

Reagents and consumables

- Acetonitrile
- ChitO from Chapter 3.6.1
- GlcNAc
- $(GlcNAc)_2$
- $(GlcNAc)_3$
- Storing buffer for oxidized standards: 50 mM Tris/HCl pH 8.0

Laboratory equipment

- Corning® 96 well filter plate
- Eppendorf thermomixer C

Method:

3 mM GlcNAc, $(GlcNAc)_2$, and $(GlcNAc)_3$ were prepared in 50 mM Tris-HCl pH 8.0 and incubated with 0.12 mg/mL ChitO. The solutions were incubated overnight in an Eppendorf thermomixer C at 20 °C. Native standard solutions of GlcNAc, $(GlcNAc)_2$, and $(GlcNAc)_3$ without ChitO were also prepared. The standard solutions were filtered using a Corning® 96 well filter plate and stored at -20 °C.

3.7 ENZYMATIC ACTIVITY OF *Af*AA11B ON SOLUBLE SUBSTRATES

Enzymatic activity of *Af*AA11B WT on soluble substrates has been shown previously by Rieder et al. (2021b). Time-course experiments were performed to compare of oxidative cleavage of glycosidic bonds in the soluble substrate $(GlcNAc)_4$ catalyzed by *Af*AA11B WT and the gatekeeper mutants under oxygen and hydrogen peroxide conditions.

3.7.1 *IN-SITU* PEROXYGENASE ACTIVITY

Enzymatic activity of an LPMO under oxygen conditions was first proposed by Vaaje-Kolstad et al. in 2010. However, it has since been discussed whether the so-called monooxygenase reaction occurs at all (Bissaro et al., 2020b, Courtade et al., 2020, Hangasky et al., 2018, Wang et al., 2020). It is hypothesized that H_2O_2 is the true cosubstrate of LPMOs and reactions occurring under oxygen conditions are reliant on *in-situ* H_2O_2 production (Bissaro et al., 2017).

Hence, for this thesis LPMO activity under oxygen conditions has been titled "*in-situ* peroxygenase activity".

Materials:

Reagents and consumables

- *Af*AA11B WT and gatekeeper mutants
- Ascorbic acid
- Bis-Tris pH 6.5
- $(GlcNAc)_4$
- NaOH

Laboratory equipment

- Corning® 96 well filter plate
- Thermomixer C shaking incubator

Method:

A master mix containing 187.5 µL was prepared for each enzyme, consisting of 1 mM $(GlcNAc)_4$, 50 mM Bis-Tris pH 6.5, and Milli-Q water. The reactions were preheated for two minutes before adding 1 µM LPMO and then 1 mM AscA to initiate the reaction. Notably, the LPMO was added to the reactions right before AscA was added, to avoid a reaction between the substrate's reducing end and the LPMO. Each experiment included one control without enzyme and one without AscA. 25 µL was subtracted from the master mix and terminated with 175 µL of 200 mM NaOH after 5, 10, 30, 60, 120, 180, and 300 minutes. The experiment was performed for three independent replicates for *Af*AA11B WT and the gatekeeper mutants E160Q, E160N, and E160D. All samples were filtered through a Corning® 96 well filter plate prior to detection of oxidized products.

3.7.2 INFLUENCE ON *IN-SITU* PEROXYGENASE ACTIVITY BY CATALASE

Catalase is an enzyme which catalyzes the oxidation of two hydrogen peroxide molecules to oxygen and water. Adding catalase to the *Af*AA11B *in-situ* peroxygenase activity assay may reveal a connection between *in-situ* hydrogen peroxide generation and substrate oxidation catalyzed by the LPMOs. Similar experiments have been previously performed with *Af*AA11B WT and HRP (Rieder et al., 2021b).

Materials:

Reagents and consumables

- *Af*AA11B WT and gatekeeper mutants
- Catalase from bovine liver

Method:

*Af*AA11B WT and the apparent most active gatekeeper mutant E160D were included in the catalase experiment. The catalase experiment was performed with minor modifications to the *in-situ* peroxygenase activity experiment (Chapter 3.7.1). Two concentrations of catalase (500 and 3000 U/mL) were added to the master mixes before preheating the reagents. Reactions were sampled at 5, 10, 30, and 180 minutes.

3.7.3 PEROXYGENASE ACTIVITY

Bissaro et al. (2017) proposed the peroxygenase reaction catalyzed by a LPMO, showing that hydrogen peroxide was the true cosubstrate.

Materials:

Reagents and consumables

- *Af*AA11B WT and gatekeeper mutants
- H_2O_2
- N_2 (g)
- Reductants:
  AscA, cysteine, and gallic acid

Laboratory equipment

- Schlenk line
- Whitley A95 TG anaerobic workstation

Method:

The peroxygenase experiment design was similar to the *in-situ* peroxygenase activity experiment described in Chapter 3.7.1, with minor modifications. 300 µM H_2O_2 was added to the master mixes prior to reaction initiation with 1 mM of reductant. Different reducing agents were also compared in the peroxygenase experiment. Reactions were sampled at 15, 30, 60, 120, 240, 360, 600, and 1800 seconds after reaction initiation.

The peroxygenase experiment was performed in both aerobic and anaerobic conditions to observe whether *in-situ* hydrogen peroxide production from molecular oxygen contributed to excess oxidized product formation. A Whitley A95 Workstation was used to achieve anaerobic conditions. 500 mM Bis-Tris pH 6.5 and Milli-Q water were deoxygenated using a Schlenk line under N_2 (g) flux for 45 minutes and incubated overnight in the workstation to ensure oxygen-free reagents. Plastic laboratory equipment needed for the experiment was also incubated overnight, as plastic binds molecular oxygen. The reductants, LPMOs, and substrate $(GlcNAc)_4$ were prepared separately in gas chromatography vials and made oxygen-free on the experimental day by applying a N_2 (g) flux using a Schlenk line for 5 minutes.

3.7.4 DETECTION OF OXIDIZED PRODUCTS

3.7.4.1 HIGH-PERFORMANCE ANION EXCHANGE CHROMATOGRAPHY

High-performance liquid chromatography (HPLC) is a favored version of liquid chromatography due to the separation method's high speed, resolution, sensitivity, and accuracy (Miller, 2005). High-performance anion-exchange chromatography (HP-AEC) is one such technique used to separate anions in a sample solution. HP-AEC is commonly used in oligosaccharide analysis as it is more sensitive and gives higher resolution than other liquid chromatographic methods (Lee, 1990).

HP-AEC uses a basic mobile phase, such as sodium hydroxide and sodium acetate, to generate oxyanions from the carbohydrates. A stationary phase which tolerates such a high pH is used in the CarboPac PA1 column. Oxyanions are separated with high resolution due to the strong anionic sites present in the column's resin (Rohrer et al., 2013). Separated oxyanions are then detected by direct detection technique pulsed amperometric detection (PAD). A voltage between two electrodes in the column effluent oxidizes the oxyanions at the working anode. This results in a change in current, which is monitored as a function of time (Rohrer et al., 2013).

Materials:

Reagents and consumables

- HP-AEC mobile phase A: 1.0 M sodium acetate and 0.1 M NaOH
- HP-AEC mobile phase B: 0.1 M NaOH
- NaOH
- Oxidized chitooligosaccharide standards (Chapter 3.6.2)
- Time course samples from Chapter 3.7.1, 3.7.2, and 3.7.3
- Sodium acetate

Laboratory equipment

- HP-AEC analytical column: CarboPac PA1
- HP-AEC guard column: CarboPac PA1
- HP-AEC instrument: Dionex ICS5000
- HP-AEC software: Chromeleon 7

Method:

A Dionex Ion Chromatographic System 5000 (ICS5000) was equipped with a CarboPac PA1 analytical column (2 × 250 mm, 30 °C) and a CarboPac PA1 guard column (2 × 50 mm, 30 °C), equilibrated with HP-AEC mobile phase A, to perform HP-AEC with PAD analysis. Sample components were separated by applying an 18-minute gradient with a 0.5 mL/min flow rate,

increasing the HP-AEC mobile phase B concentration to 10% after 5.0 minutes, then to 100% after 8.5 minutes. Separated oxidized products were detected with PAD and the resulting chromatograms were analyzed in the Chromeleon software including blank subtraction and peak integration. In-house prepared oxidized standards, *i.e.,* oxidized $(GlcNAc)_2$ and $(GlcNAc)_3$, with concentrations ranging from 2.5 to 150 µM were used to quantify the oxidized products (Chapter 3.6.2). Microsoft Excel was used for plot preparation.

3.7.4.2 TROUBLESHOOTING

High-Performance Hydrophilic Interaction Chromatography

The HPLC technique hydrophilic interaction chromatography (HILIC) separate carbohydrates in complex samples based on polarity (Waters, 2009). The mobile phase of HILIC may be an organic solvent, such as a mixture of acetonitrile with Milli-Q water. Milli-Q water adsorbs on the resin of the stationary phase, which generates acetonitrile and water partitioning. Analytes will elute at reducing polarity depending on the acetonitrile-water ratio, with the most polar compound eluting first (Alpert, 1990, Buszewski and Noga, 2012). Carbohydrate elution may be monitored by diode array detection (DAD). DAD can monitor the UV-Vis spectrum over an extensive range of wavelengths (Miller, 2005).

Materials:

Reagents and consumables

- HILIC buffer A: Acetonitrile (100%)
- HILIC buffer B: 15 mM Tris/HCl pH 8.0
- Oxidized chitooligosaccharide standards (Chapter 3.6.2)
- Time course samples from Chapter 3.7.1, 3.7.2, and 3.7.3

Laboratory equipment

- Heat block
- HILIC column: Acquity UPLC BEH Amide 1.7 µm
- HILIC detector: Agilent 1200 Infinity Series Diode Array Detector (G4212A)
- HILIC software: Chromeleon 7
- HILIC instrument: Agilent 1290 Infinity II HPLC system

Method:

HILIC was the first considered analytical method to analyze products from the oxidation of the soluble $(GlcNAc)_4$. Samples were prepared was according to Chapters 3.7.1 and 3.7.3, except that the reactions were heat terminated for 15 minutes at 100 °C. Sample equilibration to the HILIC mobile phase was performed by diluting the samples to a final concentration of 74% acetonitrile. HILIC was performed using an Agilent 1290 Infinity II HPLC system with a 150 mm Acquity UPLC ethylene bridged hybrid (BEH) Amide 1.7 µM column. The column was

equilibrated with 26% HILIC buffer A and 74% HILIC buffer B. Carbohydrate elution was performed using a 12-minute method at 0.4 mL/min, starting with 26% buffer A and 74% buffer B. The buffer B concentration was decreased to 62% after 5 minutes and was stable for 2 minutes. Next, buffer B concentration was increased to 74% over 2 minutes and stayed constant for the rest of the method time. Carbohydrate elution was detected with DAD at a fixed wavelength (194 nm). The samples were compared to oxidized standards (Chapter 3.6.2) and analyzed using Chromeleon software.

High-Performance Ion-Exclusion Chromatography

High-performance ion-exclusion chromatography (HP-IEC) is an HPLC technique which separates sample components based on the degree of ionization and the analyte's affinity to the HP-IEC resin. Affinity for the resin is negatively proportional to the carbohydrate's degree of dissociation. As a result, the analyte's retention time decreases with the increasing strength of the electrolyte (Lodi et al., 2017).

Materials:

Reagents and consumables

- HP-IEC mobile phase: 5 mM H_2SO_4
- Oxidized chitooligosaccharide standards (Chapter 3.6.2)
- Time course samples from Chapter 3.7.1, 3.7.2, and 3.7.3

Laboratory equipment

- HP-IEC analytical column: ROA-Organic Acid
- HP-IEC guard column: ROA-Organic Acid
- HP-IEC detector: Dionex UltiMate 3000 VWD Variable Wavelength Detector
- HP-IEC software: Chromeleon 7
- HP-IEC instrument: Dionex UltiMate 3000 HPLC system

Method:

HP-IEC was another analytical method considered to analyze the oxidized products. Test reactions of *in-situ* peroxygenase and peroxygenase activity were prepared as described in Chapters 3.7.1 and 3.7.3, though the reactions were terminated with 50 mM H_2SO_4 to equilibrate samples with the mobile phase of HP-IEC. A Dionex UltiMate 3000 HPLC system was used for HP-IEC equipped with a ROA-Organic Acid analytical column (300 × 7.8 mm) and a guard column of the same material. Carbohydrate products were separated isocratically over 30 minutes with the HP-IEC mobile phase at a 1 mL/min flow rate and column temperature at 85 °C. This protocol was adapted from the standard protocol used in the

laboratory to achieve optimal resolution. Product detection was performed by the Dionex UltiMate 3000 VWD Variable Wavelength Detector at a fixed wavelength (λ =194 nm). Due to the co-elution of oxidized products, the amount of formed native products was quantified. The samples were compared to in-house made native standard solutions ranging from 50 to 1000 µM using Chromeleon 7 software.

The validity of analyzing the products from $(GlcNAc)_4$ oxidation by HP-IEC was investigated by analyzing the same reactions using HP-AEC as described in Chapter 3.7.4.1.

3.8 STOPPED-FLOW SPECTROSCOPY OF *Nc*AA9C

Rapid stopped-flow UV/Vis spectroscopy was used to monitor the reactivity of *Nc*AA9C-Cu(I) WT and gatekeeper mutants with hydrogen peroxide in the absence of glycosidic substrate. Unfortunately, as the purification yield of *Af*AA11B was low, the required LPMO amount needed to perform stopped-flow analysis on *Af*AA11B was not obtained. The methods were adapted and optimized from Hedison et al. (2021) and Jones et al. (2020) by Dr. Ivan Ayuso-Fernandez.

Materials:

Reagents and consumables

- Ascorbic acid
- Bis-Tris/HCl pH 6.5
- H_2O_2
- N_2 (g)
- *Nc*AA9C WT and gatekeeper mutants
- TraceSELECT® water

Laboratory equipment

- Fisher Scientific Polystat 36 Chiller
- NanoPhotometer® C40
- Stopped-flow software: Bio-Kine 32 V4.74.2
- Schlenk line
- Stopped-flow detector: TIDAS® S 500 MCS UV/NIR 1910 DAD
- Stopped-flow instrument: SFM-4000 Stopped-flow mixing system
- Whitley A95 TG anaerobic workstation

Method:

500 mM Bis-Tris/HCl pH 6.5 and TraceSELECT® water were deoxygenated using a Schlenk line under N_2 (g) flux and incubated in a Whitley A95 TG anaerobic workstation for a minimum of 16 hours prior to stopped-flow analysis. All plastic laboratory equipment was also equilibrated with the oxygen-free environment. Stocks of H_2O_2 (100 mM) and AscA (5 mM) were prepared fresh on the experiment day in the anaerobic workstation using TraceSELECT®

water to avoid side reactions between the reagents and free copper as described by Stepnov et al. (2021). A NanoPhotometer® C40, Beer-Lamberts law, and the molar extinction coefficient (ε = 43.6 $M^{-1}cm^{-1}$) confirmed the hydrogen peroxide concentration. *Nc*AA9C WT and the gatekeeper mutants were transferred to sealed, air-tight vials and deoxygenated for 10 minutes by an N_2 (g) flux using a Schlenk line. Separate sealed syringes were filled with anaerobic LPMO, one molar equivalent of AscA, and 40 molar equivalents of H_2O_2.

The SFM-4000 stopped-flow mixing system was flushed with a large excess of anaerobic 50 mM Bis-Tris/HCl pH 6.5 prior to analysis. *Nc*AA9C WT and the gatekeeper mutants with concentrations ranging from 163 to 237 µM were reduced with one molar equivalent of AscA in the mixing system and incubated for 30 seconds. The SFM-4000 stopped-flow mixing system mixed 40 molar equivalents of hydrogen peroxide with 75 µL LPMO-Cu(I) without glycosidic substrate. Fisher Scientific Polystat 64 chiller ensured a reaction temperature of 4 °C, which slowed down amino acid radical formation. TIDAS® S 500 MCS UV/NIR 1910 DAD monitored UV/Vis absorbance changes, indicating possible generated amino acid radicals.

Data processing was performed with Bio-Kine32 V4.74.2 software and plotted with Microsoft Excel. The reaction time required to achieve maximum change in UV/Vis absorbance after mixing LPMO-Cu(I) with H_2O_2 was reported with the corresponding absorbed wavelength. The formation and decay of each signal was fitted to a single exponential equation to obtain the observed rates for radical formation and decay (Equation 7), respectively. Differences in LPMO starting concentrations were standardized by subtracting the baseline of each signal and normalizing the concentrations to *Nc*AA9C WT concentration.

$$y = at + b + ce^{-kt} \quad (7)$$

Equation 7: Formation and decay of the UV signal. Each signal (y) was fitted to a single exponential equation to generate the observed formation or decay rate (k). The intercept (a), offset (b), amplitude (c) and reaction time (t) are included in the radical formation equation.

4 RESULTS

4.1 CLONING OF FUNGAL LPMO GENES: EXPRESSION ISSUES

4.1.1 *Af*AA11B EXPRESSION ISSUES

Expression issues for all *Af*AA11B variants were encountered during this experimental work. Repeated purifications of *Af*AA11B revealed a loss of enzymatic activity (Figure 4.1A) and a change in *Af*AA11B behavior during gel electrophoresis. The typical *Af*AA11B behavior during gel electrophoresis after isolation of *Af*AA11B is presented in Figure 4.1B showing the characteristic SDS-PAGE band splitting of *Af*AA11B, representing the *Af*AA11B catalytic domain (~ 70 kDa) and the X278 module with linker (~ 20 kDa). This characteristic band splitting has also been observed previously by Rieder et al. (2021b). However, the band splitting disappeared during repetitions of *Af*AA11B purifications. Instead of the band splitting during gel electrophoresis, one separate protein band appeared at ~ 50 kDa (Figure 4.1C). Additionally, the bands in this SDS-PAGE gel were sharper than those in the SDS-PAGE gels analyzed during the initial isolation processes. In later purifications, the *Af*AA11B expression was lost entirely (Figure 4.1D).

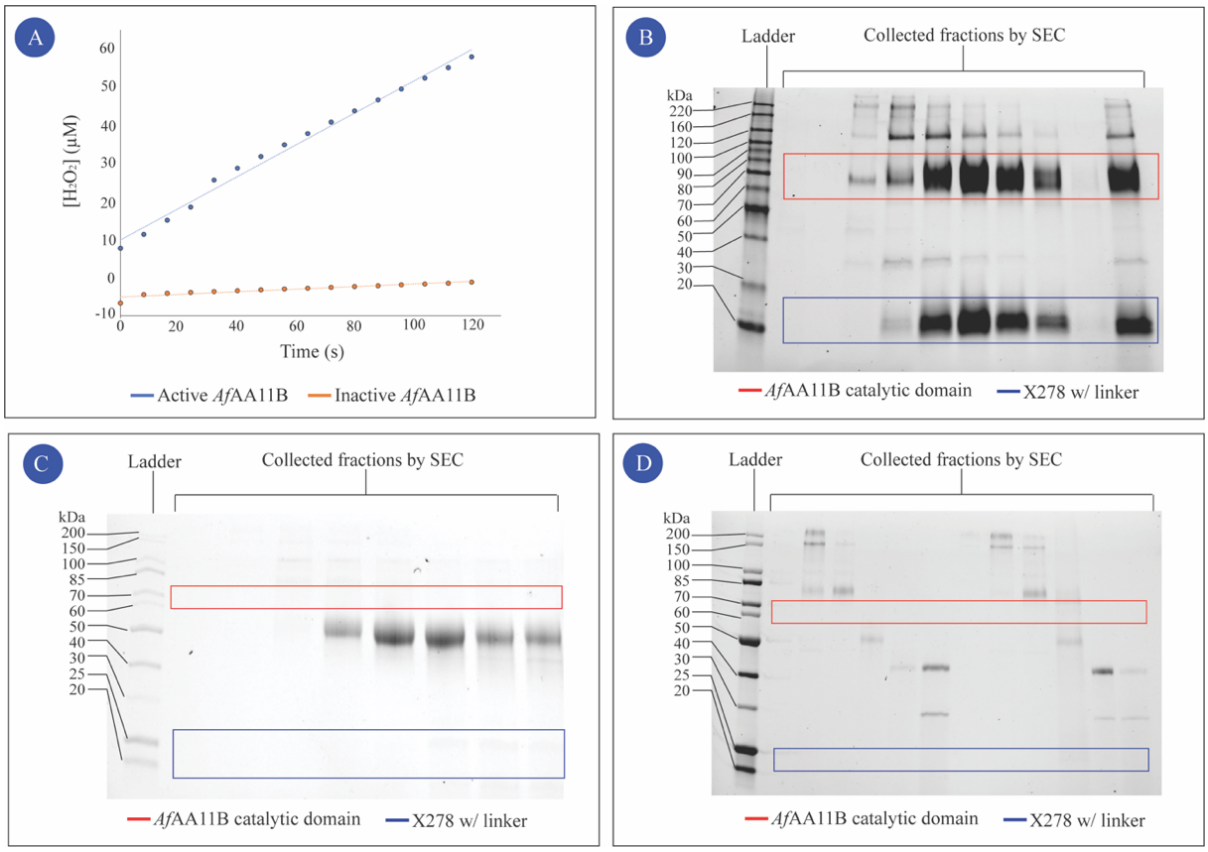

Figure 4.1: Presentation of the change in AfAA11B behavior exemplified by the wild type. *(A) An example of the decreased oxidase activity for repurified AfAA11B (orange) compared with the initial purified AfAA11B (blue) in the Amplex Red assay. (B) An SDS-PAGE gel indicating regular AfAA11B expression. The splitting of the AfAA11B catalytic domain (~70 kDa) and X278 module with linker (~20 kDa) is highlighted in red and blue, respectively. A BenchMark Protein Ladder was used as the reference. (C) An SDS-PAGE gel indicating one separate protein band (~50 kDa) rather than splitting of AfAA11B into the catalytic domain and the X278 module with a linker. The sizes of the regular band splitting are presented in red and blue, and the reference was a BioLab Protein Ladder. (D) An SDS-PAGE gel after isolation of AfAA11B with no AfAA11B expression. The highlighted bands (red and blue squares) show no protein bands at the apropos sizes. A BioLab Protein Ladder was used as the reference.*

The expression loss for all *Af*AA11B variants raised questions if the *Af*AA11B gene was present in the *P. pastoris* BSYBG11 strains. Hence, a PCR screen was performed.

4.1.2 *P. PASTORIS* CELL COLONY PCR SCREEN

Due to the loss of enzymatic activity and expression for all variants of *Af*AA11B, a PCR screen was performed to inspect the *P. pastoris* BSYBG11 strains for the presence of the *Af*AA11B gene (Figure 4.2). The PCR screen was performed on the *P. pastoris* expression strains grown in YPD media and on YPD-zeocin agar plates. Primers designed by Dr. Kelsi Hall were used to amplify the *Af*AA11B gene specifically.

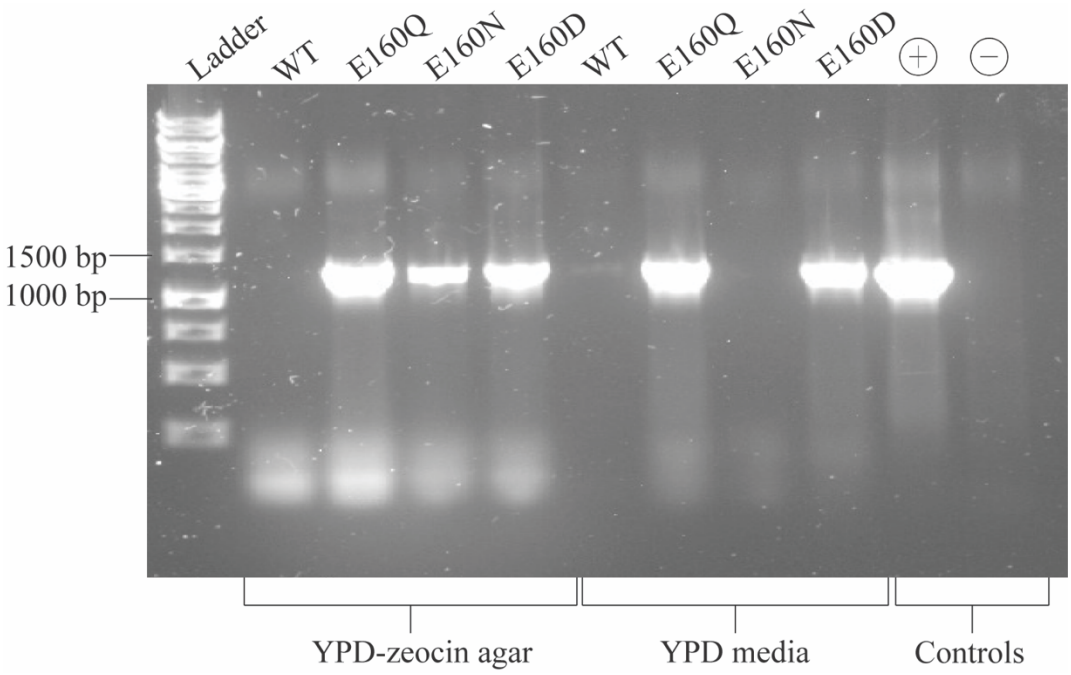

Figure 4.2: P. pastoris PCR screen. *The PCR screen was performed on P. pastoris cells grown in YPD cell cultures and on YPD-zeocin agar plates. Results from each origin are highlighted as "YPD-zeocin agar" and "YPD media". The positive control was the sequence-verified AfAA11B plasmids provided by Dr. Lukas Rieder (highlighted as +). A negative control without template was included to control if there were any contaminations in the master mix or primers (highlighted as -). A GeneRuler 1 kb ladder was used as the reference to compare DNA fragments by base pairs (bp). The predicted size of the amplified AfAA11B gene was 1257 bp.*

The bands from the PCR screen of *Af*AA11B gatekeeper mutants appeared comparable to the positive control and the predicted size of 1257 base pairs (bp). However, no amplification was evident in the *Af*AA11B WT PCR screen, indicating that the gene was absent. Even though the *Af*AA11B WT strain was the only one not containing the correct gene, it was decided to generate new *P. pastoris* strains of all *Af*AA11B variants due to the loss of *Af*AA11B expression and activity.

4.1.3 SCREENING OF *P. PASTORIS* COLONIES: PROTEIN EXPRESSION TEST

New *P. pastoris* strains harboring the *Af*AA11B plasmids were prepared to try to improve the *Af*AA11B expression levels. During the experimental work of generating new *P. pastoris* strains, colony screening was performed on 7 *P. pastoris* colonies. Multiple colonies were screened as recombinant protein expressed from *P. pastoris* colonies differs depending on how many plasmid copies are integrated into the genome and where they are integrated (Cregg et al., 1985). Because expressed protein by *P. pastoris* is secreted to the supernatant, protein

expression was assessed by performing a protein expression test of the supernatant (Chapter 3.1.4). Expressed *Af*AA11B WT and gatekeeper mutant protein was extracted from the supernatant by chloroform-methanol precipitation to separate the proteins from salts present in the growth media, enabling visualization of the proteins on an SDS-PAGE gel. This visualization enabled *P. pastoris* colonies with the highest *Af*AA11B expression to be identified (Figure 4.3).

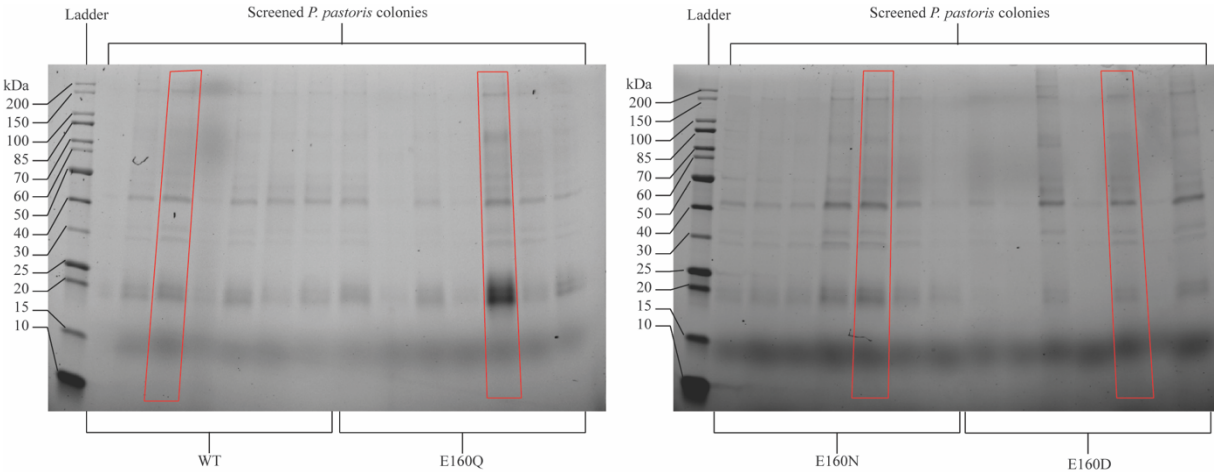

Figure 4.3: Expression test of AfAA11B WT and gatekeeper mutants. *A BioLabs Protein Ladder was used as the reference. The red boxes indicate the P. pastoris colony with the highest AfAA11B expression. These colonies were used to generate glycerol stocks of AfAA11B.*

The colonies considered to have the highest *Af*AA11B expression were used to generate glycerol stocks for future large-scale cultivation and isolation of *Af*AA11B and are highlighted by red squares. Among the screened colonies, only one single *P. pastoris* colony was highly expressing the gatekeeper mutant E160Q. However, *Af*AA11B WT, E160N, and E160D were not expressed highly by any screened *P. pastoris* colonies. Hence, colony screening optimization was attempted to identify *P. pastoris* colonies that expressed *Af*AA11B WT, E160N, and E160D at a higher level.

Colony screening optimization involved increasing the number of screened colonies due to the protein expression variability, depending on the location and number of gene copies integrated within the genome (Cregg et al., 1985). For this reason, the number of *P. pastoris* cell colonies included in the colony screening optimization was increased from 7 to 60. However, to perform a protein expression test on such a high amount of cell colonies would be very time-consuming. Hence, the number of colonies to include in the protein expression test was narrowed down by comparing the absorption monitored during the colorimetric Bradford protein assay and OD_{600}

for 60 *P. pastoris* cell colonies expressing *Af*AA11B WT and the gatekeeper mutants E160N and E160D. The Bradford protein assay was performed to estimate the secreted protein concentration, whereas the OD_{600} measurements quantified the number of grown cells in a culture based on light scattering in a cell-containing sample (Chapter 3.1.5). Table 8.1 in Appendix I presents monitored absorbance during the Bradford assay and OD_{600}, including the calculated ratio between the variables. The ratio between the variables was used to normalize cell growth, as high protein concentrations did not necessarily indicate high protein expression. The 14 *P. pastoris* cell colonies with the highest Bradford/OD_{600} ratio from the 60 cultivated cell colonies were tested for protein expression on an SDS PAGE gel as described in Chapter 3.1.5. The highest Bradford/OD_{600} ratio indicated which cell colony exhibited the highest protein expression. However, only low-expressing colonies were identified even after colony screening optimization (Figure 8.1**,** Appendix I). Thus, attempts were made to optimize the expression of *Af*AA11B.

4.1.4 OPTIMIZING EXPRESSION OF *Af*AA11B

Optimizing of *Af*AA11B expression by *P. pastoris* colonies was attempted by exploring the effect of gene promoters and growth media (Chapter 3.1.6). An expression test was performed on *P. pastoris* strains harboring the expression plasmids pBSYP$_{DC}$ZZ_*Af*AA11B to evaluate if the *Af*AA11B expression issues were strain specific (Figure 8.2, Appendix I). However, the strains did not show any positive effect on *Af*AA11B expression. For this reason, the focus was changed to investigate the components of the growth media. An expression test was performed on *P. pastoris* colonies grown in different growth media (Figure 4.4). Three different growth media were tested; YPD prepared with peptone from different manufacturers (Merck and VWR), YPD prepared with Milli-Q from a different water tank, and BMD1 media.

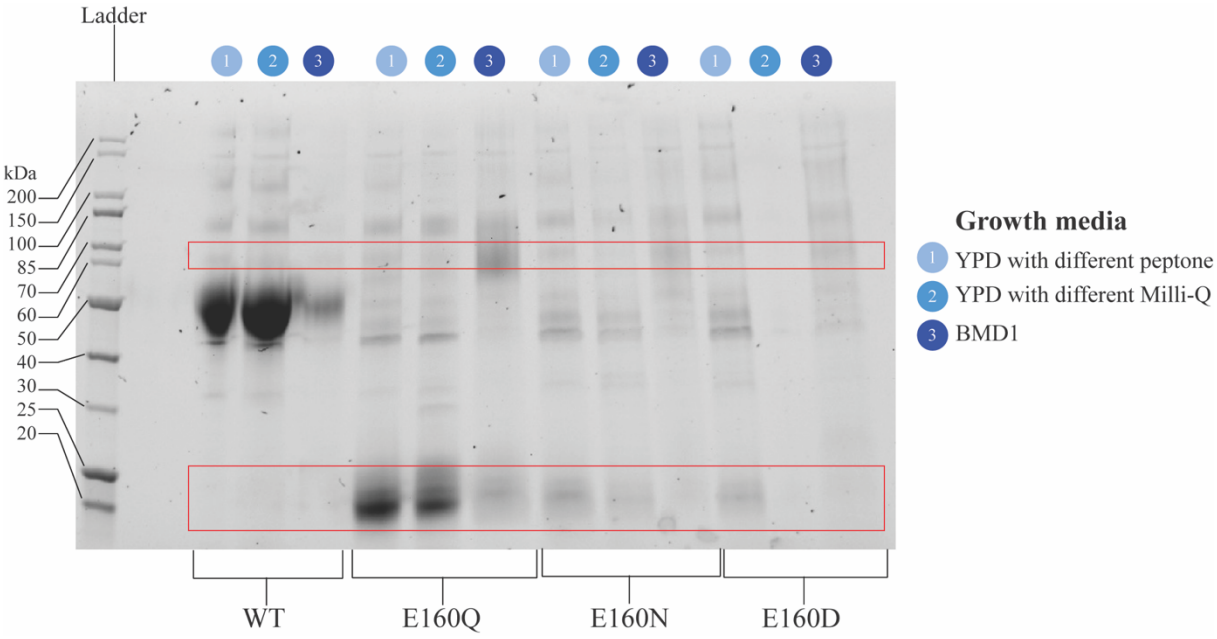

Figure 4.4: SDS-PAGE gel of AfAA11B expression by P. pastoris using different growth media components. *Growth media (1) was YPD prepared with peptone produced by Merck, i.e., the peptone used for initial AfAA11B purification. The second growth media (2) was YPD prepared with peptone produced by VWR, i.e., the peptone used for repeating AfAA11B purification. The Milli-Q water used to prepare this YPD was collected from a different water tank than previously. An alternative media, buffered minimal media (BMD1) (3), was also tested. The upper and lower red boxes highlight the sizes of the AfAA11B catalytic domain and the X278 module, respectively, and indicate where the bands should be obtained during this expression test.*

There were no substantial differences in *Af*AA11B WT expression using the different growth media compared with the gel presented in Figure 4.1C, as the expression test revealed the sharp band at ~ 50 kDa. However, the characteristic band-splitting present in the typical *Af*AA11B presenting gel (Figure 4.1B) was faintly appearing for the expressed gatekeeper mutants. This characteristic splitting was highlighted by red squares red squares to show where the band representing the *Af*AA11B catalytic domain (~ 70 kDa) and the X278 module (~ 20 kDa) of *Af*AA11B should appear.

Unfortunately, the reason(s) for the expression issues of all *Af*AA11B strains was(were) not obtained during this master's thesis work. Nevertheless, low, though not optimal, expression of all *Af*AA11B variants were obtained by screening multiple *P. pastoris* colonies and generate new *P. pastoris* strains for all *Af*AA11B variants.

4.2 PRODUCTION AND ISOLATION OF FUNGAL ENZYMES

4.2.1 PRODUCTION STEP 1: HYDROPHOBIC INTERACTION CHROMATOGRAPHY

*Af*AA11B and *Nc*AA9C WT and gatekeeper mutants were purified as described in Chapter 3.2 using hydrophobic interaction chromatography as the first isolation step, which separates the proteins based on affinity to the hydrophobic stationary phase. The proteins of interest eluted after approximately 2-3 CV of mobile phase after the salt gradient application. This protein eluate was collected as fractions, and SDS-PAGE was used to analyze a selection of the collected fractions for protein identification. Hydrophobic interaction chromatograms of wild type *Af*AA11B and *Nc*AA9C were similar to the respective gatekeeper mutants. Therefore, chromatograms with corresponding SDS-PAGE gels are presented in Figure 4.5 using the wild types as examples. Representative examples of hydrophobic interaction chromatograms with associated SDS-PAGE gels of *Af*AA11B and *Nc*AA9C gatekeeper mutants are presented in Figure 8.3 and Figure 8.4 in Appendix II, respectively.

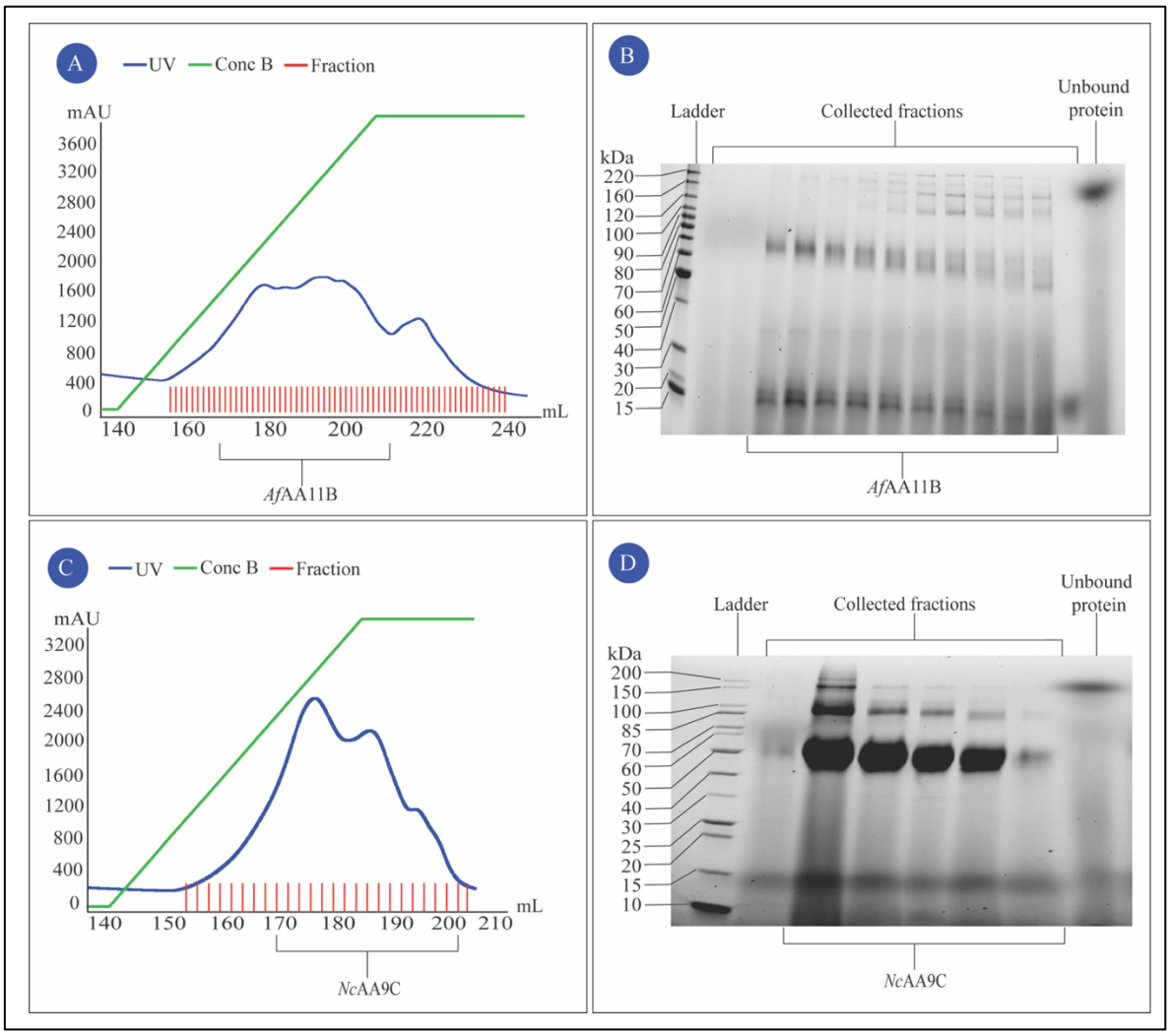

Figure 4.5: Hydrophobic interaction chromatograms with corresponding SDS-PAGE gels. *Representative chromatograms from the first isolation step during purification of (A) AfAA11B and (C) NcAA9C, using the wild types as examples. Generated UV signal (y-axis, mAU) is represented by a blue curve in the chromatograms, whereas the green curve illustrates the salt gradient applied for protein elution. The volume of the mobile phase is presented on the x-axis in mL. Red, vertical lines along the x-axis represent the collected fractions, and the collected fractions which contained the respective LPMO are highlighted in black bars. The SDS-PAGE gels from HIC isolation of (B) AfAA11B and (D) NcAA9C are also presented. A reference ladder, i.e., BenchMark Protein Ladder or BioLabs Protein Ladder, was loaded in the first well of the SDS-PAGE gel in (B) and (D), respectively. The protein markers sizes are highlighted in kDa. Fractions that contained the protein of interest are highlighted in black bars.*

*Af*AA11B and *Nc*AA9C yields per 500 mL growth media were estimated post-HIC purification using the A_{280} method and were reported as median (quartile 1 (Q1), quartile 3 (Q3)) due to asymmetry in the data. HIC isolation of *Af*AA11B resulted in 48 (35, 121) mg WT, 126 (106, 146) mg E160Q, and 99 (50, 99) mg. *Af*AA11B E160N was produced and isolated on one occasion and was estimated to have a protein yield of 52 mg. *Nc*AA9C WT and the gatekeeper mutants Q180E and Q180N were purified and isolated on one occasion and yielded 158, 55, and 120 mg, respectively. HIC isolation of *Nc*AA9C Q180D generated 90 (71, 109) mg of

isolated protein. Even though the reported yields of *Af*AA11B and *Nc*AA9C appeared comparable, the reported yields were most likely overestimations and not absolute. The HIC-isolated proteins contained a varying level of color pigments from the YPD media, which was interfering with the A_{280} measurements.

4.2.2 PURIFICATION STEP 2: SIZE EXCLUSION CHROMATOGRAPHY

Size exclusion chromatography was the final isolation step when purifying *Af*AA11B and *Nc*AA9C, which separates proteins based on size. The increase in UV signal indicated that the proteins of interest eluted approximately 0.3 column volumes of mobile phase after loading the protein sample to the column. Figure 4.6 shows representative size-exclusion chromatograms with the corresponding SDS-PAGE gels from *Af*AA11B and *Nc*AA9C isolation using the wild types as examples. Examples from the isolation of the *Af*AA11B and *Nc*AA9C gatekeeper mutants are shown in Appendix II (Figure 8.5 and Figure 8.6).

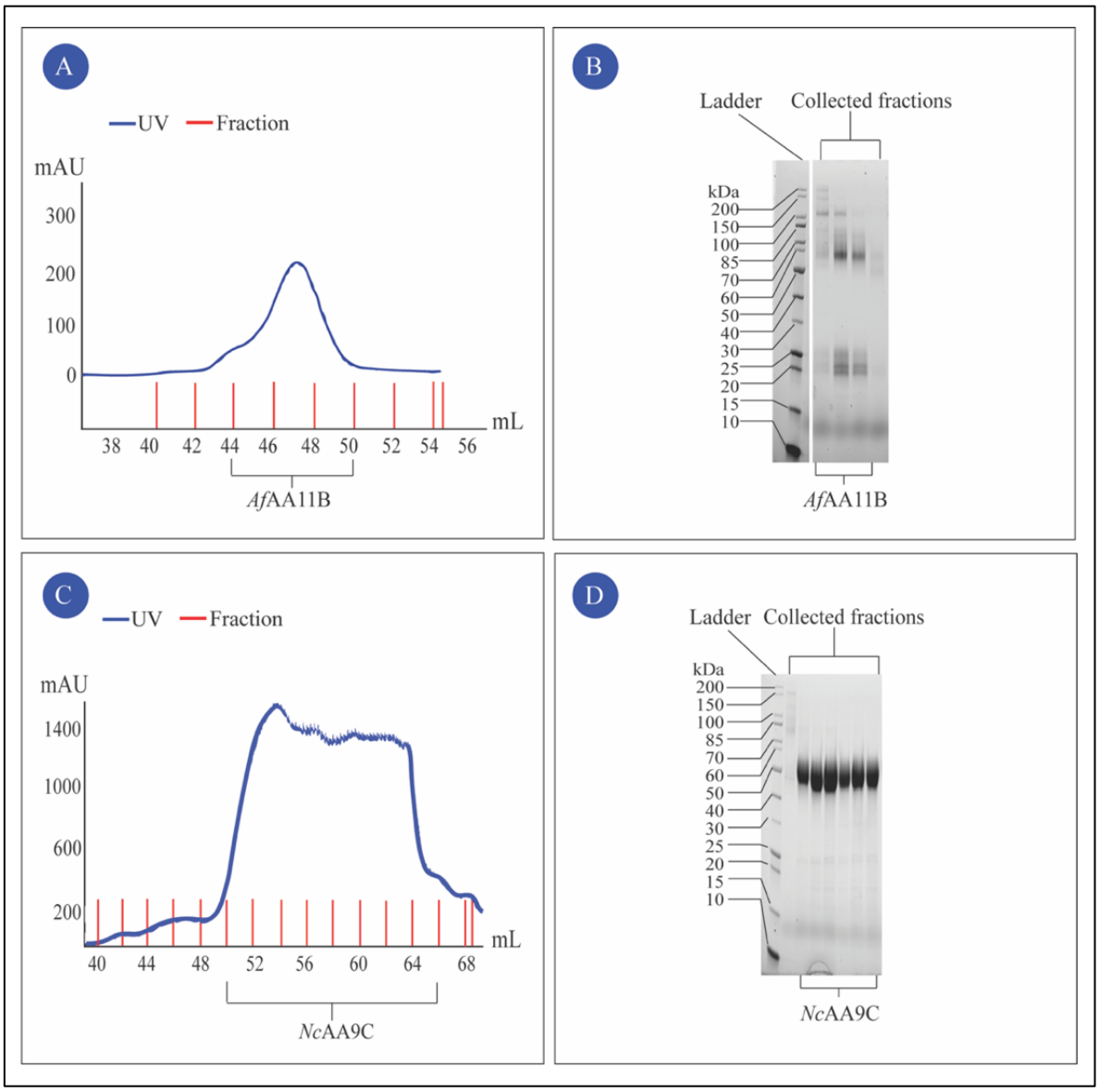

Figure 4.6: Size exclusion chromatograms with corresponding SDS-PAGE gels. *Representative size exclusion chromatograms generated by isolation of AfAA11B (A) and NcAA9C (C). The volume of the consumed mobile phase is presented on the x-axis in mL. Generated UV signal (mAU) is presented on the y axis and is represented by a blue line in the size exclusion chromatograms. The collected fractions and the fractions exhibiting the protein of interest are highlighted in red vertical lines and black bars, respectively. The chromatograms' corresponding SDS-PAGE gels are presented in Panel (B) and (D) for AfAA11B and NcAA9C, respectively. A selection of the collected fractions and the fractions exhibiting the protein of interest are highlighted by black bars. The BioLabs protein ladder was used to reference the protein markers sizes in kDa.*

The yield of *Af*AA11B and *Nc*AA9C post-SEC isolation per 500 mL growth media was estimated by measuring the protein absorbance at A_{280}. Asymmetrical data strained yield presentation to the median value and quartiles. *Af*AA11B WT (3 (2, 4) mg) and the gatekeeper mutant E160D (0.5 (0.5-1.2) mg) obtained a lower protein yield compared with the amide gatekeeper mutants E160Q (37 (35, 40) mg) and E160N (14 mg). The *Nc*AA9C variants from a single purification yielded 54, 25, and 5 mg of *Nc*AA9C WT, Q180N, and Q180E,

respectively. The yield of *Nc*AA9C Q180D was estimated to be 25 (11, 38) mg. Purification of *Nc*AA9C generated a higher yield compared with purification of *Af*AA11B. However, the yield estimations were still believed to be overestimations due to the variating presence of color pigments generated by the YPD media, which interfered with the A_{280} measurements.

4.2.3 COPPER SATURATION

*Nc*AA9C and *Af*AA11B were copper saturated to ensure all active sites contained a bound copper ion, allowing for maximum enzymatic activity and functionality of the LPMOs. After copper saturation, the final protein yields were estimated using the Bradford protein assay for more accurate yield estimations compared with yield estimations obtained from the A_{280} method (Chapter 3.2.5). *Af*AA11B and *Nc*AA9C yields per 500 mL growth cell culture are visualized in Figure 4.7. Even though the yield data was approximately symmetrical after copper saturation, the data was presented with the median value and quartiles for comparison reasons. A complete table of *Af*AA11B and *Nc*AA9C yield throughout the purification steps is presented in Table 8.2 and Table 8.3 in Appendix II, respectively. *Af*AA11B and *Nc*AA9C variants exhibiting amide gatekeeper residues obtained the highest purification median yield. Specifically, the glutamine gatekeeper mutant of *Af*AA11B (15 (9, 20) mg) and *Nc*AA9C (10 mg) obtained the highest purification yield among the protein variants. The asparagine gatekeeper mutant obtained a point estimate yield of 3 mg for *Af*AA11B and 10 mg for *Nc*AA9C. In contrast, the carboxylic acid gatekeeper variants obtained the lowest purification median yield among the LPMO variants. The wild type and E160D yielded 0.2 (0.2, 0.7) mg and 0 (0, 1) mg for *Af*AA11B, respectively. Similarly, *Nc*AA9C Q180E yielded 1 mg, and Q180D yielded 3 (1-5) mg.

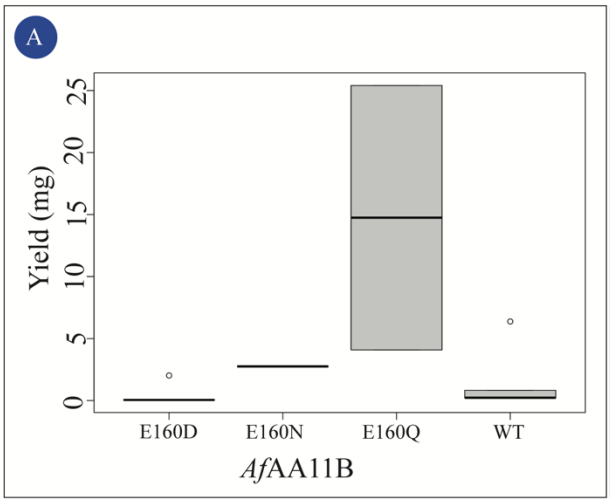

B

DESCRIPTIVE PROPERTY	*Af*AA11B [Median (Q1, Q3)]			
	WT	E160Q	E160N	E160D
CONCENTRATION (µM)	82 (53, 122)	475 (317, 633)	68	24 (21, 42)
CONCENTRATION (mg/mL)	3 (2, 5)	20 (14, 27)	3	1 (1, 2)
YIELD (mg)	1 (0, 2)	15 (9, 20)	3	0 (0, 1)
VOLUME (µL)	275 (125, 525)	700 (650, 750)	1000	75 (63, 438)

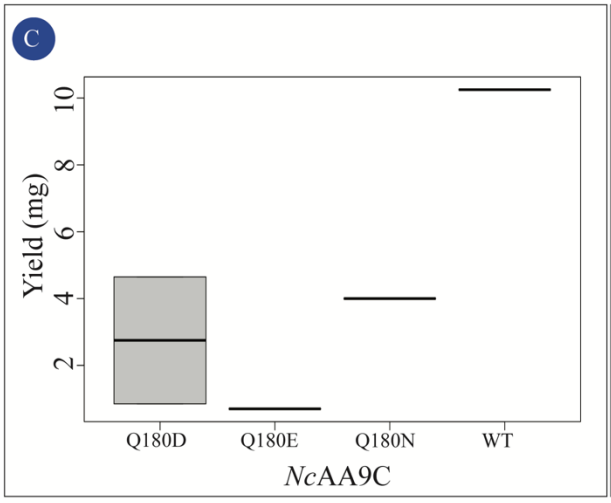

D

DESCRIPTIVE PROPERTY	*Nc*AA9C [Median (Q1, Q3)]			
	WT	Q180E	Q180N	Q180D
CONCENTRATION (µM)	383	158	608	358 (193, 523)
CONCENTRATION (mg/mL)	14	6	22	13 (7, 19)
YIELD (mg)	10	0.7	5	3 (1, 5)
VOLUME (µL)	750	125	250	188 (125, 250)

Figure 4.7: Final protein yields with variation normalized by 500 mL growth media. *The variation in protein yields (mg) resulting from multiple isolations of AfAA11B (A) and NcAA9C (C) are presented as box plots. R studio highlighted susceptive outliers in protein yield as white dots. Thick, black lines represent the median protein yield or the point estimate of protein yield from a single replicate of isolated protein. The descriptive statistics after the final isolation step of AfAA11B (B) and NcAA9C (D) are presented in the tables reported as median (Q1, Q3). Obtained results are estimated with the Bradford protein assay.*

The SDS-PAGE gels presenting the final pure and copper saturated proteins are in Figure 4.8. Two amounts of each protein (0.2 and 2.0 µg) were loaded on the gel to highlight any contaminating proteins.

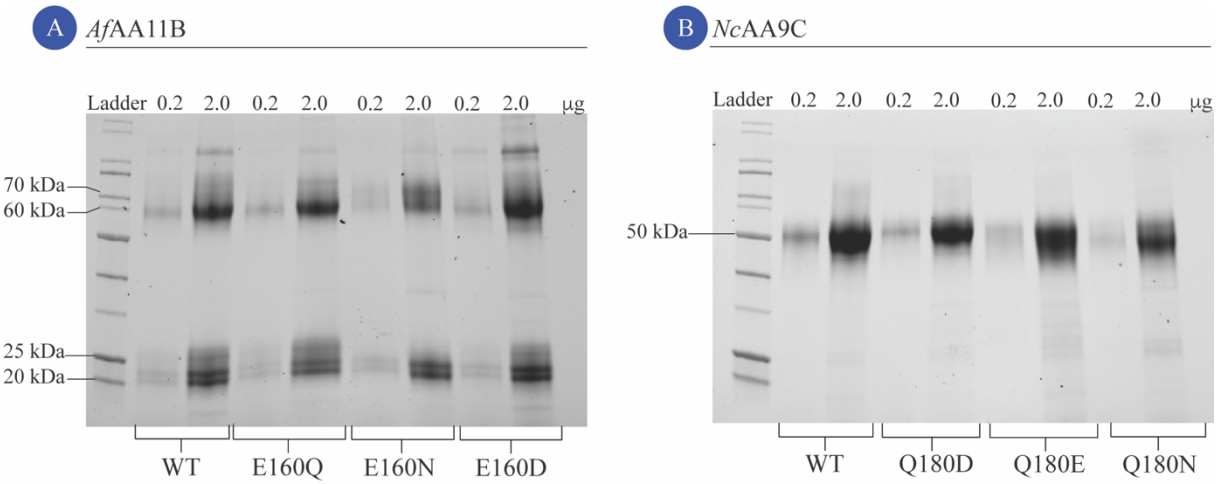

Figure 4.8: SDS-PAGE gel presenting the final copper saturated AfAA11B and NcAA9C WT and gatekeeper mutants. *(A) AfAA11B WT and gatekeeper mutants. (B) NcAA9C WT and gatekeeper mutants. 0.2 and 2.0 µg were loaded in each well for each LPMO. The BioRad Protein Ladder was used as a reference with protein marker sizes shown in kDa.*

4.3 REDOX MEASUREMENTS OF *Af*AA11B AND *Nc*AA9C

Redox measurements were performed to estimate the redox potential of *Af*AA11B and *Nc*AA9C WT and the gatekeeper mutants, indicating the relative ease of reducing LPMO-Cu(II) to Cu(I) state by the reductant TMP_{red}. Unfortunately, the experimental conditions during *Af*AA11B analysis were not perfectly anaerobic, as it later was discovered that O_2 (g) was leaking into the anaerobic chamber. Due to the low purification yield from *Af*AA11B purification presented in Chapter 4.2.3, the high protein demand to repeat the experiments prevented a repeat of the experiments within the time frame of the thesis work. We assume that the redox trends of *Af*AA11B WT and gatekeeper mutants are valid, though we do not have full confidence in the estimated redox potential for each enzyme. Nevertheless, the redox potential for the enzymes is presented in Figure 4.9. The reduction potentials were estimated by the equations presented in Chapter 3.3.

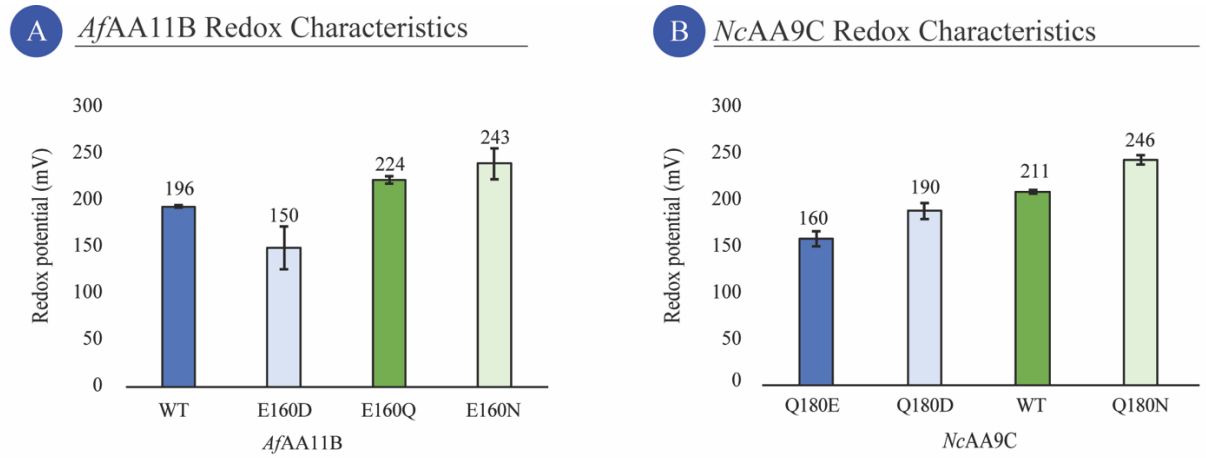

Figure 4.9: Estimated redox potentials for AfAA11B, NcAA9C WT, and gatekeeper mutants. *(A) AfAA11B WT and the gatekeeper mutants E160D, E160Q, and E160N are presented in dark blue, light blue, dark green, and light green, respectively. (B) The dark blue, light blue, dark green, and light green bars represent NcAA9C Q180E, Q180D, WT, and Q180N, respectively. The redox potential is highlighted in blue for a carboxylic acid side-chain or green for an amide side-chain. Three individual replicates were included to estimate the redox potential in mV, and the estimates were based on the equations presented in Chapter 3.3. Each error bar indicates the standard deviation for the proteins. Dr. Kelsi Hall performed the NcAA9C redox measurements.*

An analysis of variance (ANOVA) was performed to investigate whether the observed difference in redox potential for the gatekeeper variants of *Af*AA11B and *Nc*AA9C was significant. *Af*AA11B WT, E160Q, E160N, and E160D gave reported redox potentials of 196 ± 1, 224 ± 4, 243 ± 17, and 150 ± 23 mV, respectively. Indeed, the redox potential for all variants of *Af*AA11B was stated as significantly different on a 5% significance level. The significant difference in redox potential was also observed for *Nc*AA9C WT, Q180N, Q180E, and Q180D, where the variants gave reported redox potentials of 211 ± 2, 246 ± 5, 160 ± 8, and 190 ± 9 mV, respectively.

Moreover, it was of interest to investigate if this difference in redox potentials was observed specifically between LPMO variants with gatekeeper residues of different nature. Hence, contrast analyses were performed comparing the redox potential of carboxylic acid and amide gatekeeper variants. Certainly, contrast analyses verified a significantly lower redox potential for the studied LPMOs containing a carboxylic acid side-chain for the gatekeeper residue. Furthermore, differences in redox potential were also observed within the gatekeeper residues of same nature, and it was interesting to investigate if this difference, possibly caused by side-chain length of the gatekeeper residue, was significant. Interestingly, the difference in redox potential for *Af*AA11B E160Q and E160N was not classified as significant. However, the difference in redox potential for *Af*AA11B WT and E160D was stated as significant. *Nc*AA9C

Q180E/Q180D and WT/Q180N followed the same significant trend in redox potential. The statistical procedure and generated results are presented in more detail in Appendix III.

4.4 OXIDASE ACTIVITY OF *Af*AA11B AND *Nc*AA9C

The oxidase activity of *Af*AA11B and *Nc*AA9C WT and gatekeeper mutants were estimated by performing the Kittl assay (Chapter 3.4). Kittl et al. (2012) showed that hydrogen peroxide produced *in-situ* by the LPMO reduces the compound Amplex Red to resorufin in a coupled reaction with HRP. Produced resorufin is quantified spectrophotometrically and is assumed to be proportional to the *in-situ* production of hydrogen peroxide by the LPMO, *i.e.,* the oxidase activity. The estimated oxidase activity of *Af*AA11B and *Nc*AA9C WT and gatekeeper mutants is presented in Figure 4.10. Hydrogen peroxide calibration curves were used to estimate hydrogen peroxide produced *in-situ* by the LPMOs from change in absorbance at $\lambda = 563$ nm (Figure 8.9, Appendix IV (Part I)). The initial rate of oxidase activity was estimated based on the first 120 seconds of the reaction using a simple linear regression analysis. A short statistical comment related to this statistical model is presented in Appendix IV, Part II.

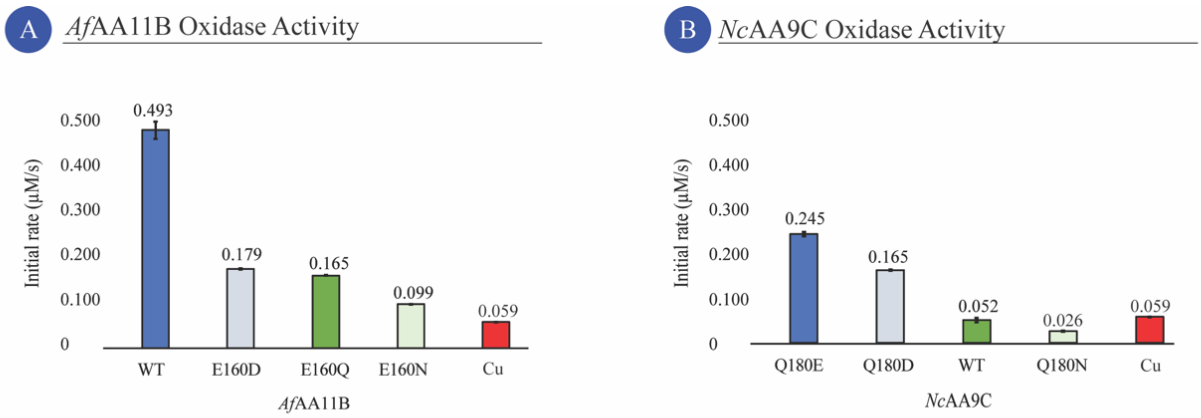

Figure 4.10: Oxidase activity of AfAA11B and NcAA9C and gatekeeper mutants. *(A) The initial rate of in-situ hydrogen peroxide production (µM/s) of AfAA11B WT and the gatekeeper mutants E160D, E160Q, and E160N is shown in blue, light blue, green, and light green, respectively. Three individual replicates were used for the estimations. (B) NcAA9C gatekeeper mutants Q180E, Q180D, WT, and Q180N are presented with initial oxidase rates (µM/s) in blue, light blue, green, and light green, respectively. Two individual replicates were used for estimating the initial rates, except for NcAA9C Q180D, which included three individual replicates. Blue bars represent carboxylic acidic side-chains in the gatekeeper residue, whereas green bars represent amide side-chains. The red bar gives free copper. Standard deviations of the replicates are presented with error bars.*

The oxidase activity of *Af*AA11B WT and the gatekeeper mutants E160D, E160Q, and E160N were estimated to 0.493 ± 0.019, 0.179 ± 0.001, 0.165 ± 0.001, and 0.099 ± 0.001 µM/s,

respectively. 0.052 ± 0.005, 0.026 ± 0.001, 0.245 ± 0.005, and 0.165 ± 0.001 µM/s were the estimated initial rates of *in-situ* hydrogen peroxide production for *Nc*AA9C WT, and the gatekeeper mutants Q180N, Q180E, and Q180D, respectively. Wild type *Af*AA11B produced hydrogen peroxide *in-situ* at a higher rate than wild type *Nc*AA9C and all gatekeeper mutants. For this reason, the *Af*AA11B's ability to produce hydrogen peroxide *in-situ* appeared notable. Moreover, the oxidase activity of *Af*AA11B appeared remarkable as every variant of *Af*AA11B was reported with a higher initial rate of hydrogen peroxide production than free copper (0.059 ± 7.89 × 10^{-5} µM/s). This is interesting, as free copper in most cases produces hydrogen peroxide faster than an LPMO alone (Stepnov et al., 2021). The notable behavior of *Af*AA11B has also been observed previously by Rieder et al. (2021b). Interestingly, *Nc*AA9C also produced hydrogen peroxide faster than free copper when the gatekeeper residue was mutated to either glutamate or aspartate. The carboxylic acid nature of the gatekeeper residue seemed crucial to *in-situ* hydrogen peroxide production.

Besides comparing *Af*AA11B and *Nc*AA9C with free copper, copper was included in the Amplex Red assay as the assay is very copper sensitive. The copper sensitivity of the Amplex Red assay was why three replicates of flow-through obtained during the final washing step post-copper saturation for each LPMO were included in the assay. These flow-through samples were included to ensure no unbound copper was present in the final LPMO samples. However, samples with flow-through did not indicate any oxidase activity. Hence, the flow-through results were not included in this section.

Differences in oxidase activity was not only observed between *Af*AA11B and *Nc*AA9C, but also between the gatekeeper variants of each studied LPMO. The observed difference in *in-situ* hydrogen peroxide production among the *Af*AA11B and *Nc*AA9C variants was investigated by performing an ANOVA. Indeed, the analysis established a significant difference in oxidase activity for mutating the gatekeeper residue in *Af*AA11B and *Nc*AA9C on a 5% significance level. Moreover, the observed difference in oxidase activity was hypothesized to relate to the nature of the gatekeeper residue, as the carboxylic acid gatekeeper variants' oxidase activity was higher than the estimated oxidase activity for the amide gatekeeper variants. By performing contrast analyses in R studio, this difference in oxidase activity was established as significant. Moreover, contrast analyses confirmed the trend of highest oxidase activity for the glutamate gatekeeper variants of *Nc*AA9C and *Af*AA11B at a 5% significance level. Contrast analyses also confirmed a significant difference in oxidase activity between the glutamate/aspartate and

glutamine/asparagine gatekeeper variants of *Nc*AA9C and *Af*AA11B, *i.e.,* the longer side-chain generated the highest oxidase activity. The statistical analyses performed in this regard are described in detail in Part II of Appendix IV.

4.5 PEROXIDASE ACTIVITY OF *Af*AA11B AND *Nc*AA9C

The peroxidase activity of *Af*AA11B, *Nc*AA9C WT and gatekeeper mutants was estimated by performing the Breslmayr assay (Chapter 3.5). Breslmayr et al. (2018) proposed a reaction where the reductant 2,6-DMP reduces LPMO-Cu(II). LPMO-Cu(I) then utilizes hydrogen peroxide to catalyze the oxidation of the now substrate acting 2,6-DMP. The product of the Breslmayr reaction is the compound coerulignone which is monitored spectrophotometrically at 563 nm. The estimated initial rates of hydrogen peroxide consumption by *Af*AA11B are presented in Figure 4.11. A trend was observed for lower rate of hydrogen peroxide consumption with the lower redox potentials for *Af*AA11B and *Nc*AA9C.

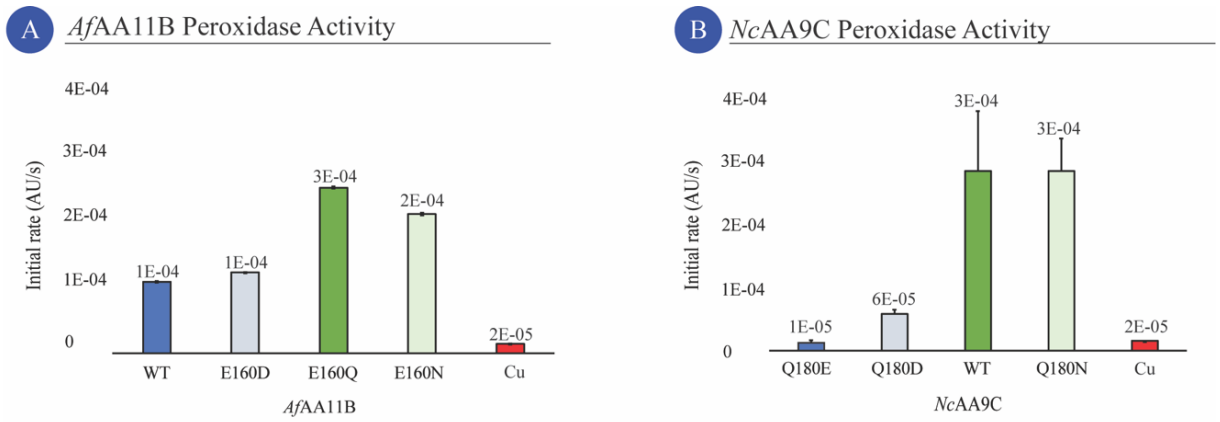

Figure 4.11: Peroxidase activity of AfAA11B and NcAA9C WT and gatekeeper mutants. *The estimated initial rate of hydrogen peroxide consumption (AU/s) based on three individual replicates for (A) AfAA11B WT and gatekeeper mutants E160D, E160Q, and E160N, presented in dark blue, light blue, dark green, and light green, respectively, and for two individual replicates of (B) NcAA9C and the gatekeeper mutants Q180E, Q180D, WT, and Q180N shown in dark green, dark blue, light blue and light green bars respectively. The characteristics of the gatekeeper side-chain are color-coded with green bars representing enzymes exhibiting an amide gatekeeper residue and blue bars representing enzymes exhibiting a carboxylic acid gatekeeper residue. The red bar gives the peroxidase activity of free copper. The standard deviation is indicated with error bars.*

The difference in peroxidase activity for *Nc*AA9C and *Af*AA11B variants were evaluated by performing an ANOVA in R studio. A detailed description of the statistical approach is presented in Appendix V. The peroxidase activity was estimated to be $1 \times 10^{-4} \pm 9 \times 10^{-7}$, $1 \times 10^{-4} \pm 6 \times 10^{-7}$, $3 \times 10^{-4} \pm 1 \times 10^{-6}$, and $2 \times 10^{-4} \pm 2 \times 10^{-6}$ AU/s for *Af*AA11B WT and the gatekeeper mutants E160D, E160Q, and E160N, respectively. The initial rate of hydrogen

peroxide consumption was estimated to $1 \times 10^{-7} \pm 4 \times 10^{-2}$ µM/s for free copper. *Nc*AA9C WT, Q180E, Q180D, and Q180N obtained an estimated peroxidase activity of $3 \times 10^{-4} \pm 9 \times 10^{-5}$, $1 \times 10^{-5} \pm 1 \times 10^{-5}$, $6 \times 10^{-5} \pm 7 \times 10^{-6}$, and $3 \times 10^{-4} \pm 5 \times 10^{-5}$ AU/s, respectively. Interestingly, the estimated peroxidase activity was established as different for all variants of *Nc*AA9C and *Af*AA11B at a 5% significance level.

Furthermore, the peroxidase trend appeared to depend on the nature of the gatekeeper residue. Exhibiting a gatekeeper residue with a carboxyl group in the side-chain generated significantly lower initial rates in hydrogen peroxide consumption for *Af*AA11B compared with a *Af*AA11B variant with an amide gatekeeper residue. The significance was confirmed by contrast analyses (Appendix V). Moreover, the performed contrast analyses also confirmed that *Af*AA11B and *Nc*AA9C consumed hydrogen peroxide at the lowest rate when the gatekeeper residue was glutamate. The relationship between peroxidase activity and the side-chain length of the gatekeeper residue was also investigated by contrast analyses. However, these differences in peroxidase activity were not stated as significant (Appendix V).

4.6 DETECTION OF OXIDIZED PRODUCTS

4.6.1 PRODUCTION AND PURIFICATION OF CHITO

Large-scale cultivation and purification of ChitO were performed as per Chapter 3.6.1. Purification of ChitO was a two-step process, including anion exchange chromatography and size exclusion chromatography. ChitO was initially isolated from the generated lysate (Chapter 3.6.1.1) by anion exchange chromatography (AEC). AEC utilizes the charges on the protein surface and exchangeable anions of the resin, where sample separation follows. The protein eluted with the flow-through, approximately 12 CVs of mobile phase after loading the protein sample to the column because ChitO had a relatively low affinity to the resin, which also was observed by Heuts et al. (2008). SDS-PAGE was used to analyze the unbound protein fractions and separate AEC isolated ChitO.

Furthermore, AEC isolated ChitO was purified by size exclusion chromatography as the last isolation step, where the sample's proteins were separated based on size. ChitO eluted approximately 0.3 CVs of mobile phase after loading the protein sample to the column, which

was confirmed by analyzing the collected fractions by SDS-PAGE. The resulting chromatograms' and corresponding SDS-PAGE gels are presented in Figure 4.12.

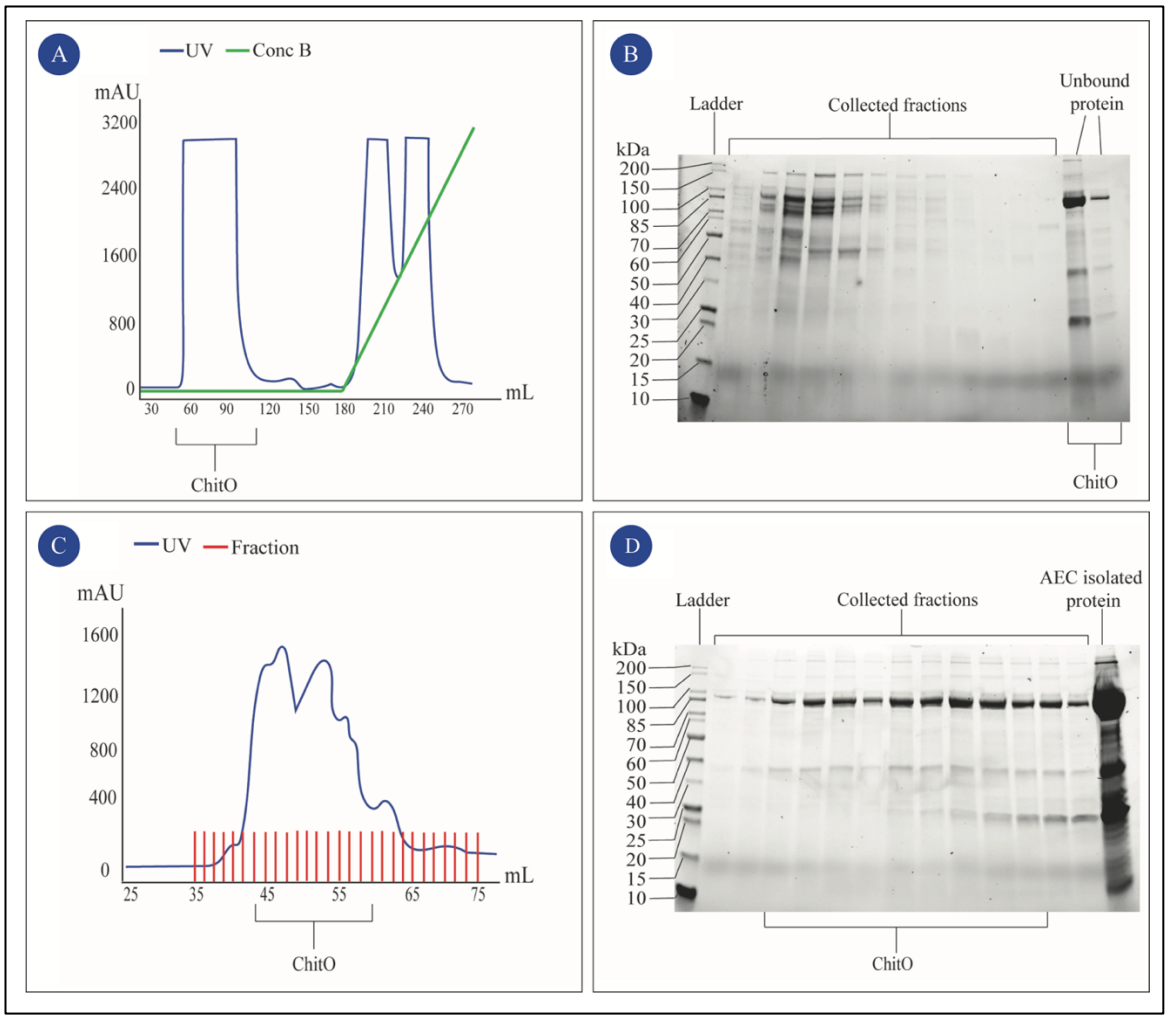

Figure 4.12: Purification of ChitO by anionic exchange chromatography and size exclusion chromatography. *The two-step purification process of ChitO generated an anionic exchange chromatogram (A) and a size exclusion chromatogram (C). The absorbance in mAU (blue line) and volume of mobile phase (mL) are presented on the y- and x-axis, respectively. A green line is included in the anionic exchange chromatogram to show the increase of elution buffer. Collected fractions during size exclusion chromatography are highlighted as red vertical lines. Isolated ChitO is presented with black bars. The corresponding SDS-PAGE gels to the chromatograms are presented in (B) after anionic exchange chromatography and (C) after size exclusion chromatography. A BioLabs protein ladder was used as the protein markers' size indicator (kDa). The collected fractions and the fractions that contained ChitO are highlighted with black bars.*

The final concentration of ChitO (713 µM, 68 mg/mL) was estimated using the A_{280} method and obtained a final yield of 162 mg from a 1 L culture (Table 4.1). Following, the newly isolated enzyme ChitO was used to prepare in-house made oxidized standards for detection of oxidized products.

Table 4.1. The obtained yield after isolation of ChitO. The obtained yield is summarized with concentration (µM and mg/mL), yield (mg), and final volume of protein (µL).

DESCRIPTIVE PROPERTY	ChitO
CONCENTRATION (µM)	713
CONCENTRATION (mg/mL)	68
YIELD	162
VOLUME (µL)	2400

4.6.2 DETECTION OF OXIDIZED PRODUCTS

Three different detection techniques were evaluated when analyzing oxidized products after *Af*AA11B catalyzed oxidation of $(GlcNAc)_4$ (A4): high-performance anion exchange chromatography (HP-AEC), high-performance hydrophilic interaction chromatography (HILIC), and high-performance ion-exclusion chromatography (HP-IEC). Rieder et al. (2021b) showed that *Af*AA11B catalyzed oxidation of $(GlcNAc)_4$ generates oxidized $(GlcNAc)_2$ ($A2_{OX}$) and $(GlcNAc)_3$ ($A3_{OX}$) with the corresponding native dimer (A2) and monomer (A1).

HILIC was the first evaluated HPLC technique, as this chromatographic is well-suited to separate neutral, polar compounds such as carbohydrates based on the analytes' polarity (Chapter 3.7.4.2). Sample reactions were prepared according to Chapters 3.7.1 and 3.7.3, and the reactions were heat terminated for 15 minutes at 100 °C. Figure 4.13 presents a representative chromatogram from a HILIC analysis of the products generated from $(GlcNAc)_4$ oxidation.

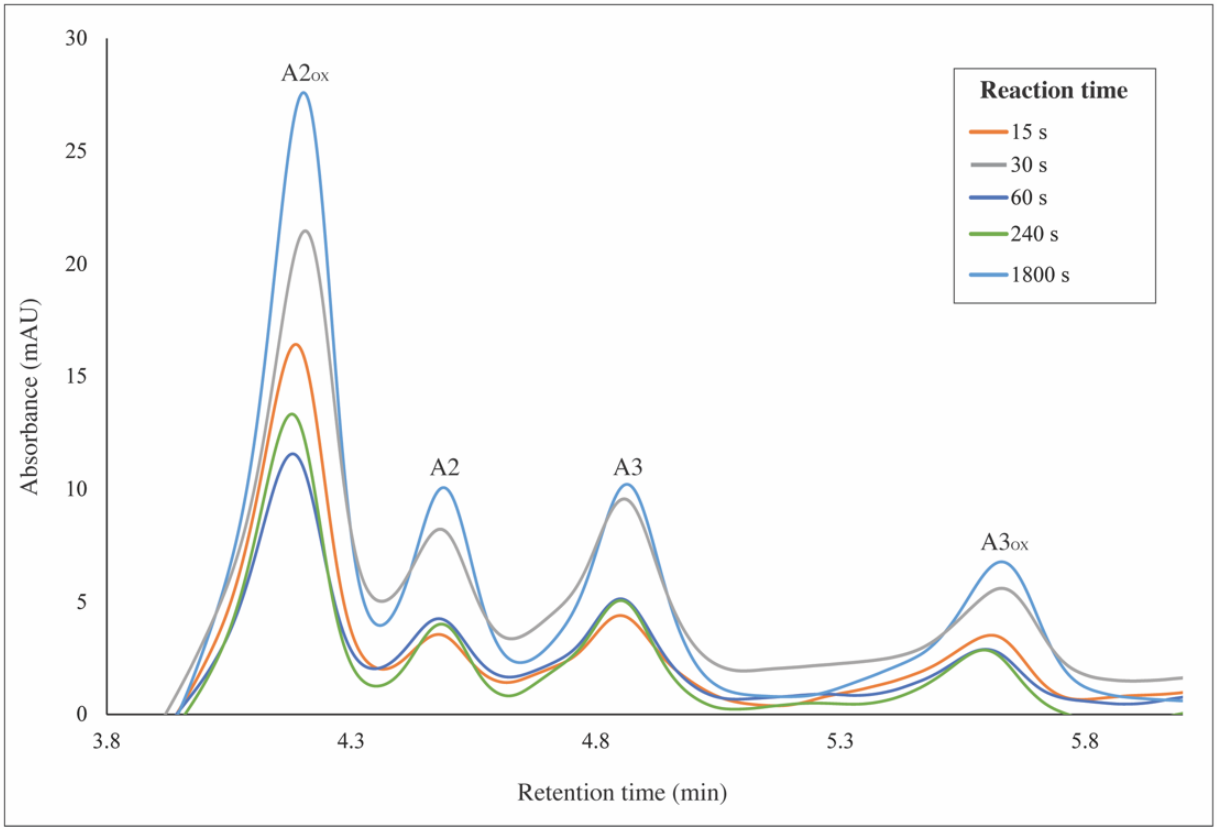

Figure 4.13: Chromatogram generated by HILIC separation. *The chromatogram presents the elution of oxidized ($A2_{OX}$ and $A3_{OX}$) and native products (A2 and A3) after AfAA11B WT catalyzed oxidative cleavage of glycosidic bonds in $(GlcNAc)_4$ under H_2O_2 conditions. The retention time is presented in minutes on the x-axis, and the absorbance is presented in mAU on the y-axis. One replicate is used for clarity in this representation, and five time points are included, i.e., 15 seconds (orange), 30 seconds (grey), 60 seconds dark blue), 4 minutes (green), and 30 minutes (light blue).*

The obtained chromatogram showed that the concentration of oxidized products ($A2_{OX}$ and $A3_{OX}$) was not logically progressing between the timepoints and also showed high experimental variation between replicates. Therefore, product formation was evaluated with high-performance ion-exclusion (HP-IEC).

HP-IEC was the second evaluated HPLC technique for quantification of oxidized products. This technique separates the sample components based on the analytes' degree of ionization. Sample reactions were prepared as described in Chapters 3.7.1 and 3.7.3, and the reactions were terminated with sulfuric acid. The sulfuric acid was responsible for the ionization of the samples. A representative (simplified) chromatogram generated by HP-IEC analyzing 250 µM of native (A1-A4) and oxidized ($A1_{OX}$-$A3_{OX}$) chitooligosaccharide standards is presented in Figure 4.14.

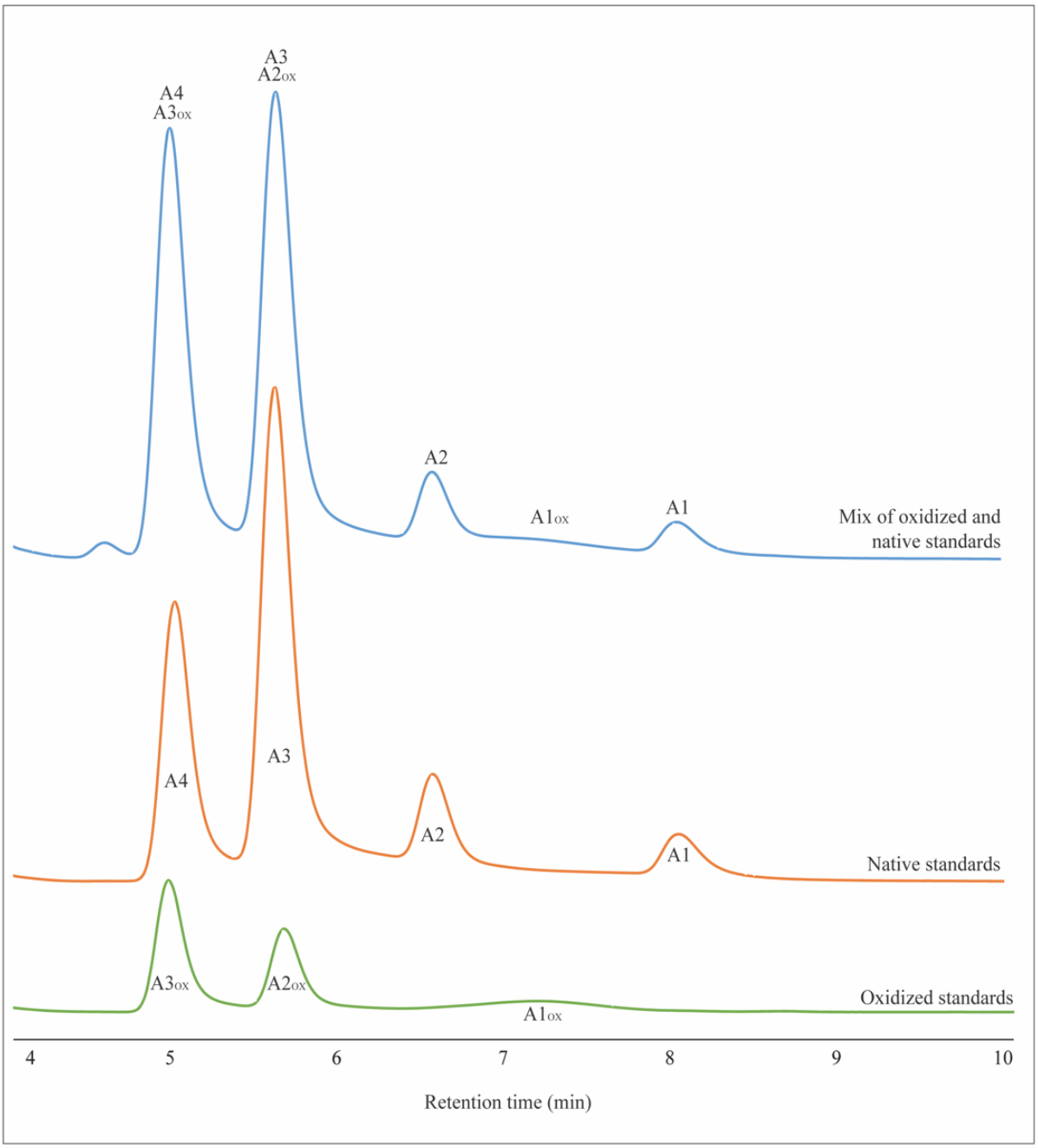

Figure 4.14: Chito-oligosaccharide standards analyzed with HP-IEC. *The figure presents the elution of 250 µM native (A1-A4) and oxidized ($A1_{OX}$-$A3_{OX}$) chitooligosaccharide standards from one mixed sample (blue curve). Native standards and oxidized standards were also analyzed separately and are presented by orange and green lines, respectively. The x-axis gives the retention time in minutes.*

The presented chromatogram resulted from optimizing the standard protocol used in the laboratory to achieve optimal chromatogram resolution. Nevertheless, co-elution of A4/$A3_{OX}$ and A3/$A2_{OX}$ occurred. The amount of produced A1 and A2 was assumed equivalent to the amount of produced $A3_{OX}$ and $A2_{OX}$, respectively. Hence, this protocol using HP-IEC generated high-resolution chromatograms and was considered an optimal method for in-direct quantification of oxidized products generated by hydrolysis of $(GlcNAc)_4$ bonds.

The validity of analyzing the products from $(GlcNAc)_4$ oxidation by HP-IEC was investigated by a time course under hydrogen peroxide conditions using three replicates of *Af*AA11B WT, where the samples were analyzed on both the Dionex UltiMate 3000 HPLC system and the ICS5000, comparing product detection by HP-IEC and HP-AEC, respectively (Figure 4.15).

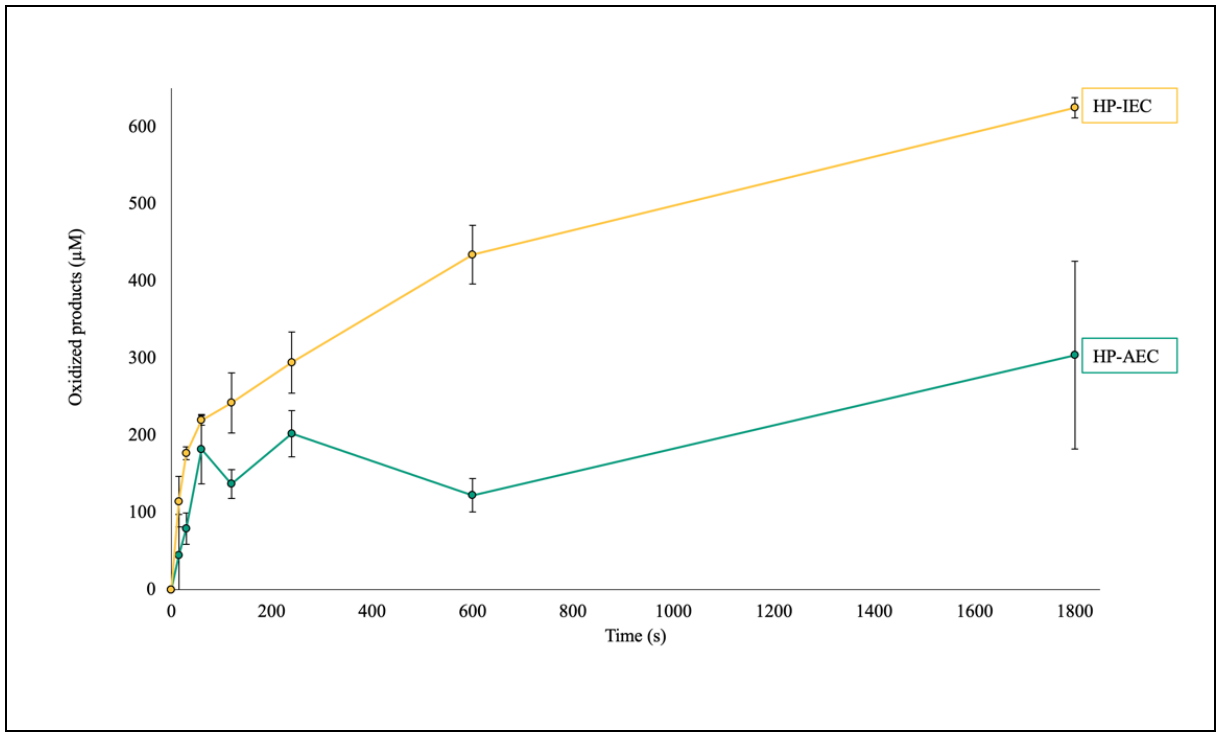

Figure 4.15: Comparison of product analyzation from AfAA11B WT catalyzed glycosidic bond oxidative cleavage using HP-IEC and HP-AEC. *Generated oxidized products are presented on the y-axis in µM, and time reaction time is presented on the x-axis in seconds. Samples were analyzed in triplicates with HP-AEC and HP-IEC, presented in green and yellow, respectively. The error bars show the standard deviation between the triplicates.*

Notably, the reactions analyzed with HP-IEC generated approximately twice as much product as when the reactions were analyzed with HP-AEC, which is stoichiometrically impossible, considering 300 µM H_2O_2 is the limiting reagent. The reactions analyzed using HP-AEC generated the appropriate amount of product, whereas the product concentration was overestimated using HP-IEC. For this reason, the chromatographic method of choice was high-performance anion-exchange chromatography.

High-performance anion-exchange chromatography (HP-AEC) was considered the optimal way of analyzing the enzyme assays performed during this thesis work. Besides, HP-AEC is a very sensitive method that is advantageous when analyzing complex samples like the degradation of carbohydrate substrates.

4.7 *IN-SITU* PEROXYGENASE ACTIVITY OF *Af*AA11B

It is hypothesized that the LPMO reactions occurring under oxygen conditions in the presence of an external reductant are reliant on *in-situ* hydrogen peroxide production (Bissaro et al., 2017). Time-course experiments were performed in the presence of oxygen and ascorbic acid to analyze formation of oxidized products for the *in-situ* hydrogen peroxide production conditions. Sample reactions were prepared as described per Chapter 3.7.1. Generated oxidized products from the *Af*AA11B catalyzed oxidation of $(GlcNAc)_4$ were separated and detected by HP-AEC-PAD in three replicates and quantified by $A2_{OX}$ and $A3_{OX}$ calibration curves (Figure 8.9, Appendix VI). Product formation during the 300-minute reaction is presented in Figure 4.16.

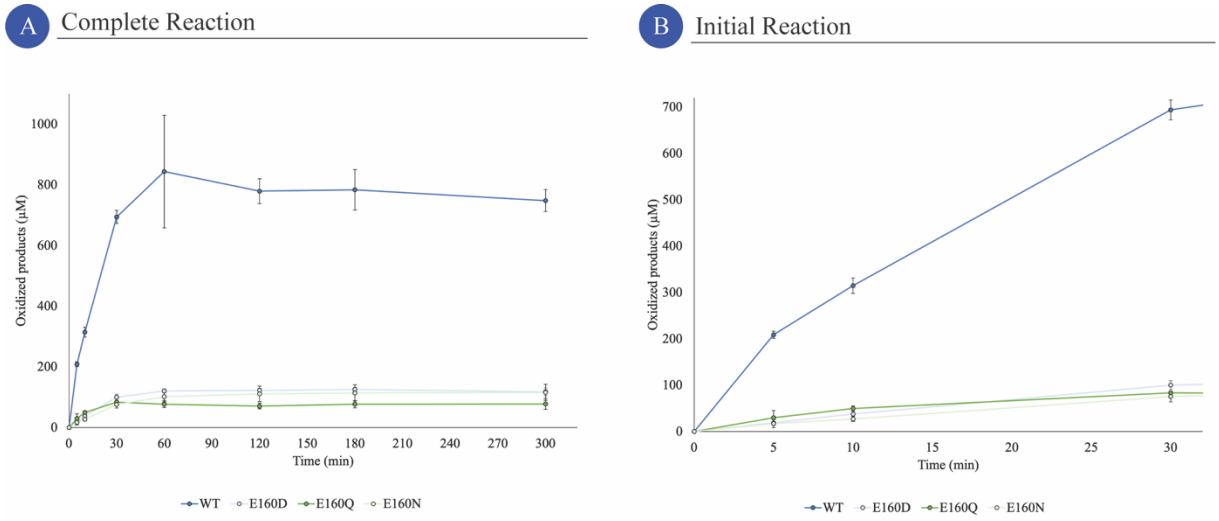

Figure 4.16*: *In-situ hydrogen peroxygenase activity of AfAA11B WT and gatekeeper mutants. *The enzyme activity (y-axis) was monitored over 5 hours (x-axis), using 1 µM LPMO, 1 mM (GlcNAc)4, and 1 mM reductant (AscA) (A). Zoomed in of the first 30 reaction minutes to show the initial rate of the reaction (B). Obtained oxidized products are presented in blue, light blue, light green, and green for the AfAA11B WT, E160D, E160N, and E160Q catalyzed reaction, respectively. The gatekeeper side-chain characteristics are color-coded green for amide side-chains and blue for carboxylic acid side-chains. Error bars are included to present the standard deviation between each triplicate.*

All *Af*AA11B variants exhibited some level of *in-situ* peroxygenase activity. A clear trend is that the gatekeeper variants appeared to be less stable than the wild type as the reaction curves were flattening after 30 minutes before the reactions had gone to completion. Zooming in on the first 30 reaction minutes, one may see how fast each enzyme catalyzes the reactions, regardless of final product concentration of oxidized products. It was suboptimal to estimate an accurate initial rate of LPMO catalyzed oxidation of $(GlcNAc)_4$ under these reaction conditions because the number of observations during the LPMOs steady state is too low. Hence, the initial

rate is not included. Ideally, this experiment should have been repeated with different reaction conditions, such as using a lower enzyme concentration or lower reaction temperature.

Nevertheless, one may compare the enzymatic trends between the *Af*AA11B variants. Mutating the gatekeeper residue lowered the *Af*AA11B enzymatic activity. *Af*AA11B E160D was the most active variant among the gatekeeper mutants of *Af*AA11B, producing the highest amounts of oxidized products. The carboxylic acidic gatekeeper side-chain seems favorable in catalyzation of $(GlcNAc)_4$ oxidation.

The effect of adding catalase to the reactions described above was attempted for the *Af*AA11B variants exhibiting a gatekeeper residue with a carboxylic acid functional group, *i.e.,* the wild type and E160D, as these *Af*AA11B variants appeared to be the most catalytic active. A catalase enzyme decreases *in-situ* produced hydrogen peroxide from the reaction by catalyzing the oxidation of H_2O_2, generating H_2O and O_2. The sample reactions were prepared as described in Chapter 3.7.2, and the oxidized products were detected and quantified by HP-AEC-PAD. Figure 4.17 presents the results from *Af*AA11B catalyzed oxidative cleavage of glycosidic bonds in the presence of catalase. The concentration of oxidized product was calculated using the calibration curves presented in Figure 8.9, Appendix VI.

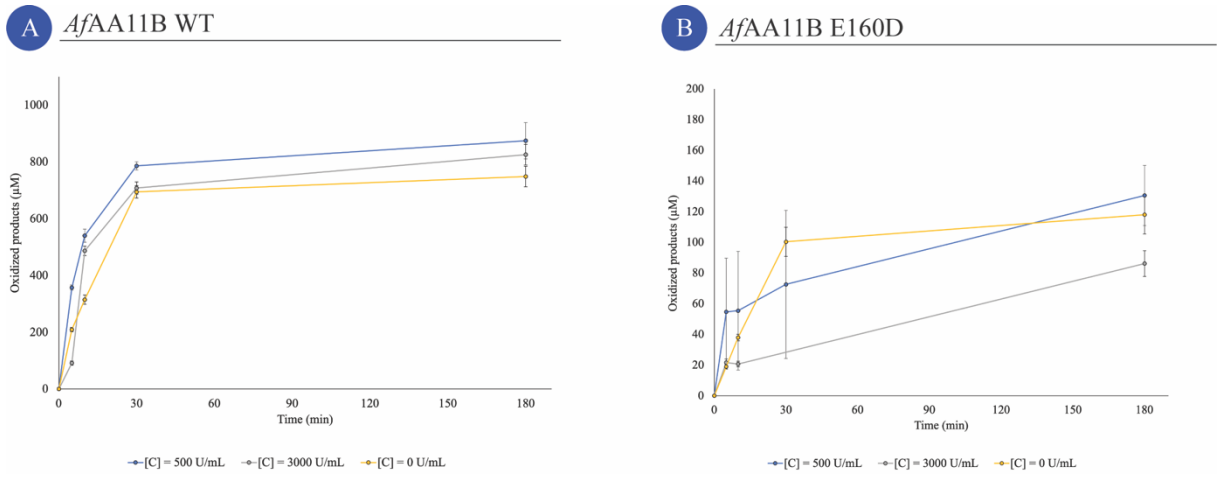

Figure 4.17: Influence of catalase on AfAA11B in-situ hydrogen peroxygenase activity. *Oxidized products generated under O_2 conditions in the presence of catalase during $(GlcNAc)_4$ oxidation catalyzed by (A) Wild type AfAA11B or (B) The gatekeeper mutant AfAA11B E160D. Reactions included 1 µM LPMO, 1 mM AscA, 1 mM $(GlcNAc)_4$, and catalase from bovine liver (500 or 3000 U/mL). Generated oxidized products in µM (y-axis) were monitored over 180 minutes (x-axis). A control without catalase was also included. The blue, grey, and yellow graph corresponds to 500, 3000 and 0 U/mL catalase, respectively. Error bars indicate the standard variation between triplicates.*

Catalase did not affect the reaction catalyzed by *Af*AA11B WT. However, catalase did seem to influence the reaction with the gatekeeper mutant E160D, where the aspartate gatekeeper

mutant had a shorter side-chain compared with the wild type. By adding an increased amount of catalase, the generated oxidized products from E160D catalyzed oxidation of $(GlcNAc)_4$ were reduced.

4.8 PEROXYGENASE ACTIVITY OF *Af*AA11B

Enzymatic activity under hydrogen peroxide conditions was investigated, as described in Chapter 3.7.3. *Af*AA11B catalyzed oxidation of glycosidic bonds in the soluble $(GlcNAc)_4$ were monitored in triplicates over 30 minutes with H_2O_2 as the cosubstrate. The products were separated and detected by HP-AEC-PAD (Calibration curves in Figure 8.9, Appendix VI). It was predicted that the *in-situ* hydrogen peroxide production of *Af*AA11B may generate more oxidized products than can be accounted from the externally added H_2O_2 concentration. For this reason, every peroxygenase experiment was performed in both aerobic and anaerobic conditions. The effect of the reductant on enzymatic activity was also investigated, and the experiments were performed with either ascorbic acid, cysteine, or gallic acid. The obtained results are presented in Figure 4.18.

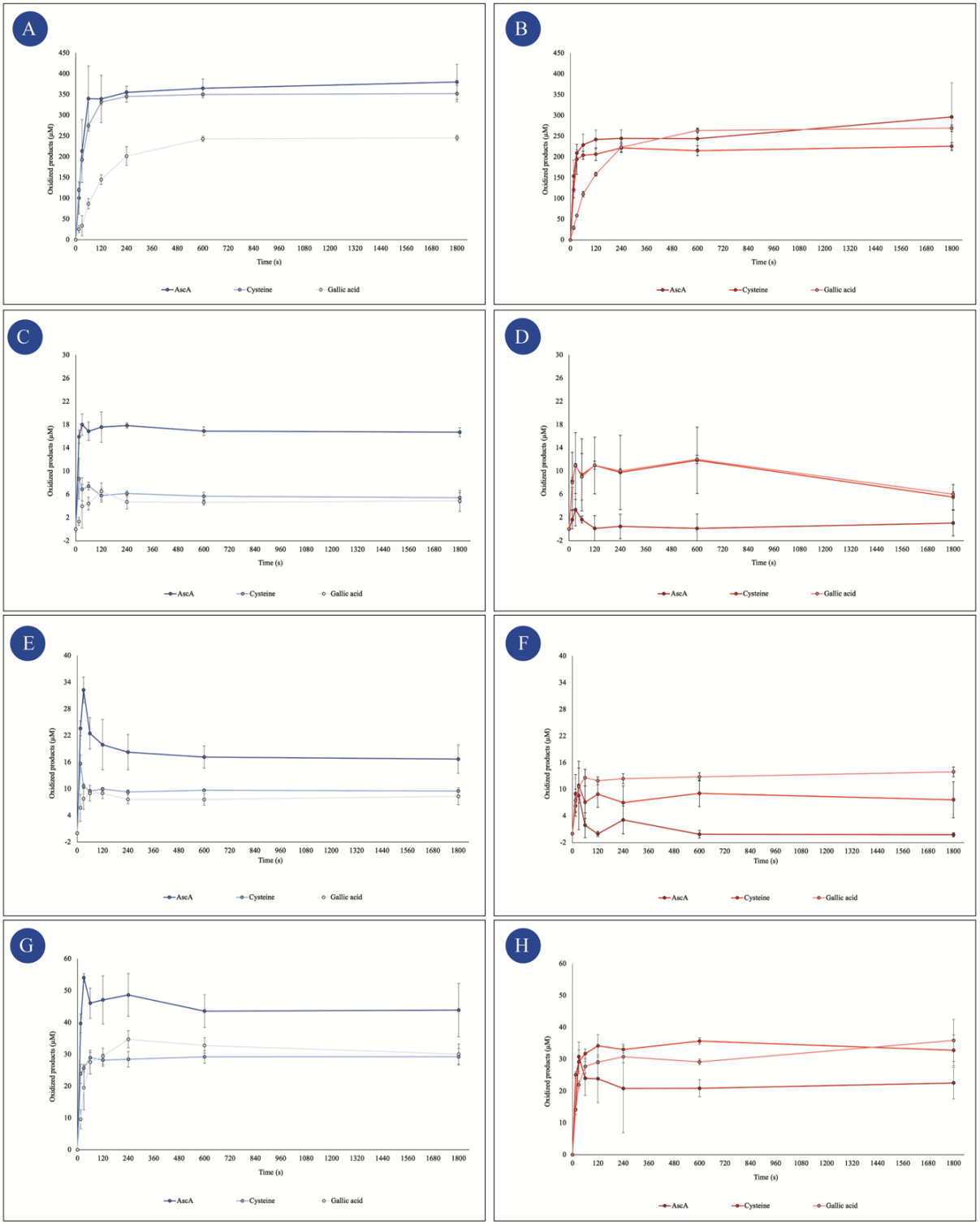

Figure 4.18: Peroxygenase activity of AfAA11B. *The peroxygenase activity of AfAA11B (A/B), E160Q (C/D), E160N (E/F), and E160D (G/H) was monitored in aerobic (blue) and anaerobic (red) conditions. Following the hydrolysis of glycosidic bonds in $(GlcNAc)_4$, resulting oxidized products in µM is plotted (y-axis) relative to reaction time in seconds (x-axis). Note the µM scale is different for each AfAA11B variant. The reductants AscA, cysteine, and gallic acid are presented in color gradients, ranging from dark to light color. Standard deviations from each triplicate are presented as error bars.*

All *Af*AA11B catalyzed $(GlcNAc)_4$ oxidations went to completion after approximately 120 seconds of reaction. Determining the catalytic rates of the *Af*AA11B catalyzed reaction was, for this reason, inaccurate, as the *Af*AA11B catalyzed turnovers appeared at a too fast rate for collecting samples for the analyses. Nevertheless, the catalytic trends may be evaluated. *Af*AA11B WT obtained the highest catalytic activity among the *Af*AA11B variants. A carboxylic acid functional group was favored among the gatekeeper mutations in terms of peroxygenase activity. Thus, the trend in peroxygenase activity indicated how essential the gatekeeper residue is regarding catalytic turnover.

The total amount of oxidized products generated after 30 minutes of reaction is presented in Figure 4.19, comparing the amount of generated product using different reductants in aerobic and anaerobic conditions for each *Af*AA11B variant.

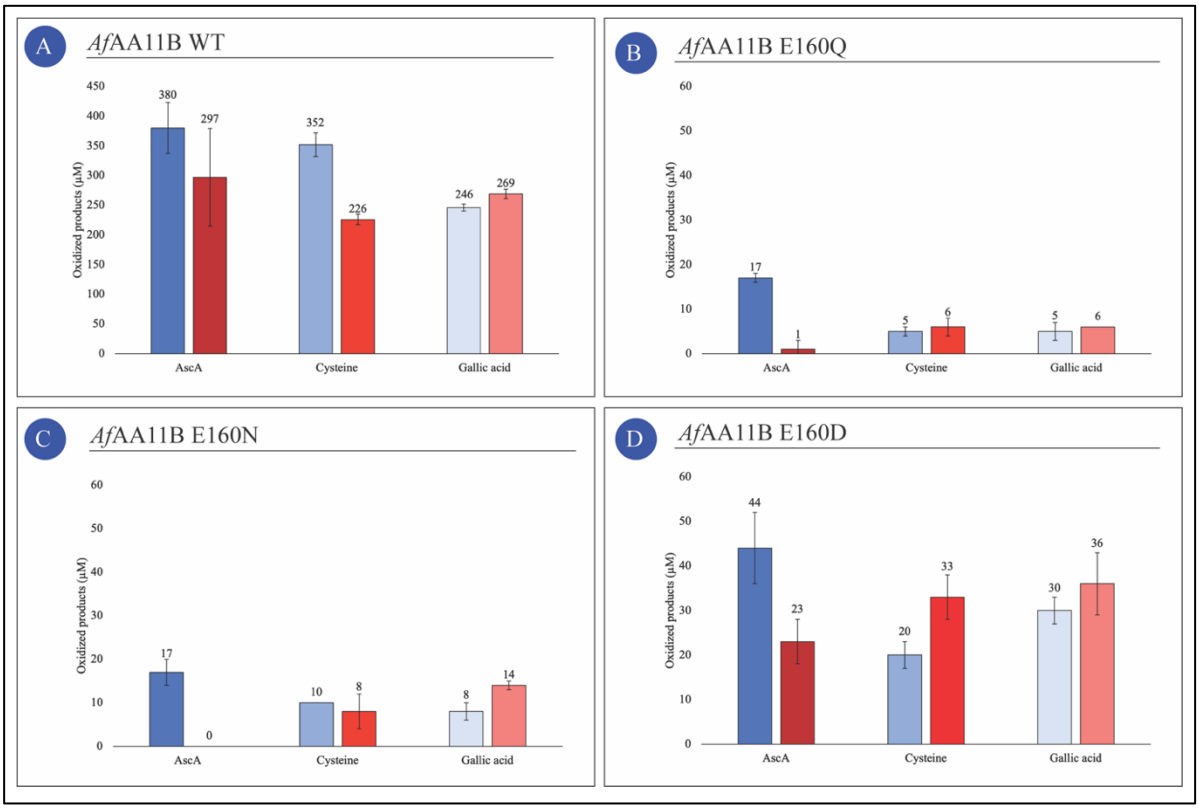

Figure 4.19: Total oxidized product formed after 30 minutes of AfAA11B catalyzed oxidation of $(GlcNAc)_4$. *The product formation after oxidative cleavage of glycosidic bonds catalyzed by (A) AfAA11B WT, (B) E160Q, (C) E160N, and (D) E160D are presented with error bars indicating the standard deviation of the triplicates. The oxidized products are obtained from the 30-minute data in Figure 4.18. Three different reductants were used: AscA, cysteine, and gallic acid (dark to light color gradient) under aerobic (blue) and anaerobic (red) conditions.*

For the *Af*AA11B WT catalyzed oxidation in aerobic (anaerobic) conditions using AscA, cysteine, and gallic acid as reductant, this total amount of oxidized product generated after 30

minutes was estimated to be 380 ± 43 (297 ± 82), 352 ± 20 (226 ± 9), and 246 ± 6 (269 ± 8) µM, respectively. The *Af*AA11B E160Q catalyzed oxidation of $(GlcNAc)_4$ in aerobic (anaerobic) conditions generated 17 ± 1 (1 ± 2), 5 ± 1 (6 ± 2), and 5 ± 2 (6 ± 0) µM oxidized products after 30 minutes when AscA, cysteine, and gallic acid was reducing the *Af*AA11B E160Q copper center, respectively. When AscA, cysteine, and gallic acid was acting as reducing agent in the *Af*AA11B E160N catalyzed the oxidative cleavage of the glycosidic bonds, 17 ± 3 (0 ± 0), 10 ± 0 (8 ± 4), and 8 ± 2 (14 ± 1) µM oxidized products were generated after 30 minutes, respectively. Generated oxidized products after 30 minutes were estimated to 44 ± 8 (23 ± 5), 20 ± 3 (33 ± 5), and 30 ± 3 (36 ± 7) µM when *Af*AA11B E160D catalyzed the oxidative cleavage of the glycosidic bonds over 30 minutes using AscA, cysteine, and gallic acid, respectively. The yield after *Af*AA11B catalyzed oxidation of $(GlcNAc)_4$ was approximately the same regardless of the external reductant (aerobic or anaerobic conditions disregarded). Hence, the LPMO-Cu(II) were "activated" by the reduction to LPMO-Cu(I) regardless of the reductant nature. This reductant behavior correlates with the assumption of the reductant not being rate-determining in enzymatic catalysis, as previously stated (Stepnov et al., 2021).

However, Stepnov et al. (2021) proposed that the *in-situ* hydrogen peroxide production by the LPMO is more relevant for the catalytic rate, than the "priming" reduction of the LPMO. Indeed, the amount of generated products after 30 minutes reaction is lowered by changing from aerobic to anaerobic conditions, *i.e.,* removing excess hydrogen peroxide from *in-situ* production by the LPMO. However, due to this experiment's high variation, no statistical tests were performed to confirm if this difference in generated products were significant.

4.9 STOPPED-FLOW SPECTROSCOPY *Nc*AA9C

Reactivity of *Nc*AA9C-Cu(I) with hydrogen peroxide was monitored by rapid stopped-flow UV/Vis spectroscopy in the absence of glycosidic substrate (Chapter 3.8). In the absence of a glycosidic substrate, introducing H_2O_2 to the reduced LPMO is thought to lead to the formation of OH• with a subsequent oxidation of aromatic amino acids residues close to the LPMO's monocopper center, such as tyrosine and tryptophan (Jones et al., 2020). Generation of amino acid radicals and the transportation of the oxidative hole may be detected with stopped-flow spectrophotometry, as a changed UV signal at the maximum absorbed wavelength for these aromatic residues indicates the formation and decay of tyrosine ($\lambda \approx 420$ nm) and tryptophan

($\lambda \approx 520$ nm) (Bensasson, 1983). The change in UV signal at different wavelengths for *Nc*AA9C WT and gatekeeper mutants are presented in Figure 4.20.

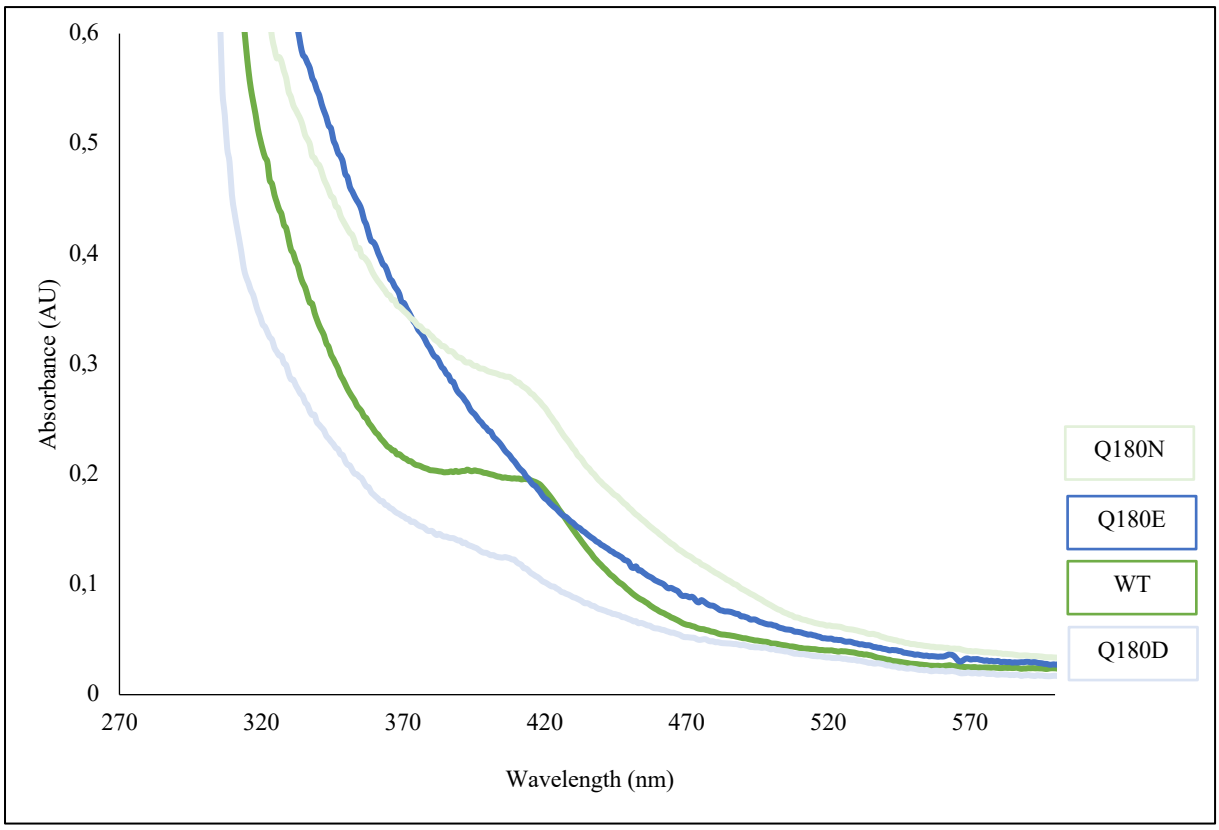

Figure 4.20: Maximum signal wavelength obtained in the reaction involving NcAA9C (WT and the gatekeeper mutants) and hydrogen peroxide in the absence of glycosidic substrate. *The wavelength in nm and absorbance in AU are presented on the x- and y-axis, respectively. NcAA9C WT (dark green), Q180N (light green), Q180E (dark blue), and Q180D (light blue) are color-coded as aforementioned based on the nature of the gatekeeper residue side-chains.*

The obtained results corresponded with previous research on *Nc*AA9C WT (Hedison et al., 2021). After mixing *Nc*AA9C-Cu(I) with hydrogen peroxide (t = 0 ms), 110, 140, and 110 ms was required to generate the maximum increase in UV signal for *Nc*AA9C Q180N ($\lambda_1 \approx 408$, $\lambda_2 \approx 520$ nm), the wild type ($\lambda_1 \approx 415$, $\lambda_2 \approx 520$ nm), and Q180D ($\lambda_1 \approx 415$, $\lambda_2 \approx 520$ nm). Hence, it was believed that amino acid radicals of tyrosine and tryptophan were generated in the *Nc*AA9C variants. The nature of the gatekeeper mutant appeared important during radical formation, as the glutamate mutant of *Nc*AA9C did not generate signals. Moreover, *Nc*AA9C with gatekeeper mutants of amide character generated higher signals compared with *Nc*AA9C with gatekeeper mutants of carboxylic acid character.

Five UV measurements were made for each *Nc*AA9C variant between the mixing time (t = 0 ms) and the presented time for maximum increase in UV signal. Moreover, five UV measurements were monitored from the time for maximum UV signal until the signal

disappeared (4000 ms). Based on these UV measurements, the formation and decay of UV signals are presented in Figure 4.21.

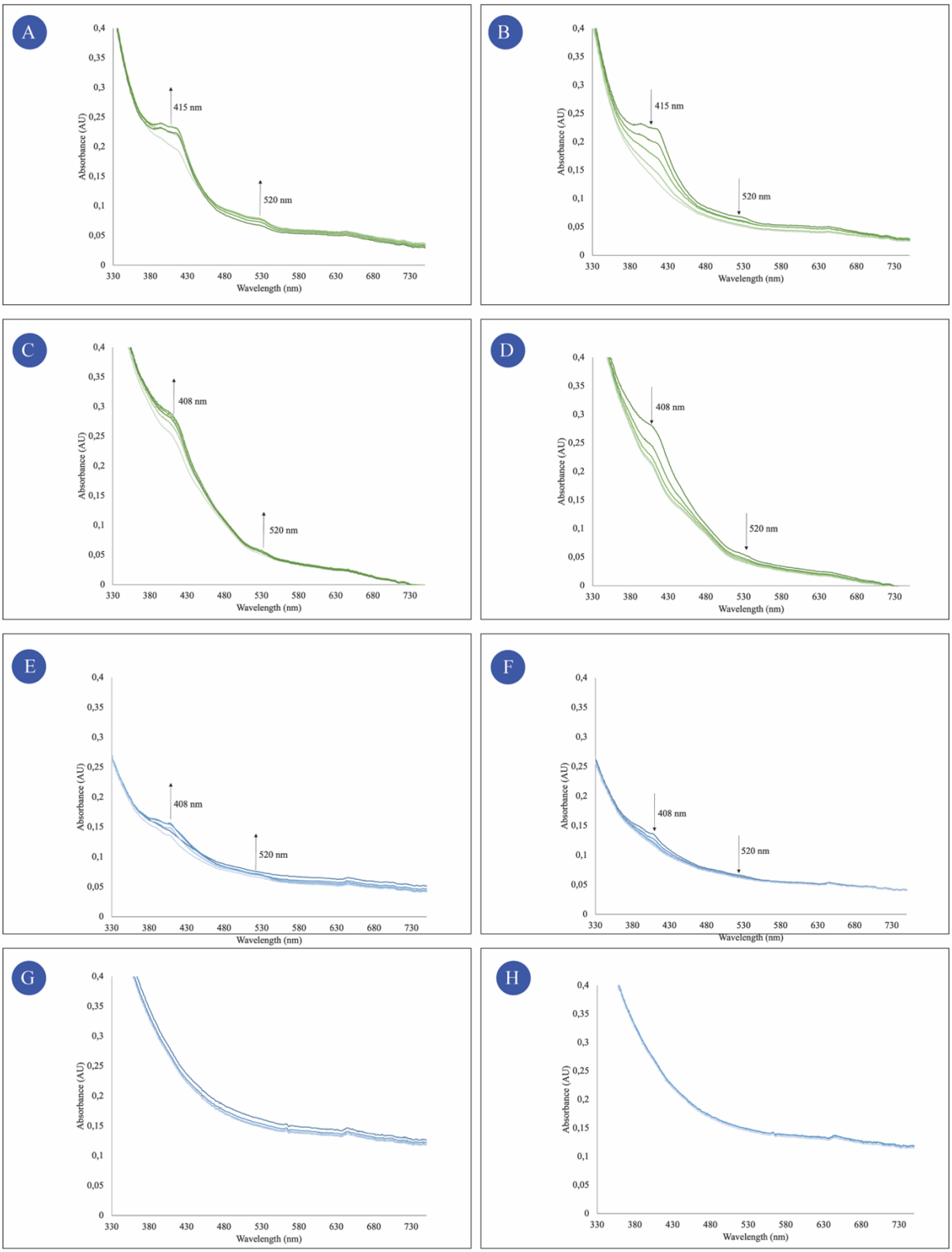

Figure 4.21: Formation and decay of UV signals by NcAA9C-Cu(I) WT and gatekeeper mutants. *NcAA9C reactivity is presented for the WT (A/B), Q180N (C/D), Q180D (E/F), and Q180E (G/H) with the formation of UV signal (left) and decrease of UV signal (right). Five absorbance measurements were monitored during the formation and decay of the UV signal. Green and blue color codes indicated the carboxylic acid and amide gatekeeper side-chains, respectively.*

A single exponential equation was used to estimate the observed amino acid radical formation and decay rates with a baseline correction factor (Equation 7, Chapter 3.8). The estimated rates are presented in Table 4.2.

Table 4.2. Tyrosine and tryptophan radical formation and decay rate for *Nc*AA9C WT and the gatekeeper mutants. The formation and decay rate of the maximum signal wavelengths, *i.e.*, ~ 420 and 520 nm, are presented in s^{-1}. The measurements were based on one biological replicate. Signals generated too fast to quantify, or not occurring signals are marked as not available (NA).

***Nc*AA9C**	**$\lambda_{max} \approx$ 420 nm**		**$\lambda_{max} \approx$ 520 nm**	
	Formation rate (s^{-1})	Decay rate (s^{-1})	Formation rate (s^{-1})	Decay rate (s^{-1})
WT	68	1	NA	10
Q180N	65	3	3	4
Q180E	NA	NA	NA	NA
Q180D	42	1	34	2

The formation rates for the signal at $\lambda \approx 420$ nm were very similar for the *Nc*AA9C variants with amide gatekeeper residue (WT: 68 s^{-1} and Q180N: 65 s^{-1}), whereas this formation rate was different for *Nc*AA9C Q180E (42 s^{-1}) and Q180E (NA). Hence, the nature of the gatekeeper residue might affect the formation and decay rate of the UV signals. Because the presented results were based on one replicate only, and the differences in formation and decay rate were so low, it is hard to say if there is a significant difference between the *Nc*AA9C variants in terms of radical formation. The signals formed at $\lambda \approx 520$ nm were very low and generated very fast, hence, no conclusion may be made from these estimated rates.

5 DISCUSSION

LPMOs greatly enhance recalcitrant polysaccharides' degradation by catalyzing the oxidative cleavage of glycosidic bonds in such substrates. This property makes these redox enzymes important in biomass conversion research, a renewable and sustainable source for products of value. Understanding how we can convert biomass into valuable products is essential for advancing new environmental technologies to address the sustainability goals set forth by the United Nations. To achieve the full potential of LPMOs in biomass conversion, it is of paramount importance to understand their catalytic mechanism. However, there is hardly any research covering the roles of individual amino acids involved in catalysis.

In this work, we have investigated the impact of the gatekeeper residue of *Af*AA11B and *Nc*AA9C in catalysis since this residue is conserved across all LPMO families (Vaaje-Kolstad et al., 2017). In this regard, the gatekeeper residue of *Nc*AA9C (Q180) and *Af*AA11B (E160) was mutated. The gatekeeper residue in *Nc*AA9C was mutated to either glutamate (Q180E), asparagine (Q180N), or aspartate (Q180D), and the equivalent position in *Af*AA11B (E160) was mutated to either glutamine (E160Q), asparagine (E160N), or aspartate (E160D). Mutation of the gatekeeper residue changed the side-chain properties in terms of length and charge, which might have changed the electronic structure of the active copper site (Figure 5.1). The gatekeeper residues with a carboxylic acid functional group in the side-chain, *i.e.,* glutamate or aspartate, are likely deprotonated at the experimental conditions used during this thesis work (pH 6.5). In contrast, the gatekeeper residues with an amide functional group in the side-chain (glutamine or asparagine) are likely neutral at pH 6.5. Moreover, mutation of the gatekeeper residue might have changed the "caging" of the reactive LPMO intermediate (Bissaro et al., 2020b, Wang et al., 2018). The possible changed "caging" of the reactive LPMO intermediate might prevent oxidative damage and possibly change the positioning of the reactive LPMO intermediate for productive catalysis during turnover (Bissaro et al., 2020b, Wang et al., 2018).

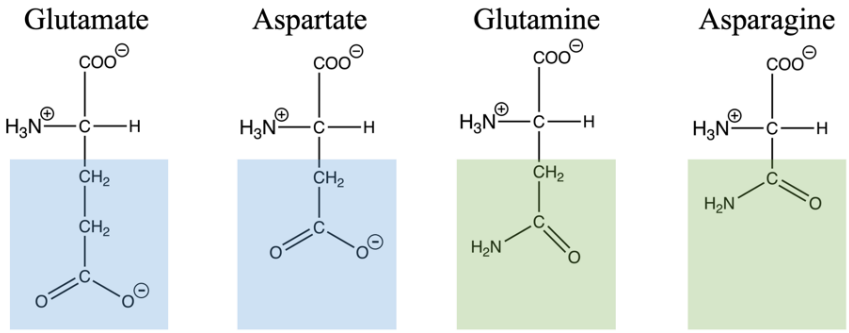

Figure 5.1: The amino acids introduced into the gatekeeper position of NcAA9C and AfAA11B. *The effect of glutamate, aspartate, glutamine, or asparagine as the gatekeeper residue of NcAA9C and AfAA11B was examined in catalysis. Blue and green color codes were used to highlight the gatekeeper residue's carboxylic acid and amide functional groups.*

Our results demonstrate that gatekeeper residue is essential in key features such as substrate turnover, *in-situ* hydrogen peroxide production, and consumption, as well as electronic properties of the copper center. Indeed, our results provide new insights into the mechanism of LPMO catalysis of recalcitrant polysaccharide degradation.

5.1 GATEKEEPER RESIDUE EFFECT ON REDOX POTENTIAL

The effect of the gatekeeper residue on *Af*AA11B and *Nc*AA9C redox potential was estimated as described in Chapter 3.3. We showed that carboxylic acid gatekeeper variants of *Nc*AA9C and *Af*AA11B exhibited the lowest redox potential (Figure 4.9, Chapter 4.3). The negative charge close to the copper center, due to the carboxylic acid nature of the gatekeeper residue, generated an overall lower electron affinity for the LPMOs containing glutamate or aspartate as the gatekeeper residue compared to glutamine or asparagine. A low electron affinity is in line with a low redox potential.

Significant differences in redox potential caused by the gatekeeper residue's side-chain length were also observed. The amide gatekeeper variants of *Af*AA11B and *Nc*AA9C with the shortest gatekeeper side-chain (*Af*AA11B E160N and *Nc*AA9C Q180N) obtained the highest redox potential. Moreover, the lowest redox potential among the carboxylic acid gatekeeper variants of *Nc*AA9C was obtained by the gatekeeper mutant with the longest side-chain, *i.e.,* *Nc*AA9C Q180E. Hence, a longer side-chain of the gatekeeper residue appeared to be lowering the enzymes' redox potential. Longer side-chains of the gatekeeper residue reduce the distance between the copper center and the functional group of the gatekeeper residue. This reduced distance may increase a possible cage complex formation between the LPMO-Cu(II) and the reductant. Such a complex may stabilize the LPMO-Cu(II) due to hydrogen-bonding (Ibanez et

al., 1988). The caging effect increases with increasing hydrogen-bonding strength, which may be associated with both increasing electron affinity (gatekeeper nature) and relative hydrogen-bonding distance (side-chain length). Hence, the LPMO with the lowest redox potential may also had the highest caging effect. If the reductant is complexing with the LPMO-Cu(II), this may explain the observed lower redox potential.

5.2 GATEKEEPER RESIDUE EFFECT ON OXIDASE ACTIVITY

The Amplex Red assay was performed as described by Kittl et al. (2012) to estimate the effect of the gatekeeper residue in *Af*AA11B and *Nc*AA9C on the oxidase activity (Figure 4.10, Chapter 4.4). We observed that the studied LPMOs with a gatekeeper residue of carboxylic acid character obtained significantly higher oxidase activity than the amide gatekeeper mutants. Moreover, the difference in oxidase activity between the glutamate/aspartate and glutamine/asparagine gatekeeper variants was also significant. Indeed, the oxidase activity of the gatekeeper variants of the same nature (carboxylic acid or amide) increased with increasing gatekeeper residue side-chain length. Firstly, this indicates that the closer the functional group of the gatekeeper residue approaches the copper center, the better the *in-situ* H_2O_2 production by the LPMO. Secondly, the oxidase activity is higher for LPMOs with a gatekeeper residue of carboxylic acid nature than an amide functional group in the gatekeeper position. We hypothesize that a close proximity of the gatekeeper's functional group to the copper center generates either a strong electrostatic-electrostatic interaction (carboxylic acid functional group) or a less strong electrostatic-dipole interaction (amide functional group) between the LPMO-Cu(I) and the gatekeeper residue. The close proximity of a carboxylic acid functional group to the copper center generates a possible improved caging effect of the $O_2^{\bullet-}$ radicals generated under O_2 reduction to H_2O_2. Hence, the combination of a long gatekeeper residue sidechain and a net negative charge of the LPMOs catalytic center is required to obtain the high *in-situ* H_2O_2 production observed.

Having Glu in the gatekeeper position yielded the highest *in situ* oxidase activity of the studied LPMOs verified at a significance level of 5%. However, Glu in the gatekeeper position may not be beneficial for activity in other LPMOs. The catalytic triad comprises the gatekeeper residue and two additional amino acid residues in the second sphere of the LPMO, and it is hypothesized that this catalytic triad is essential regarding the LPMO enzymatic activity and stability (K. Hall, pers. com., 2021). This catalytic triad is Tyr-Gln-His for *Nc*AA9C WT and

Tyr-Glu-Asn for *Af*AA11B WT. In this regard, most LPMOs of family AA10 have glutamate as the gatekeeper mutant, although this LPMO family has poor oxidase activity (Stepnov et al., 2021). The catalytic triad of AA10s with a glutamate gatekeeper residue (Phe-Glu-Arg or Phe-Glu-Asn) is different from the LPMOs studied here and could explain the poor oxidase activity of this LPMO family. However, even though it is hypothesized that these three amino acid residues are linked, the poor oxidase activity may also be explained by other amino acid residues in the second sphere, as there are likely more amino acid residues that are important for controlled hydrolyzation of glycosidic linkages. Still, our results clearly demonstrate the importance of the chemical nature of the gatekeeper.

5.3 GATEKEEPER RESIDUE EFFECT ON PEROXIDASE ACTIVITY

The Breslmayr assay was performed as described per Chapter 3.5 to compare the effect of the gatekeeper mutants on the LPMO peroxidase activity. This peroxidase activity is proposed as an estimate for the peroxygenase activity of the LPMO, as the substrate 2,6-DMP is oxidized to coerulignone in the presence of LPMO and H_2O_2. Generated coerulignone is measured spectrometrically at 569 nm, and this formation rate is assumed equivalent to the rate of consumed H_2O_2 by the LPMO (Figure 4.11, Chapter 4.5).

The first step of the Breslmayr reaction is an electron transfer from 2,6-DMP to LPMO-Cu(II). Interestingly, Kracher et al. (2016b) observed a clear correlation between the redox potential of reductants and the rate of LPMO catalysis. We observe that the LPMOs with the highest redox potential have the highest peroxidase activity assessed using the Breslmayr assay. Considering our results and the observations by Kracher et al. (2016b), the observed H_2O_2 consumption rates may reflect the ability of the LPMOs to be reduced by 2,6-DMP, which again is dependent on the redox potentials of the LPMOs. Our results demonstrate a correlation of the much-used Breslmayr assay to assess peroxidase activity and LPMO peroxygenase activity with the redox potential of LPMOs, which we demonstrate that is an essential feature of LPMO catalysis.

Interestingly, we observed a lower peroxidase activity for the carboxylic acid gatekeeper mutants of *Af*AA11B and *Nc*AA9C than the amide gatekeeper variants. This trend is the reverse of what we observed in the oxidase activity assay. Summarizing the *Af*AA11B and *Nc*AA9C trends observed in estimating the redox potential, oxidase activity, and peroxidase activity, we state that there is likely a correlation between the studied LPMO's redox potential, the observed oxidase activities, and the observed peroxidase activities. For *Af*AA11B, the carboxylic acid

gatekeeper mutants (Glu and Asp) displayed the lowest redox potentials, the highest oxidase activities, and the lowest peroxidase activities. The amide gatekeeper variants (Gln and Asn) had the highest redox potentials, lowest oxidase activities, and highest peroxidase activities. Similar trends were observed for *Nc*AA9C, as *Nc*AA9C WT and Q180N displayed the highest redox potentials, the lowest oxidase activities, and the highest peroxidase activities. The opposite was observed for *Nc*AA9C Q180E and Q180D, with the lowest redox potentials, the highest oxidase activities, and the lowest peroxidase activities. Combined, our results show that a carboxylic functional group in the gatekeeper position, independent of the nature of the LPMO, yields low redox potential, high oxidase activity assessed by the Amplex Red assay, and low peroxidase activity as assessed by the Breslmayr assay, compared to when an amide is the functional group of the gatekeeper residue.

It also appears that there is a connection between the distance of the functional group of the gatekeeper residue and the copper center related to redox potential and oxidase activity. A relatively close proximity of the gatekeeper's functional group to the copper center (Glu and Gln) lowers the redox potential and increases the oxidase activity, compared to a relatively long distance (Asn and Asp), which increases the redox potential and lowers the oxidase activity. The oxidase activity estimates the *in-situ* hydrogen peroxide production by the LPMO, where the first step in this reduction is the endergonic formation of $O_2^{\bullet-}$ from O_2. Converting O_2 to $O_2^{\bullet-}$ is more energetically favorable for an LPMO with a low redox potential than an LPMO with high redox potential. So, LPMOs with low redox potential, *i.e.,* LPMOs with gatekeeper residues exhibiting carboxylic functional groups, will reduce molecular oxygen and produce hydrogen peroxide *in-situ* to a greater extent than the amide gatekeeper mutants.

5.4 DETECTION OF OXIDIZED PRODUCTS

The choice of analytical technique for analyzing *Af*AA11B catalyzed oxidation of $(GlcNAc)_4$ was investigated (Chapter 3.7). Three techniques were evaluated: high-performance hydrophilic interaction chromatography (HILIC), high-performance ion-exclusion chromatography (HP-IEC), and high-performance anion-exchange chromatography (HP-AEC). HILIC was disregarded as the variation in amount of generated products from $(GlcNAc)_4$ oxidation using this analytical technique was too high. It was believed that the heat termination of the reaction caused this high variation (Figure 4.13, Chapter 4.6.2). Because the *Af*AA11B catalyzed oxidation of $(GlcNAc)_4$ occurs very fast, heat termination of the reaction was not

quenching the reaction instantly. Hence, the reaction termination was not equal for each time point. Another reaction termination method was suggested (termination with the mobile phase compatible chemical acetonitrile). However, the chemical acetonitrile is highly volatile, and adding acetonitrile to the samples lead to variation in the sample concentration. For this reason, HILIC was not the preferred method to analyze the oxidized products.

The second analytical method considered to analyze the oxidized products was HP-IEC. The sample reactions could be terminated using sulfuric acid if the oxidized products were analyzed by HP-IEC, as sulfuric acid was the mobile phase of the HP-IEC system, allowing for rapid reaction termination (Dionex UltiMate 3000 HPLC system). However, this analytical method was also disregarded due to the product overestimation presented in Figure 4.15 in Chapter 4.6.2. The reason for the overestimation of product was not discovered, though unrevealed coelution is likely an explanation (Figure 4.14, Chapter 4.6.2). For this reason, HP-AEC was chosen to analyze the sample reactions describing the peroxygenase activity of *Af*AA11B as this method appeared to yield reproducible results.

5.5 GATEKEEPER RESIDUE EFFECT ON *IN-SITU* PEROXYGENASE ACTIVITY

Bissaro et al. (2017) showed that LPMO reactions occurring under oxygen conditions rely on *in-situ* hydrogen peroxide production, further elaborated by Stepnov et al. (2021). Hence, the *Af*AA11B time-course experiments presented in Chapter 3.7.1 were analyzed to investigate the gatekeeper residue's effect on the *in-situ* hydrogen peroxide production. A higher enzymatic activity followed for the glutamate gatekeeper of *Af*AA11B (WT) when only oxygen and an external reductant were present compared with the gatekeeper mutants (Figure 4.16, Chapter 4.7). This trend correlated with the observations made in the oxidase assay and the redox measurements. *Af*AA11B containing glutamate at the gatekeeper position produced more *in situ* H_2O_2 and hence, more oxidized products than the gatekeeper mutants. Thus, a more effective $(GlcNAc)_4$ oxidation was observed under oxygen conditions if the oxidation was catalyzed by *Af*AA11B wild type.

The *Af*AA11B gatekeeper mutants obtained a low product yield (< 1 mM) when catalyzing $(GlcNAc)_4$ oxidation because they were inactivating faster than the wild type, which may be explained by ongoing side reactions besides the oxidative catalysis. Transition metals present in the solution, such as free Cu(II) ions, might catalyze the enzyme-independent autooxidation

of the reductant, which generates excess H_2O_2 (Bissaro et al., 2017). AscA is sensitive to even micromolar concentrations of free copper, and excess H_2O_2 in solution might boost the enzyme activity (Bissaro et al., 2020a, Stepnov et al., 2021). As such, LPMO-Cu(I) may catalyze the oxidation of glycosidic substrates using the additional H_2O_2. However, the excess H_2O_2 can also oxidize the residues in close proximity or comprising the LPMO's active site (Bissaro et al., 2017). Such oxidations occur in the absence of a glycosidic substrate or if the LPMO-binding to the substrate is weak or inaccurate (Forsberg et al., 2018, Loose et al., 2018). The gatekeeper residue is believed to be involved in the substrate-binding by caging H_2O_2 through the hydrogen-bonding pattern between the gatekeeper residue's side-chain, LPMO-Cu(I), and the substrate, hence, optimally aligning the LPMO to the substrate (Bissaro et al., 2020b, Wang et al., 2018). Because of this gatekeeper-involvement in substrate-binding, mutating the gatekeeper residue might have led to a weaker or more inaccurate substrate binding than having glutamate in the gatekeeper position of *Af*AA11B (Bissaro et al., 2020b). The suboptimal enzyme-dependent substrate-binding with following oxidation of the active site might generate free Cu(II) ions. The reductant reduces free Cu(II) ions to free Cu(I) ions, which can drive unproductive side reactions, such as the H_2O_2 production from O_2 reduction (Stepnov et al., 2021). The increased speed of H_2O_2 production may generate more reactive oxygen species in the catalytic center of the LPMO. Generated ROS in the catalytic center is likely caged to a lower extent for the gatekeeper mutants of *Af*AA11B. Bissaro et al. (2020b) showed a hydrogen-bonding network postulated to control the relative positioning of ROS generated from H_2O_2 through caging. The negatively charged carboxylic acid residues will interact stronger (electrostatic interactions and hydrogen-bonding) than the amide residues (hydrogen bonding) with H_2O_2. Moreover, the interaction decreases with decreasing distance between the functional group and H_2O_2 with respect to the distance to the copper center. The formed ROS would be caged to a lower extent and react more freely for the gatekeeper mutants of *Af*AA11B compared with *Af*AA11B WT. These assumptions correlate with these *Af*AA11B gatekeeper mutants being the least active in this experiment, as this unproductive negative cycle of H_2O_2 accumulation might lead to enzyme inactivation.

The *in-situ* peroxygenase activity was investigated further by performing an experiment supplemented with catalase (Chapter 3.7.2). A catalase enzyme catalyzes the oxidation of two hydrogen peroxide molecules to water and molecular oxygen, thus, removing the *in-situ* produced hydrogen peroxide from the reaction. The catalase experiment was performed on the carboxylic acid gatekeeper variants of *Af*AA11B, as these enzymes were the most active (Figure

4.17, Chapter 4.7). It was observed that the catalase enzyme did not affect the $(GlcNAc)_4$ oxidation catalyzed by *Af*AA11B WT. The inability of the catalase to inhibit catalysis of oxidation may be because the *Af*AA11B WT catalyzed reaction is so fast that the *in-situ* produced hydrogen peroxide is consumed for $(GlcNAc)_4$ oxidation hence, not being available for the catalase enzyme. Moreover, the inability of the catalase to inhibit oxidative catalysis may also be explained by the K_M of *Af*AA11B for H_2O_2 (8.9 ± 1.0 µM) (Rieder et al., 2021b). In contrast, the K_M of the catalase enzyme used in this experiment for H_2O_2 is 93 mM (Switala and Loewen, 2002). However, the catalase enzyme influenced the E160D catalyzed reaction by consuming the *in-situ* produced H_2O_2. Adding an increased amount of catalase generated a lower amount of oxidized products than what was observed for the wild type. This observed effect is in line with *Af*AA11B E160D having a shorter side-chain than the WT gatekeeper residue. Even though E160D exhibited a relatively high oxidase activity, this gatekeeper appeared less capable of caging the $O_2^{\bullet-}$ generated from O_2 reduction to H_2O_2 and less capable of caging the later formed •OH, compared with the wild type. Moreover, as the oxidase activity assay estimates the oxidase activity in the absence of a substrate, this *in-situ* peroxygenase activity assay reflected the reduced substrate-binding affinity resulting from the reduced caging capacity of H_2O_2 (described above). Consequently, *Af*AA11B E160D was affected by the catalase enzyme in oxidative catalysis.

5.6 GATEKEEPER RESIDUE EFFECT ON PEROXYGENASE ACTIVITY

As hydrogen peroxide is believed to be the true cosubstrate of LPMOs, the effect of the gatekeeper residue on the *Af*AA11B's enzymatic activity was examined when hydrogen peroxide was provided (Chapter 3.7.3). *Af*AA11B WT (glutamate gatekeeper residue) obtained the highest catalytic activity among the *Af*AA11B variants. *Af*AA11B E160D was the second most active *Af*AA11B variant during the peroxygenase activity assay. The catalytic activity of the carboxylic acid gatekeeper variants of *Af*AA11B indicates the importance of the negative charge near the copper center. Moreover, the distance of the negative charge to the copper center is likely also important, as the mutation of the gatekeeper residue from glutamate to aspartate reduced the catalytic activity. The reduced side-chain length was hypothesized to weaken the strength of the hydrogen-bonding pattern caging the hydroxy radicals, as this hydrogen-bonding pattern is essential in directing the two unbound •OH during hydrogen peroxide activation (Bissaro et al., 2020a, Wang et al., 2018).

The peroxygenase activity of all four *Af*AA11B gatekeeper variants was investigated under both aerobic and anaerobic conditions (Figure 4.18, Chapter 4.8). In all cases, the amount of products was higher for the aerobic conditions than the anaerobic conditions when ascorbic acid was used as the external electron donor. This was expected, as the *in-situ* hydrogen peroxide production by the LPMOs, as well as autooxidation by ascorbic acid, occur under aerobic conditions, producing more hydrogen peroxide to be used in the peroxygenase reaction (Stepnov et al., 2021). This does not occur under anaerobic conditions. Rieder et al. (2021b) also observed this trend for *Af*AA11B WT.

As pointed out previously, the reduction of LPMOs is a central step in the catalytic cycle both with respect to creating *in situ* H_2O_2 production as well in the peroxygenase reaction. There are clear indications of *in-situ* hydrogen peroxide production by the LPMO being reductant dependent (Rieder et al., 2021c, Stepnov et al., 2021). In this regard, performing peroxygenase reactions using gallic acid and cysteine, in addition to ascorbic acid under both aerobic and anaerobic conditions affected the product yield differently depending on the reductant (Figure 4.19, Chapter 4.8). It is difficult to interpret the results. The use of gallic acid as the reductant yields no significant differences in product formation for all four *Af*AA11B gatekeeper variants, either under anaerobic or aerobic conditions. When cysteine is used as the reductant, *Af*AA11B WT (E160) produced less product anaerobically, while E160D produced more. No significant changes were observed for the amide functional group gatekeepers. Again, it is difficult to rationalize the results when gallic acid and cysteine were used as reductants.

5.7 GATEKEEPER RESIDUE EFFECT ON RADICAL FORMATION

The reactivity of the gatekeeper variants of *Nc*AA9C-Cu(I) with H_2O_2 was examined by stopped-flow spectrophotometry (Chapter 3.8), where a change in UV signal is proposed to originate from either generated tyrosine (λ = 420 nm) or tryptophan (λ = 520 nm) radicals (Bensasson, 1983, Jones et al., 2020). During this experiment, the carboxylic acid gatekeeper variants of *Nc*AA9C generated a lower UV signal, than the amide gatekeeper variants when mixing the reduced LPMO with H_2O_2 in the absence of glycosidic substrate (Figure 4.20, Chapter 4.9). Three hypotheses might explain this trend. The first hypothesis is that the carboxylic acid gatekeeper variants produce no or little amounts of amino acid radicals. This is unlikely, as the carboxylic acid gatekeeper variants have shown catalytic activity in the presence of oxygen and an external reductant (K. Hall, pers. com., 2022). Hence, these LPMO shows *in-*

situ peroxygenase activity on cellopentaose, which implies that the LPMOs are capable of H_2O_2 activation and performing catalysis of substrate oxidation.

The second hypothesis is that the radical reacts so fast that it cannot be monitored. This second hypothesis is also unlikely, as the dead time of the SFM-4000 stopped-flow mixing system is as low as 200 µs (BioLogicSciencesInstruments, 2022).

Finally, the third hypothesis is that the radical is transferred somewhere else than through the tyrosine and tryptophan residue route which Jones et al. (2020) proposed, meaning that we cannot measure the change in absorbance using this experimental setup due to a lack of a chromophore for residues that transport the oxidative hole away from the active site. Our results clearly suggest that there are two different routes for escaping the generated radicals.

5.8 *Af*AA11B EXPRESSION ISSUES

The stopped-flow spectrophotometry was not performed on the *Af*AA11B gatekeeper variants due to the low purification yield resulting from *Af*AA11B expression issues. *Af*AA11B expression issues were encountered after repeated purifications of *Af*AA11B, which resulted in loss of enzymatic activity and change in *Af*AA11B behavior during gel electrophoresis (Figure 4.1, Chapter 4.1.1). Multiple explanations were suggested for the *Af*AA11B expression issues. First, *Af*AA11B may have lost its enzymatic activity during the purification process. As yeast expression hosts generally express high protein levels, the protein might accumulate in solution and precipitate. Protein precipitation may explain the low activity in the Amplex Red assay presented in Chapter 4.1.1.

However, the *Af*AA11B expression was not high, and possible protein precipitation cannot explain the loss of the characteristic SDS-PAGE band splitting between the *Af*AA11B catalytic domain and the X278 module with a linker. This characteristic band splitting was likely occurring during the gel electrophoresis due to breaking of the linker by the applied heat and chemical treatment. However, when the band splitting disappeared, one separate protein band appeared instead. Later, the *Af*AA11B expression was lost entirely.

The disappearance of the SDS-PAGE band splitting and, later, *Af*AA11B expression during gel electrophoresis led to the second plausible explanation for the *Af*AA11B expression issues, that the *P. pastoris* colonies were expressing a protein other than *Af*AA11B. This protein

contamination was supported by the multiple bands present in the SDS-PAGE gel when *Af*AA11B expression was lost entirely, indicating a significant amount of other expressed proteins by the *P. pastoris* cells (Figure 4.1D, Chapter 4.1.1). These SDS-PAGE gels also showed sharper protein bands than the gels generated initially. Blurry protein bands are commonly observed during gel electrophoresis of yeast-expressed glycosylated proteins. Therefore, the sharp appearing bands in the SDS-PAGE gels could indicate bacterial contamination of the *P. pastoris* strains.

We hypothesize that *P. pastoris* was not the optimal expression host for *Af*AA11B. *P. pastoris* contains chitin, which may be a problem when overexpressing the chitin active *Af*AA11B, as chitin is required for the structural integrity of *P. pastoris* (Figure 5.2). This might generate a toxic environment for *Af*AA11B expression. A possible toxic environment will lead to selection against the gene, as a cell will kick out any gene that is damaging to the cell. This might explain why the gene was lost, which correlates with the not visible amplification in the *Af*AA11B WT PCR screen presented in Figure 4.2 (Chapter 4.1.2). However, this behavior was not observed for the gatekeeper mutants. One hypothesis is that the *Af*AA11B gatekeeper mutants are not as active on the chitin derivatives as *Af*AA11B WT in the degradation of chitin oligosaccharides (Chapters 4.7 and 4.8).

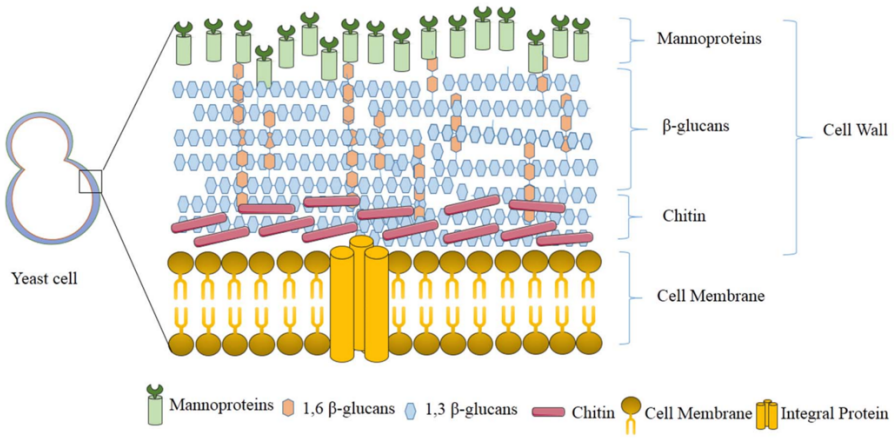

Figure 5.2: Yeast cell wall. *The yeast cell includes the cell wall and the cell membrane, where the cell wall comprises mannoproteins, β-glucans and chitin. The illustration was derived from (Anwar et al., 2017).*

The invisible gene amplification in the *Af*AA11B WT PCR screen indicates the loss of the *Af*AA11B gene through DNA recombination. Because the *Af*AA11B genes were integrated into the *P. pastoris* genome, this makes DNA recombination difficult, though not impossible. Initially, in the production of *Af*AA11B, the *P. pastoris* strains harboring the expression

plasmids were streaked out on YPD-agar plates containing zeocin. The zeocin-resistant markers in the *Af*AA11B expression plasmids allow for selection on zeocin during cloning and cultivation of the strains. Hence, it is unlikely that the *Af*AA11B plasmids were rejected during these 48 hours of incubation time, in the presence of zeocin. However, the following 60 hours of cultivation of *P. pastoris* biomass with the *Af*AA11B genes integrated into the *P. pastoris* genome occurred in the absence of zeocin. It is more likely that the *Af*AA11B was lost at this point, as the incubation time was longer and no zeocin was present in the media accounting for the selection of *Af*AA11B. Ideally, this PCR experiment should have been repeated to confirm the *Af*AA11B WT gene's behavior.

Variables like growth media components (Figure 4.4, Chapter 4.1.4) and if the expression issues were strain-specific were also evaluated to explain the expression issues of *Af*AA11B (Figure 8.2, Appendix I), though without revealing any answers. Optimizing the *P. pastoris* screening protocol also did not improve *Af*AA11B expression. The unsolved expression mystery will be for future research.

6 CONCLUSION AND FUTURE PERSPECTIVES

This master's thesis provides insight into the impact of the gatekeeper residue of *Af*AA11B (E160) and *Nc*AA9C (Q180) in LPMO catalysis. During this study, the gatekeeper residue was mutated to glutamate, glutamine, aspartate, or asparagine to investigate the catalytic effect of changing the length and charge of the gatekeeper residue functional group. A carboxylic acid gatekeeper residue generated a negative charge close to the copper center in the studied LPMOs, whereas an amide gatekeeper residue was neutrally charged. The effect of the relative distance from the gatekeeper functional groups to the copper center was assessed when the side-chain of the gatekeeper residue was either Glu or Asp, or Gln or Asn.

Our study revealed that both changing the charge and length of the side-chain had a major impact on several key features of LPMO activity. A negatively charged functional group and a relative long side-chain resulted in low redox potential of the copper site with concomitant low peroxidase activity and increased *in-situ* oxidase activity. This *in-situ* oxidase activity also increased catalytic activity of substrate oxidation when oxygen and an external reductant were present during turnover. When H_2O_2 was provided, substrate turnover was most efficient if the gatekeeper residue was with a long carboxylic acid functional group. Importantly, we observe these equal trends in two different LPMO families (AA9 and AA11) with different substrate specificity (cellulose and chitin). Furthermore, the *Nc*AA9C gatekeeper residue clearly influences the transportation of oxidative holes from the active site. Here, our results suggest two different routes through the LPMO for the transport of oxidative holes dependent on the nature of the functional group of the gatekeeper residue.

The stopped-flow spectrophotometry performed in this thesis was the first of its kind to analyze the radical formation in an AA9 LPMO with a Tyr-Gln-His catalytic triad where the conserved Gln was mutated as described previously. Future research should include a comparative study of this phenomenon with the same mutations for *Af*AA11B as for *Nc*AA9C described in this thesis. Moreover, since we observe that there is a connection between the nature of the functional group and its distance to the active site with respect to the observed redox potentials, it would be interesting to monitor the kinetics of the reduction of all eight gatekeeper variants to complement the re-oxidation experiments with H_2O_2. Furthermore, it would be interesting to

design an experiment displaying the two different routes for the transport of oxidative holes from the catalytic site with respect to the nature of the functional group of the gatekeeper residue. Such an experiment can be time-resolved quantitative stopped-flow proteomics, inspired by the previous work by Bissaro et al. (2017), where oxidative damages were mapped in *Sc*AA10C. These experiments may identify where the oxidative damages occur over time during re-oxidation of the copper center, providing essential information on the transport of oxidative holes.

This work clearly demonstrates the importance of the gatekeeper residue as part of a catalytic triad in two different systems. The gatekeeper residue is essential in critical LPMO features such as electronic properties of the copper center, *in-situ* H_2O_2 production and consumption, as well as substrate turnover. Hence, this study represents a step forward to understanding the LPMO catalysis mechanism of recalcitrant polysaccharide degradation.

7 REFERENCES

AGGER, J. W., ISAKSEN, T., VARNAI, A., VIDAL-MELGOSA, S., WILLATS, W. G. T., LUDWIG, R., HORN, S. J., EIJSINK, V. G. H. & WESTERENG, B. 2014. Discovery of LPMO activity on hemicelluloses shows the importance of oxidative processes in plant cell wall degradation. *Proceedings of the National Academy of Sciences of the United States of America,* 111**,** 6287-6292.

ALPERT, A. J. 1990. Hydrophilic-interaction chromatography for the separation of peptides, nucleic-Acids and other polar compounds. *Journal of Chromatography,* 499**,** 177-196.

ANWAR, M. I., MUHAMMAD, F., AWAIS, M. M. & AKHTAR, M. 2017. A review of β-glucans as a growth promoter and antibiotic alternative against enteric pathogens in poultry. *World's Poultry Science Journal,* 73**,** 651-661.

APPLIEDPHOTOPHYSICS. 2018. *Stopped-flow technology* [Online]. Available: https://www.photophysics.com/stopped-flow-spectrometry/stopped-flow-technology/ [Accessed 10th of March 2022].

AYUSO-FERNANDEZ, I., RENCORET, J., GUTIERREZ, A., RUIZ-DUENAS, F. J. & MARTINEZ, A. T. 2019. Peroxidase evolution in white-rot fungi follows wood lignin evolution in plants. *Proceedings of the National Academy of Sciences of the United States of America,* 116**,** 17900-17905.

BAGSHAW, C. R. 2013. Stopped-flow techniques. *In:* ROBERTS, G. C. K. (ed.) *Encyclopedia of Biophysics.* Berlin, Heidelberg: Springer Berlin Heidelberg.

BECKHAM, G. T. & CROWLEY, M. F. 2011. Examination of the α-chitin structure and decrystallization thermodynamics at the nanoscale. *The Journal of Physical Chemistry B,* 115**,** 4516-4522.

BECKHAM, G. T., MATTHEWS, J. F., PETERS, B., BOMBLE, Y. J., HIMMEL, M. E. & CROWLEY, M. F. 2011. Molecular-level origins of biomass recalcitrance: decrystallization free energies for four common cellulose polymorphs. *The Journal of Physical Chemistry B,* 115**,** 4118-4127.

BEESON, W. T., VU, V. V., SPAN, E. A., PHILLIPS, C. M. & MARLETTA, M. A. 2015. Cellulose degradation by polysaccharide monooxygenases. *Annual Review of Biochemistry,* 84**,** 923-946.

BENSASSON, R. V. 1983. Flash-photolysis, pulse-radiolysis - contribution to the chemistry of free-radicals in biological-systems. *Bulletin Des Societes Chimiques Belges,* 92**,** 615-616.

BERTINI, L., BREGLIA, R., LAMBRUGHI, M., FANTUCCI, P., DE GIOIA, L., BORSARI, M., SOLA, M., BORTOLOTTI, C. A. & BRUSCHI, M. 2018. Catalytic Mechanism of Fungal Lytic Polysaccharide Monooxygenases Investigated by First-Principles Calculations. *Inorganic Chemistry,* 57**,** 86-97.

BIOLOGICSCIENCESINSTRUMENTS. 2022. *SFM-2000, SFM-3000, SFM-4000 stopped-flow* [Online]. Available: https://www.biologic.net/products/sfm2000-3000-4000-stopped-flow/ [Accessed 16th of April 2022].

BISSARO, B., ISAKSEN, I., VAAJE-KOLSTAD, G., EIJSINK, V. G. H. & ROHR, A. K. 2018. How a lytic polysaccharide monooxygenase binds crystalline chitin. *Biochemistry,* 57**,** 1893-1906.

BISSARO, B., KOMMEDAL, E., ROHR, A. K. & EIJSINK, V. G. H. 2020a. Controlled depolymerization of cellulose by light-driven lytic polysaccharide oxygenases. *Nature Communications,* 11.

BISSARO, B., ROHR, A. K., MULLER, G., CHYLENSKI, P., SKAUGEN, M., FORSBERG, Z., HORN, S. J., VAAJE-KOLSTAD, G. & EIJSINK, V. G. H. 2017.

Oxidative cleavage of polysaccharides by monocopper enzymes depends on H2O2. *Nature Chemical Biology,* 13**,** 1123-1128.

BISSARO, B., STREIT, B., ISAKSEN, I., EIJSINK, V. G. H., BECKHAM, G. T., DUBOIS, J. L. & RØHR, Å. K. 2020b. Molecular mechanism of the chitinolytic peroxygenase reaction. *Proceedings of the National Academy of Sciences,* 117**,** 1504-1513.

BORISOVA, A. S., ISAKSEN, T., DIMAROGONA, M., KOGNOLE, A. A., MATHIESEN, G., VARNAI, A., ROHR, A. K., PAYNE, C. M., SORLIE, M., SANDGREN, M. & EIJSINK, V. G. H. 2015. Structural and functional characterization of a lytic polysaccharide monooxygenase with broad substrate specificity. *Journal of Biological Chemistry,* 290**,** 22955-22969.

BRADFORD, M. M. 1976. A rapid and sensitive method for the quantitation of microgram quantities of protein utilizing the principle of protein-dye binding. *Analytical Biochemistry: Methods in the Biological Sciences,* 72**,** 248-254.

BRESLMAYR, E., HANZEK, M., HANRAHAN, A., LEITNER, C., KITTL, R., SANTEK, B., OOSTENBRINK, C. & LUDWIG, R. 2018. A fast and sensitive activity assay for lytic polysaccharide monooxygenase. *Biotechnology for Biofuels,* 11.

BRETTEL, K. & BYRDIN, M. 2010. Reaction mechanisms of DNA photolyase. *Current Opinion in Structural Biology,* 20**,** 693-701.

BUSZEWSKI, B. & NOGA, S. 2012. Hydrophilic interaction liquid chromatography (HILIC)-a powerful separation technique. *Analytical and Bioanalytical Chemistry,* 402**,** 231-247.

CANTAREL, B. L., COUTINHO, P. M., RANCUREL, C., BERNARD, T., LOMBARD, V. & HENRISSAT, B. 2009. The Carbohydrate-Active EnZymes database (CAZy): an expert resource for Glycogenomics. *Nucleic Acids Research,* 37**,** D233-D238.

CHEAH, W. Y., SANKARAN, R., PAU, L. S., IBRAHIM, T. N. B. T., CHEW, K. W., CULABA, A. & CHANG, J. S. 2020. Pretreatment methods for lignocellulosic biofuels production: current advances, challenges and future prospects. *Biofuel Research Journal,* 7**,** 1115-1127.

CHYLENSKI, P., BISSARO, B., SORLIE, M., ROHR, A. K., VARNAI, A., HORN, S. J. & EIJSINK, V. G. H. 2019. Lytic polysaccharide monooxygenases in enzymatic processing of lignocellulosic biomass. *ACS Catalysis,* 9**,** 4970-4991.

COURTADE, G., CIANO, L., PARADISI, A., LINDLEY, P. J., FORSBERG, Z., SORLIE, M., WIMMER, R., DAVIES, G. J., EIJSINK, V. G. H., WALTON, P. H. & AACHMANN, F. L. 2020. Mechanistic basis of substrate-O-2 coupling within a chitin-active lytic polysaccharide monooxygenase: An integrated NMR/EPR study. *Proceedings of the National Academy of Sciences of the United States of America,* 117**,** 19178-19189.

CREGG, J. M., BARRINGER, K. J., HESSLER, A. Y. & MADDEN, K. R. 1985. Pichia-pastoris as a host system for transformations. *Molecular and Cellular Biology,* 5**,** 3376-3385.

CYTIVA. 2020a. *HiTrap HIC selection kit* [Online]. cytiva.com. Available: https://cdn.cytivalifesciences.com/dmm3bwsv3/AssetStream.aspx?mediaformatid=10061&destinationid=10016&assetid=11530 [Accessed 11th of November 2021].

CYTIVA. 2020b. *Superdex prep grade and prepacked HiLoad columns* [Online]. cytiva.com. Available: https://cdn.cytivalifesciences.com/dmm3bwsv3/AssetStream.aspx?mediaformatid=10061&destinationid=10016&assetid=11217 [Accessed 11th of November 2021].

DEVI, J., DEB, U., BARMAN, S., DAS, S., SUNDAR BHATTACHARYA, S., FAI TSANG, Y., LEE, J.-H. & KIM, K.-H. 2020. Appraisal of lignocellusoic biomass degrading potential of three earthworm species using vermireactor mediated with

spent mushroom substrate: compost quality, crystallinity, and microbial community structural analysis. *Science of The Total Environment,* 716**,** 135-215.

DING, S. Y. & HIMMEL, M. E. 2006. The maize primary cell wall microfibril: a new model derived from direct visualization. *Journal of Agricultural and Food Chemistry,* 54**,** 597-606.

EIJSINK, V. G. H., PETROVIC, D., FORSBERG, Z., MEKASHA, S., ROHR, A. K., VARNAI, A., BISSARO, B. & VAAJE-KOLSTAD, G. 2019. On the functional characterization of lytic polysaccharide monooxygenases (LPMOs). *Biotechnology for Biofuels,* 12.

FERRARI, A. R., GABER, Y. & FRAAIJE, M. W. 2014. A fast, sensitive and easy colorimetric assay for chitinase and cellulase activity detection. *Biotechnology for Biofuels,* 7.

FORSBERG, Z., BISSARO, B., GULLESEN, J., DALHUS, B., VAAJE-KOLSTAD, G. & EIJSINK, V. G. H. 2018. Structural determinants of bacterial lytic polysaccharide monooxygenase functionality. *Journal of Biological Chemistry,* 293**,** 1397-1412.

FORSBERG, Z., MACKENZIE, A. K., SORLIE, M., ROHR, A. K., HELLAND, R., ARVAI, A. S., VAAJE-KOLSTAD, G. & EIJSINK, V. G. H. 2014. Structural and functional characterization of a conserved pair of bacterial cellulose-oxidizing lytic polysaccharide monooxygenases. *Proceedings of the National Academy of Sciences of the United States of America,* 111**,** 8446-8451.

FORSBERG, Z., SORLIE, M., PETROVIC, D., COURTADE, G., AACHMANN, F. L., VAAJE-KOLSTAD, G., BISSARO, B., ROHR, A. K. & EIJSINK, V. G. H. 2019. Polysaccharide degradation by lytic polysaccharide monooxygenases. *Current Opinion in Structural Biology,* 59**,** 54-64.

FRANDSEN, K. E. H., SIMMONS, T. J., DUPREE, P., POULSEN, J.-C. N., HEMSWORTH, G. R., CIANO, L., JOHNSTON, E. M., TOVBORG, M., JOHANSEN, K. S., VON FREIESLEBEN, P., MARMUSE, L., FORT, S., COTTAZ, S., DRIGUEZ, H., HENRISSAT, B., LENFANT, N., TUNA, F., BALDANSUREN, A., DAVIES, G. J., LO LEGGIO, L. & WALTON, P. H. 2016. The molecular basis of polysaccharide cleavage by lytic polysaccharide monooxygenases. *Nature Chemical Biology,* 12**,** 298-303.

FROMMHAGEN, M., KOETSIER, M. J., WESTPHAL, A. H., VISSER, J., HINZ, S. W. A., VINCKEN, J. P., VAN BERKEL, W. J. H., KABEL, M. A. & GRUPPEN, H. 2016. Lytic polysaccharide monooxygenases from Myceliophthora thermophila C1 differ in substrate preference and reducing agent specificity. *Biotechnology for Biofuels,* 9.

GARDNER, K. H. & BLACKWELL, J. 1974. Hydrogen-bonding in native cellulose. *Biochimica et Biophysica Acta,* 343**,** 232-237.

GARDNER, K. H. & BLACKWELL, J. 1975. Refinement of structure of beta-chitin. *Biopolymers,* 14**,** 1581-1595.

GEHEALTHCARE. 2007. *PD-10 desalting columns* [Online]. Uppsala, Sweeden: GE Healthcare. Available: http://wwwuser.gwdg.de/~jgrossh/protocols/protein-purification/PD10.pdf [Accessed 25th of October 2021].

GRAY, H. B. & WINKLER, J. R. 2015. Hole hopping through tyrosine/tryptophan chains protects proteins from oxidative damage. *Proceedings of the National Academy of Sciences of the United States of America,* 112**,** 10920-10925.

GUPTA, P. K., RAGHUNATH, S. S., PRASANNA, D. P., VENKAT, P., SHREE, V., CHITHANANTHAN, C., CHOUDHARY, S., SURENDER, K. & GEETHA, K. 2019. An update on overview of cellulose, its structure and applications. *Cellulose.*

HAMRE, A. G., STROMNES, A. G. S., GUSTAVSEN, D., VAAJE-KOLSTAD, G., EIJSINK, V. G. H. & SORLIE, M. 2019. Treatment of recalcitrant crystalline

polysaccharides with lytic polysaccharide monooxygenase relieves the need for glycoside hydrolase processivity. *Carbohydrate Research,* 473**,** 66-71.

HANGASKY, J. A., IAVARONE, A. T. & MARLETTA, M. A. 2018. Reactivity of O-2 versus H2O2 with polysaccharide monooxygenases. *Proceedings of the National Academy of Sciences of the United States of America,* 115**,** 4915-4920.

HARRIS, P. V., WELNER, D., MCFARLAND, K. C., RE, E., POULSEN, J. C. N., BROWN, K., SALBO, R., DING, H. S., VLASENKO, E., MERINO, S., XU, F., CHERRY, J., LARSEN, S. & LO LEGGIO, L. 2010. Stimulation of lignocellulosic biomass hydrolysis by proteins of glycoside hydrolase family 61: structure and function of a large, enigmatic family. *Biochemistry,* 49**,** 3305-3316.

HASHIMOTO, M., IKEGAMI, T., SEINO, S., OHUCHI, N., FUKADA, H., SUGIYAMA, J., SHIRAKAWA, M. & WATANABE, T. 2000. Expression and characterization of the chitin-binding domain of chitinase A1 from Bacillus circulans WL-12. *Journal of Bacteriology,* 182**,** 3045-3054.

HEDISON, T. M., BRESLMAYR, E., SHANMUGAM, M., KARNPAKDEE, K., HEYES, D. J., GREEN, A. P., LUDWIG, R., SCRUTTON, N. S. & KRACHER, D. 2021. Insights into the H2O2-driven catalytic mechanism of fungal lytic polysaccharide monooxygenases. *FEBS Journal,* 288**,** 4115-4128.

HEMSWORTH, G. R., DAVIES, G. J. & WALTON, P. H. 2013. Recent insights into copper-containing lytic polysaccharide mono-oxygenases. *Current Opinion in Structural Biology,* 23**,** 660-668.

HEMSWORTH, G. R., HENRISSAT, B., DAVIES, G. J. & WALTON, P. H. 2014. Discovery and characterization of a new family of lytic polysaccharide monooxygenases. *Nature Chemical Biology,* 10**,** 122-126.

HEUTS, D. P. H. M., JANSSEN, D. B. & FRAAIJE, M. W. 2007. Changing the substrate specificity of a chitooligosaccharide oxidase from Fusarium graminearum by model-inspired site-directed mutagenesis. *FEBS Letters,* 581**,** 4905-4909.

HEUTS, D. P. H. M., WINTER, R. T., DAMSMA, G. E., JANSSEN, D. B. & FRAAIJE, M. W. 2008. The role of double covalent flavin binding in chito-oligosaccharide oxidase from Fusarium graminearum. *Biochemical Journal,* 413**,** 175-183.

HORN, S. J., VAAJE-KOLSTAD, G., WESTERENG, B. & EIJSINK, V. 2012. Novel enzymes for the degradation of cellulose. *Biotechnology for Biofuels,* 5**,** 45.

IBANEZ, J. G., GONZALEZ, I. & CARDENAS, M. A. 1988. The effect of complex-formation upon the redox potentials of metallic-ions - cyclic voltammetry experiments. *Journal of Chemical Education,* 65**,** 173-175.

IGARASHI, K., UCHIHASHI, T., KOIVULA, A., WADA, M., KIMURA, S., OKAMOTO, T., PENTTILA, M., ANDO, T. & SAMEJIMA, M. 2011. Traffic Jams Reduce Hydrolytic Efficiency of Cellulase on Cellulose Surface. *Science,* 333**,** 1279-1282.

IGARASHI, K., WADA, M. & SAMEJIMA, M. 2007. Activation of crystalline cellulose to cellulose IIII results in efficient hydrolysis by cellobiohydrolase. *FEBS Journal,* 274**,** 1785-1792.

ISAKSEN, T., WESTERENG, B., AACHMANN, F. L., AGGER, J. W., KRACHER, D., KITTL, R., LUDWIG, R., HALTRICH, D., EIJSINK, V. G. H. & HORN, S. J. 2014. A C4-oxidizing lytic polysaccharide monooxygenase cleaving both cellulose and cello-oligosaccharides. *Journal of Biological Chemistry,* 289**,** 2632-2642.

JIANG, N., KUZNETSOV, A., NOCEK, J. M., HOFFMAN, B. M., CRANE, B. R., HU, X. Q. & BERATAN, D. N. 2013. Distance-independent charge recombination kinetics in cytochrome c-cytochrome c peroxidase complexes: compensating changes in the electronic coupling and reorganization energies. *Journal of Physical Chemistry B,* 117**,** 9129-9141.

JONES, S. M., TRANSUE, W. J., MEIER, K. K., KELEMEN, B. & SOLOMON, E. I. 2020. Kinetic analysis of amino acid radicals formed in H2O2-driven Cu-I LPMO reoxidation implicates dominant homolytic reactivity. *Proceedings of the National Academy of Sciences of the United States of America,* 117**,** 11916-11922.

JĘDRZEJCZYK, M., SOSZKA, E., CZAPNIK, M., RUPPERT, A. M. & GRAMS, J. 2019. Physical and chemical pretreatment of lignocellulosic biomass. *In:* BASILE, A. & DALENA, F. (eds.) *Second and Third Generation of Feedstocks.* Elsevier.

KAYA, M., MUJTABA, M., EHRLICH, H., SALABERRIA, A. M., BARAN, T., AMEMIYA, C. T., GALLI, R., AKYUZ, L., SARGIN, I. & LABIDI, J. 2017. On chemistry of gamma-chitin. *Carbohydrate Polymers,* 176**,** 177-186.

KITTL, R., KRACHER, D., BURGSTALLER, D., HALTRICH, D. & LUDWIG, R. 2012. Production of four Neurospora crassa lytic polysaccharide monooxygenases in Pichia pastoris monitored by a fluorimetric assay. *Biotechnology for Biofuels,* 5.

KJAERGAARD, C. H., QAYYUM, M. F., WONG, S. D., XU, F., HEMSWORTH, G. R., DAVIES, G. J., WALTON, P. H., JOHANSEN, K. S., HODGSON, K. O., HEDMAN, B. & SOLOMON, E. I. 2014. Spectroscopic and computational insight into the activation of O-2 by the mononuclear Cu center in Polysaccharide monooxygenases. *Abstracts of Papers of the American Chemical Society,* 248.

KRACHER, D., ANDLAR, M., FURTMULLER, P. G. & LUDWIG, R. 2018. Active-site copper reduction promotes substrate binding of fungal lytic polysaccharide monooxygenase and reduces stability. *Journal of Biological Chemistry,* 293**,** 1676-1687.

KRACHER, D., SCHEIBLBRANDNER, S., FELICE, A. K. G., BRESLMAYR, E., PREIMS, M., LUDWICKA, K., HALTRICH, D., EIJSINK, V. G. H. & LUDWIG, R. 2016a. Extracellular electron transfer systems fuel cellulose oxidative degradation. *Science,* 352**,** 1098-1101.

KRACHER, D., SCHEIBLBRANDNER, S., FELICE ALFONS, K. G., BRESLMAYR, E., PREIMS, M., LUDWICKA, K., HALTRICH, D., EIJSINK VINCENT, G. H. & LUDWIG, R. 2016b. Extracellular electron transfer systems fuel cellulose oxidative degradation. *Science,* 352**,** 1098-1101.

KUMAR, A. K. & SHARMA, S. 2017. Recent updates on different methods of pretreatment of lignocellulosic feedstocks: a review. *Bioresources and Bioprocessing,* 4.

KURITA, K., TOMITA, K., ISHII, S., NISHIMURA, S.-I. & SHIMODA, K. 1993. β-chitin as a convenient starting material for acetolysis for efficient preparation of N-acetylchitooligosaccharides. *Journal of Polymer Science,* 31**,** 2393-2395.

KUUSK, S., BISSARO, B., KUUSK, P., FORSBERG, Z., EIJSINK, V. G. H., SORLIE, M. & VALJAMAE, P. 2018. Kinetics of H2O2-driven degradation of chitin by a bacterial lytic polysaccharide monooxygenase. (vol 293, pg 523, 2018). *Journal of Biological Chemistry,* 293**,** 12284-12284.

KUUSK, S., KONT, R., KUUSK, P., HEERING, A., SORLIE, M., BISSARO, B., EIJSINK, V. G. H. & VALJAMAE, P. 2019. Kinetic insights into the role of the reductant in H2O2-driven degradation of chitin by a bacterial lytic polysaccharide monooxygenase. *Journal of Biological Chemistry,* 294**,** 1516-1528.

LEE, Y. C. 1990. High-performance anion-exchange chromatography for carbohydrate analysis. *Analytical Biochemistry,* 189**,** 151-162.

LEVASSEUR, A., DRULA, E., LOMBARD, V., COUTINHO, P. M. & HENRISSAT, B. 2013. Expansion of the enzymatic repertoire of the CAZy database to integrate auxiliary redox enzymes. *Biotechnology for Biofuels,* 6.

LI, X., BEESON, W. T., PHILLIPS, C. M., MARLETTA, M. A. & CATE, J. H. D. 2012. Structural basis for substrate targeting and catalysis by fungal polysaccharide monooxygenases. *Structure,* 20**,** 1051-1061.

LIMAYEM, A. & RICKE, S. C. 2012. Lignocellulosic biomass for bioethanol production: current perspectives, potential issues and future prospects. *Progress in Energy and Combustion Science,* 38**,** 449-467.

LIU, B., KOGNOLE, A. A., WU, M., WESTERENG, B., CROWLEY, M. F., KIM, S., DIMAROGONA, M., PAYNE, C. M. & SANDGREN, M. 2018. Structural and molecular dynamics studies of a C1-oxidizing lytic polysaccharide monooxygenase from Heterobasidion irregulare reveal amino acids important for substrate recognition. *FEBS Journal,* 285**,** 2225-2242.

LIU, Y. N., SEEFELDT, L. C. & PARKER, V. D. 1997. Entropies of redox reactions between proteins and mediators: the temperature dependence of reversible electrode potentials in aqueous buffers. *Analytical Biochemistry,* 250**,** 196-202.

LODI, G., STORTI, G., PELLEGRINI, L. A. & MORBIDELLI, M. 2017. Ion Exclusion Chromatography: Model Development and Experimental Evaluation. *Industrial & Engineering Chemistry Research,* 56**,** 1621-1632.

LOOSE, J. S. M., ARNTZEN, M. Ø., BISSARO, B., LUDWIG, R., EIJSINK, V. G. H. & VAAJE-KOLSTAD, G. 2018. Multipoint precision binding of substrate protects lytic polysaccharide monooxygenases from self-destructive off-pathway processes. *Biochemistry,* 57**,** 4114-4124.

LOOSE, J. S. M., FORSBERG, Z., FRAAIJE, M. W., EIJSINK, V. G. H. & VAAJE-KOLSTAD, G. 2014. A rapid quantitative activity assay shows that the Vibrio cholerae colonization factor GbpA is an active lytic polysaccharide monooxygenase. *FEBS Letters,* 588**,** 3435-3440.

LU, Y. & MARSHALL, N. M. 2013. Redox potential. *In:* ROBERTS, G. C. K. (ed.) *Encyclopedia of Biophysics.* Berlin, Heidelberg: Springer Berlin Heidelberg.

MAURYA, D. P., SINGLA, A. & NEGI, S. 2015. An overview of key pretreatment processes for biological conversion of lignocellulosic biomass to bioethanol. *3 Biotech,* 5**,** 597-609.

MEIER, K. K., JONES, S. M., KAPER, T., HANSSON, H., KOETSIER, M. J., KARKEHABADI, S., SOLOMON, E. I., SANDGREN, M. & KELEMEN, B. 2018. Oxygen Activation by Cu LPMOs in Recalcitrant Carbohydrate Polysaccharide Conversion to Monomer Sugars. *Chemical Reviews,* 118**,** 2593-2635.

MENON, V. & RAO, M. 2012. Trends in bioconversion of lignocellulose: biofuels, platform chemicals & biorefinery concept. *Progress in Energy and Combustion Science,* 38**,** 522-550.

MERINO, S. T. & CHERRY, J. 2007. *Progress and challenges in enzyme development for Biomass utilization,* Berlin, Springer-Verlag Berlin.

MILAZZO, G., CAROLI, S. & SHARMA, V. K. 1978. Tables of standard electrode potentials. New York: Wiley.

MILLER, J. M. 2005. *Chromatography: concepts & contrasts,* New Jersey, John Wiley & Sons.

MILLIPORE. 2018. *Amicon ultra-15 centrifugal filter devices for volumes up to 15 mL* [Online]. Darmstadt, Germany: Merck KGaA. Available: https://images-na.ssl-images-amazon.com/images/I/71A8g+u8BrL.pdf [Accessed 17th of February 2021].

MINKE, R. & BLACKWELL, J. 1978. Structure of alpha-chitin. *Journal of Molecular Biology,* 120**,** 167-181.

MINNIHAN, E. C., NOCERA, D. G. & STUBBE, J. 2013. Reversible, long-range radical transfer in E. coli class la ribonucleotide reductase. *Accounts of Chemical Research,* 46**,** 2524-2535.

MOLLATT, M. & SKAALI, R. 2021. Isolation and initial characterization of fungal LPMOs [Unpublished work]. Ås: NMBU.

MU, D., SEAGER, T., RAO, P. S. & ZHAO, F. 2010. Comparative life cycle assessment of lignocellulosic ethanol production: biochemical versus thermochemical conversion. *Environmental Management,* 46**,** 565-578.

NARESH KUMAR, M., RAVIKUMAR, R., THENMOZHI, S., RANJITH KUMAR, M. & KIRUPA SHANKAR, M. 2019. Choice of pretreatment technology for sustainable production of bioethanol from lignocellulosic biomass: bottle necks and recommendations. *Waste and Biomass Valorization,* 10**,** 1693-1709.

O'SULLIVAN, A. C. 1997. Cellulose: the structure slowly unravels. *Cellulose,* 4.

OMEGABIO-TEK. 2019. *E.Z.N.A.® plasmid DNA mini kit I* [Online]. Norcross, USA. Available: http://2015.igem.org/wiki/images/1/18/NUDT_CHIAN-Protoco1.pdf [Accessed 11th of January 2022].

PHILLIPS, C. M., BEESON, W. T., CATE, J. H. & MARLETTA, M. A. 2011. Cellobiose Dehydrogenase and a Copper-Dependent Polysaccharide Monooxygenase Potentiate Cellulose Degradation by Neurospora crassa. *Acs Chemical Biology,* 6**,** 1399-1406.

POMA, A. B., CHWASTYK, M. & CIEPLAK, M. 2016. Coarse-grained model of the native cellulose Iα and the transformation pathways to the Iβ allomorph. *Cellulose,* 23**,** 1573-1591.

PRASAD, A., SOTENKO, M., BLENKINSOPP, T. & COLES, S. R. 2016. Life cycle assessment of lignocellulosic biomass pretreatment methods in biofuel production. *International Journal of Life Cycle Assessment,* 21**,** 44-50.

PRASHANTH, K. V. H. & THARANATHAN, R. N. 2007. Chitin/chitosan: modifications and their unlimited application potential - an overview. *Trends in Food Science & Technology,* 18**,** 117-131.

QUINLAN, R. J., SWEENEY, M. D., LO LEGGIO, L., OTTEN, H., POULSEN, J.-C. N., JOHANSEN, K. S., KROGH, K. B. R. M., JØRGENSEN, C. I., TOVBORG, M., ANTHONSEN, A., TRYFONA, T., WALTER, C. P., DUPREE, P., XU, F., DAVIES, G. J. & WALTON, P. H. 2011. Insights into the oxidative degradation of cellulose by a copper metalloenzyme that exploits biomass components. *Proceedings of the National Academy of Sciences of the United States of America,* 108**,** 15079-15084.

RAPIER, R. 2020. *Fossil fuels still supply 84 percent of world energy — and other eye ppeners from BP's annual review* [Online]. Forbes.com. Available: https://www.forbes.com/sites/rrapier/2020/06/20/bp-review-new-highs-in-global-energy-consumption-and-carbon-emissions-in-2019/ [Accessed 18th of April 2022].

REILLY, P. J. 2007. *Chapter 5 - Amylase and Cellulase Structure and Function,* Ansterdan, Elsevier.

REYNOLDS, J. A. & TANFORD, C. 1970. Gross conformation of protein-sodium dodecyl sulfate complexes. *Journal of Biological Chemistry,* 245**,** 5161-5165.

RIEDER, L., EBNER, K., GLIEDER, A. & SORLIE, M. 2021a. Novel molecular biological tools for the efficient expression of fungal lytic polysaccharide monooxygenases in Pichia pastoris. *Biotechnology for Biofuels,* 14.

RIEDER, L., PETROVIC, D., VALJAMAE, P., EIJSINK, V. G. H. & SORLIE, M. 2021b. Kinetic characterization of a putatively chitin-active LPMO reveals a preference for soluble substrates and absence of monooxygenase activity. *ACS Catalysis,* 11**,** 11685-11695.

RIEDER, L., STEPNOV, A. A., SØRLIE, M. & EIJSINK, V. G. H. 2021c. Fast and specific peroxygenase reactions catalyzed by fungal mono-copper enzymes. *Biochemistry,* 60**,** 3633-3643.

RINAUDO, M. 2006. Chitin and chitosan: properties and applications. *Progress in Polymer Science,* 31**,** 603-632.

RITCHIE, H. & ROSER, M. 2017. *Air pollution* [Online]. Or World in Data. Available: https://ourworldindata.org/air-pollution [Accessed 18th of April 2022].

ROHRER, J. S., BASUMALLICK, L. & HURUM, D. 2013. High-performance anion-exchange chromatography with pulsed amperometric detection for carbohydrate analysis of glycoproteins. *Biochemistry (Moscow),* 78**,** 697-709.

ROONI, V., RAUD, M. & KIKAS, T. 2017. The freezing pre-treatment of lignocellulosic material: a cheap alternative for Nordic countries. *Energy,* 139**,** 1-7.

SCIENTIFIC, T. F. 2015. *One Shot™ TOP10 chemically competent E. coli* [Online]. Available: https://www.thermofisher.com/document-connect/document-connect.html?url=https%3A%2F%2Fassets.thermofisher.com%2FTFS-Assets%2FLSG%2Fmanuals%2Foneshottop10_chemcomp_man.pdf [Accessed 27th of January 2022].

SHARMA, H. K., XU, C. B. & QIN, W. S. 2019. Biological pretreatment of lignocellulosic biomass for biofuels and bioproducts: an overview. *Waste and Biomass Valorization,* 10**,** 235-251.

SORLIE, M., SEEFELDT, L. C. & PARKER, V. D. 2000. Use of stopped-flow spectrophotometry to establish midpoint potentials for redox proteins. *Analytical Biochemistry,* 287**,** 118-125.

STEPNOV, A. A., FORSBERG, Z., SORLIE, M., NGUYEN, G. S., WENTZEL, A., ROHR, A. K. & EIJSINK, V. G. H. 2021. Unraveling the roles of the reductant and free copper ions in LPMO kinetics. *Biotechnology for Biofuels,* 14.

SWITALA, J. & LOEWEN, P. C. 2002. Diversity of properties among catalases. *Archives of Biochemistry and Biophysics,* 401**,** 145-154.

TEERI, T. T. 1997. Crystalline cellulose degradation: New insight into the function of cellobiohydrolases. *Trends in Biotechnology,* 15**,** 160-167.

TRINCONE, A. 2018. Update on marine carbohydrate hydrolyzing enzymes: biotechnological applications. *Molecules,* 23.

VANDERHART, D. L. & ATALLA, R. H. 1984. Studies of microstructure in native celluloses using solid-state C-13 NMR. *Macromolecules,* 17**,** 1465-1472.

VARELAS, V. & LANGTON, M. 2017. Forest biomass waste as a potential innovative source for rearing edible insects for food and feed – a review. *Innovative Food Science & Emerging Technologies,* 41**,** 193-205.

VAAJE-KOLSTAD, G., FORSBERG, Z., LOOSE, J. S. M., BISSARO, B. & EIJSINK, V. G. H. 2017. Structural diversity of lytic polysaccharide monooxygenases. *Current Opinion in Structural Biology,* 44**,** 67-76.

VAAJE-KOLSTAD, G., HORN, S. J., VAN AALTEN, D. M. F., SYNSTAD, B. & EIJSINK, V. G. H. 2005a. The non-catalytic chitin-binding protein CBP21 from Serratia marcescens is essential for chitin degradation. *Journal of Biological Chemistry,* 280**,** 28492-28497.

VAAJE-KOLSTAD, G., HOUSTON, D. R., RIEMEN, A. H. K., EIJSINK, V. G. H. & VAN AALTEN, D. M. F. 2005b. Crystal structure and binding properties of the Serratia marcescens chitin-binding protein CBP21. *Journal of Biological Chemistry,* 280**,** 11313-11319.

VAAJE-KOLSTAD, G., WESTERENG, B., HORN, S. J., LIU, Z., ZHAI, H., SORLIE, M. & EIJSINK, V. G. 2010. An oxidative enzyme boosting the enzymatic conversion of recalcitrant polysaccharides. *Science,* 330**,** 219-22.

WADA, M., CHANZY, H., NISHIYAMA, Y. & LANGAN, P. 2004. Cellulose IIII crystal structure and hydrogen bonding by synchrotron X-ray and neutron fiber diffraction. *Macromolecules,* 37**,** 8548-8555.

WALTON, P. H. & DAVIES, G. J. 2016. On the catalytic mechanisms of lytic polysaccharide monooxygenases. *Current Opinion in Chemical Biology,* 31**,** 195-207.

WANG, B., WANG, Z., DAVIES, G. J., WALTON, P. H. & ROVIRA, C. 2020. Activation of O2 and H2O2 by Lytic Polysaccharide Monooxygenases. *ACS Catalysis,* 10**,** 12760-12769.

WANG, B. J., JOHNSTON, E. M., LI, P. F., SHAIK, S., DAVIES, G. J., WALTON, P. H. & ROVIRA, C. 2018. QM/MM studies into the H2O2-dependent activity of lytic polysaccharide monooxygenases: evidence for the formation of a caged hydroxyl radical intermediate. *ACS Catalysis,* 8**,** 1346-1351.

WATERS. 2009. *Acquity UPLC BEH amide columns* [Online]. Available: https://www.waters.com/webassets/cms/library/docs/720003122en.pdf [Accessed 11th of November 2021].

WOLFENDEN, R., LU, X. D. & YOUNG, G. 1998. Spontaneous hydrolysis of glycosides. *Journal of the American Chemical Society,* 120**,** 6814-6815.

WU, M., BECKHAM, G. T., LARSSON, A. M., ISHIDA, T., KIM, S., PAYNE, C. M., HIMMEL, M. E., CROWLEY, M. F., HORN, S. J., WESTERENG, B., IGARASHI, K., SAMEJIMA, M., STAHLBERG, J., EIJSINK, V. G. H. & SANDGREN, M. 2013. Crystal structure and computational characterization of the lytic polysaccharide monooxygenase GH61D from the basidiomycota fungus Phanerochaete chrysosporium. *Journal of Biological Chemistry,* 288**,** 12828-12839.

WYMAN, C. E., DALE, B. E., ELANDER, R. T., HOLTZAPPLE, M., LADISCH, M. R. & LEE, Y. Y. 2005. Coordinated development of leading biomass pretreatment technologies. *Bioresource Technology,* 96**,** 1959-1966.

YU, M. A., EGAWA, T., SHINZAWA-ITOH, K., YOSHIKAWA, S., GUALLAR, V., YEH, S. R., ROUSSEAU, D. L. & GERFEN, G. J. 2012. Two tyrosyl radicals stabilize high oxidation states in cytochrome c oxidase for efficient energy conservation and proton translocation. *Journal of the American Chemical Society,* 134**,** 4753-4761.

ZANELLO, P. 2003. *Inorganic electrochemistry: theory, practice and application*, PSC Publishing.

ZHOU, S. G. & INGRAM, L. O. 2000. Synergistic hydrolysis of carboxymethyl cellulose and acid-swollen cellulose by two endoglucanases (CelZ and CelY) from Erwinia chrysanthemi. *Journal of Bacteriology,* 182**,** 5676-5682.

ZYMORESEARCH. 2021. *DNA clean & concentrator®-5* [Online]. Available: https://files.zymoresearch.com/protocols/_d4003t_d4003_d4004_d4013_d4014_dna_clean_concentrator_-5.pdf [Accessed 30th of November 2021].

AACHMANN, F. L., SORLIE, M., SKJAK-BRAEK, G., EIJSINK, V. G. H. & VAAJE-KOLSTAD, G. 2012. NMR structure of a lytic polysaccharide monooxygenase provides insight into copper binding, protein dynamics, and substrate interactions. *Proceedings of the National Academy of Sciences of the United States of America,* 109**,** 18779-18784.

8 APPENDICES

APPENDIX I CLONING OF FUNGAL LPMO GENES

Appendix I comprises of additional material related to cloning of fungal LPMO genes.

Table 8.1. Colony Screening Optimization. The table presents the absorbance in AU monitored by Bradford protein assay and OD_{600} for secreted *Af*AA11B WT and the gatekeeper mutants E160N and E160D by *P. pastoris* cell colonies. Each row represents one screened colony. By dividing monitored Bradford absorbance with OD_{600}, a ratio was estimated for each LPMO. The ratio was used to decide which colonies to screen in the expression test (highlighted in green). Colonies highlighted in red were disregarded due to contamination or no cell growth.

Absorbance of secreted *Af*AA11B by *P. pastoris* cell colonies (AU)								
WT			**E160N**			**E160D**		
Bradford	*OD_{600}*	*Ratio*	*Bradford*	*OD_{600}*	*Ratio*	*Bradford*	*OD_{600}*	*Ratio*
0.7903	0.9293	0.8504	0.8294	0.5747	1.4432	0.7860	0.5128	1.5328
0.7733	1.1610	0.6661	0.8484	0.5663	1.4981	0.7856	1.2128	0.6478
0.7889	0.9515	0.8291	0.9054	0.7577	1.1949	0.7442	0.6329	1.1759
0.7124	0.5165	1.3793	0.8492	0.5573	1.5238	0.7842	1.0716	0.7318
0.7573	0.7124	1.0630	0.8587	0.5254	1.6344	0.7495	0.9564	0.7837
0.7363	0.8384	0.8782	0.8825	0.0458	19.2686	0.7975	0.7375	1.0814
0.7967	1.1370	0.7007	0.7311	0.2456	2.9768	0.7646	0.4024	1.9001
0.7776	0.8868	0.8769	0.8243	0.0392	21.0281	0.7809	0.8412	0.9283
0.7827	0.3468	2.2569	0.8011	0.4964	1.6138	0.7558	0.8125	0.9302
0.6963	1.1952	0.5826	0.8467	0.5173	1.6368	0.7486	0.2722	2.7502
0.7905	1.0611	0.7450	0.8138	0.4365	1.8644	0.8188	0.7401	1.1063
0.7250	0.8873	0.8171	0.8828	0.4083	2.1621	0.7618	0.3672	2.0746
0.7988	1.0764	0.7421	0.7701	0.0428	17.9930	0.6000	0.4503	1.3324
0.7256	0.6336	1.1452	0.8647	1.1219	0.7707	0.5464	0.2238	2.4415
0.7595	0.5065	1.4995	0.8357	0.7950	1.0512	0.4706	0.5223	0.9011
0.6957	0.8147	0.8539	0.8177	0.5188	1.5761	0.6156	0.3649	1.6870
0.7185	0.8235	0.8725	0.8747	0.5625	1.5550	0.5799	0.5824	0.9957
0.7984	1.0075	0.7925	0.8618	0.5059	1.7035	0.5798	0.8796	0.6592
0.9413	0.8023	1.1733	0.7345	0.7467	0.9837	0.7748	0.8142	0.9516
0.8021	0.6776	1.1837	0.7859	0.5737	1.3699	0.7081	0.5346	1.3245
0.6533	0.6139	1.0642	0.8175	0.5491	1.4888	0.6634	0.3203	2.0712
0.7636	0.6207	1.2302	0.8217	0.5983	1.3734	0.6637	0.3414	1.9441
0.9030	1.1488	0.7860	0.8277	0.4605	1.7974	0.6503	0.6630	0.9808
1.0207	0.6817	1.4973	0.8272	0.6098	1.3565	0.7080	1,3084	0.5411
0.7941	0.943	0.8421	0.7970	0.5376	1.4825	0.6990	0.2664	2.6239
0.7640	0.3682	2.0750	0.8707	0.5532	1.5739	0.7861	0.4071	1.9310
0.7922	0.6558	1.2080	0.8994	0.6588	1.3652	0.8227	0.0426	19.3122

0.6472	0.5098	1.2695	0.9394	0.6583	1.4270	0.6559	0.4398	1.4914
0.7415	0.0465	15.9462	0.8365	0.4110	2.0353	0.7508	1.1430	0.4651
0.7090	0.6886	1.0296	0.9382	0.5393	1.7397	0.7655	0.8136	0.9409
0.7883	0.8389	0.9397	0.8011	0.4698	1.7052	0.7664	0.8117	0.9442
0.7693	0.3617	2.1269	0.8207	0.5567	1.4742	0.7739	0.5921	1.3070
0.7796	0.3753	2.0773	0.8435	0.6275	1.3442	0.7404	0.9643	0.7678
0.6849	0.3350	2.0445	0.8285	0.5321	1.5570	0.6600	0.6922	0.9535
0.7435	0.044	16.8977	0.8273	0.5854	1.4132	0.7669	0.5454	1.4061
0.7386	0.3967	1.8619	0.8160	0.5137	1.5885	0.7517	0.4831	1.5560
0.7931	0.7202	1.1012	0.7926	0.4105	1.9308	0.8575	0.7952	1.0783
0.7150	0.2419	2.9558	0.7951	0.7020	1.1326	0.8340	0.7396	1.1276
0.7396	1.1819	0.6258	0.8193	0.5728	1.4303	0.8236	0.7421	1.1098
0.6973	0.6703	1.0403	0.8454	0.8864	0.9537	0.6565	0.7585	0.8655
0.7844	1.0035	0.7817	0.8402	0.4893	1.7171	0.8589	0.4587	1.8725
0.7828	0.6377	1.2275	0.8646	1.0720	0.8065	0.8680	1.1566	0.7505
0.8307	0.3790	2.1918	0.7463	0.6542	1.1408	0.7488	0.7103	1.0542
0.8457	0.1955	4.3258	0.7710	0.4592	1.6790	0.6894	0.4199	1.6418
0.8014	1.0206	0.7852	0.7923	0.6133	1.2919	0.6387	0.6066	1.0529
0.7206	1.0688	0.6742	0.7825	0.7107	1.1010	0.6578	0.7994	0.8229
0.8245	1.1948	0.6901	0.7492	0.5834	1.2842	0.7657	0.7567	1.0119
0.8130	0.0446	18.2287	0.7585	0.6111	1.2412	0.7719	0.5802	1.3304
0.7918	0.8396	0.9431	0.8057	0.8790	0.9167	0.7285	0.5405	1.3478
0.7524	0.7954	0.9459	0.8008	0.7783	1.0289	0.7816	0.6798	1.1497
0.7581	1.1423	0.6637	0.8115	0.5771	1.4062	0.6895	0.7606	0.9065
0.7744	0.4082	1.8971	0.6661	0.7649	0.8708	0.7282	0.7391	0.9853
0.7922	1.2496	0.6340	0.8234	0.6218	1.3242	0.7770	0.7662	1.0141
0.8139	0.0416	19.5649	0.7879	0.4446	1.7722	0.8142	0.4146	1.9638
0.8212	0.7925	1.0362	0.9177	0.9124	1.0058	0.7954	0.831	0.9572
0.8069	0.2794	2.8880	0.8063	0.6239	1.2924	0.6943	0.3471	2.0003
0.7753	0.9879	0.7848	0.7973	0.4716	1.6906	0.7022	0.9838	0.7138
0.7011	0.7586	0.9242	0.7669	0.7861	0.9756	0.7727	0.7388	1.0459
0.7469	1.2659	0.5900	0.7679	1.0649	0.7211	0.7646	0.5648	1.3538
0.7534	0.5088	1.4807	0.8229	0.6794	1.2112	0.7888	1.0595	0.7445

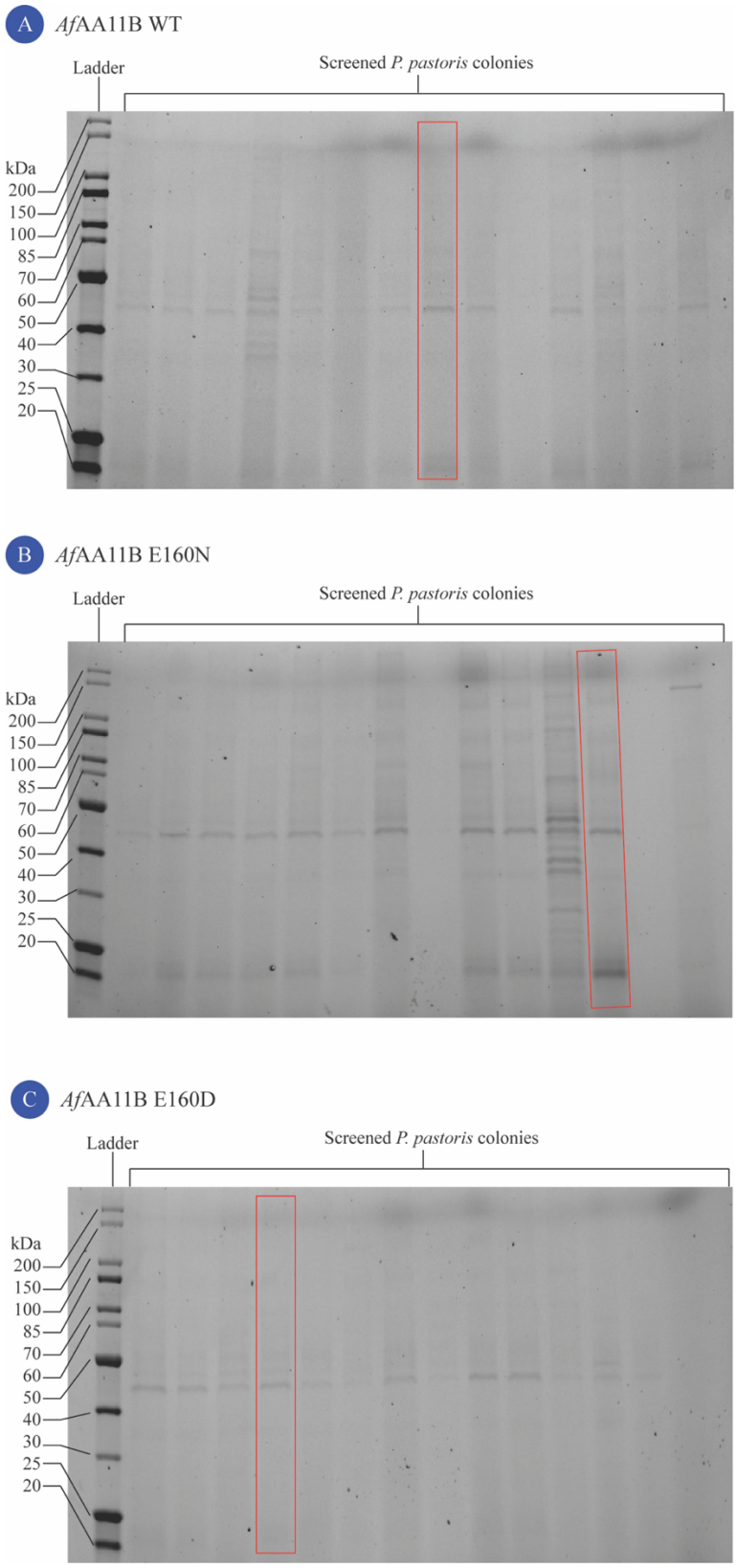

Figure 8.1: Expression test of AfAA11B WT and gatekeeper mutants E160N and E160D post colony screening optimization. *The screened P. pastoris colonies expression of (A) AfAA11B WT, (B) E160N, and (C) E160D. 14 P. pastoris cell colonies were included in the expression test and compared to the BioLabs Protein Ladder with protein markers shown in kDa. The P. pastoris cell colony with the highest protein expression is highlighted with a red square.*

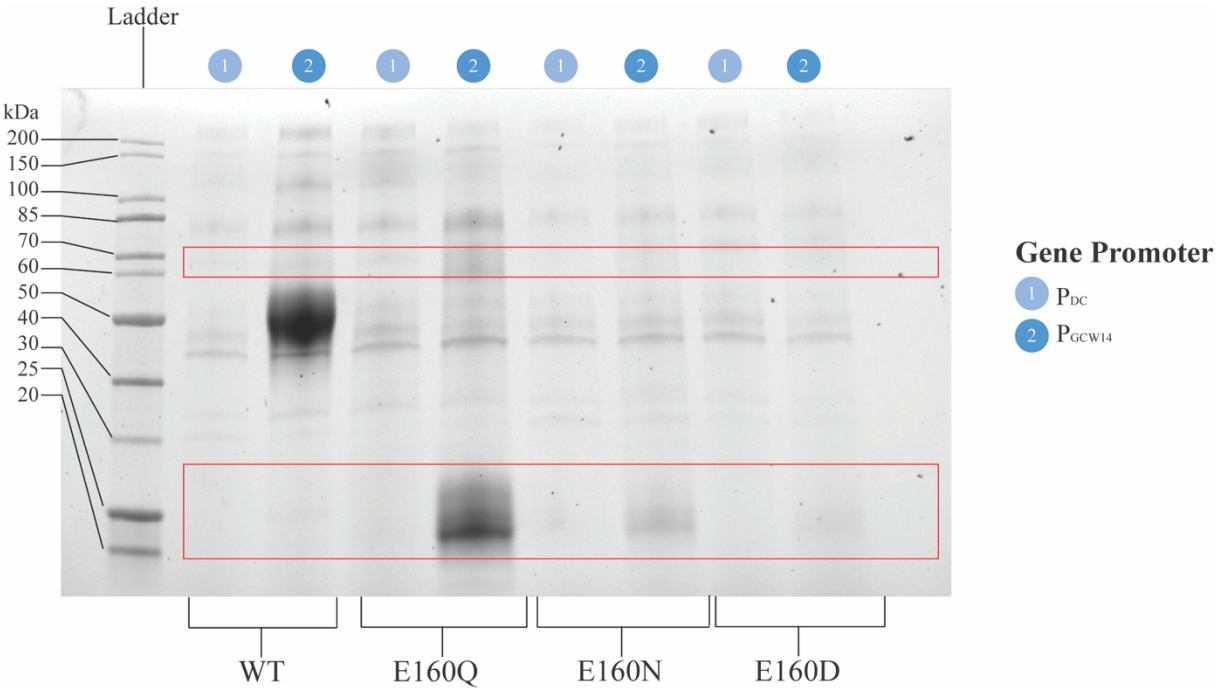

Figure 8.2: SDS-PAGE gel showing the AfAA11B expression by P. pastoris strains harboring expression plasmids with different promoters. *The different promoters were (1) P_{DC} and (2) P_{GCW14}. By performing this expression test, the hypothesis of whether the expression issues were strain-specific could be assessed. The upper and lower red boxes show where the bands for the AfAA11B catalytic domain and the X278 module should appear, respectively.*

APPENDIX II PURIFICATION OF FUNGAL ENZYMES

Appendix II presents additional material from the production and isolation of fungal enzymes during this experimental thesis work. Additional material includes chromatograms with corresponding SDS-PAGE gels generated during the purification of *Af*AA11B and *Nc*AA9C and yield development during the purification process.

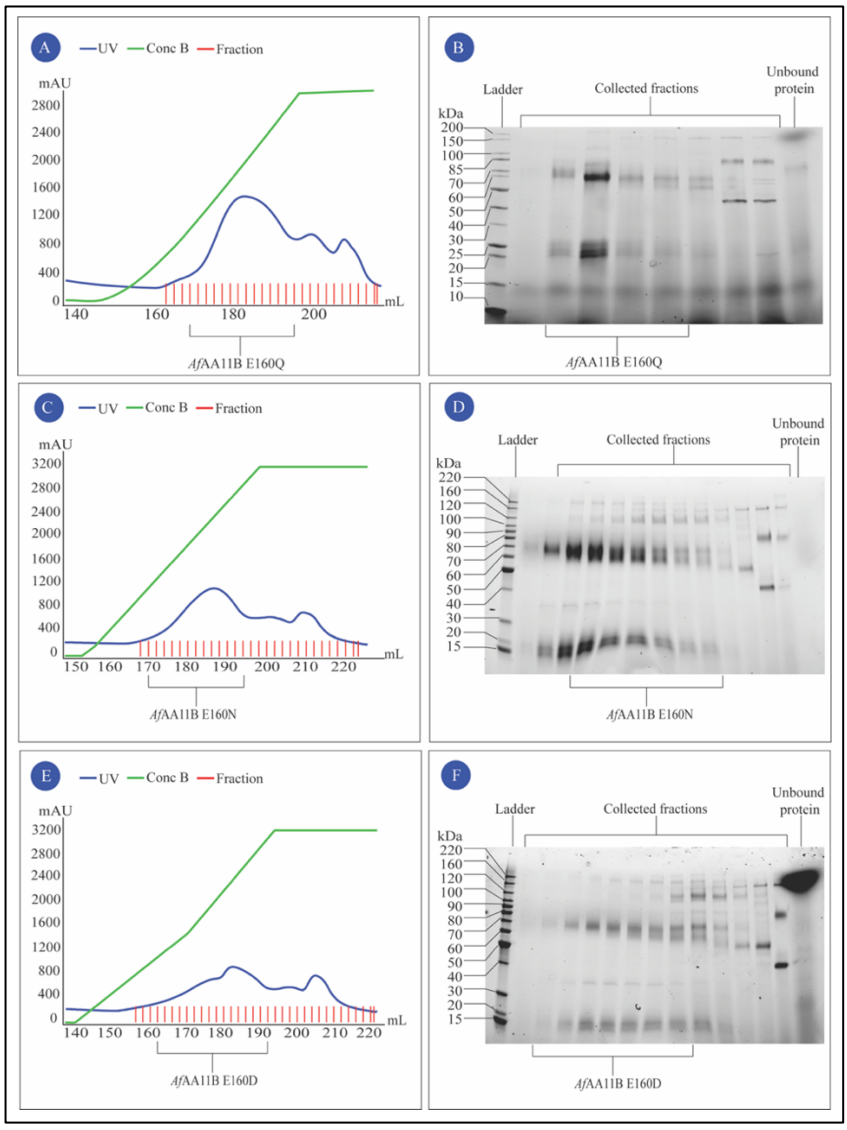

Figure 8.3: Representative chromatograms of AfAA11B gatekeeper mutants with corresponding SDS-PAGE gel generated in conjunction with HIC isolation. *The figure illustrates the hydrophobic interaction chromatograms with corresponding SDS-PAGE gel generated from the first isolation step during purification of the AfAA11B gatekeeper mutants (A/B) E160Q, (C/D) E160N, and (E/F) E160D. In these chromatograms, the UV absorption (mAU) is presented on the y-axis (blue curve) and the eluted mobile phase (mL) on the x-axis. Moreover, the applied salt gradient is presented as a green line. The red vertical lines show fractionation of the eluate, which was analyzed with SDS-PAGE. SDS-PAGE also analyzed protein that did not bound to the column. The identified proteins are highlighted with black bars. A protein ladder was used to reference the different protein markers in kDa, i.e., the BioLabs Protein Ladder for AfAA11B E160Q and the BenchMark Protein Ladder for AfAA11B E160N and E160D.*

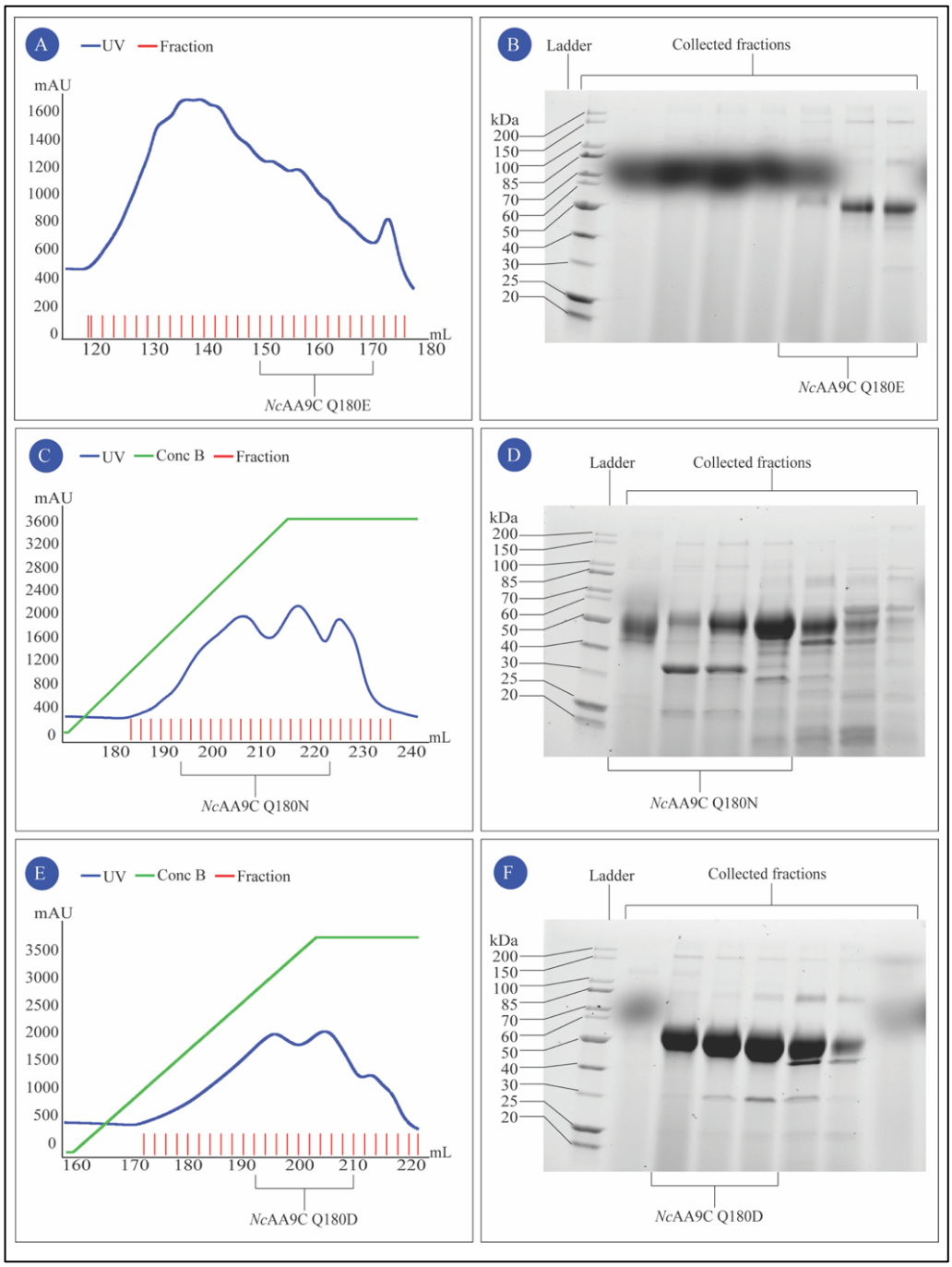

Figure 8.4: The first isolation step of purification of NcAA9C gatekeeper mutants. *The illustration presents the representative chromatograms generated from hydrophobic interaction chromatographic separation of NcAA9C Q180E (A), Q180N (C), and Q180D (E) with the UV absorbance in mAU on the y-axis and eluted mobile phase in mL on the x-axis. Protein elution occurred after the application of a salt gradient (green line) and was detected by UV absorption (blue line) and was collected as fractions (red vertical lines). A selection of the collected fractions was analyzed with SDS-PAGE, and an example of the obtained SDS-PAGE gel for NcAA9C Q180E (B), Q180N (D), and Q180D (F) are presented. A BioLabs protein ladder was used as a reference to identify the protein markers sizes in kDa. The protein of interest was highlighted with black bars.*

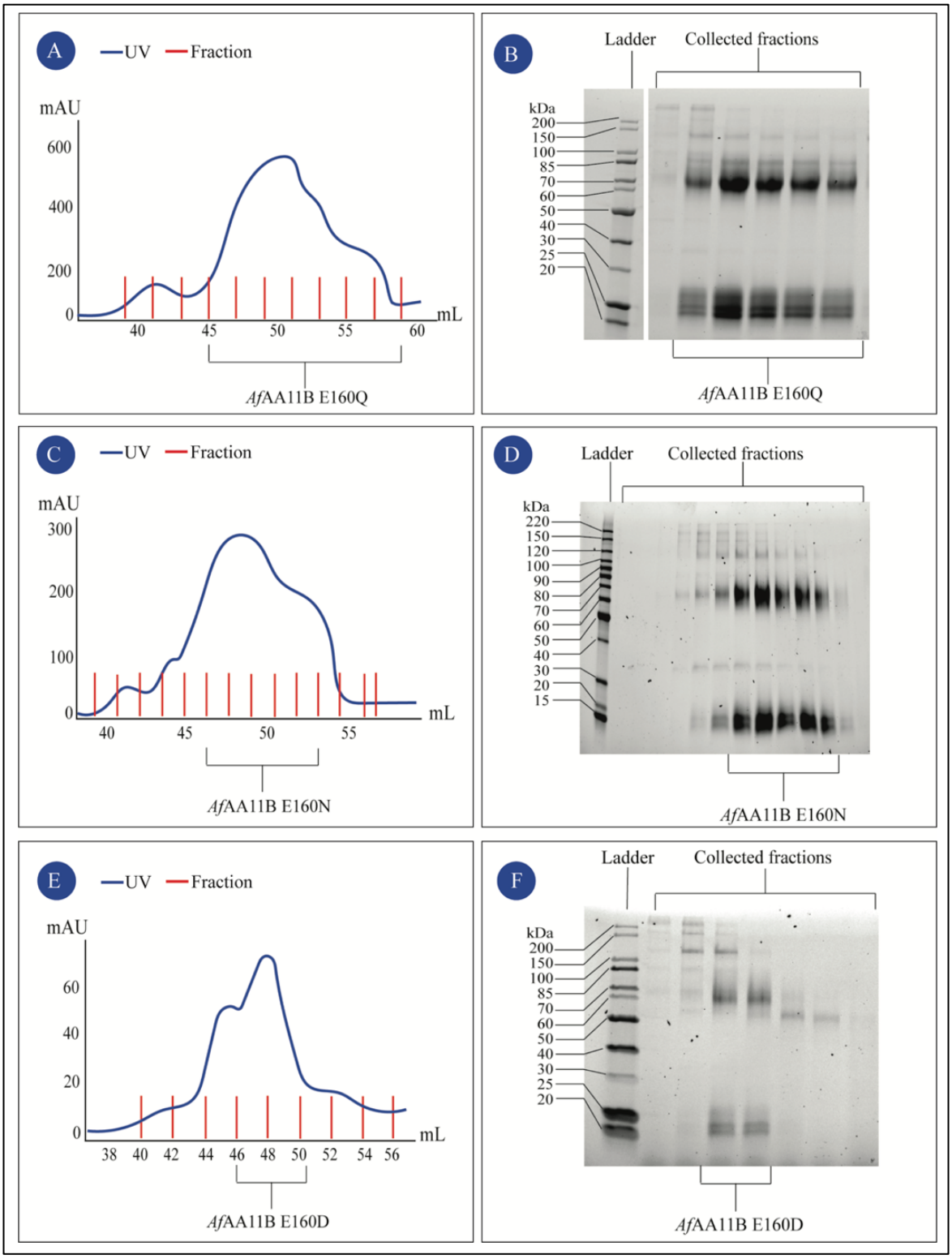

Figure 8.5: Size exclusion chromatograms with related SDS-PAGE gel presenting SEC isolation of AfAA11B gatekeeper mutants. *Representative size exclusion chromatograms are presented for AfAA11B E160Q (A), E160N (C), and E160D (E) with corresponding. SDS-PAGE gels in (B), (D), and (F), respectively. The y- and x-axis in the size exclusion chromatograms show the UV signal in mAU and consumed mobile phase in mL after sample injection, respectively. Change in UV absorption is presented as a blue line, and fractions collected are highlighted in red vertical lines. The BioLabs Protein Ladder was used to reference the protein markers in kDa in the SDS-PAGE analysis of AfAA11B E160Q and E160D, whereas the BioLabs Protein Ladder was in the SDS-PAGE analysis of E160N.*

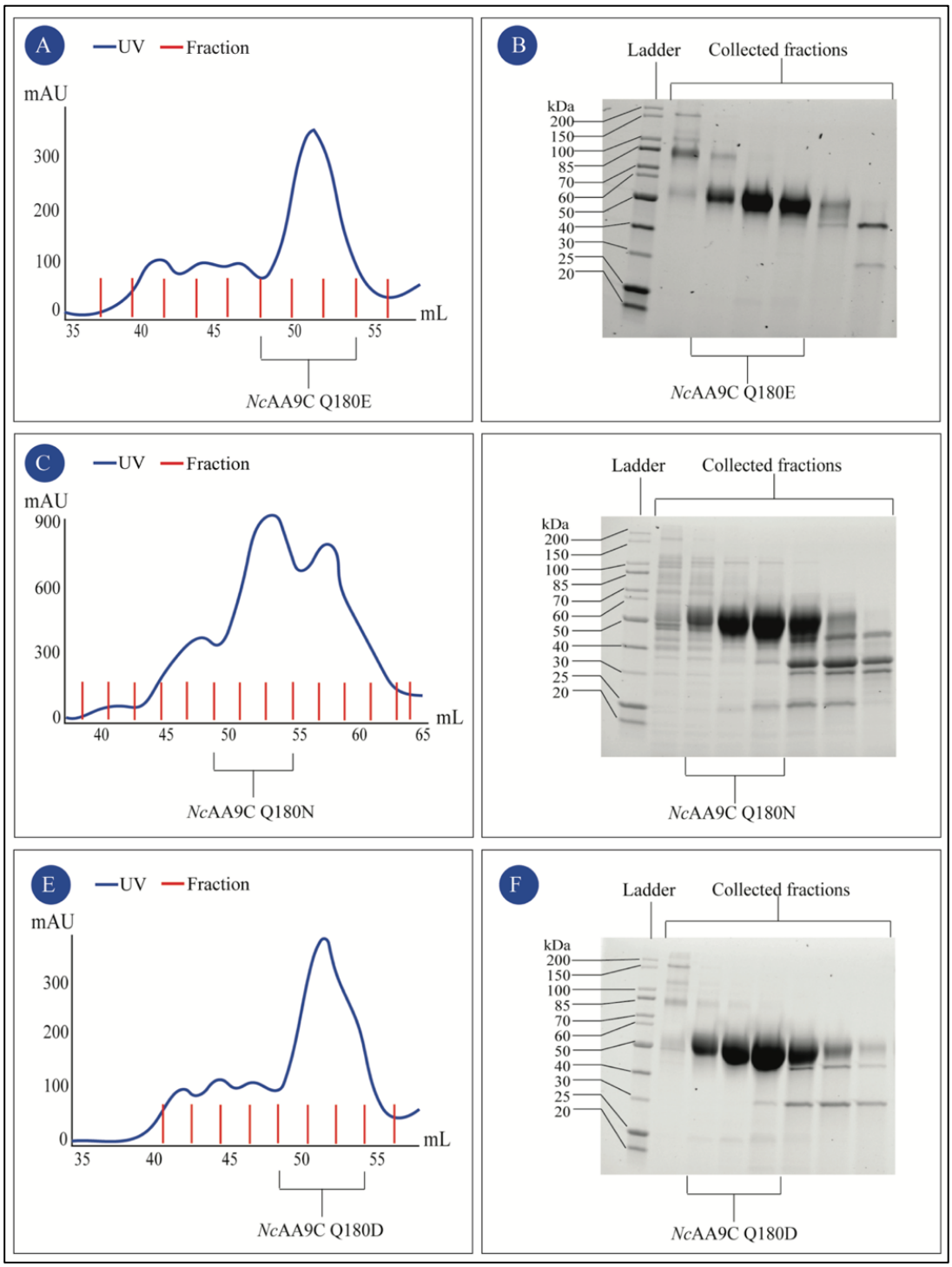

Figure 8.6: SEC isolated NcAA9C gatekeeper mutants. *Representative size exclusion chromatograms after the last isolation step of NcAA9C are presented for Q180E (A), Q180N (C), and Q180D (E), where the change in UV absorbance (blue line) is given on the y-axis in mAU and consumed mobile phase is given on the x-axis in mL. The increase in UV signal indicates protein elution, and this eluate was collected in fractions (red, vertical lines). SDS-PAGE was used to analyze the collected fractions during size exclusion isolation of NcAA9C Q180E (B), Q180N (D), and Q180D (F). The protein markers were identified in kDa by the reference ladder BioLabs Protein Ladder. The black bars indicate the presence of the protein of interest.*

Table 8.2. Estimated *Af*AA11B yield after each isolation step per 500 mL cultivated media. The table presents the descriptive properties concentration in µM and mg/mL, yield in mg, and final approximate protein volume in µL after hydrophobic interaction chromatographic separation, size exclusion chromatographic separation, and final copper saturation of *Af*AA11B WT and gatekeeper mutants. Estimated results are based on absorbance measurements using NanoDrop One. The manufacturer reports reproducibility of 2-5% on protein samples. Asymmetry in the data acquired reporting the values as median and quartiles (median (Q1, Q3)). *Af*AA11B WT and the gatekeeper mutants E160Q, E160N, and E160D yield estimations were based on 4, 2, 1, and 3 biological replicates, respectively. The single E160N replicate is reported as point estimate in yield estimation. The *Af*AA11B WT and gatekeeper mutants E160Q, E160N, and E160D biological replicates used in protein yield estimation were based on 4, 1, 0.5, and 3.5 L cultivated media.

ISOLATION PROCESS	DESCRIPTIVE PROPERTY	*Af*AA11B [Median (Q1, Q3)]			
		WT	E160Q	E160N	E160D
HIC	Concentration (µM)	1574 (730, 2569)	3169 (2594, 3744)	1336	979 (675, 2409)
	Concentration (mg/mL)	67 (31, 110)	136 (111, 160)	57	42 (29, 103)
	Yield (mg)	47 (32, 80)	126 (106, 146)	52	50 (30, 75)
	Volume (µL)	275 (125, 525)	950 (925, 975)	1500	600 (600, 900)
SEC	Concentration (µM)	36 (30, 64)	362 (214, 509)	57	28 (22, 42)
	Concentration (mg/mL)	2 (1, 3)	16 (9, 22)	2	1 (1, 83)
	Yield (mg)	3 (2, 6)	37 (35, 40)	14	1 (1, 2)
	Volume (µL)	1375 (750, 3600)	700 (650, 750)	4200	1000 (688, 2600)
FINAL	Concentration (µM)	82 (53, 122)	475 (317, 633)	68	24 (21, 42)
	Concentration (mg/mL)	3 (2, 5)	20 (14, 27)	3	1 (1, 2)
	Yield (mg)	1 (0, 2)	15 (9, 20)	3	0 (0, 1)
	Volume (µL)	275 (125, 525)	700 (650, 750)	1000	75 (63, 438)
TOTAL CULTIVATED MEDIA	Volume (mL)	3000	1000	500	3500

Table 8.3. Protein yield per 500 mL growth media estimated for *Nc*AA9C during purification. Concentration in µM and mg/mL, yield in mg, and final approximate protein volume in mL are included for each isolation step of *Nc*AA9C WT and the gatekeeper mutants. NanoDrop One was used for absorbance measurements used for protein yield estimations (2-5% reproducibility on protein samples reported by the manufacturer). The asymmetrical data were reported as median and quartiles (Q1, Q3). As absorbance measurements were performed on one biological replicate from 1 L cultivated media for *Nc*AA9C WT, and the gatekeeper mutants Q180E and Q180N, only the point estimate (median) is reported. Two biological replicates from 2 L cultivated media were used for *Nc*AA9C Q180D estimations.

ISOLATION PROCESS	DESCRIPTIVE PROPERTY	*Nc*AA9C [Median (Q1, Q3)]			
		WT	Q180E	Q180N	Q180D
HIC	Concentration (µM)	2934	1274	3359	2514 (1972, 3056)
	Concentration (mg/mL)	105	46	105	90 (70, 109)
	Yield (mg)	158	55	158	90 (71, 109)
	Volume (µL)	1500	1000	1000	1000 (1000, 1000)
SEC	Concentration (µM)	1484	126	679	689 (310, 1067)
	Concentration (mg/mL)	53	5	24	25 (11, 38)
	Yield (mg)	53	5	25	25 (11, 38)
	Volume (µL)	1000	1000	1000	1000 (1000, 1000)
FINAL	Concentration (µM)	383	158	608	358 (193, 523)
	Concentration (mg/mL)	14	6	22	13 (7, 19)
	Yield (mg)	10	0.7	5	3 (1, 5)
	Volume (µL)	750	125	250	188 (125, 250)
TOTAL CULTIVATED MEDIA	Volume (mL)	1000	1000	1000	2000

APPENDIX III REDOX MEASUREMENTS

Appendix III presents the statistical approach of the obtained redox results.

PROBABILITY MODELS

1) $Y_{ij} = \mu_i + \varepsilon_{ij}$, where $\varepsilon_{ij} \sim N(0, \sigma)$ for *Af*AA11B
2) $Y_{ij} = \mu_i + \varepsilon_{ij}$, where $\varepsilon_{ij} \sim N(0, \sigma)$ for *Nc*AA9C

We assume independent observations for mutation *i,* which are normally distributed with the expected redox potential μ_i and the mutual standard deviation σ for every observation in group *i*. Y_{ij} is the observed redox potential for LPMO replicate *j* representative for LPMO with gatekeeper residue exhibiting mutation *i.* The definition of i = 1, 2, 3, 4 is presented in Table 8.4 for Models 1 and 2.

Table 8.4. Definition of mutation *i*. *i* = 1, 2, 3, 4 is related to the gatekeeper variant of *Af*AA11B and *Nc*AA9C.

MUTATION *i*	GATEKEEPER RESIDUE	
	*Af*AA11B	*Nc*AA9C
1	E160D	Q180D
2	E160N	Q180E
3	E160Q	Q180N
4	WT	WT

LPMO replicates are *j* = 1, 2, 3. Observations *j* from each dataset is presented in Figure 8.7.

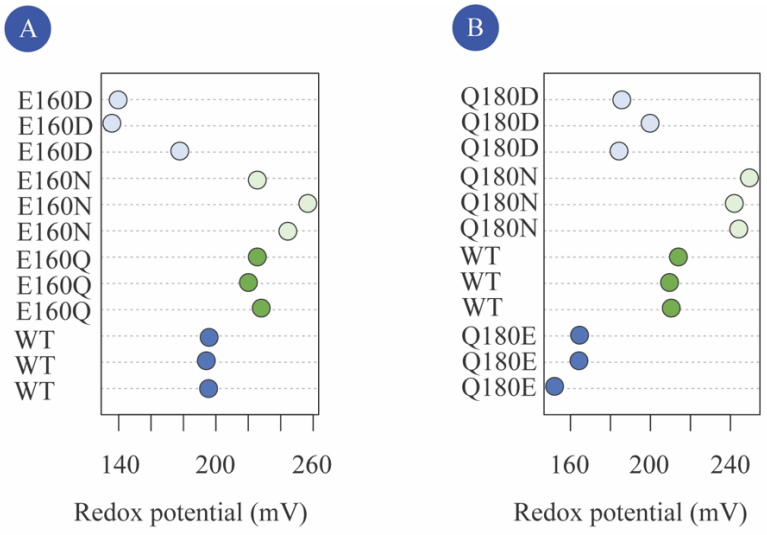

Figure 8.7: Redox potential in mV for AfAA11B and NcAA9C. *The figure illustrates the precision of (A) AfAA11B and (B) NcAA9C redox experiment. Three replicates represented each LPMO.*

MODEL ASSUMPTION EVALUATION

The model assumptions stated above were evaluated by residual plots, Q-Q plots, and box plots (Figure 8.8). The residuals were not distributed perfectly randomly around the expectation 0 in the residual plots, however, the assumption of constant variance was still accepted. This assumption was also supported by the box plots, which show relatively low in-group variation. Furthermore, even though the Q-Q plot comprises end tails, the normality assumption was considered sufficient. The boxplots are also supporting this because the median (thick, black line) is close to the average redox potential for most of the gatekeeper variants of *Af*AA11B and *Nc*AA9C. Hence, the symmetry of the models is acceptable and following, the normally distribution is valid. Finally, the assumption of independent observations was also validated, as three separate replicates were made for each LPMO variant. However, it was noted that the number of observations (n = 12) was low compared with the number of parameters (μ_1, μ_2, μ_3, μ_4, σ) for both models. A rule of thumb is to include at least 10 observations for each estimated parameter in the dataset (K. Frøslie, pers. com., 2020).

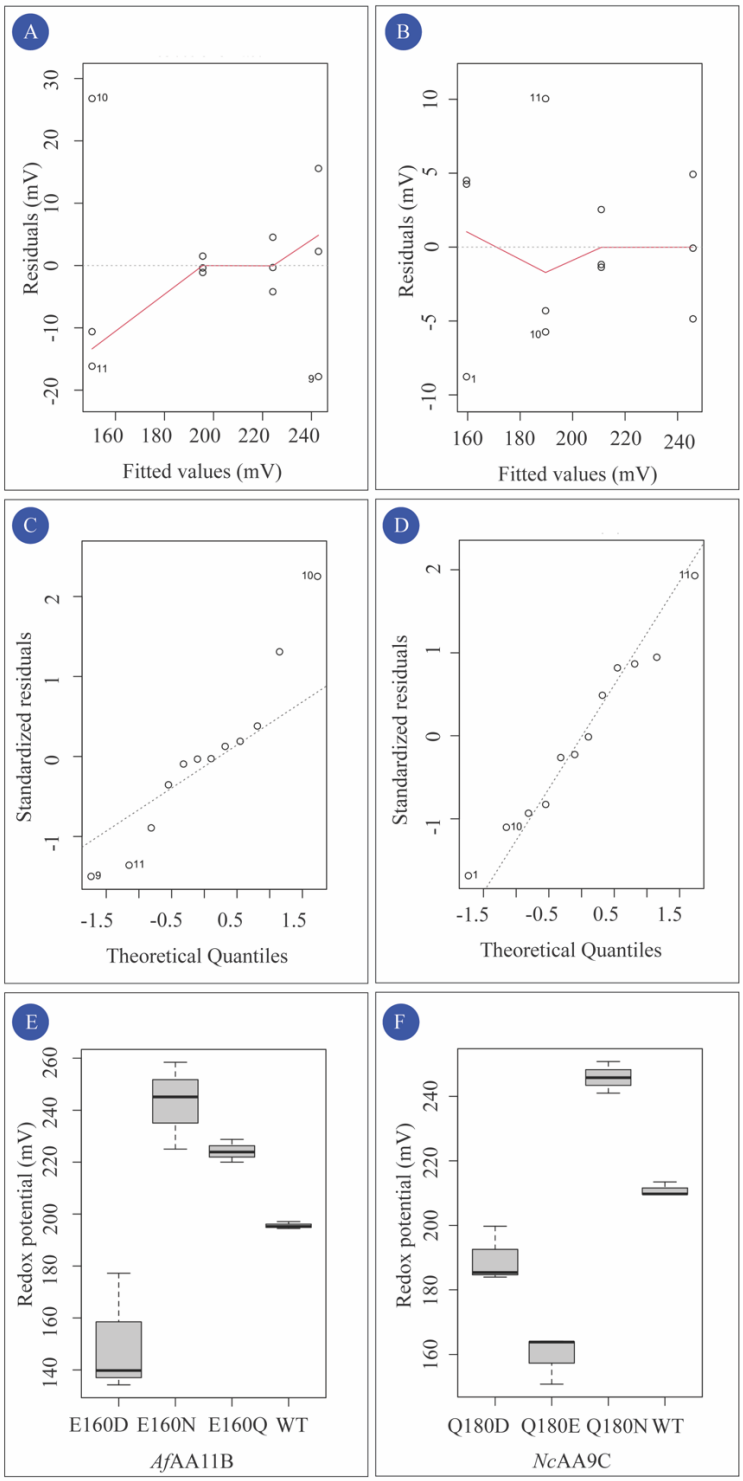

Figure 8.8: Evaluation of AfAA11B and NcAA9C redox model assumptions. *The model assumptions for the AfAA11B model by a residual plot to comment on the constant variance (A), a Q-Q plot to comment on the linearity (C), and a box plot to look for normality (E). The residual plot (B), Q-Q plot (D), and boxplot (F) are also presented for the NcAA9C model. The residual plot shows the expected residual value (mV) on the y-axis and the fitted redox potential on the x-axis (mV). Standardized residuals (y-axis) are compared with the theoretical quantiles (x-axis) in the Q-Q plot. In the box plot, the redox potential (mV) is presented on the y-axis, and the different gatekeeper variants are presented on the x-axis. The median value is highlighted with a thick, black line. Variation within mutation i is presented by the grey box (quartiles) with the maximum and minimum values represented by the dotted lines.*

ANALYSIS OF VARIANCE

The significance level α was set to 5% and was maintained throughout this thesis. To evaluate whether there was a significant difference in *Af*AA11B and *Nc*AA9C redox potential based on the gatekeeper residue mutation, following hypotheses were defined:

H_0: There is no group effect. $\mu_1 = \mu_2 = \mu_3 = \mu_4$
H_1: There is a group effect. At least one of the μ_i is different from μ_k

An Analysis of Variance (ANOVA) was performed. As the p-value for *Af*AA11B (0.0003) and *Nc*AA9C (1.23×10^{-6}) were lower than the stated significance level, the null hypothesis was rejected. There is a significant difference in redox potential between the gatekeeper variants of *Af*AA11B and *Nc*AA9C. The confidence in this conclusion was supported by the R^2 values of Model 1 and Model 2 at 0.98 and 0.99, respectively. The R^2 value expresses how much of the total variation is explained by mutation *i*.

CONTRAST ANALYSES

Contrast analyses were performed to evaluate whether there was a significant difference in redox potential between the *Af*AA11B and *Nc*AA9C variants with gatekeeper residues exhibiting carboxylic acid (Glu/Asp) or amide functional groups (Gln/Asn) in the side-chain, and if the lowest redox potentials were obtained by the carboxylic acid variants of the studied LPMOs. The defined contrasts are presented in Table 8.5. Furthermore, new hypotheses were stated:

H_0: There is no group effect. $\theta_1 = \theta_2 = 0$
H_1: The lowest redox potential is obtained for LPMOs with gatekeeper residues of carboxylic acid nature. $\theta_1 < 0$ and $\theta_2 < 0$.

Table 8.5. Contrast analyses related to the gatekeeper nature and redox potential. The contrasts θ_i are presented with its 95% CI and was calculated in R studio.

CONTRAST θ_i	GATEKEEPER VARIANT COMPARISON	95% CI FOR θi (mV)
$\theta_1 = 0.5(\mu_1 + \mu_4) + (-0.5)(\mu_2 + \mu_3)$	*Af*AA11B WT/E160D vs E160Q/E160N	[-79; -41]
$\theta_2 = 0.5(\mu_1 + \mu_2) + (-0.5)(\mu_3 + \mu_4)$	*Nc*AA9C Q180D/Q180E vs WT/Q180N	[-62; -45]

95% confidence intervals (CI) for θ_1 and θ_2 were used to draw conclusions. In a 95% CI of θ, we are 95% certain that the true value of θ is in this interval. As the 95% CI did not include 0 in the interval for *Af*AA11B ([-79, -41] mV) nor *Nc*AA9C ([-62, -45] mV), the null hypothesis was rejected. We may state that there is a significant effect on the redox potential based on the nature of the gatekeeper residue, and the redox potential of LPMOs with gatekeeper residues of carboxylic acid nature is the lowest.

Contrast analyses also examined the difference in redox potential for gatekeeper variants of the same nature. In this regard, it was interesting to investigate if the distance between the gatekeeper's functional group and the copper center generated a significant difference in redox potential for the studied LPMOs. Hence, new hypotheses were stated:

H_0: There is no group effect. $\theta_1 = \theta_2 = \theta_3 = \theta_4 = 0$

H_1: The redox potential is different for LPMOs with gatekeeper residues of same nature but with different side-chain length. $\theta_1 \neq 0$, $\theta_2 \neq 0$, $\theta_3 \neq 0$, and $\theta_4 \neq 0$.

Table 8.6. Contrast analyses related to the side-chain length of the gatekeeper residue and redox potential. The contrasts θ_i are presented with its 95% CI and was calculated in R studio.

CONTRAST θ_i	GATEKEEPER VARIANT COMPARISON	95 % CI FOR θi (mV)
$\theta_1 = 0.5(\mu_4) + (-0.5)(\mu_1)$	*Af*AA11B WT vs E160D	[9; 36]
$\theta_2 = 0.5(\mu_3) + (-0.5)(\mu_2)$	*Af*AA11B E160Q vs E160N	[-23; 4]
$\theta_3 = 0.5(\mu_2) + (-0.5)(\mu_1)$	*Nc*AA9C Q180E vs Q180D	[-21; -9]
$\theta_4 = 0.5(\mu_4) + (-0.5)(\mu_3)$	*Nc*AA9C WT vs Q180N	[-23; -11]

We can say with 95% certainty that the true value of θ is within the 95% CI of θ presented in Table 8.6. These confidence intervals tell us that the redox potential is significantly different for gatekeeper variants of the same nature but with different side-chain lengths. The 95% CIs for θ_1 and θ_3 were estimated to be [9; 36] mV and [-21; -9] mV for carboxylic acid gatekeeper variants of *Af*AA11B and *Nc*AA9C. Moreover, the 95% CI for θ_4 was estimated to be [-23; -11] mV for the amide gatekeeper variants of *Nc*AA9C. The exception was the difference in redox potential for the amide gatekeeper variants of *Af*AA11B, where the 95% CI ([-23; 4] mV) included the value 0 and for this reason, the null hypothesis was sustained for θ_2.

APPENDIX IV OXIDASE ACTIVITY

PART I: H_2O_2 CALIBRATION CURVES

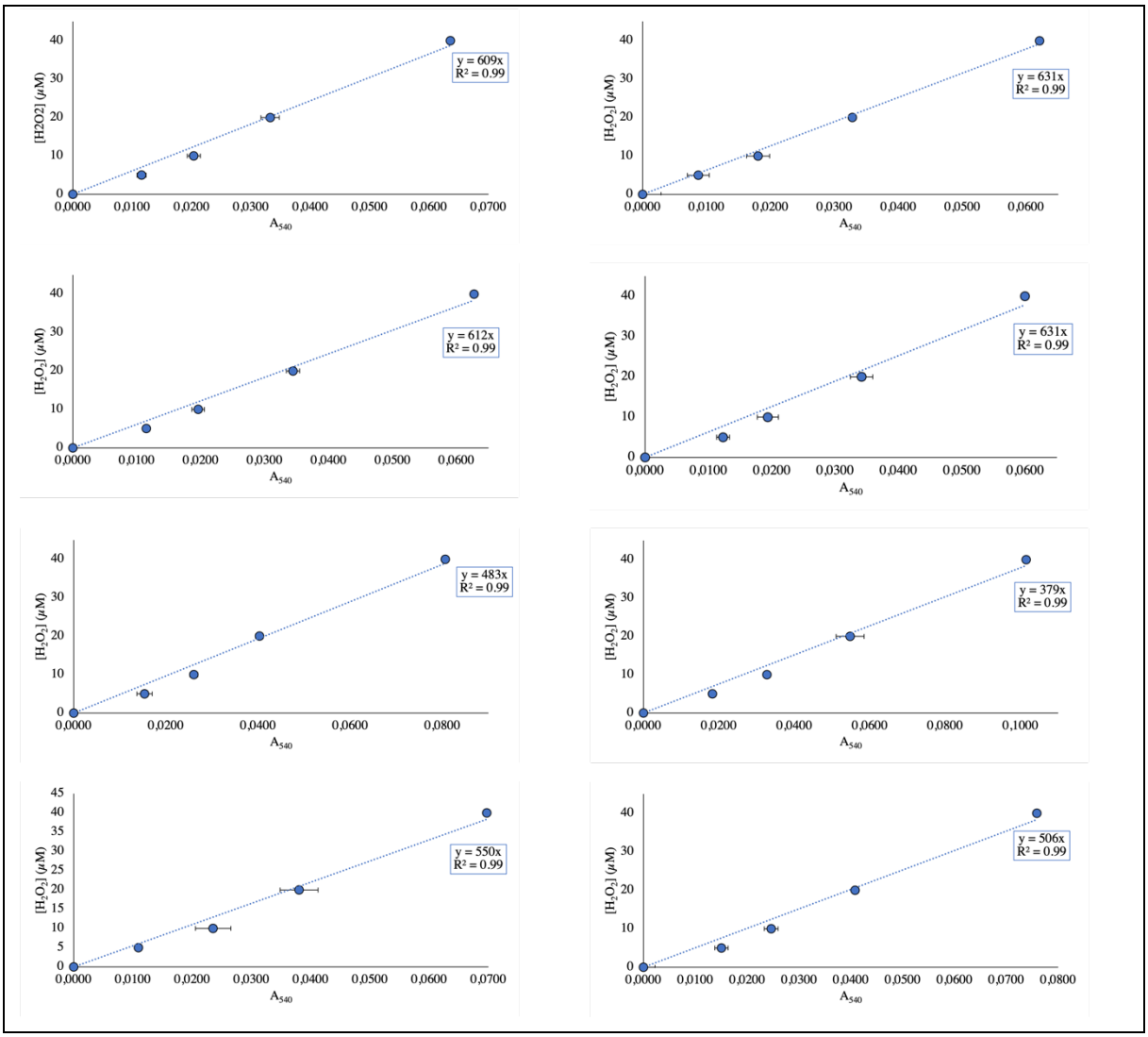

Figure 8.9: H_2O_2 calibration curves. *The calibration curves were prepared to quantify hydrogen peroxide produced in-situ by AfAA11B and NcAA9C. Monitored absorbance at λ = 540 nm is presented on the x-axis and the hydrogen peroxide concentration is given in µM on the y-axis. Each calibration cure is presented with a regression line, i.e., $y = \alpha x_i$, with the R-squared value. The error bars represent the standard deviations between the triplicates.*

PART II: STATISTICAL APPROACH

The oxidase activity presented in Chapter 4.4 were obtained by performing a simple linear regression, *i.e.,* $y_i = \alpha + \beta x_i$. This analysis assumes that there is a linear relationship between the explanatory variable *x* and the response variable *y*, and that the residuals are independent and normally distributed with a constant variation σ. However, data obtained during this analysis were not independent, as the resorufin absorbance monitored at one time point depend on the absorbance monitored previously.

One may use a mixed model with a nested design to account for this violation of model assumptions, generating a random slope with a random intercept model. Such a model would account for the dependency in the data. As this statistical approach is out of the scope of this thesis work, dependency in data was avoided (though not ignored) by analyzing the summarized values, *i.e.,* the average monitored absorbance for each time point. Hence, the model is valid, though not optimal (T. Egeland, pers. com., 2021). This statement was maintained throughout this thesis work.

ANOVA AND CONTRAST ANALYSES

Probability Models

1) $Y_{ij} = \mu_i + \varepsilon_{ij}$, where $\varepsilon_{ij} \sim N(0, \sigma)$ for *Af*AA11B
2) $Y_{ij} = \mu_i + \varepsilon_{ij}$, where $\varepsilon_{ij} \sim N(0, \sigma)$ for *Nc*AA9C

We assume independent observations in group i which are normally distributed with the expected initial rate of *in-situ* H_2O_2 production μ_i, and the mutual standard deviation σ for every observation in group i. Y_{ij} is the observed oxidase initial rate for LPMO replicate j representative for LPMO with gatekeeper residue exhibiting mutation *i.* Definitions of i = 1, 2, 3, 4 were presented in Table 8.4 (Appendix III) for Model 1 and 2. *Af*AA11B and *Nc*AA9C Q180D replicates are j = 1, …, 9. *Nc*AA9C WT, Q180E, and Q180N replicates are j = 1, …, 6. Replicates j are presented in Figure 8.10, indicating the precision in this experiment.

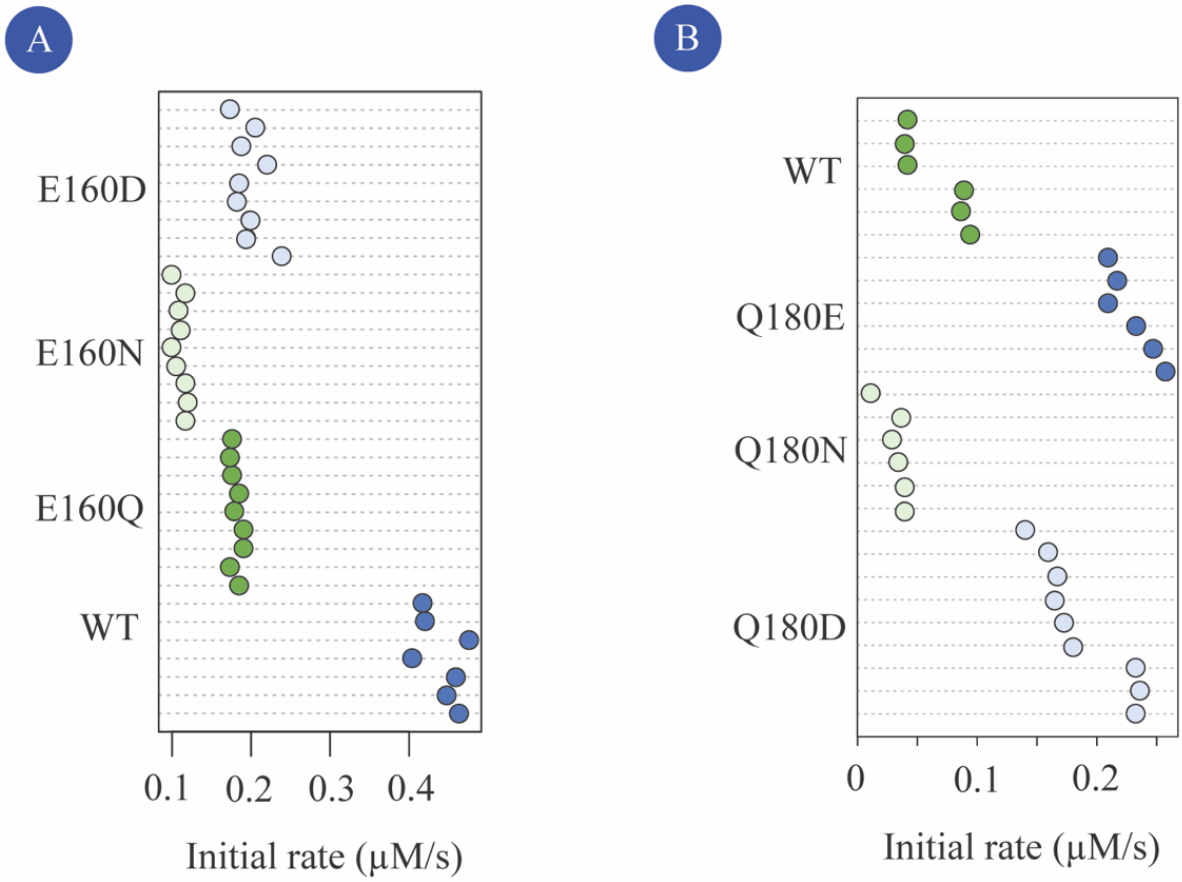

Figure 8.10: In-situ hydrogen peroxide production rate by AfAA11B and NcAA9C. *The precision of the (A) AfAA11B and (B) NcAA9C experiment was presented in this figure, showing the replicates on the y-axis and the initial rate in µM/S on the x-axis.*

MODEL ASSUMPTION EVALUATION

The models were evaluated similarly as described in Appendix III. Generated model evaluation plots are presented in Figure 8.11. However, two observations were considered outliers among the *Af*AA11B WT measurements and were removed from the dataset (observed r student values > 3). Nevertheless, Model 1 and Model 2 were assumed to be valid as the residuals were distributed relatively nicely around 0 in the residual plots, residuals followed the oblique line in the Normality Q-Q plot, and the in-group variation was relatively low in the box plots in Panel. Besides, symmetry in data was indicated by the similarity between the median and average value of oxidase activity. We also accounted for the dependency in data as described above.

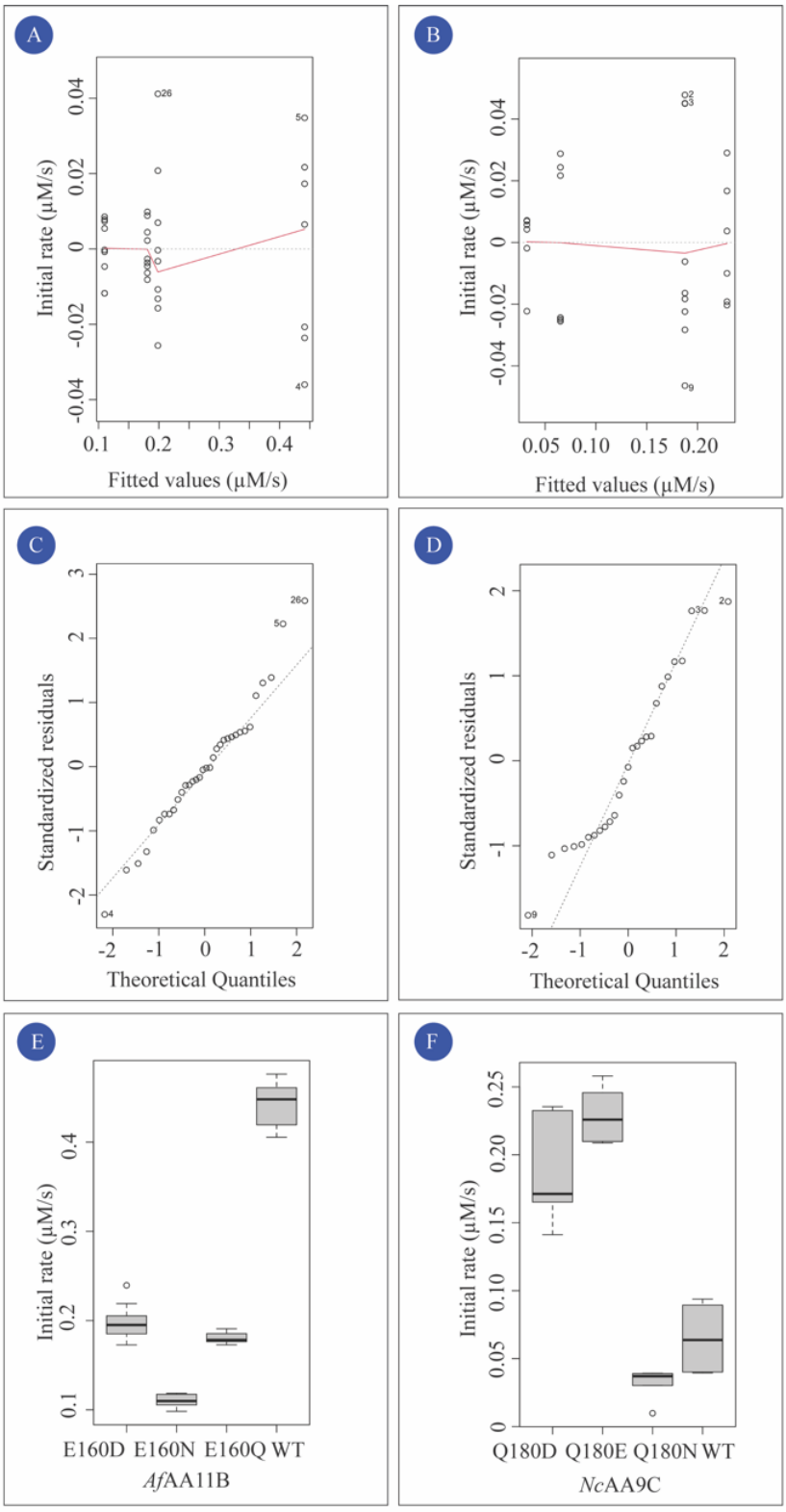

Figure 8.11: Evaluation of oxidase model assumptions for AfAA11B and NcAA9C. *Model 1 is evaluated by the plots in Panel A, C, and E. Model 2 is evaluated by the plots in Panel B, D, and F. (A/B) Residual plots. The fitted values (x-axis) versus residuals (y-axis) in mV should be distributed around 0. (C/D) Normal Q-Q plots. This plots present the theoretical quantiles (x-axis) versus standardized residuals (y-axis). (E/F) Box plots. Variation in redox potential (y-axis, mV) is presented for AfAA11B and NcAA9C WT and the gatekeeper mutants. Median (thick, black line) and quartiles (grey box) summarize the data.*

Analysis of Variance

A null hypothesis and an alternative hypothesis were defined to evaluate whether there is a significant difference in initial rates of *in-situ* H_2O_2 production by *Af*AA11B and *Nc*AA9C based on the mutated gatekeeper residue.

H_0: There is no group effect. $\mu_1 = \mu_2 = \mu_3 = \mu_4$

H_1: There is a group effect. At least one of the μ_i is different from μ_k

The null hypothesis was rejected for *Af*AA11B (p-value: $< 2 \times 10^{-16}$) and *Nc*AA9C (p-value: 3.5×10^{-12}) because the p-values for were lower than the stated significance level. The initial rates of *in-situ* H_2O_2 production by the gatekeeper variants of *Af*AA11B and *Nc*AA9C were significantly different. The confidence in this conclusion was supported by the R^2 values of Model 1 and Model 2 at 0.9 and 0.91, respectively.

Contrast Analyses

The effect of the gatekeeper residue's carboxylic acid and amide nature on the enzymes' oxidase activity was examined by contrast analyses. Moreover, it was investigated whether the *Af*AA11B and *Nc*AA9C variants exhibiting Glu in the gatekeeper position have the highest initial *in-situ* H_2O_2 production. Four contrasts were defined and are presented in Table 8.7. Further, the hypotheses were stated:

H_0: There is no effect from the nature of the gatekeeper residue. $\theta_1 = \theta_2 = \theta_3 = \theta_4 = 0$

H_1: The initial rate of *in-situ* H_2O_2 production is higher for LPMO variants with a carboxylic acid gatekeeper residue than an amide gatekeeper residue, and the highest initial rate is obtained for the LPMOs with a Glu in the gatekeeper position. θ_1, θ_2, θ_3, and $\theta_4 > 0$.

Table 8.7. Contrast analyses related to the gatekeeper residue nature and oxidase activity. The defined contrasts θ_i is presented with the estimated 95% CI for θ_i estimated in R studio.

CONTRAST θ_i	GATEKEEPER VARIANT COMPARISON	95% CI for θ_1 (µM/s)
$\theta_1 = 0.5(\mu_1 + \mu_4) + (-0.5)(\mu_2 + \mu_3)$	*Af*AA11B WT/E160D vs E160Q/E160N	[0.16; 0.18]
$\theta_2 = 0.5(\mu_1 + \mu_2) + (-0.5)(\mu_3 + \mu_4)$	*Nc*AA9C Q180D/Q180E vs WT/Q180N	[0.13; 0.18]
$\theta_3 = (-0.33)(\mu_1 + \mu_2 + \mu_3) + \mu_4$	*Af*AA11B WT vs E160Q/E160N/E160D	[0.26; 0.29]
$\theta_4 = (-0.33)(\mu_1 + \mu_3 + \mu_4) + \mu_2$	*Nc*AA9C Q180E vs WT/Q180D/Q180N	[0.11; 0.16]

We may state that there is a significant effect on the initial rate of *in-situ* H_2O_2 production based on the nature of the gatekeeper residue because the value 0 is not in the 95% CI for θ_1 ([0.16; 0.18] µM/s) and θ_2 ([0.13; 0.18] µM/s). Moreover, the 95% CI for θ_3 and θ_4 was estimated to be [0.26; 0.29] µM/s and [0.11; 0.16] µM/s, respectively. Hence, if Glu is in the gatekeeper position of the studied LPMOs, the initial rate is significantly higher compared with the other gatekeeper variants of *Af*AA11B and *Nc*AA9C. We reject the null hypothesis.

The effect of the gatekeeper residue side-chain length on the oxidase activity was also examined by contrast analyses. We thought that the gatekeeper residue with the longest side-chain length of each side-chain nature would give the highest oxidase activity. Following contrast were defined in Table 8.8. The following hypotheses were stated:

H_0: There is no effect on oxidase activity from the side-chain length of the gatekeeper residue.
$\theta_1 = \theta_2 = \theta_3 = \theta_4 = 0$
H_1: The initial rate of hydrogen peroxide production is higher for LPMO gatekeeper variants with a longer side-chain. $\theta_1, \theta_2, \theta_3,$ and $\theta_4 > 0$.

Table 8.8. Contrast analyses related to gatekeeper residue side-chain length and oxidase activity. The defined contrasts θ_i is presented with the estimated 95% CI for θ_i estimated in R studio.

CONTRAST θ_i	GATEKEEPER VARIANT COMPARISON	95% CI for θ_I (µM/s)
$\theta_1 = 0.5(\mu_4) + (-0.5)(\mu_1)$	*Af*AA11B WT vs E160D	[0.11; 0.13]
$\theta_2 = 0.5(\mu_3) + (-0.5)(\mu_2)$	*Af*AA11B E160Q vs E160N	[0.03; 0.04]
$\theta_3 = 0.5(\mu_2) + (-0.5)(\mu_1)$	*Nc*AA9C Q180E vs Q180D	[6×10^{-3}; 0.04]
$\theta_4 = 0.5(\mu_4) + (-0.5)(\mu_3)$	*Nc*AA9C WT vs Q180N	[3×10^{-4}; 0.03]

The null hypothesis was rejected. Certainly, a longer side-chain generated a significant higher oxidase activity for every gatekeeper variant of *Nc*AA9C and *Af*AA11B, as none of the 95% confidence intervals exhibited the value 0. The 95% confidence intervals for θ_1, θ_2, θ_3, and θ_4 were estimated to be [0.11; 0.13], [0.03; 0.04], [6×10^{-3}; 0.04], and [3×10^{-4}; 0.03] µM/s, respectively.

APPENDIX V PEROXIDASE ACTIVITY

Appendix V comprises of the statistical approach related to the obtained results from the Breslmayr assay.

Probability Models

1) $Y_{ij} = \mu_i + \varepsilon_{ij}$, where $\varepsilon_{ij} \sim N(0, \sigma)$ for *Af*AA11B
2) $Y_{ij} = \mu_i + \varepsilon_{ij}$, where $\varepsilon_{ij} \sim N(0, \sigma)$ for *Nc*AA9C

By stating Model 1 and Model 2, we assume that the observations in group *i* are independent and normally distributed with the expected initial rate of hydrogen peroxide consumption μ_i and the mutual standard deviation σ for every observation in group *i*. Y_{ij} is the observed initial rate for H_2O_2 consumption for LPMO replicate *j* representative for LPMO with gatekeeper residue exhibiting mutation *i*. Definition of *i = 1, 2, 3, 4* were presented in Table 8.4 (Appendix III) for Model 1 and 2. *Af*AA11B replicates are *j* = 1, …, 9. *Nc*AA9C replicates are *j* = 1, 2. Replicates *j* are presented in Figure 8.12.

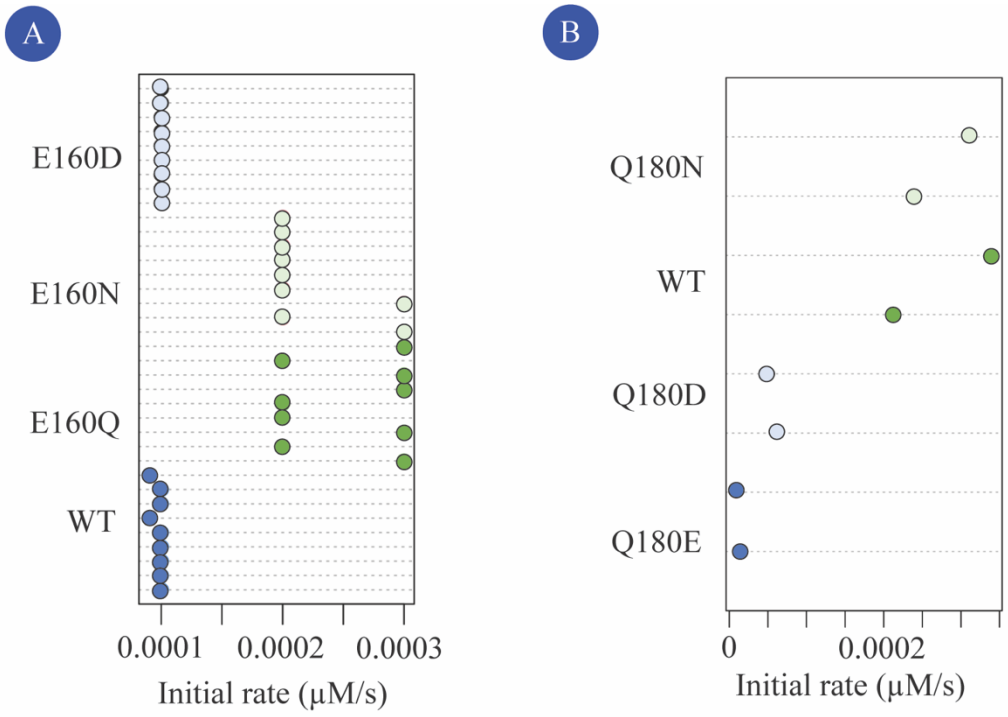

Figure 8.12: Precision of hydrogen peroxide consumption rate by AfAA11B and NcAA9C. *Observation j per (A) AfAA11B and (B) NcAA9C are presented on the y-axis and the initial rate of hydrogen peroxide consumption is presented in the x-axis in µM/S.*

MODEL ASSUMPTION EVALUATION

The protocol for evaluation of statistical models described in Appendix III was used for model evaluation of the presented models. Obtained plots during the model evaluation are presented in Figure 8.13. Model 1 and Model 2 were suboptimal but anticipated as valid for this master's thesis purpose.

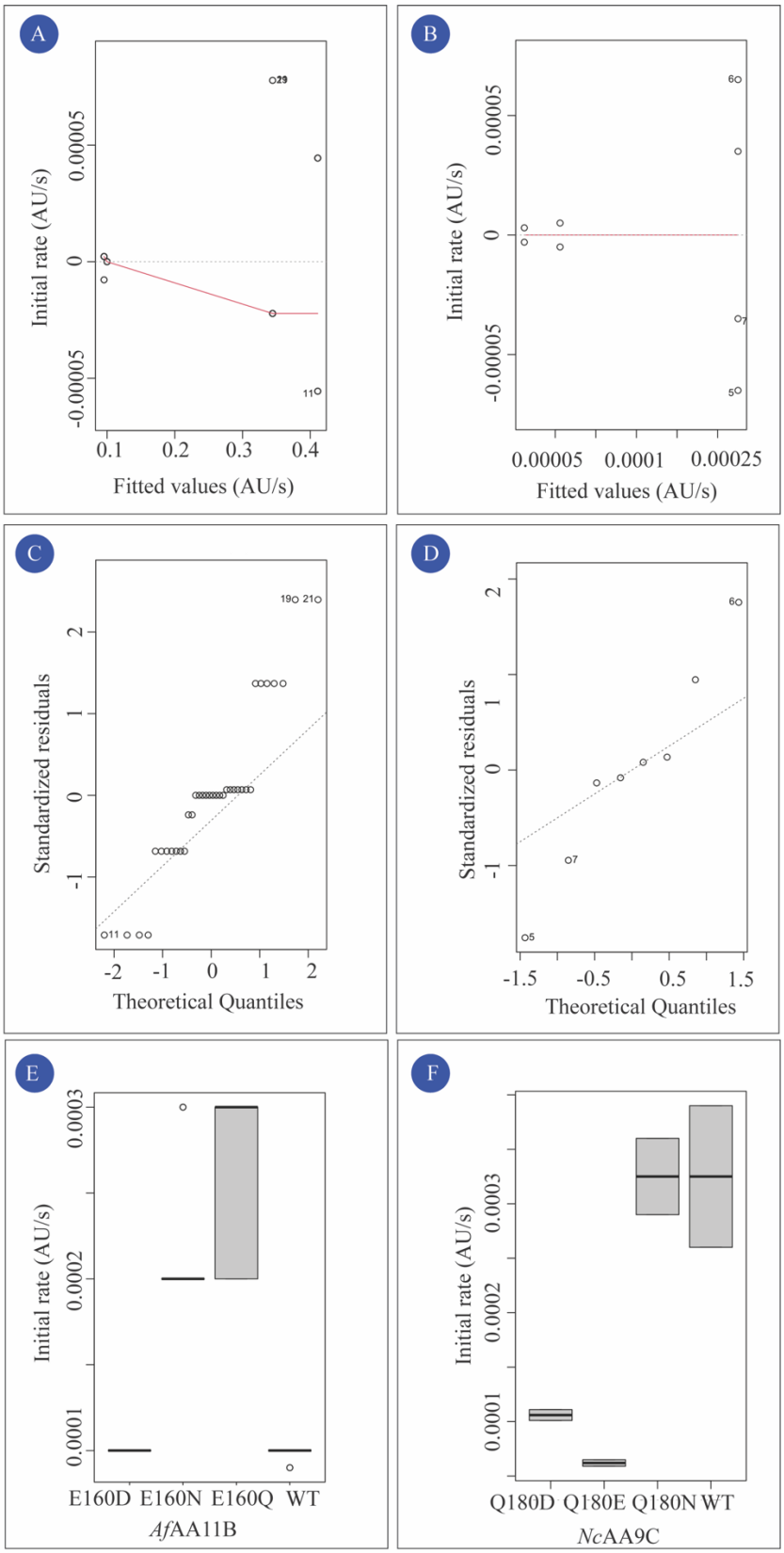

Figure 8.13: Evaluation of peroxidase model assumptions in Model 1 and Model 2. *Presentation of Model 1 (left) and 2 (right) evaluation. (A/B) Residual plot with plotted residual fitted values (AU/s) concerning the initial rates (AU/s). (C/D) Normal Q-Q plot with standardized residuals as response value and the theoretical quantiles plotted on the x-axis. (E/F) Box plot presenting the variation in initial rates (AU/s) between groups and within groups.*

ANALYSIS OF VARIANCE

Evaluation of a potentially significant difference in initial rates of hydrogen peroxide consumption by *Af*AA11B and *Nc*AA9C based on the gatekeeper residue was performed by stating the following hypotheses:

H_0: There is no group effect. $\mu_1 = \mu_2 = \mu_3 = \mu_4$
H_1: There is a group effect. At least one of the μ_i is different from μ_k

The ANOVA generated p-values for *Af*AA11B (3×10^{-12}) and *Nc*AA9C (0.0132). Because the p-values were lower than the significance value, the null hypothesis was rejected for both models. The initial rates of hydrogen peroxide consumption by the gatekeeper variants of *Af*AA11B and *Nc*AA9C were significantly different. The R^2 values of Model 1 (0.83) and Model 2 (0.92) supported the confidence of this statement, as the R squared values explain the amount of the total variation in the models, which is explained by the group variation.

CONTRAST ANALYSES

Contrast analyses examined whether the gatekeeper residue's carboxylic acid nature significantly reduced the initial rates of hydrogen peroxide consumption. Furthermore, one was interested in investigating if the glutamate mutant of *Af*AA11B and *Nc*AA9C induced the lowest initial rate of H_2O_2 consumption by the LPMOs. Table 8.9 presents the four defined contrasts. The hypotheses were stated before testing:

H_0: There is no effect from the nature of the gatekeeper residue. $\theta_1 = \theta_2 = \theta_3 = \theta_4 = 0$
H_1: The initial rate of H_2O_2 consumption is lower for LPMO variants with a carboxylic acid gatekeeper nature compared with an amide gatekeeper nature, and the lowest initial rate is obtained for the LPMOs with glutamate gatekeeper residue. $\theta_1, \theta_2, \theta_3,$ and $\theta_4 < 0$.

Table 8.9. Contrast analyses performed in R studio evaluating the peroxidase activity of *Af*AA11B and *Nc*AA9C with respect to the nature of the gatekeeper residue. The defined contrasts θ_i is presented with the estimated 95% CI for θ_i.

CONTRAST θ_i	GATEKEEPER VARIANT COMPARISON	95% CI for θ_1 (AU/s)
$\theta_1 = 0.5(\mu_1 + \mu_4) + (-0.5)(\mu_2 + \mu_3)$	*Af*AA11B WT/E160D vs E160Q/E160N	$[-2 \times 10^{-4}; -1 \times 10^{-4}]$
$\theta_2 = 0.5(\mu_1 + \mu_2) + (-0.5)(\mu_3 + \mu_4)$	*Nc*AA9C Q180D/Q180E vs WT/Q180N	$[-3 \times 10^{-4}; -1 \times 10^{-4}]$
$\theta_3 = (-0.33)(\mu_1 + \mu_2 + \mu_3) + \mu_4$	*Af*AA11B WT vs E160Q/E160N/E160D	$[-1 \times 10^{-4}; -6 \times 10^{-5}]$
$\theta_4 = (-0.33)(\mu_1 + \mu_3 + \mu_4) + \mu_2$	*Nc*AA9C Q180E vs WT/Q180D/Q180N	$[-3 \times 10^{-4}; -7 \times 10^{-5}]$

The initial rate of hydrogen peroxide consumption by the LPMOs is significantly negatively affected by the carboxylic nature of the gatekeeper residue because the value 0 is not in the 95% CI for θ_1 ($[-2 \times 10^{-4}; -1 \times 10^{-4}]$ AU/s) and θ_2 ($[-3 \times 10^{-4}; -1 \times 10^{-4}]$ AU/s). $[-1 \times 10^{-4}; -6 \times 10^{-5}]$ AU/s and $[-3 \times 10^{-4}; -7 \times 10^{-5}]$ AU/s was the estimated 95% CI for θ_3 and θ_4, respectively. For this reason, the null hypothesis was rejected. The carboxylic acid gatekeeper residue lowers the initial rate of H_2O_2 consumption compared with the amide gatekeeper variants of *Af*AA11B and *Nc*AA9C.

Contrast analyses were also performed to investigate if the side-chain length of the gatekeeper residue was affecting the LPMOs peroxygenase activity. The following hypotheses were stated:

H_0: There is no effect from the gatekeeper residue side-chain length. $\theta_1 = \theta_2 = \theta_3 = \theta_4 = 0$
H_1: The initial rate of H_2O_2 consumption is lower for LPMO variants with a longer side-chain of the same nature. $\theta_1, \theta_2, \theta_3,$ and $\theta_4 < 0$.

Table 8.10 presents the defined contrasts and 95% CI for the respective θs. Interestingly, only the difference in peroxidase activity of *Af*AA11B E160Q and E160N was stated as significant on a 5% significance level based on the gatekeeper residue side-chain length (95% CI: [0.0000001; 0.00003] AU/s). This 95% CI for θ was the only presented interval not including the value 0, as the 95% CIs for θ_1, θ_3, and θ_4 were estimated to be $[-2 \times 10^{-5}; 2 \times 10^{-5}]$, $[-9 \times 10^{-5}; 5 \times 10^{-5}]$, and $[-7 \times 10^{-5}; 7 \times 10^{-5}]$ AU/s, respectively. It should be noted that the number of observations of the *Nc*AA9C experiment were very low, and both models were approved even though the model assumptions were not ideal. Suboptimal models may affect the validity of statistical tests, such as contrast analyses.

Table 8.10. Contrast analyses performed in R studio evaluating the peroxidase activity of *Af*AA11B and *Nc*AA9C with respect to the gatekeeper residue side-chain length. The defined contrasts θ_i is presented with the estimated 95% CI for θ_i.

CONTRAST θ_i	GATEKEEPER VARIANT COMPARISON	95% CI for θ_1 (AU/s)
$\theta_1 = 0.5(\mu_4) + (-0.5)(\mu_1)$	*Af*AA11B WT vs E160D	[-0.00002; 0.00002]
$\theta_2 = 0.5(\mu_3) + (-0.5)(\mu_2)$	*Af*AA11B E160Q vs E160N	[0.0000001; 0.00003]
$\theta_3 = 0.5(\mu_2) + (-0.5)(\mu_1)$	*Nc*AA9C Q180E vs Q180D	[-0.00009; 0.00005]
$\theta_4 = 0.5(\mu_4) + (-0.5)(\mu_3)$	*Nc*AA9C WT vs Q180N	[-0.00007; 0.00007]

APPENDIX VI ENZYMATIC ACTIVITY

Calibration curves used for quantification of oxidized products during *Af*AA11B enzymatic activity evaluation are presented in Appendix VI.

A2ox

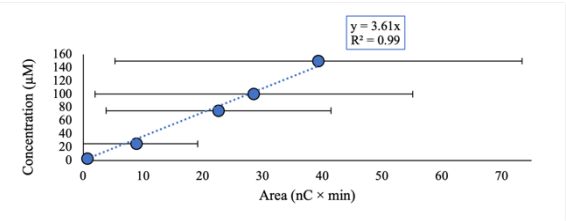

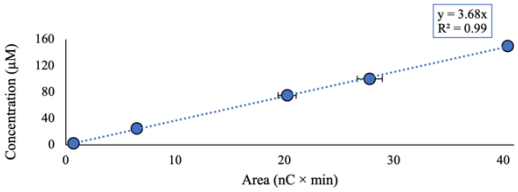

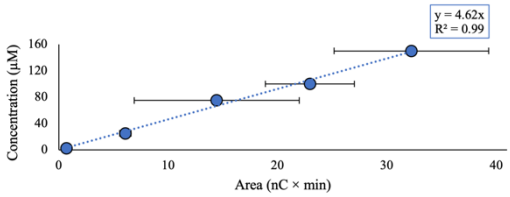

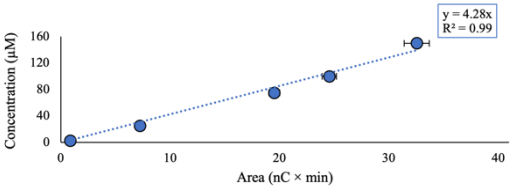

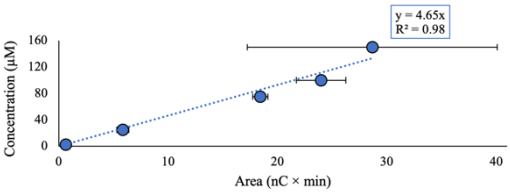

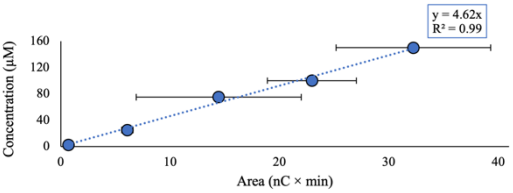

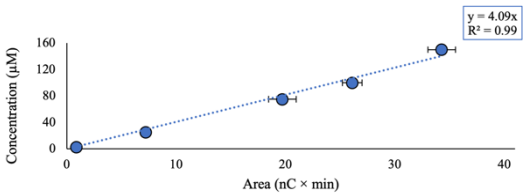

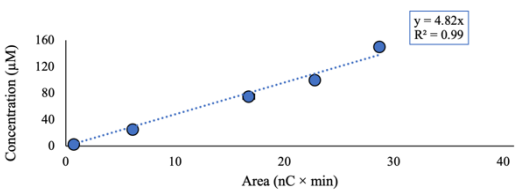

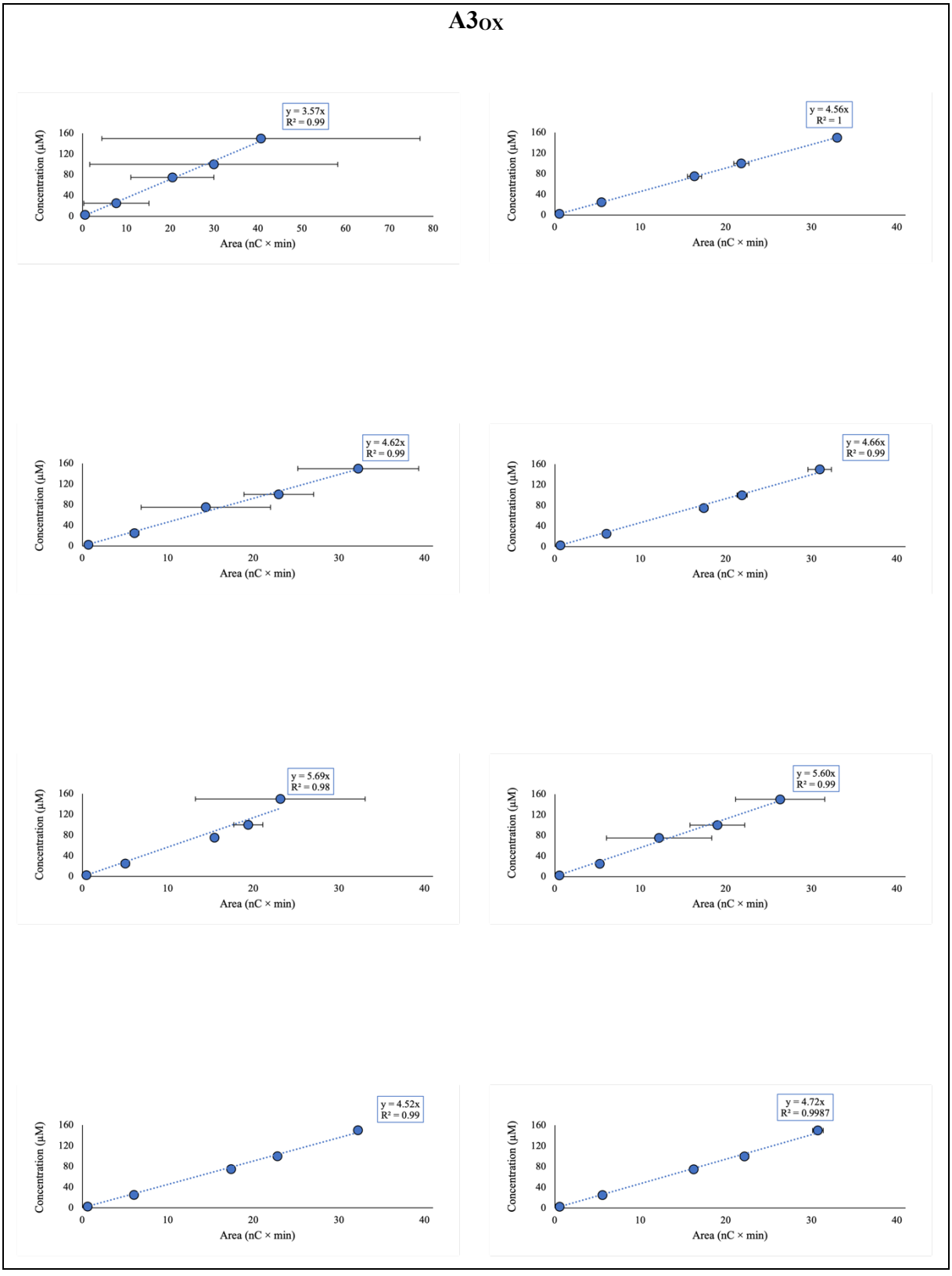

Figure 8.14: $A2_{OX}$ and $A3_{OX}$ calibration curves. *The calibration curves were used for quantification of oxidized products, i.e., oxidized dimer ($A2_{ox}$) and oxidized trimer ($A3_{ox}$) from the AfAA11B catalyzed oxidation of the soluble substrate $(GlcNAc)_4$ under various of conditions. Each calibration curve is presented with the regression line, $y = \alpha x_i$, where y is the concentration of oxidized products in µM and x is the peak area in nC × min. The R squared value of each regression line is also presented. The variation between the triplicates is presented with error bars.*

Norges miljø- og biovitenskapelige universitet
Noregs miljø- og biovitskapelege universitet
Norwegian University of Life Sciences

Postboks 5003
NO-1432 Ås
Norway